The mafic-ultramafic intrusions in the Bakhuis Granulite Belt, Western Suriname: heat source for UHT metamorphism?

A.C.D. Thijssen

Supervised by: Dr. E.W.F. de Roever

Prof. Dr. G.R. Davies

Dr. F.M. Brouwer

vrije Universiteit amsterdam

Figure front page: *Outcrop AT20 in the Zandkreek.*

The mafic-ultramafic intrusions in the Bakhuis Granulite Belt, Western Suriname: heat source for UHT metamorphism?

A.C.D. Thijssen
Student number: 1707833
Master thesis Solid Earth (course code AM_450199, 27 ECTS)

Supervised by:
- Dr. E.W.F. de Roever
- Prof. Dr. G.R. Davies
- Dr. F.M. Brouwer

Faculty of Earth and Life Sciences
Petrology Department
VU University, Amsterdam

January, 2016

ABSTRACT

The Bakhuis Granulite Belt (BGB) is a PaleoProterozoic granulite facies domain in west Suriname, South America. Mineral assemblages such as sapphirine + quartz and orthopyroxene + sillimanite + quartz indicate that the belt experienced Ultrahigh-Temperature (UHT) metamorphism, which was dated at 2,07 – 2.05 Ga (*De Roever et al., 2003a*). In the SW part of the belt charnockites dominate over granulites. Earlier research (*Klaver, 2011; Klaver et al., 2015a*) indicated that charnockite magmatism is the result of a second, younger UHT-like event at 1,99-1,98 Ga. The heat source for UHT metamorphism and the younger UHT-like event has not yet been identified, but might be related to the mafic-ultramafic intrusions which are present throughout the BGB.

Fieldwork, petrography, geochemical investigation and U-Pb dating indicated the presence of two generations of mafic magmatism in the BGB. The Moi-Moi Metagabbro is characterized by its association with ultramafic rocks and by the common presence of cm-sized poikilitic hornblende crystals in mafics and ultramafics. They contain a range of different cumulate and non-cumulate rocks, related to each other by fractionation and accumulation of olivine, pyroxene and plagioclase from a hydrous, tholeiitic parental magma. The rocks show a characteristic subduction signature in their trace elements, which, together with the hydrous nature of the magma, points to subduction-related magmatism. The Moi-Moi Metagabbro was dated at 1984 +/- 4 Ma by U-Pb zircon dating and clearly postdates the UHT metamorphism in the BGB. However, this age is identical to the age of the charnockite magmatism. Underplating of the (meta)gabbroic magma or slab detachment is suggested to have been the heat source for the charnockite magmatism.

The younger Charlie Gabbro crystallized from a tholeiitic HAB melt. Variation within the series is explained by the fractionation and accumulation of plagioclase and olivine. U-Pb baddeleyite dating resulted in an age of 1970 +/-17 Ma. Just like the Moi-Moi Metagabbro, the Charlie Gabbro rocks show characteristic subduction related trace element patterns, but they lack hydrous magmatic minerals. The Charlie Gabbro magmatism is expected to be related to the waning stage of northward subduction during the final phase of the Trans-Amazonian orogeny.

The Charlie Gabbro does not show metamorphism, whereas the Moi-Moi Metagabbro rocks show a metamorphic overprint in the high amphibolite facies to possibly granulite-facies. Its age, of 1970 +/- 17 Ma, indicates the end of Trans-Amazonian metamorphism in the BGB.

Table of contents

Appendices

Appendix I:	Sample locations
Appendix II:	Whole rock major element geochemistry (Wt-%) – XRF
	Whole rock trace element geochemistry (ppm) – XRF
	Whole rock trace element geochemistry (ppm) – ICP-MS
Appendix III:	CIPW norm
Appendix IV:	Trace element content zircons ER1109
	U-Pb data zircons LA150
Appendix V:	Kilo Drie Metagabbro composition compared to the Charlie Gabbro composition

1. INTRODUCTION

1.1 The Bakhuis Granulite Belt

The Bakhuis Granulite Belt (further abbreviated as BGB) is a NE-trending, horst-like structure in northwestern Suriname, in the central part of the Guiana Shield. It underwent metamorphism under granulite-facies conditions. Besides this belt, there are three other granulitic domains in the Guiana Shield (see Figure 2.3). The BGB stands out because of the occurrence of mineral assemblages, such as Sil + Opx + Qz and Spr + Qz, which are characteristic for Ultrahigh-temperature (UHT) metamorphism (*Harley, 1998;* > 900 ^{o}C and 7 - 14 kbar). These assemblages were first mentioned by *De Roever (1975)* and are extensively described by *De Roever et al. (2003)*.

De Groot (2008) and *Nanne (2013)* established by feldspar thermometry that peak temperatures during UHT metamorphism reached 1000 to 1050 ^{o}C. *Nanne (2013)* also found that UHT metamorphism took place throughout a large part of the BGB. A source of extreme heat is required to reach these exceptional temperatures.

1.2 Aims of this study

The source of the extreme heat for the UHT metamorphism was postulated by *Delor et al., (2003b)* to be asthenospheric mantle upwelling (Figure 1.3b). Mafic intrusions in the BGB might represent evidence of such mantle upwelling or of underplating of mafic magma. More or less synkinematic metadolerite dykes are present in the BGB, but occur only in minor amount, as small dykes of < 1 m width, and are considered to be not voluminous enough to be the heat source for the UHT metamorphism. However, larger mafic and mixed mafic-ultramafic intrusions are present throughout the BGB, but are particularly voluminous in the SW part of the BGB.

The first aim of this study is to determine whether these intrusions are the heat source of UHT metamorphism, which might be the case if they have the same age. The second aim of this study is to analyse their geochemical signature, to determine in what kind of setting they were formed and whether this setting might be related to UHT metamorphism.

1.3 Approach

Several mafic-ultramafic bodies in the SW part of the BGB will be extensively sampled. Access to the area is difficult due to the rainforest. The Kabalebo Nature Resort, a lodge in the SW of the BGB, is located close to several mafic bodies and will be used as base camp. Drill cores of the Geological and Mining Survey of Suriname (GMD) might be used as addition to samples taken in the field.

Dating of gabbroic rocks is quite difficult, in particular if the rocks do not contain (a small amount of) zircon, but baddeleyite (ZrO_2) instead. Separation of baddeleyite has not yet been carried out at the VU and baddeleyite dating would require a good standard, preferably of baddeleyite itself.

Chemical analysis of major and trace elements, together with petrography, should give a characterisation of the mafic and mafic-ultramafic intrusions. One of the major goals is to estimate the parental magma composition. Due to the scarcity of outcrops, it will probably be not possible to find 'chilled margins' which would give a good approximation of the parental magma composition. The variation in major and trace elements will be used to estimate the parental magma composition and to determine how the magma evolved within one body.

The full investigation of the mafic intrusions and metadolerite dykes is too much work for one student. Therefore, another MSc student, Bertram Uunk, will carry out the second part of the investigation, including a radiogenic isotope characterisation of the mafic intrusions as well as chemical characterisation of the metadolerites.

1.4 Project framework and funding

This research project is part of the MSc program Earth Sciences – Solid Earth of the VU University in Amsterdam and represents the Master Thesis Solid Earth (course code AM_450199). This project is supervised by Dr.

Emond W.F. de Roever, who has a guest status at the VU University and is a former employee of the GMD, and by Prof. Dr. Gareth R. Davies and Dr. Fraukje M. Brouwer, senior lecturers at the VU University, Amsterdam.

Fieldwork in Suriname was carried out in October and November 2012. Processing and chemical analysis of the samples was done at the geological laboratories of the Faculty of Earth and Life Sciences (FALW) of the VU University, Amsterdam. Only the LA-ICP-MS zircon analysis, was done at the Institut für Mineralogie of the Westfälische Wilhems-Universität Münster.

The Geological and Mining Survey of Suriname supported this project by providing drill cores, facilitating export of the field samples and by technical support. Also, Naturalis, the Dutch national museum of natural history, provided a sample for this research.

The fieldwork could not have been done without the much appreciated financial support of the Stichting Dr. Schürmann Fonds, who paid the major part of the costs for the fieldtrip, and the Stichting Molengraaff Fonds. In addition, the Faculty of Earth and Life Sciences of the VU University gave subsidy to enable the fieldwork.

1.5 Ultrahigh-temperature (UHT) metamorphism

UHT metamorphism is a relatively new concept. Before the 90's, the main theory was that granulite facies metamorphism did not exceed temperatures of 850 ^{o}C. During the 90's UHT metamorphism was introduced and defined by *Harley (1998)* and from this moment on, UHT metamorphism became a hot topic (e.g. *Brown & Korhonen, 2009; Harley, 2008; Kelsey, 2008; Kelsey and Hand, 2015;* and references therein). At this moment, there are already more than 60 places known where this special type of metamorphism has occurred, and more are still discovered (*Kelsey and Hand, 2015*).

1.5.1 UHT metamorphism: definition

UHT metamorphism is defined as crustal metamorphism at mid to deep crustal levels, with temperatures that exceed 900 ^{o}C and at moderate pressures of 7-14 kbar (*Harley, 1998*), which takes place at a regional scale (> 1000 km^2; *Harley, 1998*). Characteristic assemblages are formed in rocks with a high magnesium and aluminium content, such as metapelites, and are extensively described by *Harley (1998; 2004; 2008) and Kelsey (2008).*

The upper temperature limit of UHT metamorphism is defined by the liquidus of the crustal rocks (*Harley 1998; Brown, 2007*) which, in turn, is based on their composition since the liquidus is shifted towards higher temperatures by removing water and adding carbon dioxide to the rocks (*Winter, 2001*), making it possible for rocks to reach these extreme temperatures without melting. This suggests that UHT metamorphosed rocks would have an anhydrous or carbon dioxide-rich source rock, which is confirmed by CO_2-rich fluid inclusions that are often present in UHT rocks (*Santosh and Omori, 2008*).

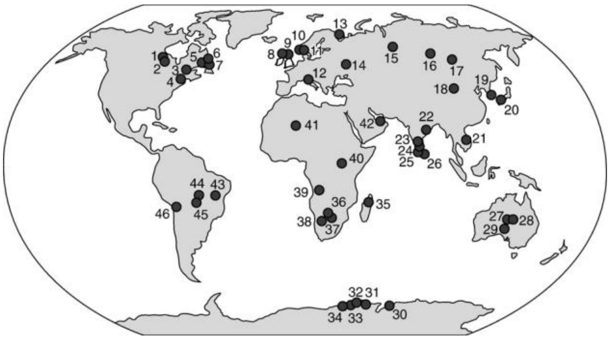

Figure 1.1: *Occurrences of known UHT rocks. Note the absence of the UHT rocks in Suriname. Figure taken from Kelsey, 2008.*

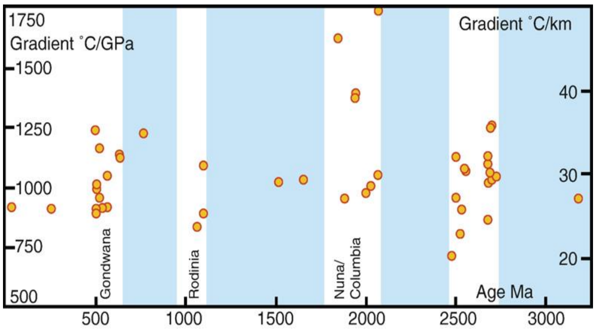

Figure 1.2: *Ages of UHT rocks. Four distinct periods, coincident with the supercontinent cycle, can be seen during Earth's history. Figure taken from Brown, 2006.*

1.5.2 Tectonic settings of UHT metamorphism

UHT metamorphism is present on every continent (Figure 1.1); in ancient cratons, more recent mobile belts (*Brown, 2007; Kelsey, 2008*) and even, but more rare, in xenoliths in kimberlites (*Dawson et al., 1997*). UHT metamorphism took place in at least four distinct periods of the Earth's history (Figure 1.2), which are often associated with the crustal aggregation of supercontinents (*Brown, 2007*) and record the closure and thickening of the continental back-arcs (*Hyndman, 2005*). In addition, many UHT granulites in Pan-African aged mobile belts show similarities to inverted and thickened back-arc basins (*Brown, 2006; 2007; Brown and Korhonen, 2009*).

A way to create UHT granulites is by post-collisional delamination and slab detachment, creating a slab window through which the asthenosphere can rise towards the overlying plate and cause UHT metamorphism (Figure 1.3a) (*Santosh and Omori, 2008; Harley, 2008*). Other proposed mechanism are an extension-magmatic accretion model, by which underplating of voluminous mafic magma takes place in the lowermost crust (*Bohlen and Mezger, 1989; Harley et al., 1990*), multiple intraplating of dykes and sills (*Jackson et al., 2003*) and contact metamorphism against intrusions with a high temperature, such as anorthosites, charnockites or gabbronorites (*McFarlane et al., 2003; Barbosa et al., 2006; Arima and Gower, 1991*). Besides these mechanisms *Guo et al. (2012)* describe several other tectonic environments in which UHT metamorphism could occur. Since most of these mechanism did probably not occur in the BGB, they will not be discussed in this thesis. The causes of UHT metamorphism are still poorly understood and a clear link between UHT metamorphism and the supercontinent cycle has not been found.

a) Post-orogenic extension (present Himalaya)

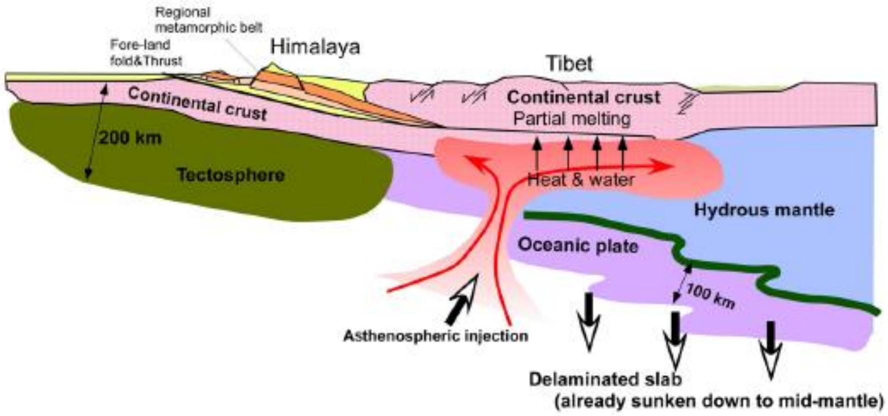

b) Continental rift

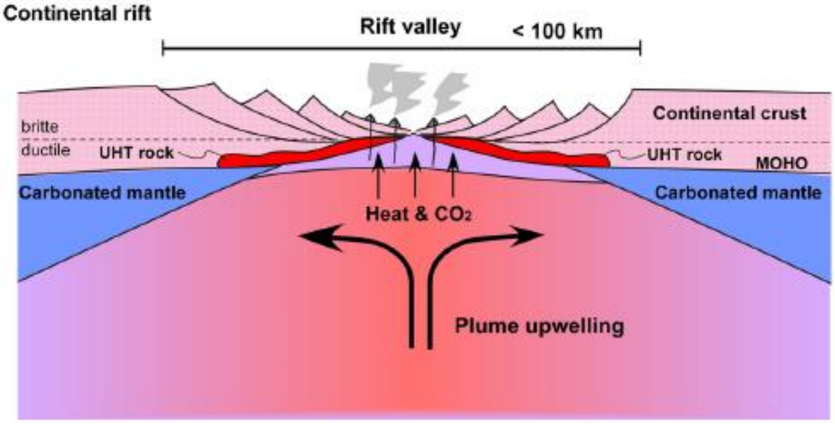

Figure 1.3: *a) Post-collisional delamination and slab break-off cause a slab window through which the hot asthenosphere can rise towards the overlying plate and may cause UHTM. b) UHT metamorphism due to mantle upwelling. Figures are taken from Santosh and Omori (2008).*

2. GEOLOGICAL SETTING

The Amazonian Craton is one of the biggest and best preserved cratons in the world and covers $1,5 \cdot 10^6$ km^2 of the northern part of South America (Figure 2.1) (*Delor et al., 2003b*). It extends from east Colombia and Venezuela, over Guyana, Suriname, French Guiana to north-eastern and central Brazil and is limited by the Phanerozoic Andean belt in the west and the Neoproterozoic Paraguai-Araguaia Fold Belt in the east and southeast (*Cordani et al, 2009; Santos et al., 2000*). The Craton is divided into a northern segment, the Guiana Shield, and a southern segment, the Guaporé, or Central Brazilian Shield by the Amazon basin, which has a Precambrian basement below the basin sediments.

A short summary of the evolution of the Guiana Shield is given in the following paragraphs. A more detailed description is given by *Delor et al. (2003b)* and *Kroonenberg & De Roever (2010).*

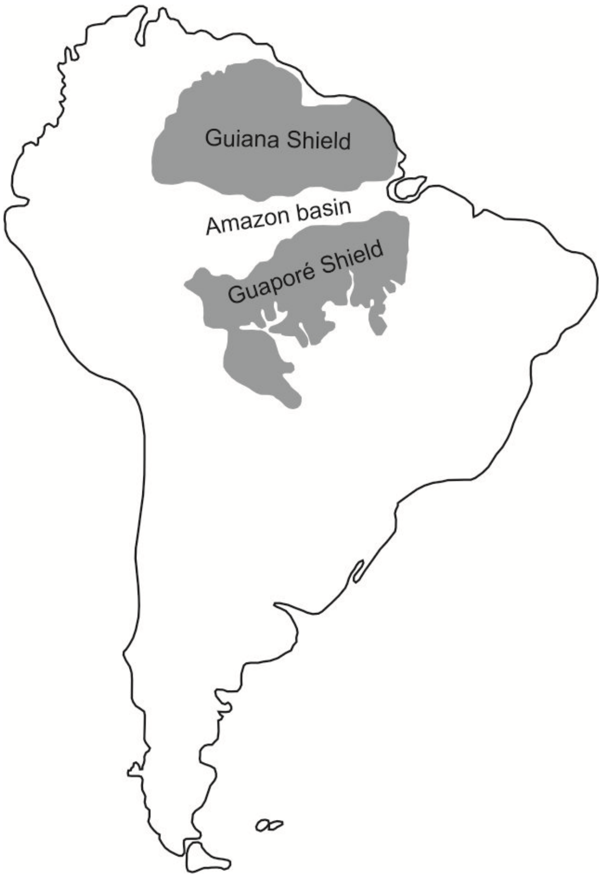

Figure 2.1: *Location of the Amazonian Craton in South America and the Guiana Shield, the Guaporé Shield and the Amazon basin in the Amazonian Craton.*

2.1 The Guiana Shield

The Guiana Shield contains two reworked granulitic terranes of Archean age, the Imataca Complex in Venezuela (dated 3,7 – 2,6 Ga; *Cordani &Teixeira, 2007; Montgomery & Hurley, 1978; Tassinari et al., 2004*) and the Amapá block in Brazil (3,3 – 2,6 Ga; *Avelar et al., 2003; Da Rosa-Costa et al., 2006; 2009*) (Figure 2.3).

The main crustal growth of the Shield was during the Trans-Amazonian orogeny, a tectonothermal event at about 2,26 to 1.93 Ga *(Delor et al. 2003a).* The orogeny resulted from the convergence of the West African shield and the Amazonian protocraton. *Delor et al. (2003a; 2003b)* divided this orogeny into two stages, the Main Trans-Amazonian event, from 2,26 to 2,08 Ga, and the Late Trans-Amazonian event, from 2.07 to 1.93 Ga. They describe the beginning of the main Trans-Amazonian event (2,26 – 2,20 Ga) as rifting of the Archean plates during which juvenile tholeiitic oceanic crust was formed (Figure 2.2A). From 2,18 to 2,13 Ga, a NS oriented convergence between the Amazonian protocraton and the West African shield took place which resulted in a supposedly southward subduction of the basaltic juvenile crust, island-arc volcanism and the formation of tonalite-trondhjemite-granodiorite (TTG) intrusions (Figure 2.2B).

During this period, the associated volcanic and sedimentary sequences were folded and metamorphosed at greenschist to amphibolites facies. The steeply folded TTG-greenstone belt was accreted against the Archean terranes in the south. The belt can be seen along the whole northern coast, from Imataca in Venezuela, along the coast of Guyana, Suriname and French Guiana, towards the Amapá block in Brazil (Figure 2.3). However, the TTG-greenstone belt is not continuous but is divided into a western and an eastern branch by the Bakhuis horst. The branches appear to have a roughly similar stratigraphy, composition and age *(Delor et al., 2003a)*.

The age of the TTG and greenstones in the belt varies between 2,18-2,12 Ga (*Day et al., 1995; Delor et al., 2003a; Norcross et al., 2000)*. A positive $\varepsilon_{(Nd)t}$ indicates the juvenile character of the TTG-greenstone belt and precludes the involvement of significant pre-Trans-Amazonian crust during its formation (*Delor et al., 2003b*).

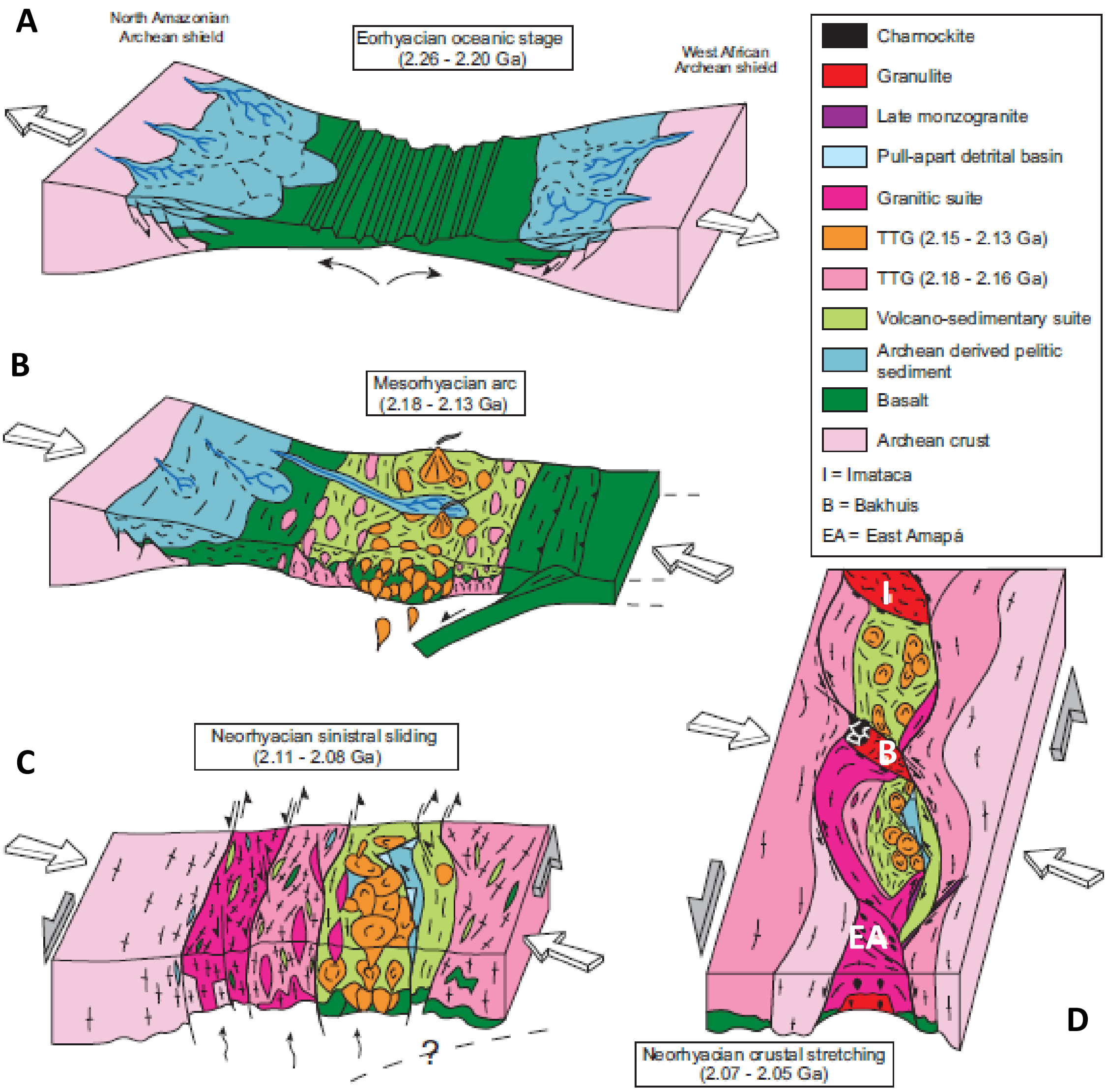

Figure 2.2: *Geodynamic evolution model for the Guiana shield. Figure taken from Delor et al. (2003b). A: Eorhyacian oceanic stage (2,26 – 2,20 Ga); rifting of the Archean plates and the creation of tholeiitic oceanic crust. B: Mesorhyacian arc (2,18 – 2,13 Ga); Convergence of the Amazonian craton and the West-African shield, subduction of oceanic crust and the generation of two pulses TTG-magmatism. C: Neorhyacian (2,11 – 2,05); Closure island-arc and a sinistral wrenching which causes pull-apart basins and strike-slip zones on places with maximum stress. D: Neorhyacian crustal stretching (2,07 – 2,05); Creation of the 'pinch-and-swell' structures, mantle upwelling, metamorphism in granulite facies and UHT metamorphism in the Bakhuis Granulite Belt.*

Around 2,10 Ga the island-arc is closed and the southward subduction changes into sinistral wrenching, causing strike-slip zones and pull-apart basins on the places with maximum stress (Figure 2.2C) (*Delor et al., 2003a; Theveniaut et al., 2006; Vanderhaeghe et al., 1998*). Additionally, granitic magmatism, generated by the melting of the TTG-greenstone belt and crustal material (*Delor et al., 2003a; 2003b*), occurs in response to the closure of the arc (Figure 2.2C) in southern French Guiana and south-eastern Surinam.

During the Late Trans-Amazonian event, sinistral wrenching and regional structuring of the TTG-greenstone belt and the granitic suite continues. This causes 'pinch and swell' structures in the belt with two E-W oriented continental-scale TTG-greenstone boudins, limited by the Imataca Complex in the west and the Amapá Block in the east, and in between the BGB (Figure 2.2D) (*Delor et al., 2003a*). The crustal stretching between the boudins allows mantle upwelling to take place, causing metamorphism in the granulite facies and even UHT metamorphism in the Bakhuis Granulite Belt (2,07 – 2,05 Ga, *De Roever et al., 2003; Delor et al., 2003a; 2003b*).

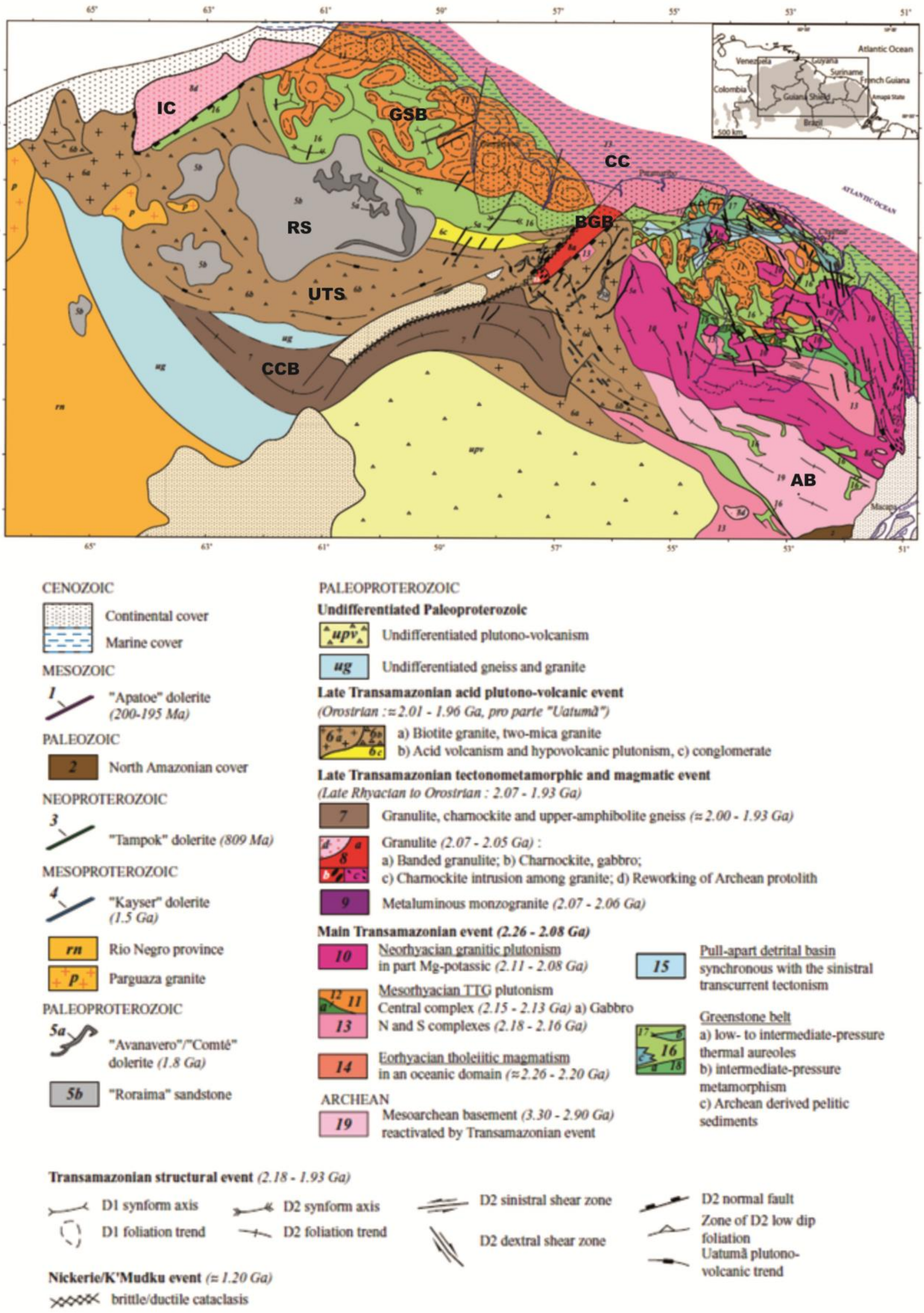

Figure 2.3: *Geological map of the Guiana shield with legend, taken from Delor et al. (2003b). Added abbreviations: IC = Imataca Complex; AB = Amapá Block; BGB = Bakhuis Granulite Belt; CCB = Coeroeni-Cauarane Belt; GSB = Greenstone belt, including TTG-plutonism; UTS = metavolcanic-granitoid suite, CSID-belt; RS = Roraima sandstone; CC = Cenozoic cover.*

The slightly younger (2,0 – 1,96 Ga), medium- to high-grade metamorphic Cauarane-Coeroeni belt is located south of the BGB (Figure 2.3). This sinuous belt connects the Coeroeni group in SW Suriname, the Kanuku Complex in central Guyana and the Cauarane group in NW Brazil (*Delor et al., 2003b; Fraga et al., 2009a*). It would be the result of ongoing collisional processes during the Late Trans-Amazonian orogeny in which a new subduction zone is suggested to have formed below the southern part of the greenstone belt, with northward subduction (*Fraga et al., 2009b; Klaver et al., 2015a*). During the collision, felsic volcanism and associated granite magmatism occurred in a large belt between the Greenstone belt and the Cauarane-Coeroeni belt (the CSID-belt, dated mainly at 1,99 – 1,98 Ga, *Fraga et al., 2009b*; *Kroonenberg & De Roever, 2010; Santos et al., 2004*).

The end of the Trans-Amazonian orogeny is marked by the deposition of the 2000 to 3000 m thick sedimentary sequences of the Roraima Group into a foreland basin environment (*Santos et al., 2003*). They consist mostly of horizontal to slightly dipping sandstones and conglomerates, which are derived from the Trans-Amazonian mountains, with common volcanic intercalations (*Santos et al., 2003*). The sediments are intruded by the (post-orogenic) gabbroic dykes and sills of the Avanavero suite, for which *Norcross et al. (2000)* and *Santos et al. (2003*) determined an age of 1,79 - 1,78 Ga by baddeleyite dating. The earliest Roraima deposition started around 1,87 Ga *(Santos et al., 2003)* or even earlier.

At 1,2 Ga (*Priem et al., 1971*), the Nickerie, a Tectonothermal episode, caused by the collision of Gondwana with Laurentia, led to resetting of Rb-Sr and K-Ar mica ages in western Suriname and Guyana and also formed mylonite zones along the BGB, creating a horst-like structure (*De Roever et al., 2003*). Hereafter, the craton remained relatively stable without significant deformation until the opening of the Atlantic Ocean around 195 Ma, resulting in extensive dyke swarms of the Apatoe dolerite.

2.2 The Bakhuis Granulite Belt

The BGB is a NE-SW trending horst-like zone in western Suriname (Figure 2.3 and 2.4) that has a width of 30 to 40 km and is about 100 km long. It consists almost entirely of banded rocks metamorphosed in the granulite facies, except for the southwestern part of the belt where charnockites with mafic intrusions dominate over high-grade metamorphic rocks (Figure 2.4). The horst is bound by NE-SW-oriented mylonite faults that separate the high-grade rocks of the BGB from the surrounding felsic metavolcanics and granites (Figure 2.3). Mylonite formation took place during the Nickerie Tectonothermal Episode, around 1,2 Ga (*Priem et al., 1971*).

The belt has a dome-shaped internal structure (*De Roever et al., 2003*) which is in particular visible on the north-east side of the belt, where the steeply dipping banding and long pelitic gneiss lenses on the map bend around from NE-SW to SW-NE. During the Tertiary, reactivation of the fault zones caused further uplift of the BGB, creating its present morphology.

2.2.1 Lithologies in the Bakhuis Granulite Belt

Banded granulites

A short description of these banded granulites, based on *De Roever et al. (2003)* will be given below. See *De Roever (1975), Bosma et al. (1983)* and *Dahlberg (1973)* for a more detailed description.

The BGB consists mainly of intermediate and mafic granulites. Felsic granulites are less common. The granulites show compositional banding at cm to m scale and foliation of both mafic and felsic minerals is present. They mainly have a granoblastic texture and the common mineral assemblage is Opx + Pl +/- Cpx +/- Hbl +/- Bt +/- Qz +/- K-fsp with magnetite, ilmenite, zircon and apatite as accessory minerals. The plagioclase is commonly antiperthitic in intermediate and felsic rocks, the K-feldspar perthitic or, more rarely, mesoperthitic.

The mafic bands often show boudinage with patches of leucoenderbite in between. Isoclinal or tight folding is common and is synkinematic with the high-grade metamorphism. The banding is generally steeply dipping, due to a later phase of deformation. Part of the banding is due to incipient migmatization. Migmatization under anhydrous granulite facies conditions is indicated by the common presence of orthopyroxene in thin leucosomes and cross-cutting leucosome veins.

The compositional banding and the intercalation of clear metasedimentary rocks, such as metapelites and quartzites, indicates a supracrustal origin. Thin pelitic gneiss intercalations and mappable metapelite lenses are present amidst the banded granulites. They contain the coarse peak-metamorphic minerals sillimanite, Mg-rich cordierite, orthopyroxene, biotite, antiperthite, perthite or mesoperthite, quartz and opaque minerals, green spinel and rarely corundum. More details about these pelitic gneisses can be found in *Nanne (2013).*

Charnockites

The SW of the Bakhuis belt consists largely of charnockites with mafic-ultramafic bodies and smaller occurrences of banded granulites and of pelitic gneisses in between (Figure 2.4). Below a short description of the charnockites, based on *Klaver (2011),* is given. See *Klaver (2011)* for a more detailed description.

The charnockites have a homogeneous, massive appearance, except where mylonitization took place. Their typical assemblage is Qz + Pl + Kfs + Opx + Cpx + Bt with zircon and apatite as common accessory minerals. The rocks contain abundant opaque minerals. Hornblende is present in part of the rocks. The rocks have a rather porphyritic texture with large, euhedral plagioclase grains (up to 1 centimetre) in a medium-grained matrix. The plagioclase grains are often strongly zoned, in cases with an antiperthitic rim. Additionally, carlsbad twinning does often occur. U-Pb dating of zircons from the charnockites *(Klaver et al., 2015a)* resulted in ages between 1984,4 – 1992,5 Ma.

Mafic and ultramafic bodies

De Goeje Gabbro

Small, gabbroic bodies of a few km in size are abundant in and near the BGB and in north- and south-west Suriname. Their composition varies from quartz-diorite to peridotite-dunite, with hornblende-bearing gabbronorite being the predominant variety (*Bosma et al., 1984*). Drill cores show that these various rock types commonly occur together, but mafic rocks predominate at the surface (*Bosma et al., 1984*).

A gradual transition from gabbronorite at the top to pyroxenite at bottom or pyroxenite at the top to peridotite at the bottom has been seen in drill cores (*Bosma et al., 1984*). Furthermore, ultramafics are locally surrounded by gabbronorite. The border zone may consist of gabbro or quartz-diorite (*Bosma et al., 1984*). These vertical and horizontal changes are considered as evidence that the compositional range in the gabbroic bodies is the result of crystallisation differentiation from one gabbroic parental magma (*Bosma et al., 1984*).

Characteristic constituents of the De Goeje gabbros are poikilitic or poikiloblastic brownish-green hornblende, up to several cm in size, and reddish-brown biotite and phlogophite (*Bosma et al., 1984*). In addition, some bodies may contain inverted pigeonite or have slightly different characteristics, such as a more granoblastic texture (*Bosma et al., 1984*).

Metamorphism in greenschist or amphibolite facies is common, but of local nature and rarely continuous throughout the bodies (*Bosma et al., 1984*). The partial replacement of pyroxene and olivine by minerals such as chlorite, tremolite-actinolite, anthophyllite, cummingtonite, and particularly in ultramafics, serpentine and talc is evidence for this metamorphism. Comparable intrusions occur in South Guyana (*Berrange, 1977*) and Roraima state, NW Brazil (*Gibbs & Barron, 1993*).

Metadolerite dykes

Narrow metadolerite dykes, consisting of fine-grained pyroxene amphibolite, are widespread throughout the core of the BGB *(De Roever et al., 2003)*. The dykes are usually straight and discordant, but in some cases partly deformed, showing a synkinematic character.

Anorthosite body

A large anorthosite body is located in the center of the BGB (*De Roever et al., 2003*). It shows igneous layering with darker, gabbroic bands. The layering is subvertical and subparallel to the banding of the surrounding granulites. Zircons of the anorthosite body have been dated at 1980 +/- 5 Ma (*De Roever et al., 2003*). The possibility that the zircons are xenocrysts, cannot be ruled out, but the surrounding granulites are much older.

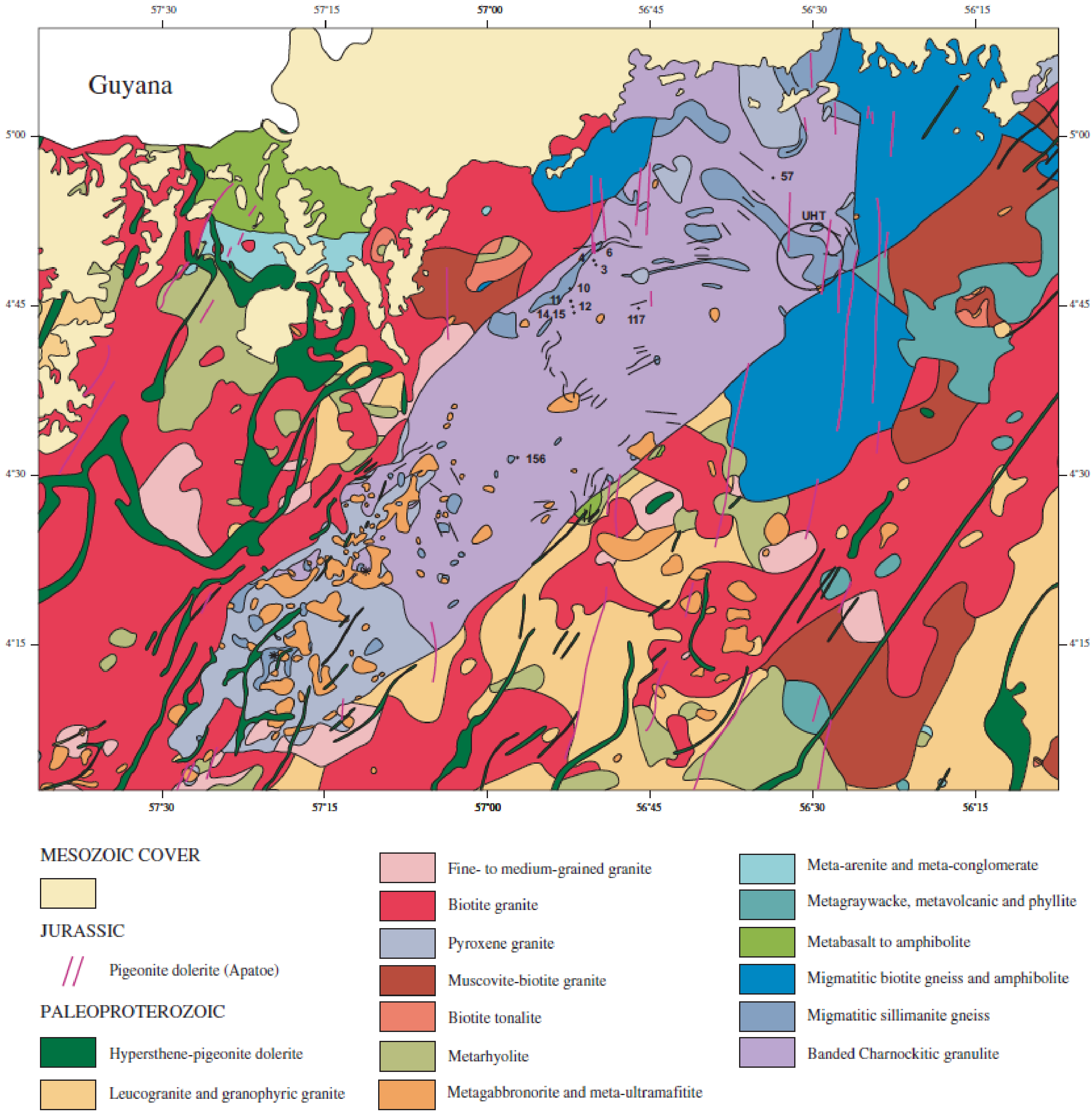

Figure 2.4: *Geological map and legend of the Bakhuis Granulite Belt. Figure taken from De Roever et al (2003a). The location of characteristic UHT assemblages in the north-eastern part of the BGB is marked by a circle.*

2.2.2 UHT metamorphism in the Bakhuis Granulite Belt

Mineral assemblages characteristic for UHT metamorphism, Opx + Sil + Qz and Spr + Qz, occur in metapelites in a relatively small area in the NE of the BGB (circle on 2.4; *De Roever et al., 2003a*). These assemblages had been described already in the 70's by *De Roever (1975*). The orthopyroxene associated with sillimanite contains 8½ - 10½ % Al_2O_3, which is another characteristic of UHT metamorphism.

The mineralogical evidence indicates a counter-clockwise P-T-t path (Figure 2.5) with I) an early assemblage consisting of Crd + Sil, followed by II) Spr + Qz and III) Sil + Opx + Qz as peak assemblage. The retrograde path is (near)isobaric and is indicated by the reduction of the Al_2O_3 level from core to rim in coarse orthopyroxene crystals and still lower Al_2O_3 in fine orthopyroxene intergrowths with sillimanite (*De Groot, 2008; De Roever et al., 2003*).

De Roever et al. (2003) estimated peak UHT conditions at 950 ^{o}C and a pressure of around 8,5 – 9 kb. As known for UHT metamorphism, characteristic assemblages occur only in metapelites of appropriate composition and no direct evidence of UHT metamorphism was found in the granulites. However, feldspar thermometry on metapelitic rocks and on mesoperthite granulites intercalated between the granulites, indicated a peak temperature > 900 ^{o}C throughout the entire BGB (*Nanne, 2013*).

The age of the UHT metamorphism has been constrained by *De Roever et al. (2003)*, by Pb-evaporation zircon dating, at 2055 – 2072 Ma. Zircon dating with the SHRIMP for two samples confirmed this range approximately (*Lafon, pers. comm*.). LA-ICP-MS dating of an UHT sample by *Nanne (2013)* gave an age of 2073 +/- 7 Ma, in agreement with the range given.

A second UHT event?

Klaver (2015a) found ages of 1984 – 1993 Ma for the charnockites of the SW part of the BGB. Feldspar thermometry of the charnockites indicated that the charnockites crystallized in the range of 950 – 990 °C. The high temperature of formation was considered to indicate a second, younger UHT-like event, as it is less probable that the temperature remained > 950 °C for more than 60 Ma after the UHT metamorphism at 2055 – 2072 Ma. However, evidence of (UHT) metamorphism around 1985-1992 Ma has not yet been found.

2.2.3 Heat source for UHT metamorphism in the Bakhuis Granulite Belt

Delor et al., (2003a; 2003b) suggested that mantle upwelling in the BGB, a zone of maximal crustal stretching of the greenstone belt, would be the heat source for the UHT metamorphism. The possibility that mafic intrusions might be the heat source of UHT metamorphism, will be investigated in this thesis.

3. METHODOLOGY

3.1 Sampling strategy and sample selection

Fieldwork in the BGB is difficult since the whole area is covered with a tropical rainforest, resulting in poor exposure. Furthermore, the dense rainforest is difficult to access due to complete lack of infrastructure. Both factors prevent systematic sampling and establishing field relations. However, the area near the Kabalebo Nature Resort in the SW of the BGB is somewhat better accessible, since boats can be used on the river and some paths have been made for tourists. Nevertheless, often a trail of several kilometres had to be cut with machetes by our guide. In this area most outcrops occur in the riverbed or in small streams and their valleys on hill slopes. The locations of the samples were determined with GPS and the old (1977) geological map of the GMD. Earlier sampling locations such as the Moi-Moi Falls, the Zandkreek and the Kilo Drie creek *(Klaver, 2011)* were sampled, as well as a new site found in 2011, the Misty Mountain creek. Additional sampling places were found in the wider surrounding of the Kabalebo Nature resort during the fieldwork.

In total 64 samples were collected and numbered from AT01 to AT38. If several samples from the same location were taken, an additional character (A - G) was added. Extra large samples were taken from places that could be interesting for geochronology. The GMD provided drill cores (LA148, LA149 and LA150) from a geophysical anomaly in the BGB, which had been investigated by diamond drilling in the 60's. Sample Sur-207, collected by prof. Dr. H.N.A. Priem in 1971, was provided by Naturalis, the national museum of natural history in Leiden.

3.2 Whole rock sample preparation

3.2.1 Coarse processing

In total, 47 samples from the BGB were processed in the Geological Technical Laboratory and the Mineral Separation Laboratory of the VU University in Amsterdam. Weathered and eroded parts were removed with a diamond blade saw. The samples were cut in small blocks, from which one was held apart for the preparation of a thin section, while all other pieces were crushed to gravel size with a steel jaw crusher. The crusher was cleaned with a steel brush, ethanol and compressed air between the different samples to prevent contamination. The crushed material was split in smaller portions and 100 gr of the split was used for further processing for XRF. Samples ER1109, LA150-16, LA150-28 and LA150-55 were used for zircon separation (see 3.4.1).

The split was crushed to powder for one minute in an agate ring mill, followed by 60 minutes in an agate planetary ball mill until a fine, homogeneous powder was achieved. About 15 gram of this powder was put in glass vials in a stove at 120°C to dry for one night and saved afterwards in a dehumidifier until further use (see the preparation of XRF beads and pellets in paragraphs 3.2.2 and 3.2.3).

During the coarse processing, agate mills were used to prevent contamination of the samples. They were cleaned by milling with quartz sand and demineralised water and were rinsed afterwards with demineralised water and ethanol.

3.2.2 Preparing XRF beads

Fused glass beads are used for major element analysis. At first, 2,5 gr of the dried sample was put in the oven at 1000°C for 30 minutes in order to remove volatiles, such as OH-groups, carbon and sulphur from the samples. A stove at 120°C was used to cool the ignited samples. Finally, the samples were put in a vacuum, to prevent water from the air to get into the sample. The sample weight was measured both before and shortly after the ignition stage, to determine the loss on ignition (LOI). This represents loss of volatile elements in the sample during the ignition phase as well as increase in weight by oxidation of bivalent iron.

For preparation of the beads, 1,000 gr of the ignited sample and 4,000 gr flux (Spectroflux110, which consists of 50% lithiummetaborate and 50% lithiumtetraborate) were mixed to a homogeneous mixture, put in a platinum crucible and placed in a Philips Switch PerlX3, where a standard program was used to melt the sample at ~1150^{o}C. The flux reduces the melting temperature of the sample drastically, making it possible to melt the powder at a relatively low temperature. Afterwards, the melted sample was dropped onto a platinum dish where it cooled down. Since cracks cause errors in the analysis, the process was repeated for cracked samples until a non-cracked bead was created. The platinum crucibles and dishes were cleaned before use for 15 minutes in an ultrasonic bath filled with 20% citric acid and rinsed afterwards with demineralised water and compressed air.

3.2.3 Preparing XRF pellets

Pressed powder pellets were used for the minor and trace element concentration analysis of the samples. During the preparation, 4,500 gr dried sample and 0,450 gr organic binder (EMU120FD) were mixed together in an agate ball mill to achieve a homogeneous powder. The powder was put in an aluminium cup, which was placed in an X-press pneumatic press and pelletized at a pressure of 20 tons for 30 seconds, after which the pressure was gradually decreased. The pellet must be carefully removed from the press to avoid small flakes to fall off the pellet. If this happened, the process was repeated to get a pellet with a smooth surface since irregular surfaces can lead to errors in the analysis. The agate ball mills were rinsed before use with demineralised water, ethanol and compressed air.

3.2.4 ICP-MS sample digestion

For ICP-MS analysis the samples need to be dissolved completely and then diluted about 5000 times to obtain accurate analytical results. Dissolution and dilution was done in the clean laboratory of the VU University which has an ultra-clean environment to minimalise pollution of the samples. In total, 21 samples were dissolved for analysis together with one blank solution and the BCR-2 and BHVO-2 standards for reference.

The fine ground rock samples were dissolved in hydrofluoric acid (HF). However, some minerals, such as zircon, do not dissolve at room pressure and temperature and therefore special PTFE bombs need to be used for dissolution at higher temperature and pressure, causing the breakdown of these minerals. Since at least some of the selected samples contain zircons, the decision was made to dissolve all selected samples with these PTFE bombs.

Before dissolving the samples, all PTFE bombs and PFA beakers, used for making the solution, were cleaned for several days with 6-7N HCl and rinsed with milli-Q water. The PTFE bombs were additionally cleaned for one night with 1,00 ml HF and 0,30 ml HNO_3 at a temperature of 200 ^{o}C and rinsed afterwards with milli-Q water. ICP-MS tubes were cleaned for several days with 5% HNO_3 and rinsed afterwards with milli-Q water.

For the dissolution of the samples, 25 – 40 mg sample was weighted and put into the PTFE bombs together with 2,00 ml HF and 0,30 ml HNO_3. The PTFE bombs were mounted into the steel-jacketed bombs and placed in an oven at 200 ^{o}C for five days in order to break down all minerals. Afterwards, the dissolved sample was put into clean 30 ml PFA beakers. Residue in the PTFE bomb was removed by putting the bomb in the oven for one night with 1,00 ml 6-7N HCl and 0,30 ml HF. Finally, the bombs were rinsed with milli-Q water. This solution was added to the PFA beakers, which were dried down for one night at a hotplate at 200 ^{o}C. To break down the chloride and fluoride salts, 1,00 ml concentrated HNO_3 was added to the beakers when the samples were dried down. This step was repeated a second time to make sure that no salts were present.

For the dissolution, 27,00 ml 3N HNO3 was added to the dried samples which were placed on a hotplate at 200^{o}C until they were completely dissolved. Finally, 2,00 mg from this solution was put into clean ICP-MS tubes that were filled with 5% HNO_3 until 10 ml solution with a dilution factor between 4500 and 5000 was reached.

3.3 Whole rock sample analysis

3.3.1 X-ray Fluorescence (XRF) analysis

X-ray Fluorescence can be used to measure the bulk element concentrations down to a few parts per million, for major, minor and trace elements. During the analysis the sample is bombarded with high-energy X-ray photons which cause ionization of the inner shell electrons, creating characteristic x-rays for each element. The intensity of these x-rays is analysed by reference to calibration standards *(Rollinson, 1993; Verma, 2007;*

Winter, 2001). Finally, all measured major elements are expressed as weight percentage oxide (e.g., SiO_2), where Fe is given as ferric iron since it can be expected that all FeO was oxidised during ignition. The expected FeO*-value of the rock is calculated from the Fe_2O_3-value. The trace elements are given in parts per million.

For this study major and trace element concentrations were measured by analysing fused glass beads resp. pressed powder tablets with a Panalytical MagiXPro X-ray Fluorescence Spectrometer (XRF) at the VU University. The analysis of the beads was done by the Majorsrh1-4 programme with an acceleration voltage of 40kV and a beam current of 90 mA, while the pellets were measured with the Spel, Metals, ReeHex-27 and VCrCoBaSc programmes with an acceleration voltage of 60 kV and a beam current of 60 mA. USGS standards AGV-1, BCR-2, BHVO-2 and GSP-1 were used to check the accuracy and precision of the spectrometer. Table 3.1 and 3.2 shows the results for the two basaltic standards. The AGV-1 and GSP-1 standards are not included into the tables, but they gave similar results.

Table 3.1 shows the weight percentage of the measured oxides in the glass beads. From this table it can be concluded that most measured standards have values in the range of one σ from the USGS recommended value and SiO_2 and MgO show values in the range of 2σ from the recommended values. Only CaO in the BHVO-2 and Na_2O in the AGV-1 standards have values outside the 2σ-range.

As to the pellet data (Appendix II), some data gave negative concentrations. Negative values could be caused if the concentration is below the XRF detection limit. This does not mean that low concentrations cannot be measured. Such low concentrations do often not match with the σ or 2σ-range of the USGS standards and the deviation from USGS may be large. The variation is less in samples with a higher concentrations, so two samples with high concentrations of each analysis program are used to compare the measured standards and the USGS recommended values (Table 3.2). For this sample, most element concentrations fit within the σ or 2σ-range and the deviation from USGS is mostly <10%, indicating that the measurements are reliable.

Sample selection for XRF analysis was based on the petrography of the samples (Chapter 4). All selected samples are analysed for both major and trace elements and their results can be found in Appendix II. The earlier mentioned negative values will not be included in this study and are deleted from the appendix. To achieve a reliable dataset, the trace elements will be also measured with the ICP-MS.

3.3.2 Inductively Coupled Plasma Mass Spectrometry (ICP-MS) analysis

ICP-MS is a multi-element analyzing method which can determine trace elemental abundances or isotopic ratios *(Rollinson, 1993; Totland et al., 1992)* by mass spectrometry of ions, which are generated in an argon inductively coupled plasma *(Jarvis, 1988)*. The stream of charged ions follows a curved path through a strong magnetic field, that is different for heavier ions due to their greater momentum, after which their mass is measured when they pass through a detector *(Winter, 2001)*.

During this study, the quadrapole Thermo X-Series II inductively coupled plasma mass spectrometer (ICP-MS) of the VU University was used to measure the trace elements of 21 samples, together with 2 standards (BCR-2 and BHVO-2) to check the accuracy and long term drift of the spectrometer, and two blanks to detect pollution during the sample preparation. ICP-MS analysis also involves an internal standard (BHVO-2) which is measured in the beginning and remeasured after every two to three samples in order to notice drift of the ICP-MS during the analysis. In this study, no significant pollution or drift was identified during the analysis.

The data from the ICP-MS analysis can be found in Appendix II and Table 3.3. When comparing the measured USGS standards with the recommended values it becomes clear that not all elements match the σ or 2σ-range from the USGS-standards. Also, the deviation from USGS is bigger than for XRF, which could be caused by drift of the ICP-MS. However, since most elements only differ a few parts per million with the recommended value and no significant drift was identified during the analysis, it can be concluded that the data is reliable.

BCR-2 (n=2)	**Fe_2O_3**	**TiO_2**	**CaO**	**K_2O**	**P_2O_3**	**SiO_2**	**Al_2O_3**	**MgO**	**Na_2O**
Average measured standard (wt%)	13,68	2,23	7,06	1,78	0,33	53,66	13,38	3,52	3,08
Average USGS-standard (wt-%)	13,80	2,26	7,12	1,79	0,35	54,10	13,50	3,59	3,16
St. dev. USGS-standard (σ)	0,20	0,05	0,11	0,52	0,02	0,80	0,20	0,05	0,11
Deviation from USGS (%)	-0,89	-1,37	-0,81	-0,75	-5,00	-0,81	-0,91	-1,84	-2,39

BHVO-2 (n=2)	**Fe_2O_3**	**TiO_2**	**CaO**	**K_2O**	**P_2O_3**	**SiO_2**	**Al_2O_3**	**MgO**	**Na_2O**
Average measured standard (wt%)	12,17	2,69	11,25	0,51	0,26	49,00	13,32	7,06	2,16
Average USGS-standard (wt-%)	12,30	2,73	11,40	0,52	0,27	49,90	13,50	7,23	2,22
St. dev. USGS-standard (σ)	0,20	0,04	0,02	0,01	0,02	0,60	0,20	0,12	0,08
Deviation from USGS (%)	-1,04	-1,52	-1,33	-1,06	-3,15	-1,80	-1,37	-2,37	-2,73

Table 3.1 : *The average concentration of the oxides (wt-%) within the BCR-2 and BHVO-2 standards measured from the fused glass beads with the XRF at the VU University in Amsterdam, the average USGS concentrations, the standard deviation of USGS-standards and the deviation from these recommended values.*

	Spel		Reehex27		METALS		VCrCoBaSc	
BCR-2 (n=1)	**Zr**	**Sr**	**La**	**Ce**	**Zn**	**Ni**	**V**	**Ba**
Average measured standard (ppm)	185,06	345,82	22,99	51,81	136,97	9,83	381,14	705.51
Average USGS-standard (ppm)	188,00	346,00	25,00	53,00	127,00	-	416,00	683.00
St. dev. USGS-standard (σ)	16,00	14,00	1,00	2,00	9,00	-	14,00	28,00
Deviation from USGS (%)	-1,56	-0,05	-8,04	-2,25	7,85	-	-8,38	-3,30

BHVO-2 (n=1)	**Zr**	**Sr**	**La**	**Ce**	**Zn**	**Ni**	**V**	**Ba**
Average measured standard (ppm)	163,46	345,82	10,57	38,79	104,03	120,08	286,79	122.81
Average USGS-standard (ppm)	172,00	346,00	15,00	38,00	103,00	119,00	317,00	130.00
St. dev. USGS-standard (σ)	11,00	14,00	1,00	2,00	6,00	7,00	11,00	13,00
Deviation from USGS (%)	-4,97	-0,05	-29,53	2,08	1,00	0,91	-9,53	-5.53

Table 3.2: *The average concentration of some trace elements within the BCR-2 and BHVO-2 standards measured from the pressed pellets with the XRF at the VU University in Amsterdam, the average USGS concentrations, the standard deviation of USGS-standards and the deviation from these recommended values.*

BCR-2 (n=1)	**Zr**	**Sr**	**La**	**Ce**	**Zn**	**Ni**	**V**	**Ba**
Average measured standard (ppm)	164,85	283,81	21,04	44,46	120,70	16,31	351,53	578,16
Average USGS-standard (ppm)	188,00	346,00	25,00	53,00	127,00	-	416,00	683,00
St. dev. USGS-standard (σ)	16,00	14,00	1,00	2,00	9,00	-	14,00	28,00
Deviation from USGS (%)	-12,31	-17,97	-15,84	-16,12	-14,29	-	-15,50	-15,35

BHVO-2 (n=1)	**Zr**	**Sr**	**La**	**Ce**	**Zn**	**Ni**	**V**	**Ba**
Average measured standard (ppm)	168,76	557,83	14,24	36,09	111,47	110,34	298,27	121,39
Average USGS-standard (ppm)	172,00	346,00	15,00	38,00	103,00	119,00	317,00	130,00
St. dev. USGS-standard (σ)	11,00	14,00	1,00	2,00	6,00	7,00	11,00	13,00
Deviation from USGS (%)	-1,88	7,48	-5,08	-5,02	8,22	-7,28	-5,91	-6,62

Table 3.3: *The average concentration of some trace elements within the BCR-2 and BHVO-2 standards measured with the ICP-MS at the VU University in Amsterdam, the average USGS concentrations, the standard deviation of USGS-standards and the deviation from these recommended values.*

3.3.3 Comparison of XRF and ICP-MS data

As seen in previous paragraphs, there are advantages and disadvantages with XRF and ICP-MS analysis. Firstly, XRF gives results that match with the USGS standards, but has a relatively high detection limit and data less than 20 ppm may be unreliable. ICP-MS has a much lower detection limit. However, due to the possibility of drift in the apparatus, the ICP-MS values might deviate more from the recommended USGS values than for XRF-measurements, creating a larger error. To get the best reliable data set, the values of the trace elements with a high concentration will be taken from the XRF measurements, while the low concentrations will be taken from ICP-MS analysis. In this report it will always be mentioned which data is used to prevent confusion.

3.4 Zircon preparation and analysis

3.4.1 Zircon separation and preparation from whole rock

Zircons from three quartz-dioritic drill cores (LA 150-16, -28 and -55m depth) and from a metagabbronorite from Moi-Moi (ER1109) were separated in the Mineral separation laboratory at the VU University. The samples were crushed with a steel jawcrusher and sieved with a sieve of 250 µm. The fraction <250 µm was used for zircon analysis.

Sample ER1109 weighted a few kilograms and enough material <250 µm was created for zircon separation. The LA150 samples were much smaller, therefore, the fraction >250 µm was passed through a Schmersal AZ15VZ hardened steel disc mill to reduce the particle size, followed by sieving at 250 µm. The disc mill was set on a smaller size and the cycle was repeated for all particles >250 µm. The <250 µm particles were treated with conventional mineral separation techniques to separate the zircons while the coarser part was put aside. The <250 µm particles were deslimed with a desliming apparatus that is based on the use of Stoke's law: big particles settle faster in a liquid under the influence of gravity than smaller particles. Afterwards, the particles, which had a size of 20-250 µm, were dried in a stove before further processing.

A Carpco roll-magnet was used to lower the non-zircon content in sample ER1109. The LA150 samples were too small for the Carpco roll-magnet so instead a Frantz magnet was used. All samples were sieved in two portions of 20-125 µm and 125-250 µm to avoid the particle size to influence the magmatic susceptibility. The samples had a high ore content which could cause accumulation in the Frantz magnet, therefore, most ore was removed by hand with a magnet before going through the Frantz magnet. With both the Carpco roll-magnet and the Frantz magnet was started with a low mA, building up after each time the sample went through the machine, until mostly non-magnetic minerals are left.

Further separation of the zircons was done by heavy liquids, which uses the difference in densities between a liquid and the minerals to separate heavy minerals from the light ones. For this process, diiodomethane (CH_2I_2) with a density of 3,31 g/ml was used. It caused the light minerals, such as quartz and plagioclase, to float on the liquid while the heavy minerals, such as zircons and pyroxene, sank to the bottom. This settling process was speed up by using a liquid overflow centrifuge (LOC-100). The resulting sink was sieved into five portions with a different size range and cleared of magnetic minerals by using a second Frantz magnet. In some sample portions it was possible to make a separation between polluted and non-polluted zircons by changing the dip of the Frantz magnet. Despite the successful zircon separation, sample LA150-28 had not enough particles in each sieved portion to use the Frantz magnet effectively, therefore the use of the magnet was skipped.

Finally, the best zircons were picked by hand. During the picking, features like the crystal shape, colour, transparency, cracks and inclusions were taken into account to gain the best zircons out of the mass. In total, 80 zircons were picked from sample ER1109 and 25 zircons were picked from each LA150 samples. The hand-picked zircons were mounted in an epoxy section and polished to reveal their interiors in the Geological Technical Lab of the VU University.

3.4.2 Back-scattered Electron and Cathodoluminescence imaging

Backscattered Electron (BSE) and Cathodoluminescence (CL) imaging enables the visualisation of internal structures within zircons, such as oscillatory and sector zoning, inherited cores and narrow metamorphic rims, which are not observable by conventional microscopy. These textures help to establish the nature and history of zircons *(Götze, 2012)*. Both techniques reveal more or less comparable images but e.g. inherited cores are better seen on CL images. CL images also show the presence of subsurface inclusions such as apatite. Besides BSE and CL-images, transmitted light microscopy pictures were taken to locate inclusions and fractures. Combining these pictures, the best spot for LA-ICP-MS analyses, avoiding inclusions and fractures, could be determined.

The Cl-images of ER1109 and LA150 were taken at different times. The cold cathode luminescence stage was broken during the LA150 session and could not be repaired in time before finishing this thesis. The absence of Cl-images for LA150 does not appear to be a big problem since the zircon morphology and internal textures are not complicated (see 5.4.1). Due to this technical failure, the transmitted light pictures, which are essential for finding good, crackless spots for analysis, had to be made with a different microscope. This explains the decrease in quality and the different appearance between the transmitted light pictures of ER1109 and LA150 in Chapter 5.

Back-scattered Electron imaging

Zircon Back-scattered Electron images were taken with the Jeol JXA-8800M electron microprobe at the VU University. These compositional images are created by high energy back-scattered electrons, revealing zoning and inherited cores. The brightness in BSE images depends on the average atomic number. Variations are mainly caused by Hf, U, Th, Y and REE. Their substitution for Zr in the zircon lattice results in an increased brightness.

Cathodoluminescence imaging

Cathodoluminescence is created by the interaction of an electron beam with a solid in a vacuum, resulting in the emission of light with a different intensity and colour depending on the trace elements in the zircons. The emission is primarily attributed by REE, especially Dy^{3+} but also Tb^{+}, Y^{3+}, Sm^{3+} and Eu^{2+}, although trace elements like Ti^{4+} and U^{4+} are also known to cause emission from zircons *(Cherniak et al., 1997; Marshall, 1988)*.

CL-images were taken with a cold cathode luminescence stage in the Optical Laboratory of the VU University. An acceleration voltage of +/- 17 keV is used which resulted in an electron current of +/- 450 mA, causing luminescence within the zircons.

3.4.3 U-Pb dating

The U-Pb dating method is based on two different decay paths with different half lives. ^{235}U decays to ^{207}Pb and ^{238}U decays to ^{206}Pb. An advantage of using these two decay paths is that open systems, which contributes to the reliability and precision of age determinations, can be detected. Both zircon and baddeleyite are suitable for U-Pb dating. They incorporate U in their crystal lattice and exclude lead from it. Therefore, the ^{207}Pb and ^{206}Pb in these minerals is expected to be radiogenic.

The measured isotope ratios are displayed in a conventional concordia diagram (*Wetherill, 1956*) where $^{207}Pb/^{235}U$ is plotted against $^{206}Pb/^{238}U$. A line, the concordia, is created when the two Pb/U-ratios correspond to a given age. In a closed system, the parent-daughter ratio's evolve along this concordia as a function of time. However, if the isotopic compositions are disturbed due to an open system, the calculated ages may deviate from the concordia and form a linear line, named the discordia. This discordia intercepts the concordia at two places. The upper intercept represents the original age of formation, while the lower intercept represents the age of the event which led to an open system behavior.

U-Pb isotope analyses were done on 75 mounted zircons, using the LA-ICPMS at the Institut für Mineralogie of the Westfälische Wilhems-Universität Münster. The used instrument is a ThermoFinnigan Element 2 mass spectrometer with a 193-nm ArF Excimer laser system (Analyte G2, Photon Machines). The laser was operated with a fluence of ≈3 J/cm^2 and a repetition rate of 10 Hz. The samples were ablated for 37 seconds, followed by a 37 second washout with He. The ICP-MS is tuned at the start of each session using a NIST-612 trace element glass.

During analysis, Z91500 and Plešovice were used as external standards to check for precision and accuracy. Mass and element fractionation was corrected by sample-standard bracketing method, where Z91500 was used as calibration standard. Z91500 was measured before the analysis and after every 12 to 13 spot analyses. Plešovice was measured four times at the end of the analysis. Since laser spot size can influence the fractionational processes, a spot diameter of 35 µm was used throughout the analyses.

During the analysis, all four lead isotopes (^{204}Pb, ^{206}Pb, ^{207}Pb and ^{208}Pb) and ^{235}U and ^{238}U were measured. These obtained isotope concentrations were used to reconstruct U-Pb concordia ages of the standard zircons. These ages are within the error of the published data (Table 3.4), indicating accurate measurements. In addition, ^{202}Hg was measured to determine the isobaric interference of ^{204}Hg on ^{204}Pb, which is necessary to make a correction for the common lead.

Data-reduction was carried out in Münster using a macro-driven Excel®spreadsheet which is constructed at the Münster University. This spreadsheet determines the presence of common lead and when present, corrects for it. Furthermore, time dependent and static fractionation during laser ablation are corrected. An extensive description of the reduction procedure is discussed in *Kooijman et al. (2011)*. After the U-Pb data reduction, the ages are calculated with Isoplot 3.75 (*Ludwig, 2012*).

Zircon standard	Measured age (Ma)	Recommended value (Ma)	Deviation from recommended value (%)
Z91500	1067,4 +/- 7,1	1062,4 +/- 10,3	0,5
Plešovice	333,9 +/- 4,0	337,13 +/- 0,37	- 0,6

Table 3.4: *Recommended U-Pb ages for the standards Z91500 and Plešovice. Ages determined by Wiedenbeck et al. (1995; Z91500) and Sláma et al. (2008; Plešovice).*

3.4.4 Trace element analysis

Zircons can endure high temperatures and preserve their internal structures due to low elemental diffusivities within the mineral *(Cherniak et al., 1997; Cherniak and Watson, 2003)*. Zircon controls the trace element concentrations of the melt from which it is crystallised *(Hoskin and Schaltegger, 2003; Lowery Claiborne et al., 2006)* by incorporating several trace elements, such as U, Th, REE, Y, Ta and Hf, which replace Zr within the crystal lattice. This replacement goes according to the rule of Goldschmidt, which states that elements with a similar radius and valence can replace each other. Zircons thus reflect the trace element concentrations in the melt at time of crystallisation, indicating the source of the original melt.

Trace element analysis of ≈70 mounted zircons was performed using the LA-ICPMS at the Institut für Mineralogie of the Westfälische Wilhems-Universität Münster. The used instrument is a ThermoFinnigan Element 2 mass spectrometer with a 193-nm Excimer laser system (Analyte G2, Photon Machines). The laser operated with an energy density of ≈5 J/cm^2, a spot size of 35 µm and a repetition rate of 10 Hz. The ICP-MS was tuned at the start of each session using a NIST-612 trace element glass which was also used as external bracketing standard. The overall measurement time for a single analysis was 60 s, including 20 s for background measurement. The element concentrations were calculated using Glitter software (*Griffin et al., 2008*) by normalising to 32.45 Wt-% SiO_2 in zircon (*Anczkiewicz et al., 2001*). Z91500 was used as reference material to monitor the precision and accuracy (n = 8), and reproducibility was better than 10 % for key trace elements.

4. FIELD OBSERVATIONS AND PETROGRAPHY

4.1 Introduction

The rainforest that covers the BGB is difficult to access and outcrops are scarce. Therefore the goal of this research was not to map the mafic intrusive bodies, but to extensively sample several bodies in the SW of the BGB in order to determine their chemical signature.

During the initial stage of this project it became clear that not only the 'De Goeje' type gabbro and ultramafitite bodies were present (*Bosma et al., 1984*), but also a second type of gabbro of unknown character. For that reason, this research was adjusted to investigate both types of mafic-ultramafic bodies. For various reasons (see e.g., *Kroonenberg et al., in press*) the name 'De Goeje' gabbro should be abolished. Therefore, the name will not be used in this thesis. Alternative names, based on the geographical occurrence of the body, are used to define the different types of gabbro. Gabbroic bodies of the type described by *Bosma et al. (1984)*, are named after the Moi-Moi Falls in the Moi-Moi creek while the second type of gabbro is named after the Charlie Falls in the Misty Mountain creek, resulting in respectively Moi-Moi Metagabbro and Charlie Gabbro.

A few samples of a possibly different type were collected from two areas but due to the low amount of samples it was not possible to make a reliable interpretation. Their petrography will be described briefly, but the emphasis of this study will be on the Charlie Gabbro and the Moi-Moi Metagabbro.

The nomenclature of the different rock types is based on the modal mineral assemblages and the classification diagrams for plutonic rocks presented by *Le Maitre (1989)*. An overview of the rock types and the GPS-coordinates of the sampling locations can be found in Appendix I. In addition, the CIPW-norm is calculated for comparison of different samples. The CIPW norm recalculates a chemical analysis of an igneous rock into amounts of normative, ideal minerals (expressed in Wt-%). The calculation of the CIPW norm was done following the methods described in *Winter (2001)*. The iron content was analysed by XRF as Fe_2O_3, therefore the FeO content is calculated from the Fe_2O_3 value. Normal rocks contain some Fe_2O_3 in addition to FeO, therefore a Fe_2O_3:FeO ratio of 0,15 was assumed. CIPW norms can be found in Appendix III.

The CIPW norm is based on anhydrous minerals, which causes problems for rocks with primary hornblende, such as the Moi-Moi Metagabbro. During the norm calculation, the elements in hornblende will be allocated to anhydrous minerals, such as anorthite and clinopyroxene. This results in a normative mineral assemblage that contains less mafic minerals than the modal composition. As a result, the CIPW norm of the Moi-Moi Metagabbro will not reflect the hydrous character of the samples and will thus not be used during this study.

4.2 Charlie Gabbro

4.2.1 Occurrences and field observations

Two bodies of the Charlie Gabbro were extensively sampled. The first body is located along the Misty Mountain creek, where it can be traced semicontinuously through the river bed from sample AT02 towards AT16 (Figure 4.1). AT16 is sampled at a small waterfall above which charnockite is the main lithology. With exception of AT16B, all samples are coarse grained, but samples AT03 - 05, along the bend of the river, are even coarser, with plagioclase laths of up to 5-10 cm in length. This suggests that the body continues in southern and western direction from the bend. The medium grain size of AT16B next to charnockite indicates that the sample represents the edge of the gabbroic body, but the rocks on the charnockite side are chaotic and contain many lenses of metadolerite. From these field relations can be concluded that the body is at least 500 x 600 metre (Figure 4.2), but it is expected to be at least twice that size. The partly very coarse grain size indicates slow cooling of the magma at great depth. The body is interpreted as a sill or a less regular pluton.

The body is cut at several locations by metadolerite dykes that vary from 20 to 100 cm in thickness (Figure 4.4A, B and C). The geochemistry of these dykes will be studied by B. Uunk for his Msc thesis (*Uunk, 2015*). In addition, a charnockite dyke (10 cm thick) and charnockite veins (Figure 4.4C and D) are found in the gabbros of this body. The charnockite dyke cuts a metadolerite dyke, making it the youngest phase to intrude in the gabbro. Another noticeable feature is the presence of several round cavities of about 5 cm in size (outcrop AT04, Figure 4.4E and F), which may represent fully weathered olivines, with pyroxene coronas.

Eight gabbroic samples were taken from this body. They can be divided into two different types. All samples collected during the fieldtrip in 2012 are classified as gabbronorites. Only one olivine gabbronorite (Sur-207) was collected from lower in the same valley by H.N.A. Priem in 1971.

The second gabbroic body is located upstream of the Moi-Moi Falls along the Moi-Moi creek (Figure 4.1). It is represented by isolated outcrops amidst the rainforest, but the lithology and distance between the outcrops indicate that they belong to the same body. A contact with the surrounding charnockites was not found and all samples are coarse grained, suggesting that none of them are located near the edge of the body. The distance between the samples indicate a gabbroic body of at least 750 x 250 metre (Figure 4.3), but it is expected to be bigger. The body is interpreted as a sill or a pluton. In total, 11 samples were collected from the body along the Moi-Moi creek. Nearly all samples are classified as olivine gabbronorites. Only one gabbronorite (AT30) was found.

Finally, an olivine gabbronorite sample was collected from an outcrop in the Kabalebo river (Figure 4.1). The outcrop sticks out above the water surface during the dry season, but the majority of the outcrop is covered by the river and the size of the body is unknown.

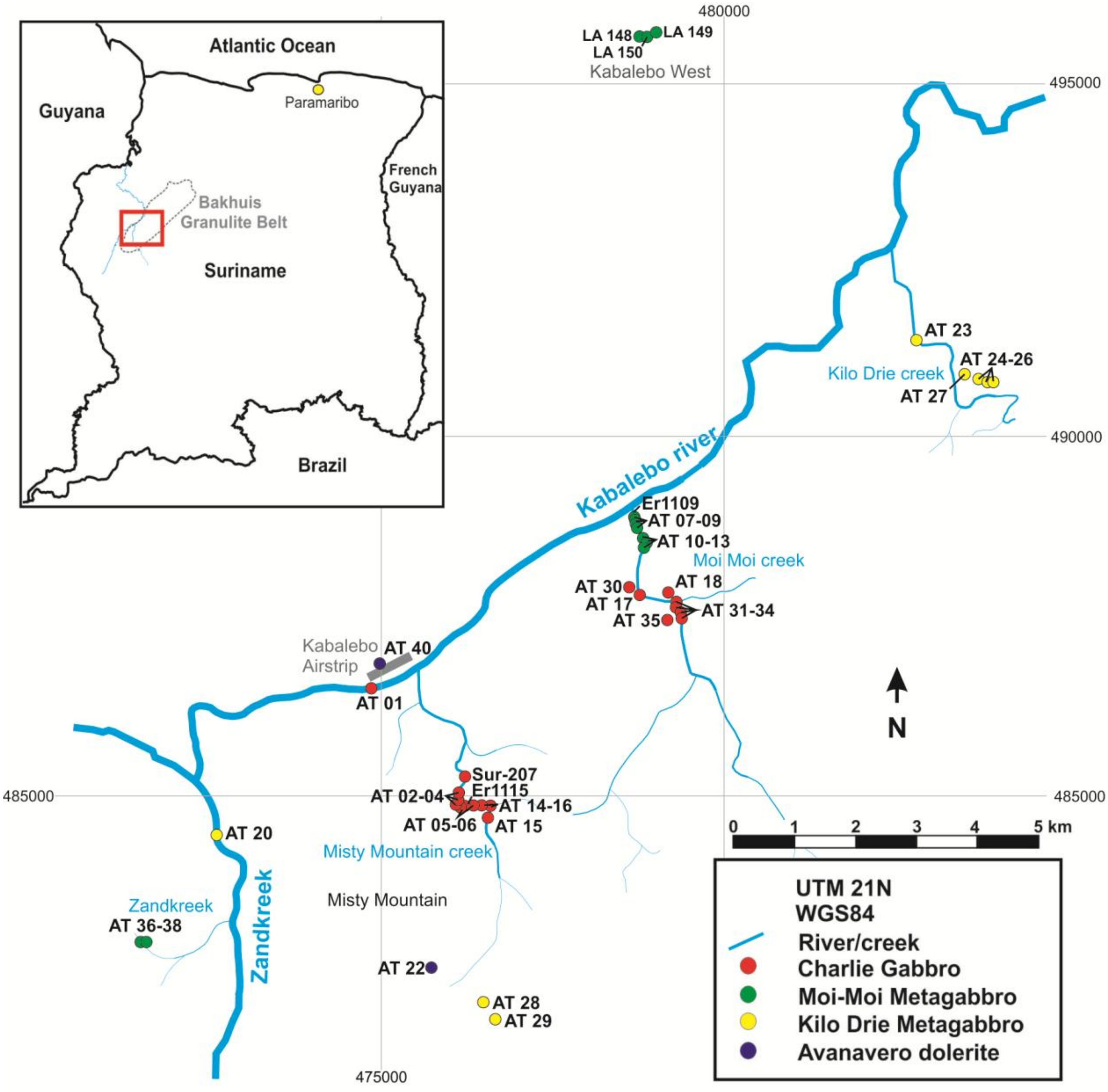

Figure 4.1: *Map with the sampling locations within the studied area in the BGB. This map includes important orientation point, such as rivers, creeks, the Kabalebo airstrip and the Misty Mountain.*

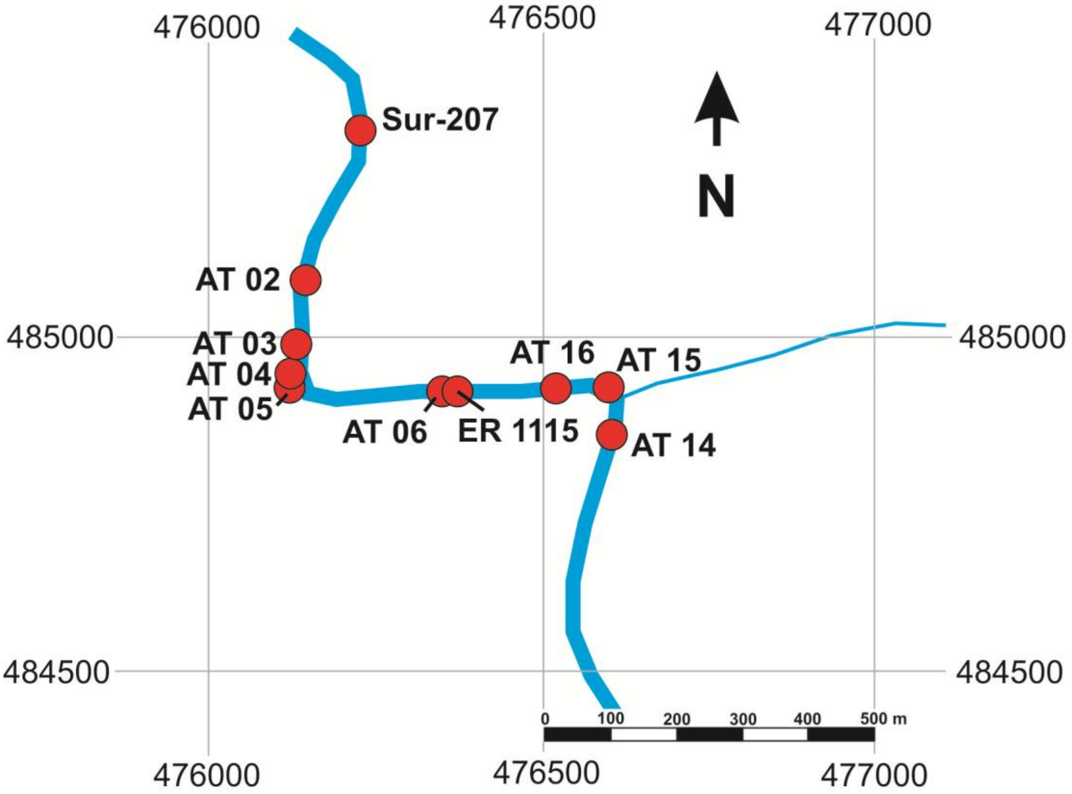

Figure 4.2: Magnified map with the sampling locations in the Misty Mountain creek. Further explanation can be found in the text. Coordinates in UTM21 WGS84. See Figure 4.1 for the location of the creek within the research area and Appendix I for the coordinates of the sampling locations.

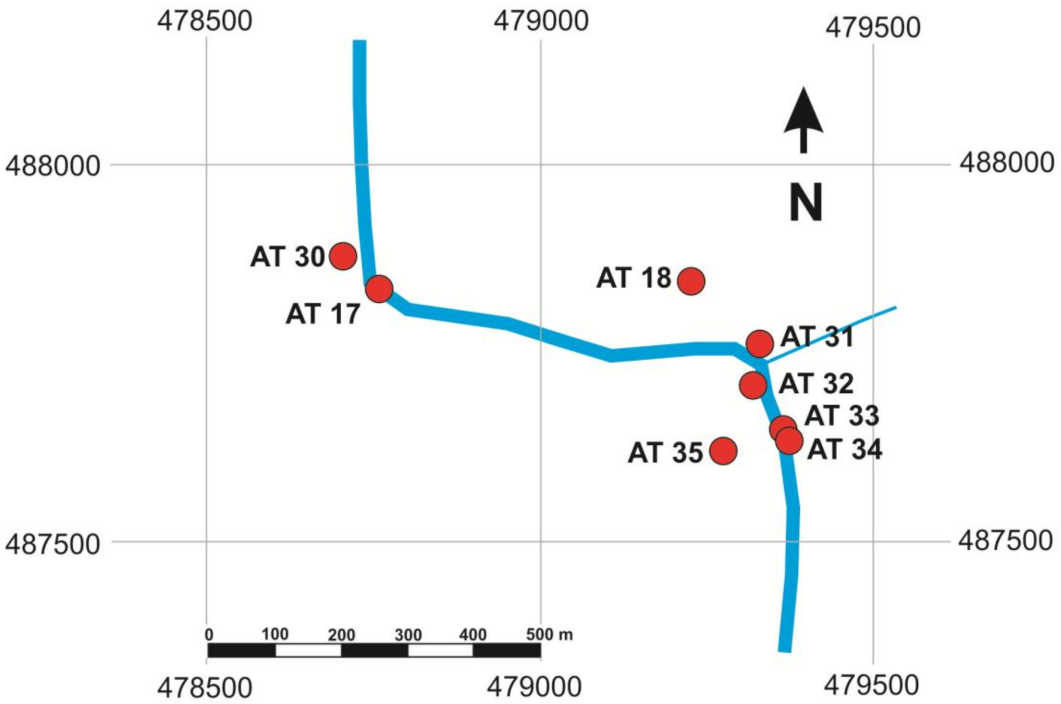

Figure 4.3: Magnified map with the sampling locations along the Moi-Moi creek. Further explanation can be found in the text. Coordinates in UTM21 WGS84. See Figure 4.1 for the location of the creek within the research area and Appendix I for the coordinates of the sampling locations.

Figure 4.4:* *A; *Part of a dolerite dyke. This block is located in the Misty Mountain creek. Hammer for scale.* ***B;*** *Dolerite dyke, 20 cm thick, located in the Misty Mountain creek.* ***C;*** *Outcrop AT04 in the Misty Mountain creek. The Charlie Gabbro is cut by a metadolerite dyke and a charnockite dyke. On the back of this outcrop the dolerite dyke is cut by the charnockite dyke. Hammer for scale.* ***D;*** *Pegmatitic dyke and vein in the Charlie Gabbro. This dyke is found in front of outcrop AT04. Hammer for scale.* ***E;*** *Close-up of one of the weathered cavities within outcrop AT04. Pencil for scale.* ***F;*** *Cavities, which are expected to be weathered olivines, within outcrop AT04. Some of them are marked by an arrow. Hammer for scale.*

4.2.2 Petrography of the Charlie Gabbro

The typical mineral assemblage of the Charlie Gabbro is Pl + Opx + Cpx +/- Ol +/- Bt with opaque minerals as accessory phases. The samples are coarse grained and have a cumulate texture (Figure 4.5 and 4.6A) where plagioclase and olivine are the cumulus phase and pyroxene the intercumulus phase. Olivine is absent from most samples of the Misty Mountain creek, but field observations (see 4.2.1) may point towards its former presence.

Plagioclase is the main constituent of the Charlie Gabbro. A clear increase of the normative plagioclase content is present from the olivine gabbronorites (47 Wt-% Pl in AT01, Table 4.1, Appendix III) to the gabbronorites (80 Wt-% Pl in AT03A; Table 4.1, Appendix III). It is present as largely euhedral laths (Figure 4.5 and 4.6A) which can reach a size up to 5-10 cm. The big plagioclase laths can be seen without a magnifying-glass in several rock samples. The plagioclase grains show carlsbad and albite twinning. Their composition varies from labradorite to bytownite. Deformation lamellae and undulose extinction are present in several grains in part of the rocks.

Olivine is a major mineral of the Charlie Gabbro. The olivine content is variable, olivine is absent from many gabbronorites but its CIPW norm amount goes up to 25 Wt-% in olivine gabbronorites (Table 4.1, Appendix III). Olivine can be recognized by its high relief and its 2nd order interference colours in XPL. It is mostly fresh or partly altered along the fractures into brownish material, possibly iddingsite. It is surrounded by inner coronas of orthopyroxene and outer coronas of brown hornblende and biotite (Figure 4.6B), but a colourless amphibole and green spinel can also be present as outer corona. The coronas lie between olivine and surrounding cumulus plagioclase or intercumulus clinopyroxene (Figure 4.6B and E). A single orthopyroxene corona separates intercumulus clinopyroxene from the olivine (Figure 4.6E), while double or triple coronas are more common between olivine and plagioclase (Figure 4.6B). The coronas are presumably formed due to disequilibrium between olivine and plagioclase during cooling of the magma. No direct contact between plagioclase and olivine is present, making it unclear which of these cumulus phases crystallised first. However, plagioclase is locally grown around the corona structures (Figure 4.6B), indicating that olivine was the first mineral phase to crystallise.

Both clinopyroxene and orthopyroxene are present as intercumulus phase (Figure 4.5 and 4.6A). The orthopyroxene can be distinguished by its characteristic colourless to pinkpleochroism and straight extinction. Clinopyroxene is colourless to pale brown and has an inclined extinction. The clinopyroxene has a small axial angle which is indicative for pigeonite. Inverted pigeonite is present in many samples. The inversion products

Sample	Olivine	Hypersthene	Diopside	Plagioclase	An:Ab (2:1)
AT01	23,22	16,67	9,05	47,40	2,26
AT02		31,60	0,92	63,83	2,31
AT03A	0,08	15,09	2,44	80,57	2,15
AT05B		26,04	3,83	66,70	1,95
AT06A		22,55	6,10	68,00	1,85
AT16B	4,53	23,20	11,02	51,01	1,74
AT16C		29,62	4,39	60,44	1,52
AT18	6,40	18,96	11,92	58,35	2,19
AT30	8,16	17,90	9,75	58,36	2,19
AT31		25,19	17,35	53,32	1,60
AT32	10,36	14,31	7,38	64,55	2,69
AT34A	10,49	16,62	6,79	60,56	2,55
AT34D	6,93	22,85	6,77	61,43	2,63
71-SUR-207	25,03	19,46	1,07	51,14	2,76
ER-1115	7,26	11,22	3,19	76,23	2,56
Avg. Gabbro*		22,13	13,70	48,86	1,41

Table 4.1: *CIPW-norm of the Charlie gabbro samples. Normative mineral assemblage of the average gabbro is taken from Cox et al. (1989).*

are visible in XPL as multiple fine intergrowths (Figure 4.6C). Inverted pigeonite normally forms during slow cooling. Other pyroxene crystals show rather coarse lamellae of orthopyroxene in a clinopyroxene host. Inversion of pigeonite would give orthopyroxene with minor lamellae of clinopyroxene, so the presence of these lamellae points to pigeonite exsolution from a clinopyroxene host, which subsequently became inverted (Figure 4.6D; cf. *Deer et al., 1992*).

Noticeable is the difference in pyroxene between the Moi-Moi creek and the Misty Mountain creek samples. The intercumulus pyroxene of Moi-Moi creek samples is mainly clinopyroxene, while orthopyroxene is mostly present in the Misty Mountain creek samples. A second difference is the general presence of olivine in the Moi-Moi creek samples and absence of olivine in the Misty Mountain creek samples. However, one olivine-free sample (AT31) with a high normative clinopyroxene content (Table 4.1, Appendix III) was collected from the Moi-Moi creek and one olivine-rich sample (Sur-207), with a high normative orthopyroxene content (Table 4.1, Appendix III) at the Misty Mountain creek.

Biotite is a minor constituent of the Charlie Gabbro and can be recognised by its pale to dark brown pleochroism and high 3rd order interference colours. It is mostly present adjacent to pyroxene on which it occurs as small lamellae or as a part of a corona texture that surrounds olivine. Most samples of the Charlie Gabbro contain a low amount of biotite (< 5 Wt-%). Only sample MKS61, which was taken from location AT01, has a high modal biotite content up to 10 Wt-%. It is unclear if the biotite in the Charlie Gabbro is of primary or secondary origin. The biotite in the olivine coronas is most likely formed during slow cooling of the magma and can be considered as late primary crystallisation. Biotite lamellae adjacent to intercumulus pyroxene could be of primary or secondary origin.

Finally, some small, rare hornblende lamellae can be present in between biotite lamellae. These hornblende lamellae can be recognised by their pale to olive green pleochroism and high 2nd to 3rd order interference colours. Opaque minerals are present as inclusions in plagioclase and pyroxene, or in cracks in olivine. The opaque mineral content increases with increasing olivine content.

The extensive presence of intact magmatic textures throughout the rocks and the lack of recrystallisation indicate that the Charlie Gabbro did not experience a period of metamorphism.

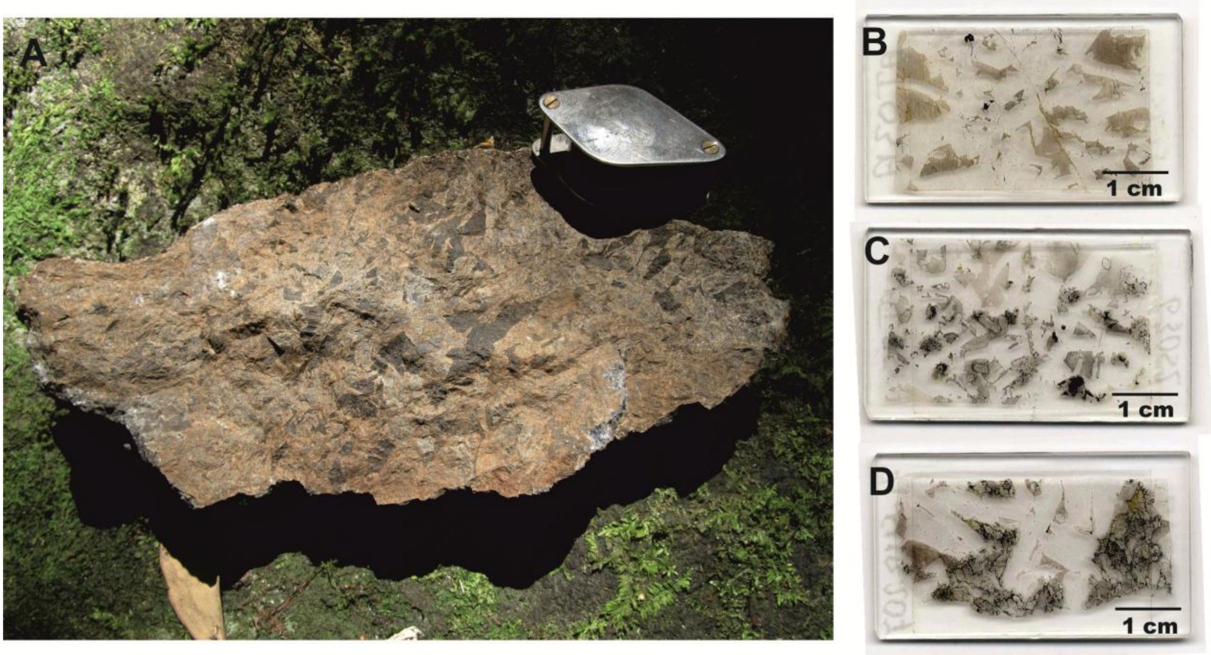

Figure 4.5: *Figure A – D show the cumulate texture of the Charlie Gabbro. All figures show light coloured lath-shaped plagioclase with dark coloured intercumulus pyroxene in between.* ***A;*** *Sample with coarse intercumulus (dark) and cumulus crystals, Misty Mountain creek. Magnifying-glass for scale.* ***B;*** *Thin section of gabbro AT03A, Misty Mountain creek.* ***C;*** *Thin section of olivine gabbro AT35 from the Moi-Moi creek. The grey coloured intercumulus minerals are pyroxene and the darker, partly black spots are cumulus olivines.* ***D;*** *Olivine gabbronorite Sur-207 from the Misty Mountain creek. Cumulus olivines can be distinguished from the pyroxenes by their darker colour.*

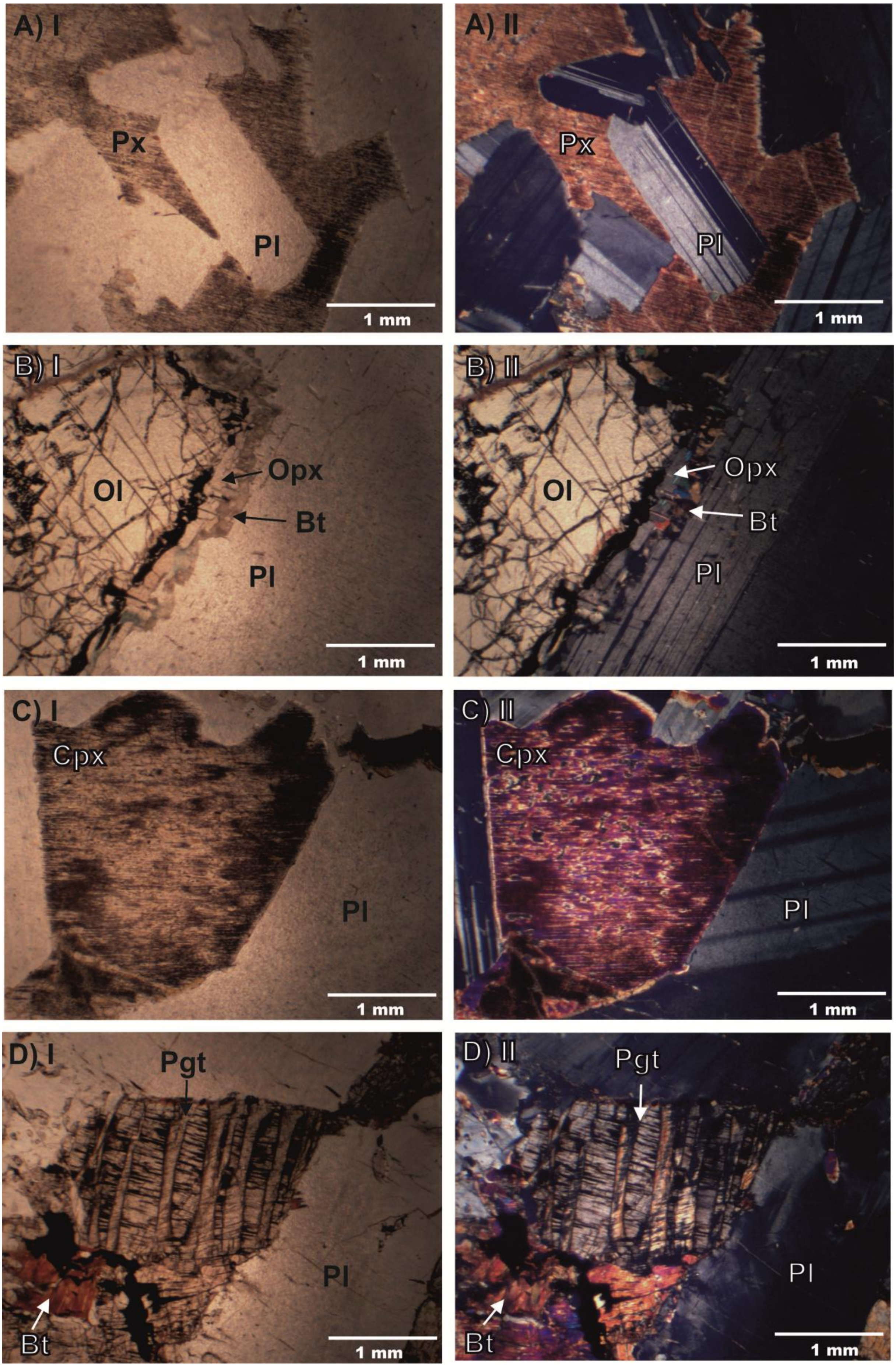
A) I
Px
Pl
1 mm
A) II
Px
Pl
1 mm
B) I
Ol
Opx
Bt
Pl
1 mm
B) II
Ol
Opx
Bt
Pl
1 mm
C) I
Cpx
Pl
1 mm
C) II
Cpx
Pl
1 mm
D) I
Pgt
Pl
Bt
1 mm
D) II
Pgt
Pl
Bt
1 mm

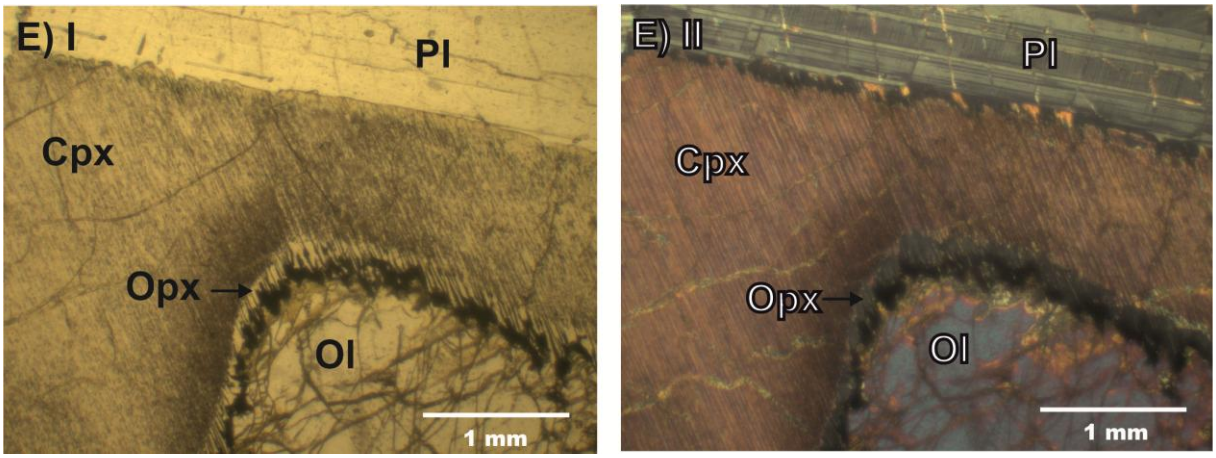

***Figure 4.6 (including previous page):** Pictures of thin sections from the Charlie Gabbro. I in PPL, II in XPL. Abbreviations: Px = pyroxene, Pl = plagioclase, Ol = olivine, Opx = orthopyroxene, Bt = biotite, Cpx = clinopyroxene, Pgt = inverted pigeonite. **A;** Cumulus plagioclase laths with intercumulus pyroxene. AT32. **B;** Olivine with corona structure surrounded by plagioclase. The inner corona consists of orthopyroxene, adjacent to the olivine and another corona of biotite. AT35. **C;** Inverted clinopyroxene surrounded by plagioclase. The inversion is clearly visible in XPL. AT06A. **D;** Inverted pigeonite (now lamellae of orthopyroxene) within a clinopyroxene host. AT06A.**E;** Olivine with corona of orthopyroxene surrounded by clinopyroxene.*

4.2.3 Charnockite contamination

Samples AT16B and 16C are taken from a small waterfall in the Misty Mountain creek. AT16B is a medium to fine grained gabbronorite and is located adjacent to the charnockite, but a direct contact is obscured and the charnockite show a chaotic alternation with angular metadolerite fragments. Therefore sample AT16B is considered to represent a chilled margin at the edge of the body. AT16C is a coarse grained gabbronorite and is taken 10 metres from AT16B.

Both samples contain the characteristic petrography of the Charlie Gabbro, of plagioclase with intercumulus pyroxene, but also contain some intercumulus K-feldspar and quartz. The latter two could indicate a more evolved magma from the gabbroic batch. In addition, plagioclase shows antiperthite exsolution, which is formed at high temperature. K-feldspar, antiperthite and quartz have not been found in other Charlie Gabbro samples.

4.3 Moi-Moi Metagabbro

4.3.1 Occurrences and field observations

The samples of the Moi-Moi Metagabbro were collected during the fieldtrip or taken from diamond drill cores, drilled by the GMD. In the 1960's a metagabbroic-ultramafic body west of the Kabalebo river (Figure 4.1), coinciding with a prominent geophysical anomaly, was investigated in search for base metals. Drill cores indicate that the body consists of a central ultramafic part surrounded by a border zone of quartz-diorite. Three quartz-diorite samples were taken from drill core LA150, and five ultramafic samples from drill cores LA148 and LA149. The latter cores are drilled east to west over the metagabbroic-ultramafic body. The distance between the two outermost cores, and thus the minimal length of the body, is 800 m. According to the GMD data from the 60's, the body measures approx. 1 x 0,6 km at the surface. Moreover, it is partly connected to another body (not drilled) measuring 1,5 x 0,6 km at the surface. The coordinates of the drill cores and sampling depths can be found in Appendix I.

In addition, two gabbroic bodies were extensively sampled (as far as possible) during the fieldtrip. The first body is located at the Moi-Moi Falls, starting directly above the Falls and continuing upstream along the Moi-Moi creek (Figure 4.1 and 4.7). The contact between the coarse grained metagabbronorites of this body and the surrounding charnockite is present directly above the Moi-Moi waterfall (Figure 4.8A), but an unexposed zone of 5m occurs at the contact. Starting from this contact, the gabbronorite can be followed semicontinuously within the riverbed until outcrop AT09. In between AT09 and AT10 occurs an alternation of metadolerite and charnockite. From sampling location AT10 the gabbronorites can be traced semicontinuously in the riverbed until the fine grained outcrop AT13. The first outcrop after AT13 consists of mylonitic charnockite and marks the end of the body.

Characteristic features are the multiple pegmatitic veins that have intruded the gabbroic body in between sampling locations ER1109 and AT09 (Figure 4.8B). In contrast, the gabbronorites between sampling locations AT10 and AT13 do not show pegmatitic veins. The discontinuity between the sample AT09 and AT10 indicates the possibility of two smaller, nearby gabbroic bodies instead of one larger body. Field relations indicate two gabbroic bodies of about 100 m in size, or one body of more than 200 m in size (Figure 4.7). The contacts with charnockite at the waterfall and shortly after AT13 indicate that the body will not be much bigger. It is interpreted as a sill or a less regular pluton. In this thesis the bodies will be treated as one intrusion due to their similar petrography and close distance to each other. In total, 11 gabbroic samples were taken from this body.

The second sampling location is in a valley near the Zandkreek where several meter scale outcrops are found. They are located at close distance from each other and most probably belong to the same body, which was investigated by the GMD in the 70's (without drilling) because it is situated at a geophysical anomaly. The sampled outcrops are located within a range of 60 x 50 metre from each other (Figure 4.1 and Appendix I). According to the GMD data from the 70's, the body exposed at the surface would be 0,5 x 0,25 km in size, but exposure was poor, and rainforest covers most of the valley. Seven samples were taken from this valley. Two samples (AT36A and B) were taken from large loose blocks at the bottom of the valley while the other samples were taken from the outcrops. One of the outcrops (AT37) shows the contact of dark pyroxenite at the bottom and a lighter coloured gabbronorite at the top, which contains several small (around 5 cm) rounded xenoliths of pyroxenite.

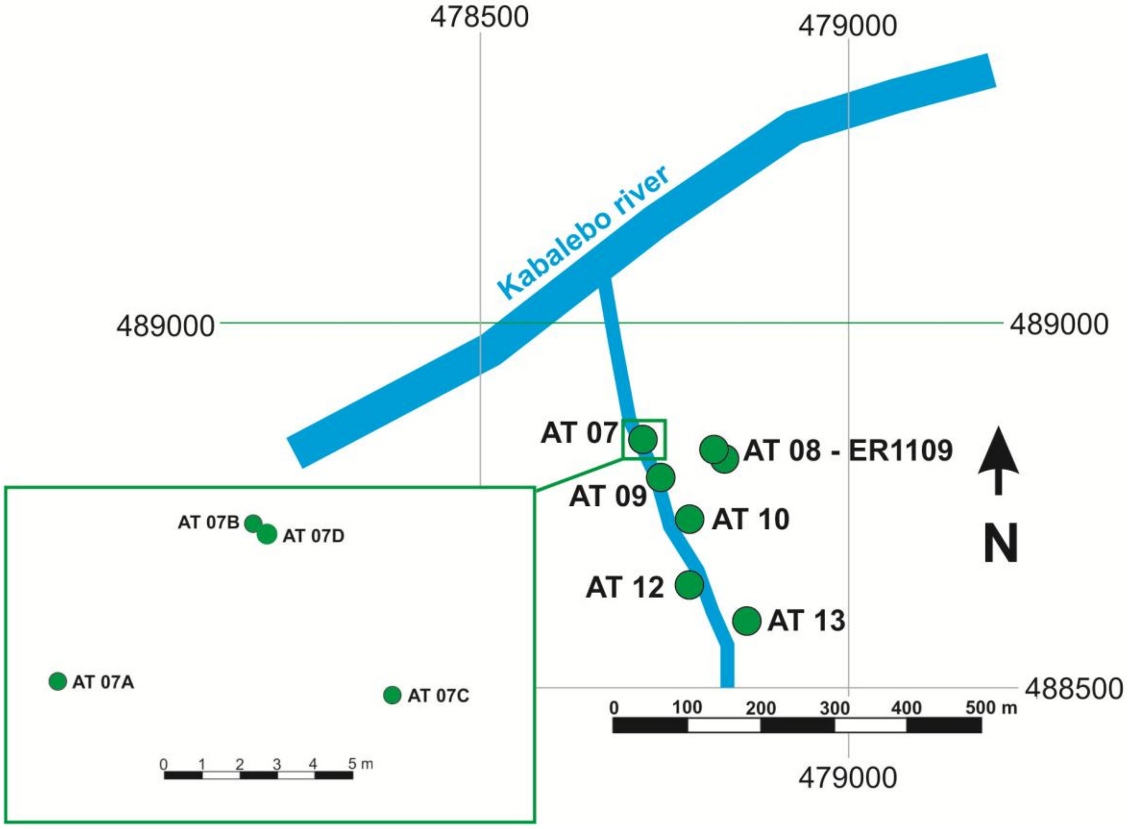

Figure 4.7: *Magnified map with the sampling locations downstream of the Moi-Moi creek. The green box shows the close distance between the different sampling locations of samples AT07A t/m D. Further explanation can be found in the text. Coordinates in UTM21 WGS84. See Figure 4.1 for the location of the creek within the research area and Appendix I for the coordinates of the sampling locations.*

4.3.2 Petrography of the Moi-Moi Metagabbro

The metagabbroic-ultramafic bodies of the Moi-Moi Metagabbro contain different lithologies which vary from olivine pyroxene hornblendites to quartz-diorites. Several lithologies can occur together in one body (e.g. quartz-diorite and olivine pyroxene hornblendite in Kabalebo West or pyroxene hornblende mela-gabbronorite and olivine hornblende pyroxenite near the Zandkreek) with a clear boundary (outcrop AT37 and drill cores, see 4.3.1) in between, but more homogeneous bodies (e.g. above the Moi-Moi Falls) are also present.

Based on the petrography, the Moi-Moi Metagabbro samples available can be subdivided into four lithologies, namely the olivine pyroxene hornblendites, the pyroxene hornblende mela-gabbronorites, including an olivine hornblende pyroxenite, the pyroxene hornblende gabbronorites and the quartz-diorites. All lithologies are coarse grained, unless mentioned differently. The different groups will be discussed separately in the following pages.

The rocks of the Moi-Moi Metagabbro can be recognized by their big poikilitic hornblende crystals, which can reach a size of several cm. These characteristic hornblende crystals are present in all mafic lithologies of the Moi-Moi Metagabbro and occur as smaller grains of a few mm in size in the quartz-diorites. They are not seen in mafic bodies of other types in the BGB.

Olivine pyroxene hornblendites

The ultramafic rocks of the Moi-Moi Metagabbro are found in drill cores LA148 and LA149 of the Kabalebo West site. These rocks contain > 90 percent modal mafic minerals and vary from olivine pyroxene hornblendite to hornblende pyroxenite, where small variations in the proportion of the main minerals result in a different rock name. Their mineral assemblage is Hbl + Opx + Cpx + Phl +/- Ol +/- Pl + Opq, with hornblende, pyroxene and olivine as major phases, phlogopite and plagioclase as minor phases and opaque minerals, including magnetite, as an accessory phase. Olivine, orthopyroxene, clinopyroxene and probably magnetite are present as cumulus phases which are surrounded by large intercumulus hornblende grains.

Hornblende is an important component. It is present as large poikilitic crystals which are olive-green or brownish green pleochroic and surround finer olivine and pyroxene grains (Figure 4.9A and B). Exsolution of Fe-Ti oxides in the form of small opaque inclusions are present in olive-green hornblende. The hornblende can be recognised by its 2nd or 3rd order interference colours and characteristic 60-120° cleavage.

Olivine is absent in the hornblende pyroxenite (LA148-58,5) but the other three samples contain 20 to 30 percent modal olivine. It forms mostly fresh, an- to subhedral crystals that contain embayments (Figure 4.9B). The poikilitic hornblende is crystallised in the resorbed parts of the olivine crystals (Figure 4.9B), indicating that the remaining interstitial liquid reacted with the cumulus olivines, resulting in the growth of the large hornblende grains. Most olivine crystals are surrounded by large poikilitic hornblende, but they can also be seen as small inclusions within the pyroxene, or within primary phlogophite (Figure 4.9C). Orthopyroxene is locally seen as a thin rim surrounding olivine. The edges of these olivines show less embayments.

Figure 4.8:* A;** *The Moi-Moi Falls, downstream Moi-Moi creek. Above this waterfall starts the Moi-Moi metagabbronorite body.* ***B; *Pegmatitic dyke which cuts the metagabbronorite body in the Moi-Moi creek. Hammer for scale.*

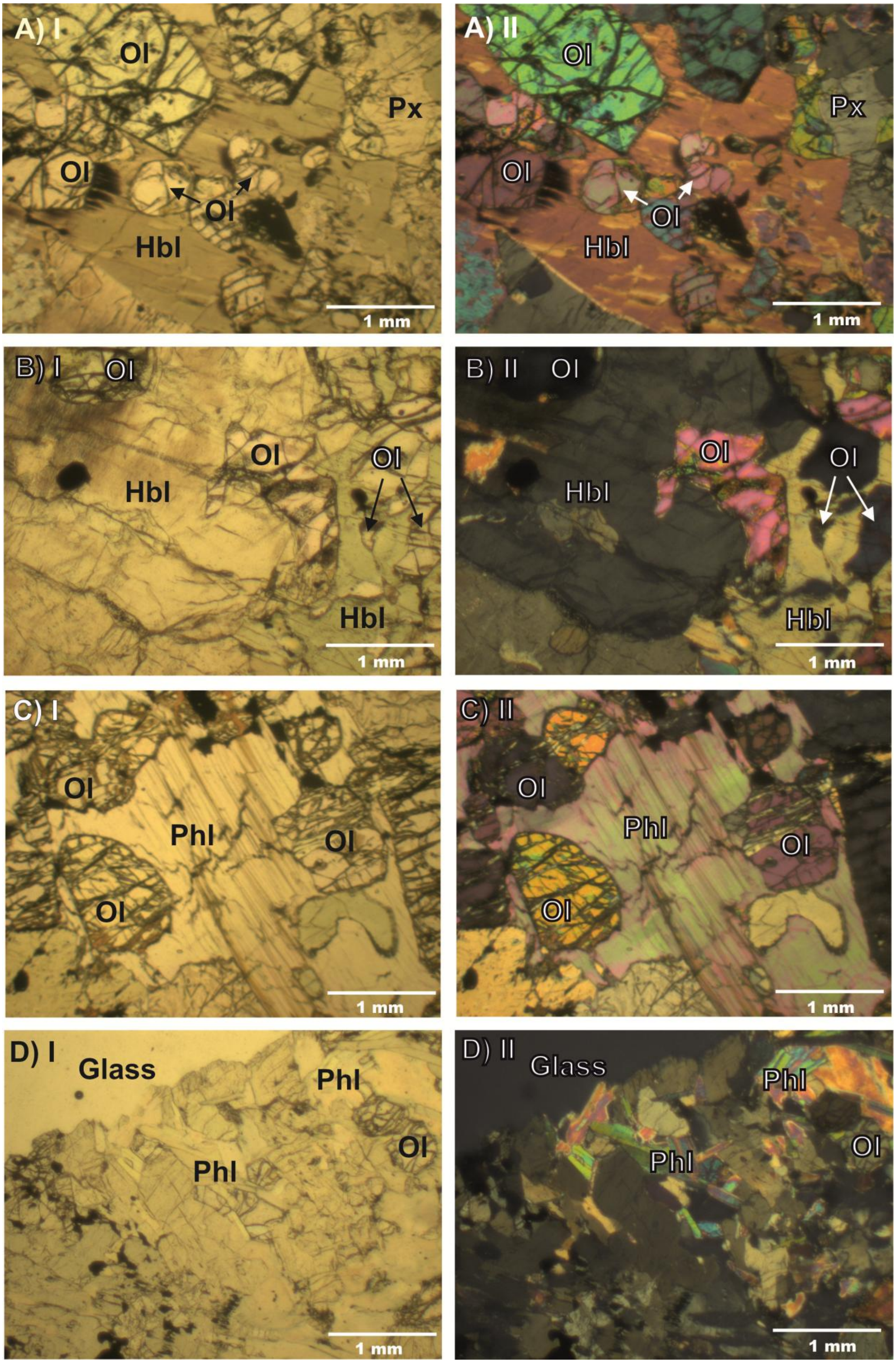
A) I
Ol
Px
Ol
Ol
Hbl
1 mm
A) II
Ol
Px
Ol
Ol
Hbl
1 mm
B) I
Ol
Ol
Ol
Hbl
Hbl
1 mm
B) II
Ol
Ol
Ol
Hbl
Hbl
1 mm
C) I
Ol
Phl
Ol
Ol
1 mm
C) II
Ol
Phl
Ol
Ol
1 mm
D) I
Glass
Phl
Ol
Phl
1 mm
D) II
Glass
Phl
Ol
Phl
1 mm

Figure 4.9 (previous page): *Pictures of thin sections from the olivine pyroxene hornblendites of Kabalebo West. I in PPL, II in XPL. Abbreviations: Px = pyroxene, Ol = olivine, Hbl = hornblende, Phl = phlogophite.* ***A;*** *Large poikilitic hornblende with incorporated olivine minerals. Picture taken from LA148-40.* ***B;*** *Olivine with embayments (middle picture) surrounded by hornblende. Only a few relicts are present of the olivine in the right side of the picture. Picture taken from thin section LA148-40.* ***C;*** *Intercumulus phlogophite with incorporated olivine grains. Picture is taken from thin section LA148-64.* ***D;*** *Secondary phlogophite in the recrystallised part of thin section LA149-72. The secondary phlogophite overgrows the granoblastic texture. This granoblastic texture is best visible in XPL. The picture is taken near the transition between the sample and the glass of the thin section.*

Pyroxenes are present as an- to subhedral grains. They contain inclusions of olivine and are often surrounded by poikilitic hornblende. Orthopyroxene can be distinguished by its pink pleochroism and straight extinction while clinopyroxene is pale brown and has an inclined extinction. The edges of clinopyroxene crystals are corroded. Both pyroxenes are a cumulus phase, but it is unclear which of them crystallised first.

Phlogopite has a nearly colourless appearance and high, 3rd order interference colours. It is present as both primary and secondary crystals. The primary crystals are an intercumulus phase which crystallised after hornblende and can be found around the cumulus minerals (Figure 4.9C). Secondary phlogophite is present as subhedral grains grown together as aggregates (Figure 4.9D). These grains are located within recrystallised areas of the rocks and are expected to have formed during a metamorphic event. Plagioclase is rare or even absent (LA149-64,5) in the samples. It is an intercumulus phase and is the last phase to crystallise. Opaque minerals are part present as anhedral grains in between the other minerals. Small euhedral sections of octahedral magnetite are common in all four samples. They occur part in olivine crystals, which indicates that they probably are an even earlier cumulus phase than olivine.

The samples are coarse grained, but local recrystallisation of the minerals into a fine grained granoblastic texture (Figure 4.9D) took place, indicating a metamorphic stage. Secondary phlogophite between the anhedral recrystallised grains is expected to have formed during this metamorphic event. LA149-64 is slightly different. It shows some signs of recrystallisation, but granoblastic texture is absent. Several micro-shear zones are present in this sample.

Pyroxene hornblende mela-gabbronorites

One olivine hornblende pyroxenite (AT38) was collected near the Zandkreek. This sample is expected to be a cumulate of the overlying pyroxene hornblende mela-gabbronorites (see 4.3.1). Both lithologies have a typical mineral assemblage of Opx + Cpx + Hbl + Opq + Pl +/- Ol +/- Bt, with orthopyroxene, clinopyroxene, olivine and hornblende as major phases and plagioclase, biotite and opaque ore minerals as minor phases. The pyroxene hornblende mela-gabbronorites contain 60 to 80 percent modal mafic minerals, while the olivine hornblende pyroxenite contains about 85 percent of modal mafic minerals. The samples have a cumulate texture with olivine, orthopyroxene and clinopyroxene as cumulus and hornblende and plagioclase are intercumulus phases.

Olivine is only found in the olivine hornblende pyroxenite, as fresh, an- to subhedral crystals with embayments in the edges (Figure 4.10A and B). It shows a corona of orthopyroxene or is surrounded by poikilitic hornblende (Figure 4.10A). The relation between the embayments of the olivines and the hornblende indicates that the intercumulus liquid reacted with olivine to form hornblende.

Pyroxene is present as an- to subhedral grains. Orthopyroxene has its typical pink pleochroism, while clinopyroxene is pale brown. Many clinopyroxene grains show exsolution of Fe-Ti oxides and of opx lamellae (Figure 4.10B). Clinopyroxene is sometimes included in or surrounded by orthopyroxene, giving the appearance that it crystallised first. However, indications that show the opposite are also present, therefore it is unclear which of the pyroxenes crystallised first.

Hornblende is present as poikilitic crystals which include orthopyroxene, clinopyroxene and olivine (Figure 4.10A). It is olive-green pleochroic with exsolved fine Fe-Ti oxide grains. Hornblende can be present both as large poikilitic crystals and as smaller intercumulus grains. It formed at the expense of olivine in sample AT38.

Intercumulus plagioclase (Figure 4.10A and B) contains both orthopyroxene and clinopyroxene as inclusions. Additionally, small pale to dark brown pleochroic biotite grains can be present as intercumulus phase. Finally, opaque minerals mostly occur as fine exsolution product, but are also present in aggregations in between the different minerals.

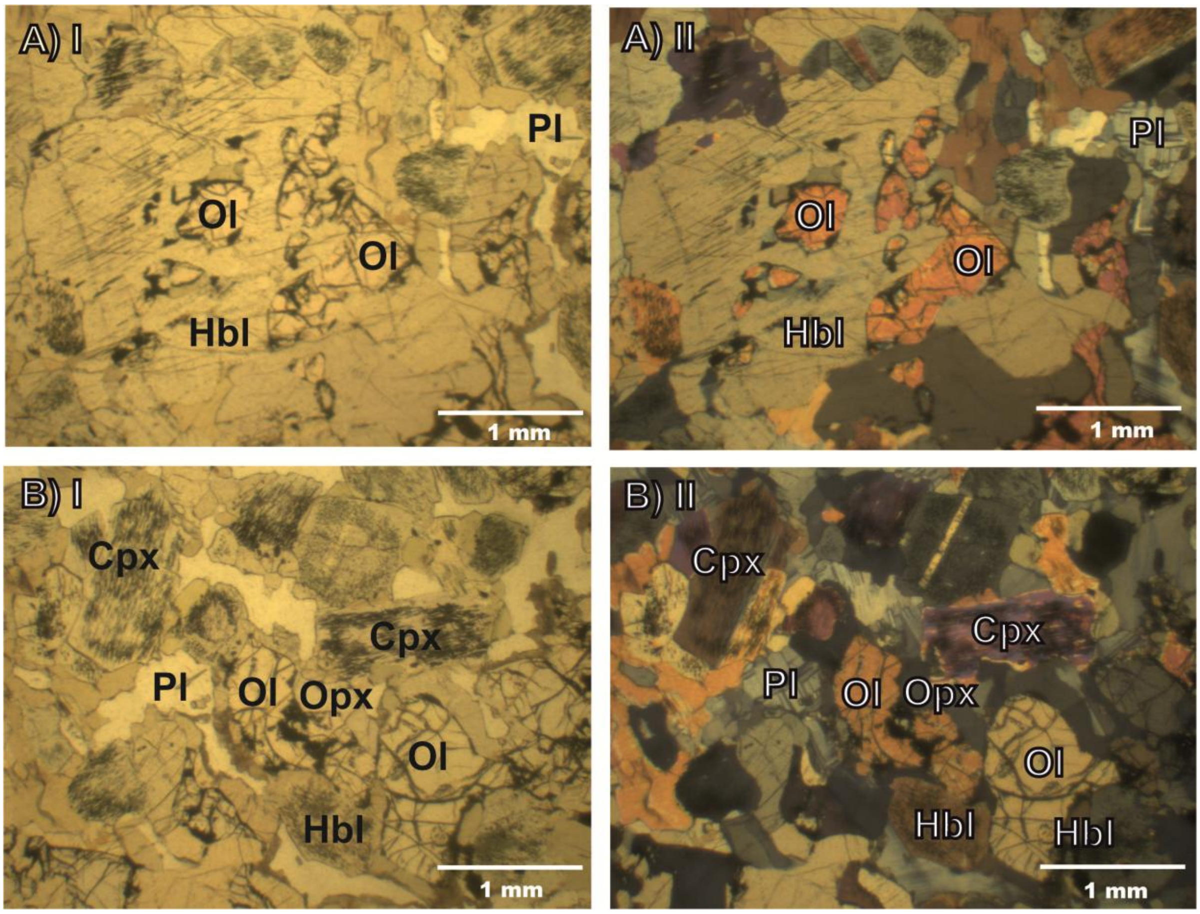

Figure 4.10: *Pictures of thin sections from the Zandkreek. I in PPL, II in XPL. Abbreviations: Pl = plagioclase, Ol = olivine, Hbl = hornblende, Opx = orthopyroxene, Cpx = clinopyroxene.* ***A;*** *Olivine relicts in large poikilitic hornblende crystal. Pyroxenes are present in the top of the picture and intercumulus plagioclase is visible in the right of the picture. Picture taken from AT38.* ***B;*** *Accumulation of olivines and pyroxenes. Olivines show embayments and are in direct contact to poikilitic hornblendes or are surrounded by an orthopyroxene rim. The exsolution of Fe-Ti oxides in clinopyroxene is clearly visible in PPL. Intercumulus plagioclase is present between the cumulus minerals. The picture is taken from thin section AT38.*

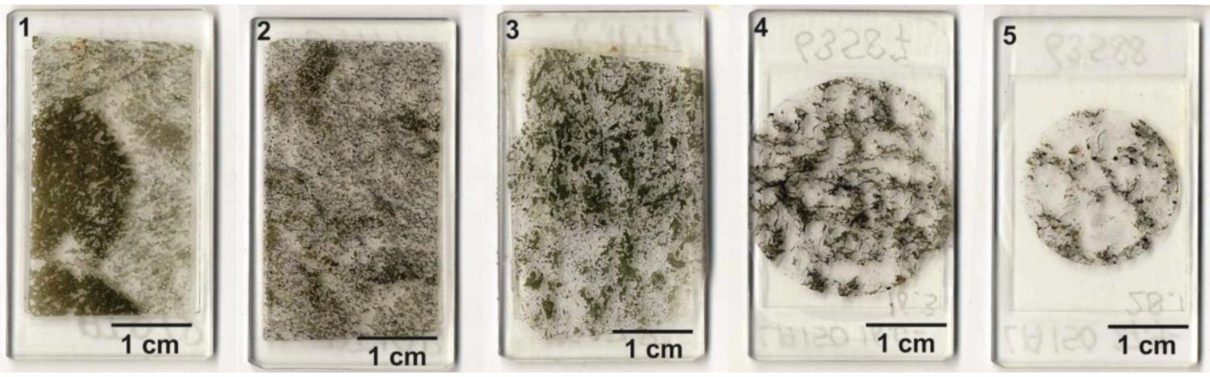

Figure 4.11: *Thin sections from the Moi-Moi metagabbronorite. See text for further explanation.* ***1;*** *Sample AT07D. Large poikilitic hornblende (dark green crystal) with incorporated plagioclase laths.* ***2;*** *Sample AT10B, granoblastic texture with recrystallised hornblende grains.* ***3;*** *Amphibolite AT07B.* ***4 and 5;*** *Overall texture of the quartz-diorites. Large felsic mineral grains with aggregations of small mafic minerals in between. Thin section LA150-16 (4) and LA150-28 (5).*

Pyroxene hornblende gabbronorites

The gabbronorites of the Moi-Moi Metagabbro have a typical mineral assemblage Hbl + Opx + Cpx + Pl +/- Bt with opaque minerals as accessory phase. The coarse grained rocks contain 40 to 60 percent of mafic minerals and are classified as pyroxene hornblende gabbronorites.

They are divided into three different groups based on their petrographic textures. The first group contains subhedral plagioclase laths and pyroxene crystals incorporated in large poikilitic hornblende crystals (Figure 4.11-1 and 4.12A). This primary hornblende has a pale to olive green colour. The plagioclase laths show carlsbad and albite twinning and have a labradorite to bytownite composition. No recrystallisation is seen in the cumulus plagioclase and pyroxene. Exsolution of Ti-Fe oxides is present as fine black spots and is the only indication of recrystallisation in the poikilitic hornblende.

The gabbronorite is completely recrystallised into a granoblastic texture outside the poikilitic hornblendes (Figure 4.12B). Smaller, blue-green hornblende grains, which are considered to be of secondary origin, are present in the groundmass or near the edge of the olive-green poikilitic hornblende crystals. Recrystallised clinopyroxene and orthopyroxene grains occur in the granoblastic mass. Part of the plagioclase, shows undulose extinction and deformation lamellae.

Small grains of biotite are common, but their shape makes it difficult to determine if they are an primary or secondary. They are mostly present in the granoblastic groundmass but small lamellae occur locally in the primary poikilitic hornblendes. Finally, opaque minerals occur as exsolution products or as smaller aggregations in between the other minerals.

The size of the poikilitic hornblende crystals and the included plagioclase and pyroxene crystals points towards an igneous origin of the hornblende. The cumulus character of the plagioclase laths and pyroxene crystals indicate that they were the first minerals to crystallise during cooling of the gabbroic magma. The recrystallisation of plagioclase and pyroxene outside the poikilitic hornblende into a granoblastic texture indicates a period of metamorphism at higher amphibolite to possibly granulite facies, but it appears that this event hardly affected the primary hornblende and the incorporated cumulus phases.

The second group lacks the large poikilitic hornblende. Instead it has a granoblastic texture where hornblende is part of the recrystallised grains, besides clino- and orthopyroxene and plagioclase (Figure 4.11-2 and 4.12C). The anhedral hornblende grains are pale to olive green pleochroic. Biotite can be present as pale to dark brown pleochroic crystals. Finally, opaque minerals are present as anhedral grains. The recrystallisation of all minerals into a granoblastic texture indicates metamorphism at higher amphibolite to possibly granulite facies. This metamorphic event completely recrystallised the rocks, leaving no evidence of the protolith. However, the mineral content suggests a gabbroic protolith.

The third group comprises two amphibolites (AT07B and C, Figure 4.11-3) from the border zone of the gabbroic body, taken just above the contact at the Moi-Moi Falls. The mineral assemblage consists only of plagioclase and hornblende as major phases and opaque minerals as accessory phase. The plagioclase occurs as subhedral laths, which are locally recrystallised into a granoblastic texture (Figure 4.12D and E). The plagioclase laths are oriented parallel to each other, indicating the possibility of magma flow during the crystallisation of the rocks. The plagioclase laths contain albite and carlsbad twinning.

The hornblende has a pale to dark green pleochroism. It crystallised in between the plagioclase laths, indicating crystallization after the plagioclase. Finally, anhedral opaque minerals occur in between the plagioclase and hornblende. The parallel oriented plagioclase laths and intercumulus hornblende indicate that the amphibolites have an igneous origin. Metamorphism took only locally place and recrystallised the rocks into a granoblastic texture.

Quartz-diorite

Three quartz-diorite samples were taken from drill core LA150. They show a similar mineralogy and texture, with Pl as major phase and Opx + Cpx + Kfsp + Q + Bt + Hbl as minor phases with Opq + Zrn + Ap + Grt as accessory minerals. The amount of the mafic minerals varies between 20 to 40 percent (Figure 4.11-4 and 5).

The plagioclase grains are anhedral and show albite and carlsbad twinning. Most grains are large, but smaller grains occur near the mafic minerals. Recrystallisation into a granoblastic texture is locally present.

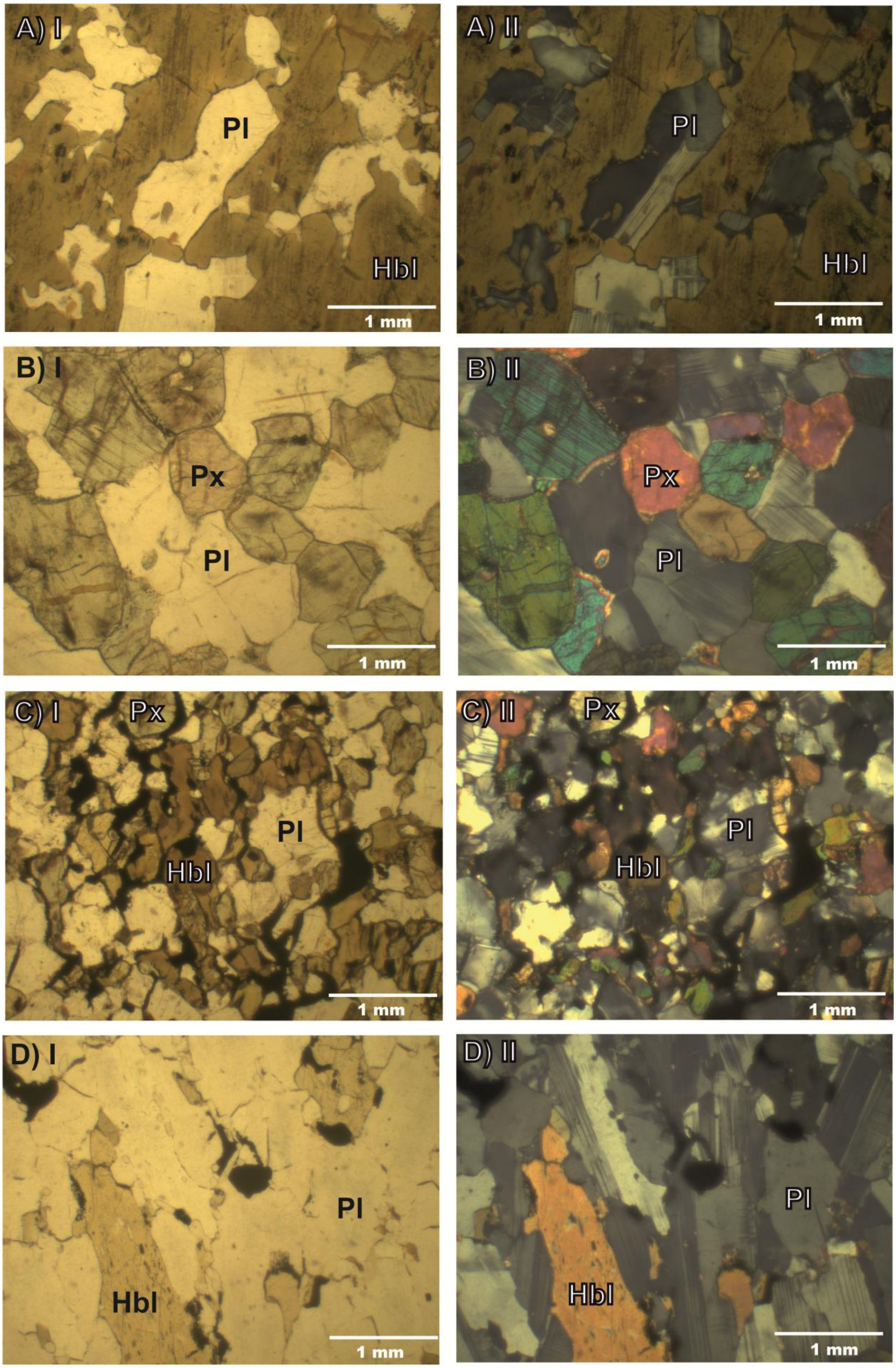
A) I
Pl
Hbl
1 mm
A) II
Pl
Hbl
1 mm
B) I
Px
Pl
1 mm
B) II
Px
Pl
1 mm
C) I
Px
Pl
Hbl
1 mm
C) II
Px
Pl
Hbl
1 mm
D) I
Pl
Hbl
1 mm
D) II
Pl
Hbl
1 mm

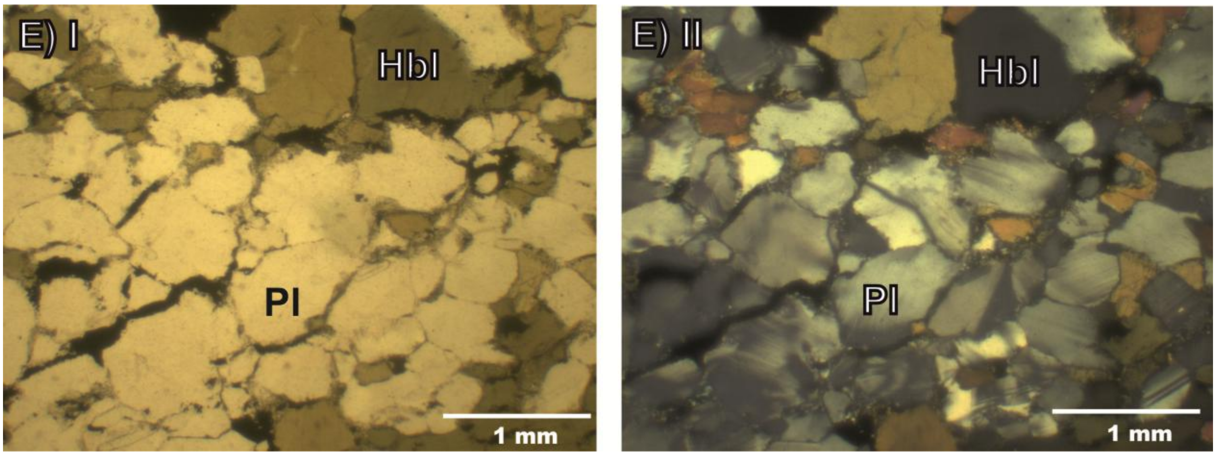

Figure 4.12 (including previous page): *Pictures of thin sections from the Moi-Moi metagabbronorites. I in PPL, II in XPL. Abbreviations: Pl = plagioclase, Hbl = hornblende, Px = pyroxene.* ***A;*** *Group 1: poikilitic hornblende including cumulus plagioclase laths. Sample AT07D.* ***B;*** *Group 1: recrystallisation of plagioclase and pyroxene into a granoblastic texture. Picture taken next to poikilitic hornblende of previous image, sample AT07D.* ***C;*** *Group 2: Granoblastic texture with plagioclase, pyroxene, hornblende and opaque minerals. Sample AT10B.* ***D;*** *Group 3: parallel oriented plagioclase laths (top – bottom orientation in picture) with intercumulus hornblende. Sample AT07C.* ***E;*** *Group 3: recrystallisation into a granoblastic texture. Sample AT07C.*

Furthermore, resorption features are present at the boundaries of big grains. Many plagioclase grains show antiperthitic exsolution at the edge, indicating an oligoclase composition of the rim.

Pyroxene, both ortho- and clinopyroxene, is present as small, subhedral grains (Figure 4.13B) as inclusions in plagioclase and probably represents a cumulus phase. Some of the pyroxene grains were recrystallised into smaller grains. Biotite occurs as small anhedral grains (Figure 4.13A and B). Hornblende is less common, it has pale green to dark green pleochroism and occurs as small anhedral grains.

Small lath-shaped zircon grain occur near the mafic minerals. They can be recognized by their very high relief and their high, 3^{rd} order interference colours in XPL. Apatite is located in close association to the mafic minerals (Figure 4.13A and B). It has a rather high relief and dark grey interference colours. The grains are equant or lath shaped and are often present as inclusions in plagioclase. Opaque minerals are mostly present as aggregations and surround anhedral garnet grains. The garnet is colourless with a smokey appearance (Figure 4.13A). It occurs locally in one of the samples, located near small shear zones, and is probably of secondary origin.

Relations between the different minerals show that pyroxene, zircon and apatite were the first phases that crystallised, followed by biotite and hornblende. Finally, the felsic minerals plagioclase, k-feldspar and quartz crystallised. Recrystallisation into a granoblastic texture is locally present in both the mafic and felsic minerals, indicating local metamorphism in higher amphibolite to granulite facies. It is assumed that the secondary garnet was created during this metamorphic episode, but its location near small, probably post-Transamazonian (possibly Nickerie Tectonothermal Episode) shear-zones suggest a later formation.

4.4 Kilo Drie metagabbro

4.4.1 Occurrences and field observations

Samples of the Kilo Drie metagabbronorite were collected at two locations. One body is found near the Kilo Drie creek, at a small hill east of the creek (Figure 4.1 and 4.14). The body is covered by dense rainforest, but several large outcrops are present. The metagabbronorites from sampling locations AT24 and AT26 are fine grained, while in between (AT25) a coarse grained metagabbronorite is present. Charnockite occurs before sampling location AT24 and after AT26, but no direct contact between the two lithologies is seen. The distance between AT24 and AT26 is about 200 metre (Figure 4.14) and the presence of the nearby charnockites indicate that the body will not be much bigger. The body is interpreted as a sill or a pluton.

Outcrop AT23 is located along the Kilo Drie creek (Figure 4.1 and 4.14). It is five by eight metres and the rocks are fine grained near the creek and medium to coarse grained towards the rain forest. Some rocks contain visible quartz grains, indicating interaction with the surrounding charnockites. No direct contact between the two lithologies is found. The petrography is similar to the other samples from the Kilo Drie creek.

Four fine to coarse grained metagabbronorites were collected from a valley south of the Misty Mountain (Figure 4.1, Appendix I). No outcrops are found, the samples were taken from loose blocks at the bottom of the valley.

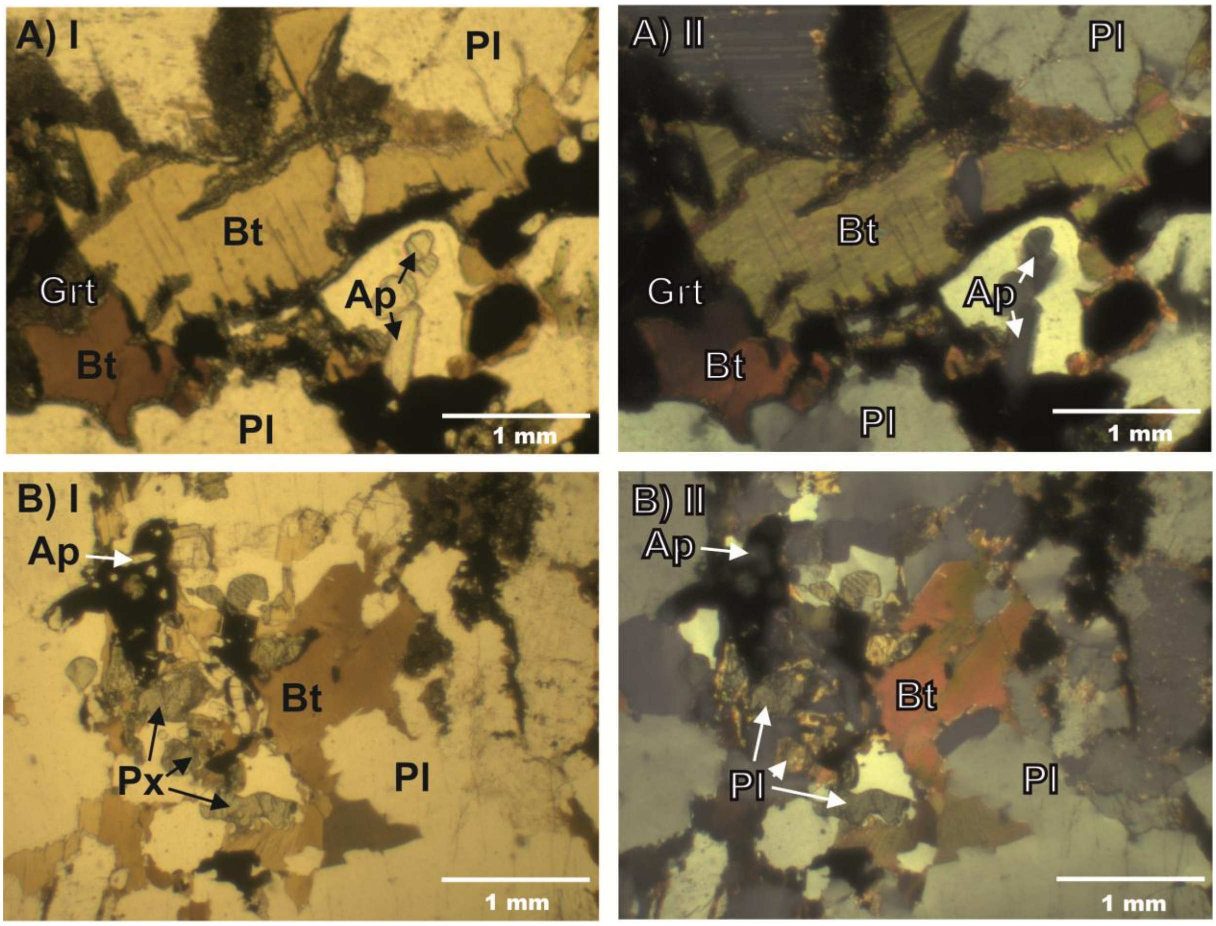

Figure 4.13: *Pictures of thin sections from the quartz-diorites. I in PPL, II in XPL. Abbreviations: Pl = plagioclase, Bt = biotite, Ap = apatite, Grt = garnet, Px = pyroxene.* ***A;*** ***A****patite, biotite and opaque minerals with secondary garnet. Small intercumulus grains are located in between the accessory minerals.* ***B;*** *Cumulus pyroxene and apatite surrounded by biotite and opaque minerals. Plagioclase fills up the space in between the cumulus pyroxene.*

4.4.2 Petrography of the Kilo Drie metagabbro

The typical mineral assemblage of the Kilo Drie metagabbro is Pl + Opx+ Cpx + Bt +/- Q with opaque minerals as accessory phase. Hornblende lamellae can occur locally. The metagabbronorite is completely recrystallised into a granoblastic texture. The recrystallisation probably occurred at high amphibolite to granulite facies conditions.

The samples contain 40 to 50 percent felsic minerals, mainly plagioclase. The plagioclase is present as anhedral, completely recrystallised grains (Figure 4.15A and B). Antiperthitic exsolution is seen in sample AT28, which indicates a more sodic composition. K-feldspar may be present in small quantity. Several samples contain rare, anhedral quartz grains. The pyroxene is completely recrystallised into smaller, anhedral grains (Figure 4.15B), which often lack cleavage, making it more difficult to distinguish between orthopyroxene and clinopyroxene. Noticeable are the rare hornblende lamellae which can be present in clinopyroxene grains. Biotite is a minor phase in all samples. Opaque minerals are often present as small inclusions in the pyroxene, or appear as bigger aggregations in between the other minerals.

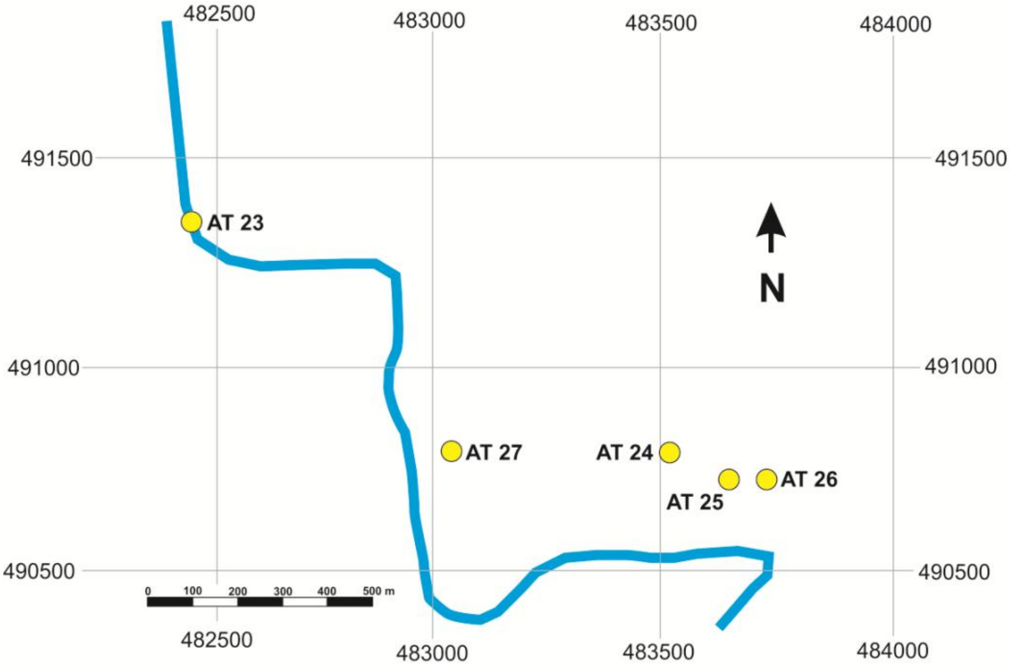

Figure 4.14: *Magnified map with the sampling locations near the Kilo Drie creek. Further explanation can be found in the text. Coordinates in UTM21 WGS84. See Figure 4.1 for the location of the creek within the research area and Appendix I for the coordinates of the sampling locations.*

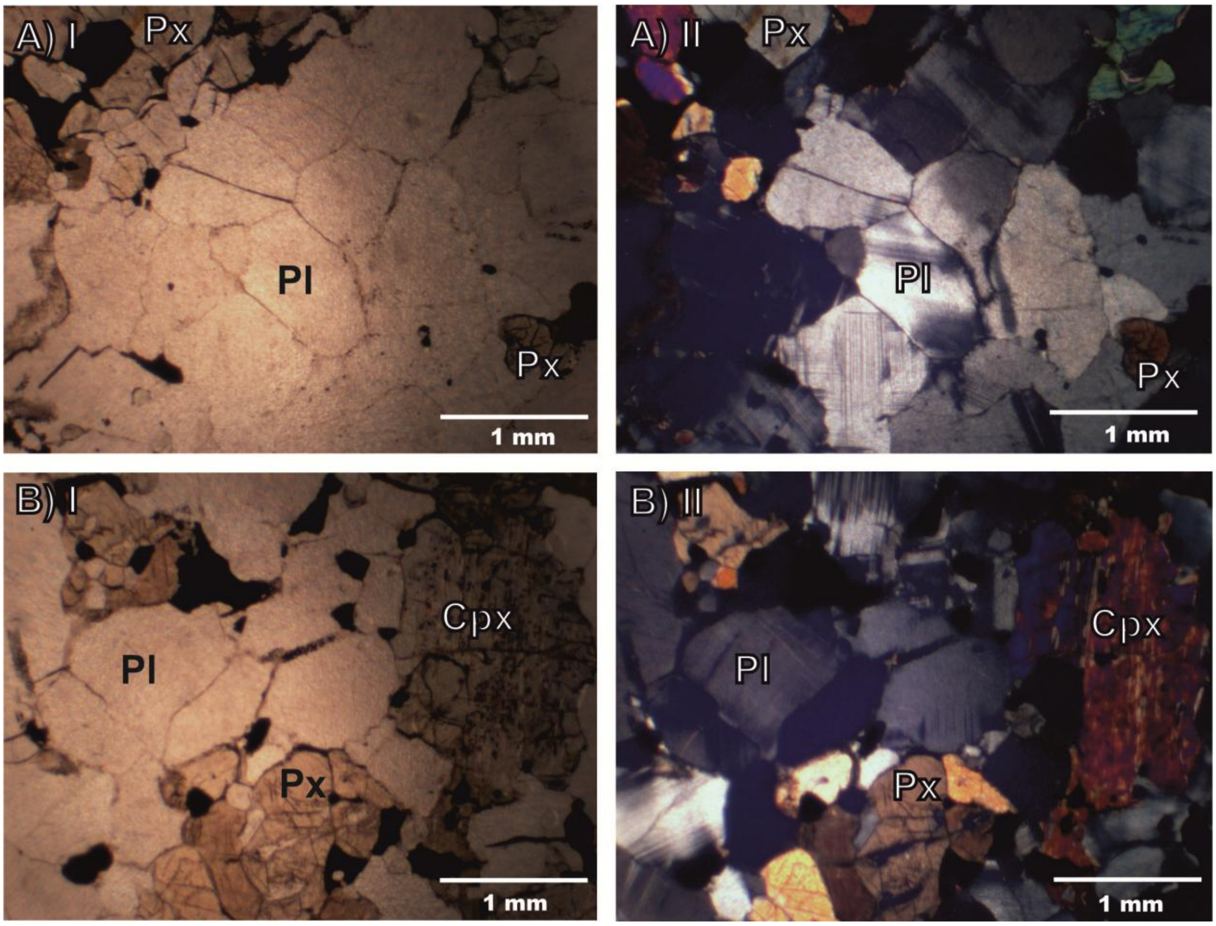

Figure 4.15: *Pictures of the Kilo Drie metagabbronorites. I in PPL, II in XPL. Abbreviations: Px = pyroxene, Pl = plagioclase, Cpx = clinopyroxene.* ***A;*** *Granoblastic texture of plagioclase and pyroxene in sample AT29D.* ***B;*** *Recrystallisation of pyroxene and plagioclase into a granoblastic texture. Sample AT29D .*

5. GEOCHRONOLOGY

5.1 Introduction

One of the main goals of this study is to determine the age of the different mafic generations. Zircon is commonly used for U-Pb dating of felsic rocks, but is absent from in (silica-) undersaturated mafic rocks, in which baddeleyite (ZrO_2) occurs instead of zircon *(Heaman and LeCheminant, 1993)*. Baddeleyite can be dated in a similar way as zircon, but recovery of baddeleyite is difficult because of its platy habit and small grain size *(Heaman and LeCheminant, 1993)*. Therefore, dating of mafic rocks may be quite complicated.

During the initial stages of this investigation, two large samples of gabbronorite (ER1115, Misty Mountain creek) and metagabbronorite (ER1109, Moi-Moi Falls) were taken by E.W.F. de Roever to help explore routes for their age determination. Polished thin sections were investigated by M. Klaver with the EMPA at the VU University to search for baddeleyite and zircon of sufficient size for mineral separation. The gabbro showed a few large baddeleyite grains (e.g. Figure 5.1) and the metagabbronorite a few large zircon grains (Figure 5.4), in both cases of sufficient size for mineral separation and age determination. In a later stage of the investigation, thin sections of the quartz-diorite (LA150) from Kabalebo West were investigated for the presence of zircons. Zircons of sufficient size for mineral separation and U-Pb dating were found in three drill-core samples of different depth, but due to the close distance and similarity, they will be treated as one sample. The methods for mineral separation, preparation and analysis can be found in chapter 3.4. The U-Pb data of the individual zircon grains are given in Appendix IV and Tables 5.1 – 5.2.

U-Pb analyses provide $^{206}Pb/^{238}U$, $^{207}Pb/^{235}U$, and $^{207}Pb/^{206}Pb$ ages. In the following paragraphs, this data will be displayed in $^{207}Pb/^{206}Pb$ probability density plots, conventional $^{206}Pb/^{238}U$ versus $^{207}Pb/^{235}U$ concordia diagrams *(Wetherill, 1959)* and $^{207}Pb/^{206}Pb$ age weighted mean plots. The +/- 2σ errors on the $^{207}Pb/^{206}Pb$ ratios are taken into account for the generation of probability density plots and the decay constant errors are displayed as ellipsoids in the concordia diagrams. The mean square of weighted deviates (MSWD), a statistical quantity to assess the amount of scatter in a regression analysis, is given in the concordia diagrams. The MSWD is near unity if the errors in the analysis are the only cause of scatter. MSWD values much less than unity indicate an overestimation of the analytical errors or unrecognizable error-correlations. MSWD values > 1 indicate either underestimated analytical errors, or the presence of other non-analytical causes that create scatter. A MSWD > 2,5 is considered to indicate an errorchron.

The individual LA-ICP-MS analyses are scattered around the concordia and both normal and reversed discordant analyses are present. Normal discordance can be explained by lead-loss or uranium-gain. Reverse discordance might be explained by lead-gain or uranium-loss, which are both geologically difficult to explain. Therefore it is more probable that the discordance is caused by elemental fractionation during laser ablation (*Mezger & Krogstad, 1997*).

The $^{207}Pb/^{206}Pb$ age is considered to be more reliable in LA-ICP-MS analyses. It eliminates the larger fractionation effects between uranium and lead. When using the $^{207}Pb/^{206}Pb$ age, it should be taken into account that this age is assumed to be concordant and that the age of discordant data points could be underestimated.

5.2 Charlie Gabbronorite dating from the Misty Mountain creek

A separation technique for baddeleyite was not available at the VU University at the initial stage of this research. R. van Elsas carried out several tests at the VU mineral separation lab and successfully produced a heavy mineral concentrate with brown grains of baddeleyite, but these grains were completely lost during subsequent dry mineral separation with the Frantz magnet.

Baddeleyite is very difficult to separate since the fine, platy grains tend to stick to metal surfaces during dry separation steps and so get lost. *Söderlund and Johansson (2002)* describe a preferred 'water-based' separation method using a special Wilfley table. Contact was made by Martijn Klaver with prof. Söderlund in Lund (Sweden), who is a member of the LIPs commission (Working Group for Reconstruction of Supercontinents back to 2.7 Ga using the Large Igneous Province – LIP – Record). The commission was quite interested in the Guiana Shield and offered assistance for baddeleyite separation and TIMS analysis. Their offer for TIMS analysis would help avoid problems with LA-ICP-MS analysis, for which a baddeleyite reference standard is preferred since standardization against zircon is far from optimal.

Additional scanning electron microscopy (SEM) by the LIPs commission showed that baddeleyite was present mainly as tiny grains of ~10 µm. The grains were located in highly evolved melt pockets which had crystallised into multiphase assemblages (Figure 5.1). Prof. Soderlund successfully separated two small fractions of baddeleyite grains from sample ER1115, using his water-based Söderlund technique *(Söderlund and Johansson, 2002)*. The samples were analysed with a thermo Finnigan Triton thermal ionization mass spectrometer (TIMS) at the Museum of Natural History in Stockholm. U-Pb dating of these fractions gave an age of 1970 +/- 17 Ma (Figure 5.2 and Table 5.1). Unfortunately the precision was, at approximately 1%, rather poor, due to problems with analysis of the first fraction. The low precision was partly caused by the small amount of material which could be separated from the sample. More information about the preparation and analysis of these baddeleyite grains can be found in *Klaver et al. (2015b)*.

5.3 Metagabbronorite from the Moi-Moi Falls

Three zircons in polished thin section ER1109 were dated by ion microprobe by a member of the LIPs commission (see 5.3.2). Afterwards, about 70 zircons were separated for trace element analysis (see 5.3.3).

5.3.1 Zircon morphology

The separated zircons from the Moi-Moi Metagabbro are mainly colourless and transparent, but a more yellowish colour is present in several grains. Most grains are heavily fractured. These cracks might have been created during mineral separation, or might have been present originally. Bigger grains are often more cracked than smaller ones.

The zircon grains have an an- to subhedral shape and vary from 50 to 700 µm in size. Their elongation, which is the length : width ratio, varies from 1:1 to 4:1, with the majority having an elongation of 2:1. No relation is seen between the size and elongation. Most grains have a columnar habit, only a few are equant (elongation 1:1) or long (elongation 4:1; Figure 5.3A, left in picture). Pointy pyramid tips, a typical morphological characteristic of zircons, are rarely present. Instead, most zircon grains have rounded tips. Some subhedral shaped grains show a rather pointy tip (Figure 5.3 C).

Several zircons longer than 400 µm have irregular shaped, (possibly) inherited cores (Figure 5.3 A, D and E). The cores vary in shape from round (Figure 5.3 D) to an irregular elongated band (Figure 5.4). They are located anywhere within the zircons and can be recognized by their dark grey appearance on BSE-images and bright appearance on Cl-images. The cores may be completely homogeneous or contain growth bands as internal texture (Figure 5.3 D and E). The irregular shaped core edges may show resorption features (Figure 5.3 E and 5.4).

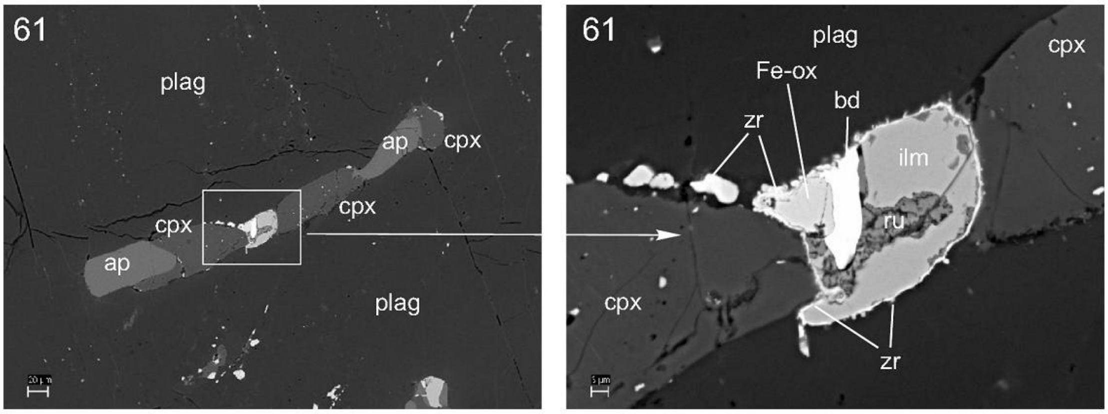

Figure 5.1: *BSE images of a highly evolved melt pocket in ER1115. Baddeleyite (bd) is bright white in the images. Additional abbreviations: cpx = clinopyroxene; ilm = ilmenite; Fe-ox = Fe oxides; zr = rare zircon rim seen in one spot; ru = rutile. BSE images are provided by the LIPs commission.*

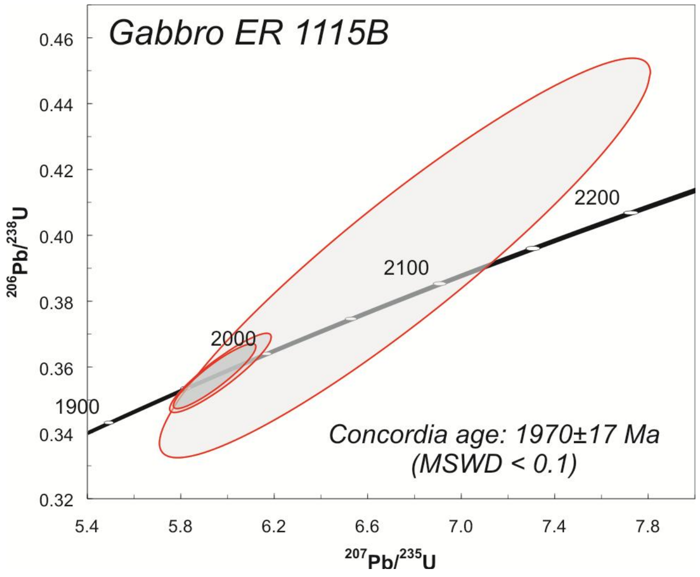

Figure 5.2: *Concordia diagram of two baddeleyite fractions of gabbro sample ER1115. Figure is provided by the LIPs commission.*

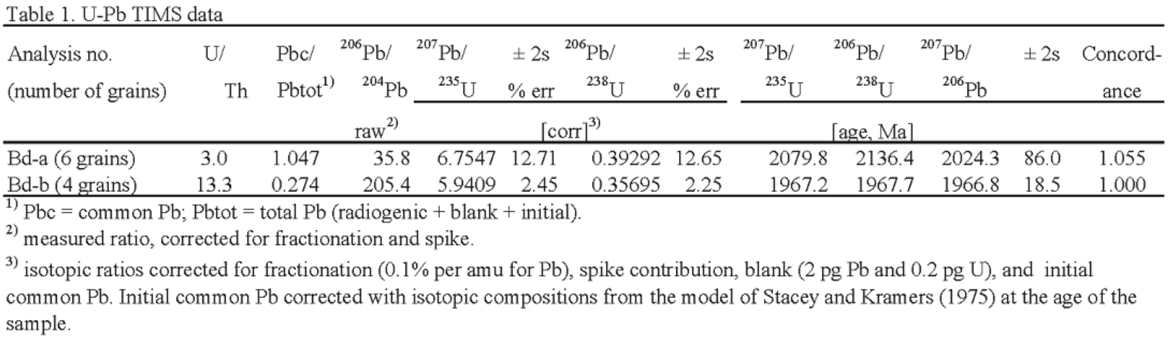

Table 1. U-Pb TIMS data

Analysis no. (number of grains)	U/ Th	Pbc/ Pbtot$^{1)}$	^{206}Pb/ ^{204}Pb	^{207}Pb/ ^{235}U	± 2s % err	^{206}Pb/ ^{238}U	± 2s % err	^{207}Pb/ ^{235}U	^{206}Pb/ ^{238}U	^{207}Pb/ ^{206}Pb	± 2s	Concord- ance
			raw$^{2)}$		[corr]$^{3)}$				[age, Ma]			
Bd-a (6 grains)	3.0	1.047	35.8	6.7547	12.71	0.39292	12.65	2079.8	2136.4	2024.3	86.0	1.055
Bd-b (4 grains)	13.3	0.274	205.4	5.9409	2.45	0.35695	2.25	1967.2	1967.7	1966.8	18.5	1.000

$^{1)}$ Pbc = common Pb; Pbtot = total Pb (radiogenic + blank + initial).

$^{2)}$ measured ratio, corrected for fractionation and spike.

$^{3)}$ isotopic ratios corrected for fractionation (0.1% per amu for Pb), spike contribution, blank (2 pg Pb and 0.2 pg U), and initial common Pb. Initial common Pb corrected with isotopic compositions from the model of Stacey and Kramers (1975) at the age of the sample.

Table 5.1: *U-Pb isotopic results of two baddeleyite fractions of gabbro ER1115.Table is provided by the LIPs commission.*

The inherited cores are surrounded by the main growth phase of the zircons. This phase is the centre of the grains if inherited cores are not present. It is grey in the BSE images and dark blue in the Cl-images (Figure 5.3). Some darker or brighter areas can occur as a result of internal textures. The main growth phase is made up of different zones, with resorption features in between. The grains, dated in-situ in polished thin section ER1109 by the LIPs commission, show three main growth zones (2 – 4 in Figure 5.4) of different composition. Zones 2 and 3 are truncated by a resorption event that predates zone 4, the main overgrowth of the resorbed older zones. Zone 4 shows concentric zoning.

A clear distinction between the three different growth zones is difficult for zircons in the epoxy mounts, but similar resorption and growth features are present within almost all grains. The main resorption event, clearly visible in the zircons in the thin section, is recognisable in only part of the zircons in the mount, mostly because many zircons show more complex internal textures or are internally homogeneous. The main resorption event might have influenced the zircon morphology, but there is no clear relation between size, internal texture, presence of inherited cores and zircon morphology.

Some zircon grains show sector zoning (Figure 5.3 A) or oscillary zoning (Figure 5.3 C and D), which is, in cases, only partly present as growth bands (Figure 5.3 A and B). Sector zoning and oscillatory zoning are typical for magmatic zircons (*Hoskin & Schaltegger, 2003*).

Finally, all zircons > 200 µm, and many < 200 µm, show a Cl-bright and BSE-dark metamorphic rim (#5 in Figure 5.4; Figure 5.3). This rim truncates the main growth zones and varies in thickness from (very) thin to a thick, cracked rim.

Small inclusions of an unidentified mineral are common in the zircon grains. They are not visible in the transmitted light or BSE images, but can be recognized by their red colour in the Cl-images (Figure 5.3 D and E). The inclusions are mostly located near the edges of the grains or within cracks. Therefore, they are expected to have formed after the formation of the zircons.

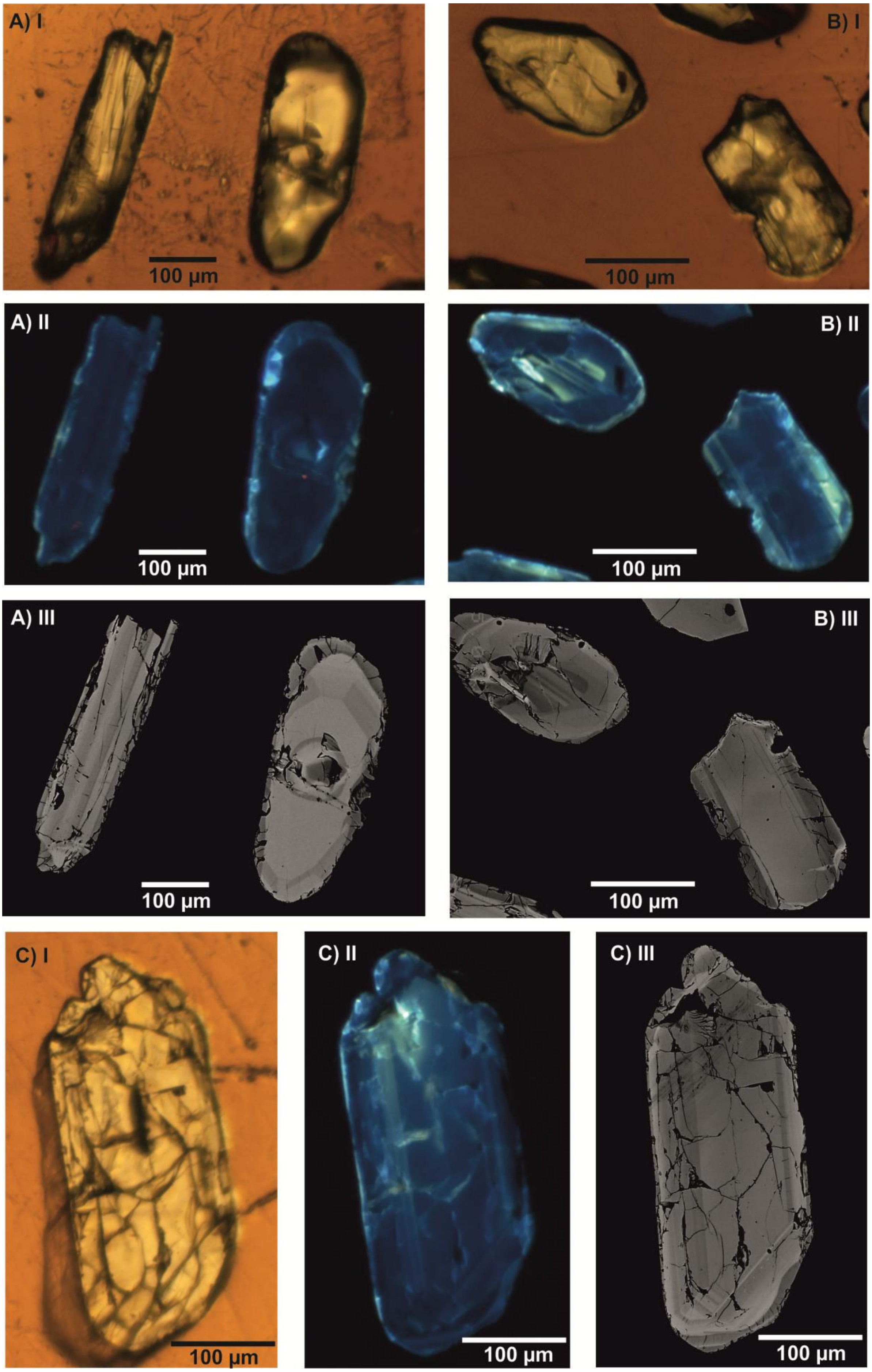
A) I
100 µm
B) I
100 µm
A) II
100 µm
B) II
100 µm
A) III
100 µm
B) III
100 µm
C) I
100 µm
C) II
100 µm
C) III
100 µm

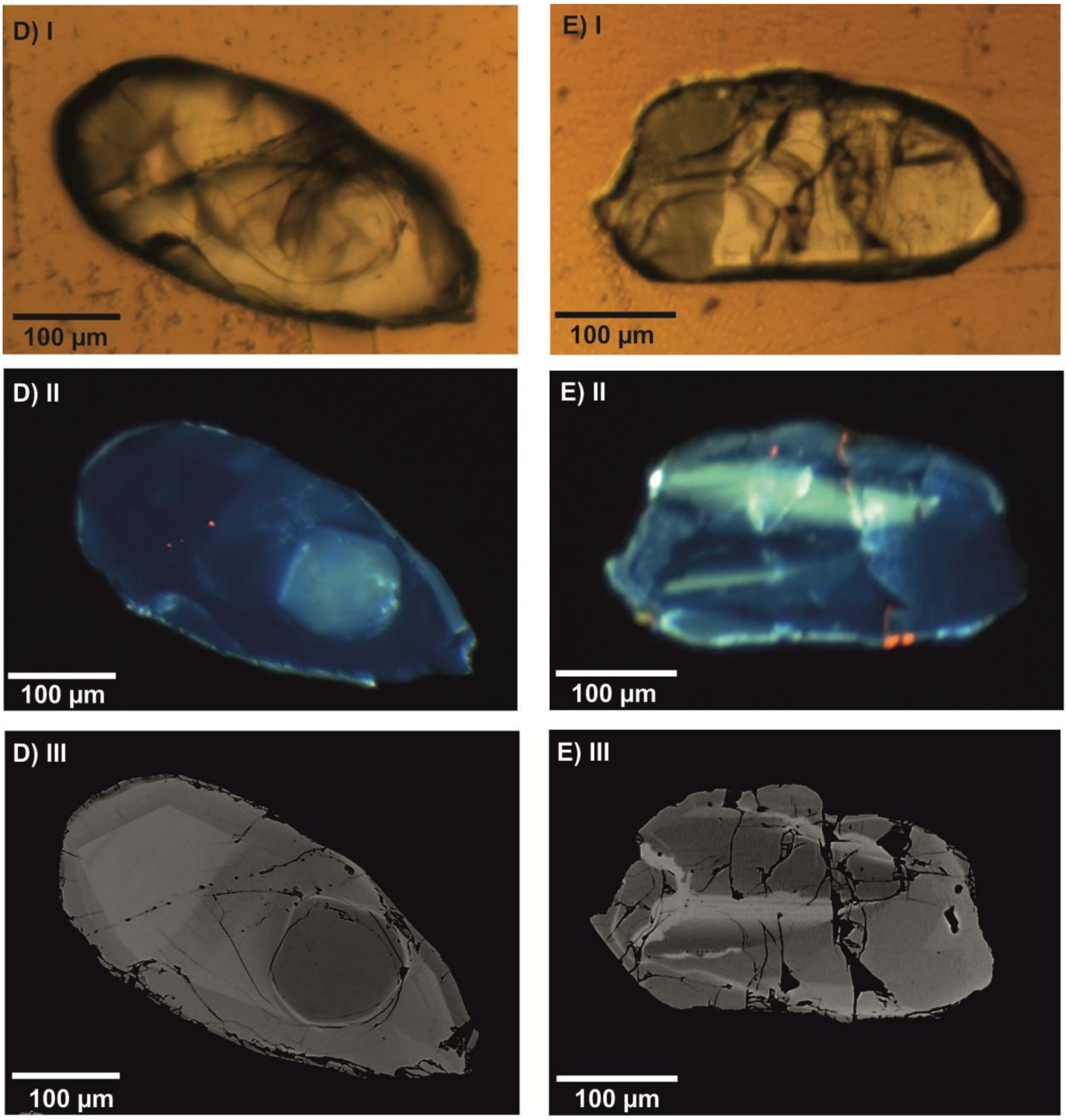

Figure 5.3: *Transmitted light (I), CL-imaging (II) and BSE-imaging (III) pictures of several typical zircons from sample ER1109. Previous page:* ***A;*** *Left: Anhedral, elongated zircon with growth bands that are visible in the CL- and BSE-images. BSE-dark and CL-bright rim is present. Right: Anhedral zircon with a (probably) inherited core, located in the middle of the grain The dark blue colour in the CL-image in this grain is a good example of the major crystallisation phase. This is also one of the rare grains that show sector zoning, which is visible on the BSE-image. Dark grey (BSE), CL-bright rim is present.* ***B;*** *Left: Anhedral zoned zircon with in the centre compositional banding, surrounded by a major growth phase (dark blue CL) with oscillatory zoning. BSE-dark and CL-bright rim present. Right: Anhedral, rounded shape. The long sides of the crystal show compositional banding, possibly from oscillatory zoning.* ***C;*** *Nearly euhedral shaped zircon, extremely cracked. This is one of the rare zircons with a pyramid tip. Oscillatory zoning is visible in the edges of the grain, especially on the left side (CL + BSE). The zoning is parallel to the euhedral outline. At the bottom resorption features are visible (CL + BSE, curved boundary between light and dark grey areas in BSE). A new BSE-dark and CL-bright rim is crystallised against these resorption features. This page:* ***D;*** *Zircon with an anhedral, rounded shape. It contains a round BSE-dark, CL-bright inherited core with a homogeneous composition. The major crystallisation phase is dark blue in the CL-image and compositional zoning can be seen in the BSE-image. A thin metamorphic rim (dark grey BSE, light blue CL) is present. The red spots in the CL-image are inclusions in the zircon.* ***E;*** *Anhedral grain with an irregularly shaped inherited core (dark grey area with white/grey bands in BSE, bright in CL). Core surrounded by a major growth zone. Red spots are inclusions in the zircon.*

5.3.2 U-Pb dating

During the initial stage of this research, two polished thin sections of sample ER1109 were investigated with the EMPA at the VU University by M. Klaver. The thin sections showed a few large zircons, of sufficient size for mineral separation. The zircons showed extensive zoning in BSD and Cl-images made by the LIP's commission. According to the commission, the zoning would be too complex for analysis with LA-ICPMS in view of the relatively large number of spots needed per zone to reach a good precision and the difficulty of recognising the zones.

The LIPs commission advised against the use of the LA-ICP-MS for this sample and offered to analyse the complex zircons by ion microprobe. Half a year later K. Chamberlain analysed a number of spots with the CAMECA *ims*1270 ion microprobe at the University of California Los Angeles, following methods described in *Schmitt et al. (2010)*. A ~18x27 µm diameter analytical area was used for most pits. However, if the Cl-domains were narrower than this diameter an aperture in the transfer section of the probe was closed enough to limit the spot to the narrow Cl-domains. More information about the preparation and analysis of these zircons can be found in *Klaver et al. (2015b)*.

Due to time limitations, only 11 spots were analysed in three zircon grains. Two spots in irregular, highly resorbed, Cl-bright cores yielded a weighted mean ^{207}Pb/^{206}Pb age of 2091 +/- 32 Ma (Table 5.2 and Figure 5.4 and 5.5). This age confirms the idea that the cores are inherited zircon grains (see 5.3.1). Seven spots on the dominant growth zones (2 – 4 in Figure 5.4) yield a weighted mean ^{207}Pb/^{206}Pb age of 1984 +/- 4 Ma (Table 5.2 and Figure 5.5). These zones predate (2 – 3) or postdate (4) a resorption event that gave the zircons their irregular shape, but due to the limited number of spots it was not possible to resolve the age of the different zones. One spot from the thin, outermost rim (zone 5, Spot #5 in Figure 5.4b) and one internal spot (Spot #1, also in Figure 5.4b) yielded a weighted mean ^{207}Pb/^{206}Pb age of 1950 +/- 13 Ma (Table 5.2 and Figure 5.5). Zone 5 is interpreted to reflect metamorphic zircon growth. Spot #1 in zircon grain 585 (Figure 5.4b) either sampled a thin rim of zone 5, or a local zone of metamorphic alteration facilitated by abundant nearby cracks.

5.3.3 Trace element analysis

Most trace elements in zircon are present in a concentration of a few ppm, but hafnium can be present up to 2 Wt-% (*Hoskin and Schaltegger, 2003; Lowery Claiborne et al., 2006*) due to its similar behaviour as zirconium. Nevertheless, zirconium is preferred in the crystal lattice, resulting in a low Zr/Hf ratio in the coexisting melt (*Lowery Claiborne et al., 2006*). A low Zr/Hf ratio, and thus a high hafnium concentration, in zircon indicates that it crystallised from a fractionated melt (*Lowery Claiborne et al., 2006*). With other words, the hafnium content of a zircon increases with magmatic differentiation (*Hosking and Schaltegger, 2003*). Therefore the variation diagrams of the trace elements in the zircons are plotted against hafnium.

36 spots on 21 zircons from sample ER1109 were analysed for trace elements. Spot selection was based on the transmitted light, BSE and Cl-images. The most reliable spots were chosen in the inherited cores and the younger growth zones, which resulted in analysis of 3 inherited cores and 33 younger growth zones. The results of these analyses can be found in Appendix IV.

The hafnium concentration varies from ≈6.600 to 10.000 ppm and most trace elements show a positive correlation with Hf (only U and Nb shown in Figure 5.6). The trace element levels divide the zircon population into two groups. The first group contains the majority of the zircons. It also includes the inherited cores due to identical trace element concentrations (Figure 5.6). The second group is enriched in U, Th and Nb and the total rare earth element level (ΣREE) and has a low hafnium content compared to the first group (Figure 5.6). This second group corresponds with the zircons that are both BSE and Cl-bright.

The Cl-chondrite normalised REE-patterns (Figure 5.7) show a steep increase from the light rare earth elements (LREE) to the heavy rare earth elements (HREE) and a large positive Ce-anomaly ($Ce/Ce^* = Ce_N/(0{,}5 * (La_N + Pr_N)) = 3 - 95$), which is typical of igneous zircons (*Hoskin and Schaltegger, 2003; Hinton and Upton, 1991*). Additionally, the zircons from sample ER1109 show a small negative Eu-anomaly ($Eu/Eu^* = Eu_N/(0{,}5 * (Sm_N + Gd_N)) = 0{,}3 – 0{,}9$; Figures 5.6 and 5.7). The only exception is zircon 4-1 #13, with slightly positive Eu-anomalies for the younger growth zones (Eu/Eu* = 1,1 – 1,4). The negative Eu-anomaly could be caused by the larger ionic radius and lower charge of europium (Eu^{2+} = 1,25 Å; *Shannon, 1976*), which makes Eu incorporation in the zircon lattice rather difficult . Another possibility is that the negative anomaly is inherited from the melt in which the zircon is crystallised.

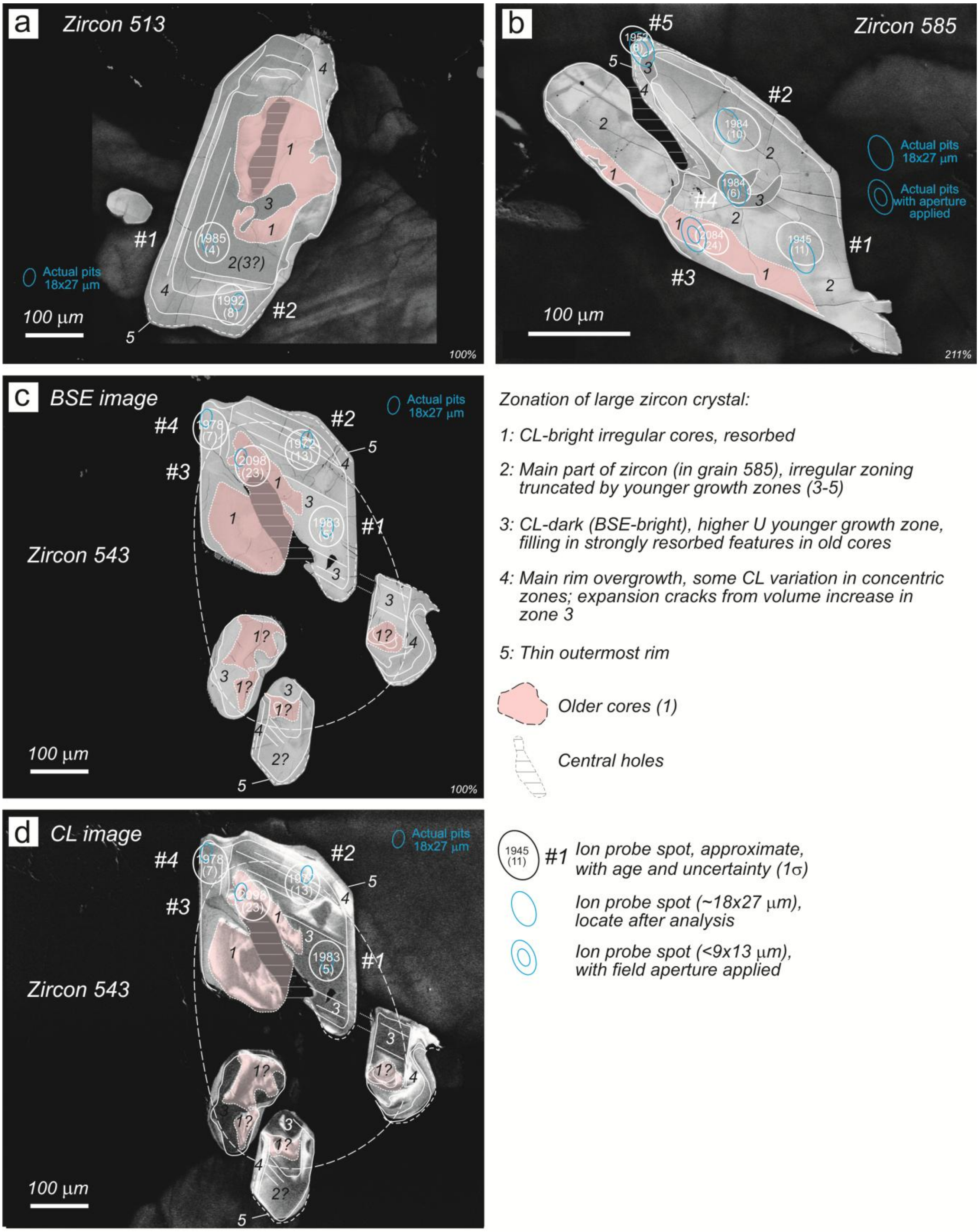

Zonation of large zircon crystal:

1: CL-bright irregular cores, resorbed

2: Main part of zircon (in grain 585), irregular zoning truncated by younger growth zones (3-5)

3: CL-dark (BSE-bright), higher U younger growth zone, filling in strongly resorbed features in old cores

4: Main rim overgrowth, some CL variation in concentric zones; expansion cracks from volume increase in zone 3

5: Thin outermost rim

Older cores (1)

Central holes

1945 (11) #1 Ion probe spot, approximate, with age and uncertainty (1σ)

Ion probe spot (~18x27 µm), locate after analysis

Ion probe spot (<9x13 µm), with field aperture applied

Figure 5.4: *BSE and CL-images of in-situ zircons from sample ER1109. Legend in figure. Figure provided by the LIPs-commission.*

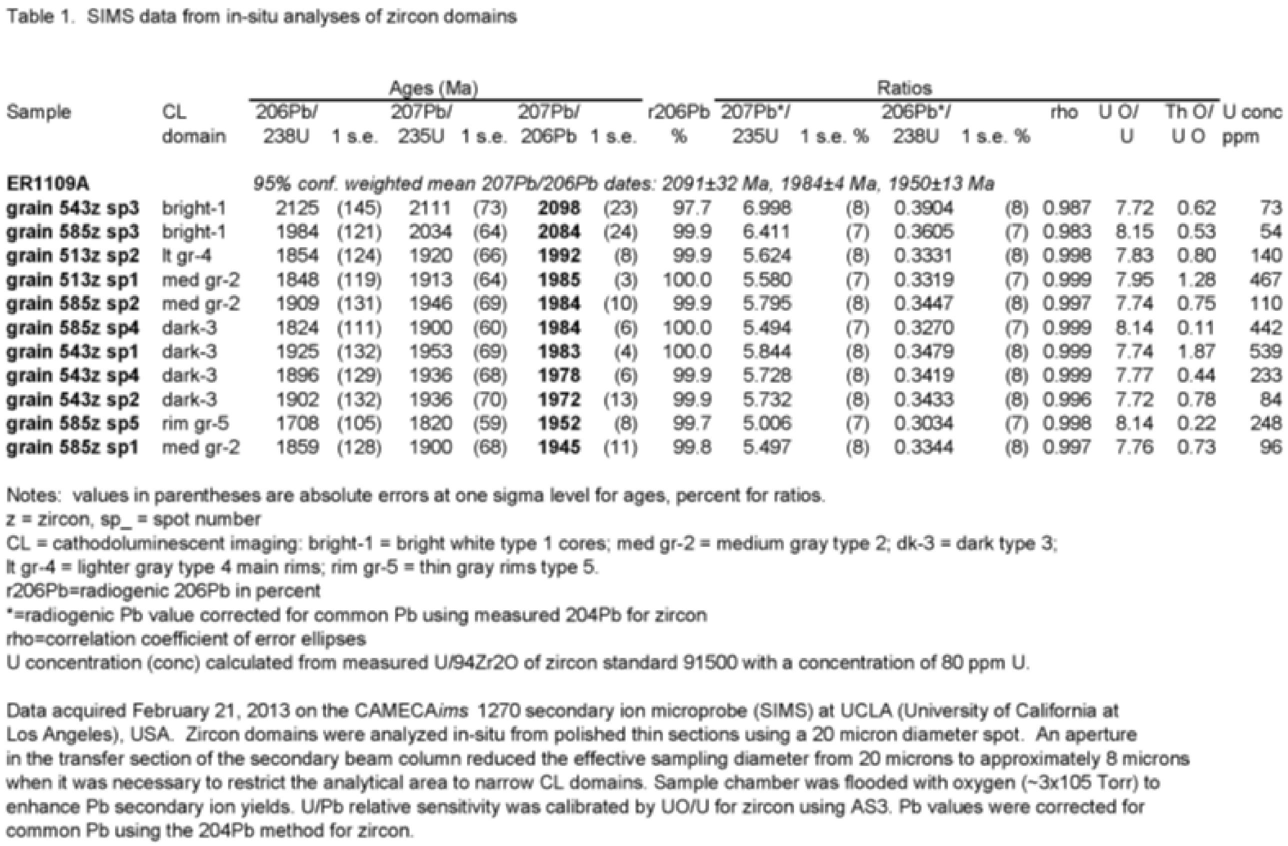

Table 1. SIMS data from in-situ analyses of zircon domains

Sample	CL domain	Ages (Ma) 206Pb/238U	1 s.e.	207Pb/235U	1 s.e.	207Pb/206Pb	1 s.e.	r206Pb %	Ratios 207Pb*/235U	1 s.e. %	206Pb*/238U	1 s.e. %	rho	U O/U	Th O/U O	U conc ppm
ER1109A		*95% conf. weighted mean 207Pb/206Pb dates: 2091±32 Ma, 1984±4 Ma, 1950±13 Ma*														
grain 543z sp3	bright-1	2125	(145)	2111	(73)	**2098**	(23)	97.7	6.998	(8)	0.3904	(8)	0.987	7.72	0.62	73
grain 585z sp3	bright-1	1984	(121)	2034	(64)	**2084**	(24)	99.9	6.411	(7)	0.3605	(7)	0.983	8.15	0.53	54
grain 513z sp2	lt gr-4	1854	(124)	1920	(66)	**1992**	(8)	99.9	5.624	(8)	0.3331	(8)	0.998	7.83	0.80	140
grain 513z sp1	med gr-2	1848	(119)	1913	(64)	**1985**	(3)	100.0	5.580	(7)	0.3319	(7)	0.999	7.95	1.28	467
grain 585z sp2	med gr-2	1909	(131)	1946	(69)	**1984**	(10)	99.9	5.795	(8)	0.3447	(8)	0.997	7.74	0.75	110
grain 585z sp4	dark-3	1824	(111)	1900	(60)	**1984**	(6)	100.0	5.494	(7)	0.3270	(7)	0.999	8.14	0.11	442
grain 543z sp1	dark-3	1925	(132)	1953	(69)	**1983**	(4)	100.0	5.844	(8)	0.3479	(8)	0.999	7.74	1.87	539
grain 543z sp4	dark-3	1896	(129)	1936	(68)	**1978**	(6)	99.9	5.728	(8)	0.3419	(8)	0.999	7.77	0.44	233
grain 543z sp2	dark-3	1902	(132)	1936	(70)	**1972**	(13)	99.9	5.732	(8)	0.3433	(8)	0.996	7.72	0.78	84
grain 585z sp5	rim gr-5	1708	(105)	1820	(59)	**1952**	(8)	99.7	5.006	(7)	0.3034	(7)	0.998	8.14	0.22	248
grain 585z sp1	med gr-2	1859	(128)	1900	(68)	**1945**	(11)	99.8	5.497	(8)	0.3344	(8)	0.997	7.76	0.73	96

Notes: values in parentheses are absolute errors at one sigma level for ages, percent for ratios.
z = zircon, sp_ = spot number
CL = cathodoluminescent imaging: bright-1 = bright white type 1 cores; med gr-2 = medium gray type 2; dk-3 = dark type 3;
lt gr-4 = lighter gray type 4 main rims; rim gr-5 = thin gray rims type 5.
r206Pb=radiogenic 206Pb in percent
*=radiogenic Pb value corrected for common Pb using measured 204Pb for zircon
rho=correlation coefficient of error ellipses
U concentration (conc) calculated from measured U/94Zr2O of zircon standard 91500 with a concentration of 80 ppm U.

Data acquired February 21, 2013 on the CAMECA*ims* 1270 secondary ion microprobe (SIMS) at UCLA (University of California at Los Angeles), USA. Zircon domains were analyzed in-situ from polished thin sections using a 20 micron diameter spot. An aperture in the transfer section of the secondary beam column reduced the effective sampling diameter from 20 microns to approximately 8 microns when it was necessary to restrict the analytical area to narrow CL domains. Sample chamber was flooded with oxygen (~3x105 Torr) to enhance Pb secondary ion yields. U/Pb relative sensitivity was calibrated by UO/U for zircon using AS3. Pb values were corrected for common Pb using the 204Pb method for zircon.

Table 5.2: *U-Pb isotopic results of the zircons from ER1109.Table is provided by the LIPs commission.*

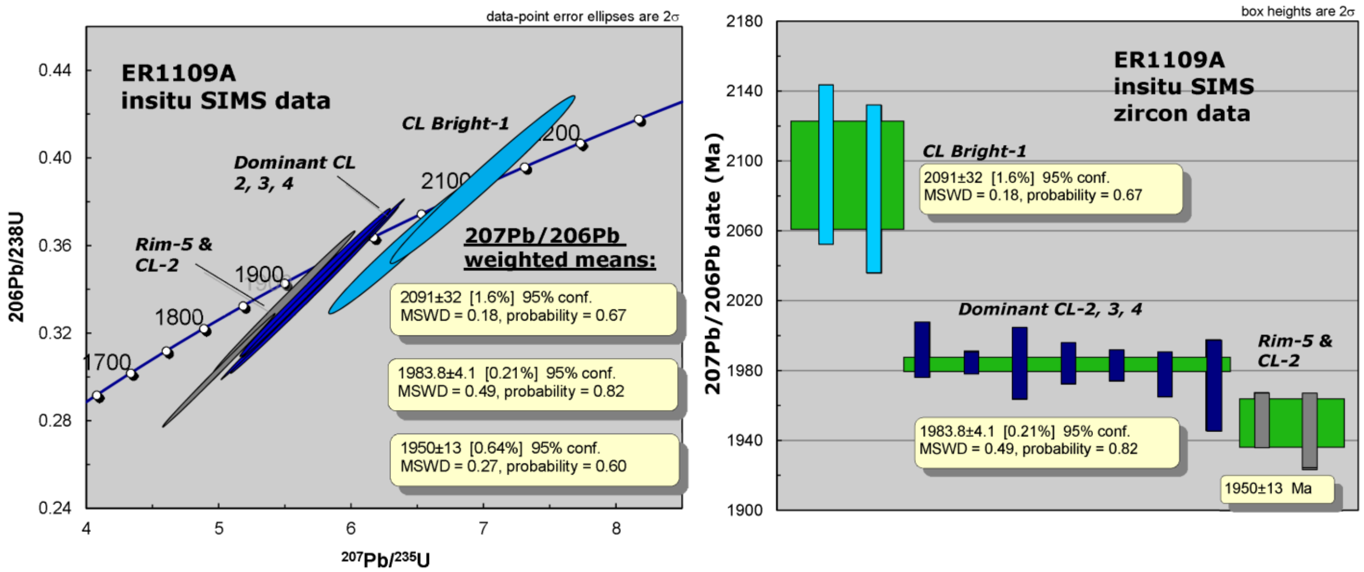

Figure 5.5: *Left: concordia diagram of the analysed zircons from ER1109. Right:* ^{207}*Pb/*^{206}*Pb weighted mean diagram of the zircon ages of sample ER1109. Figures are provided by the LIPs commission.*

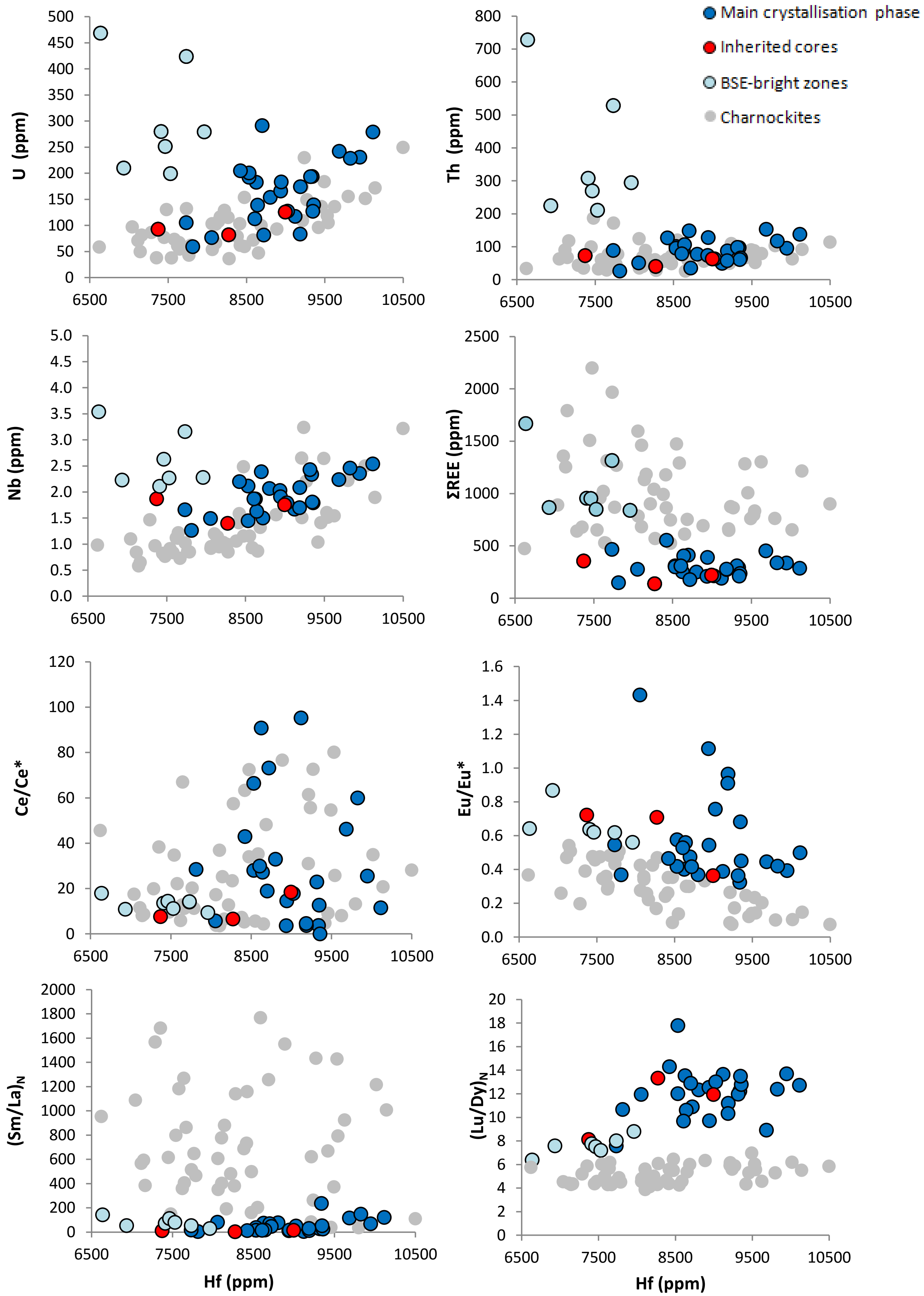

***Figure 5.6:** Trace element variation diagrams of the zircons from sample ER1109.*

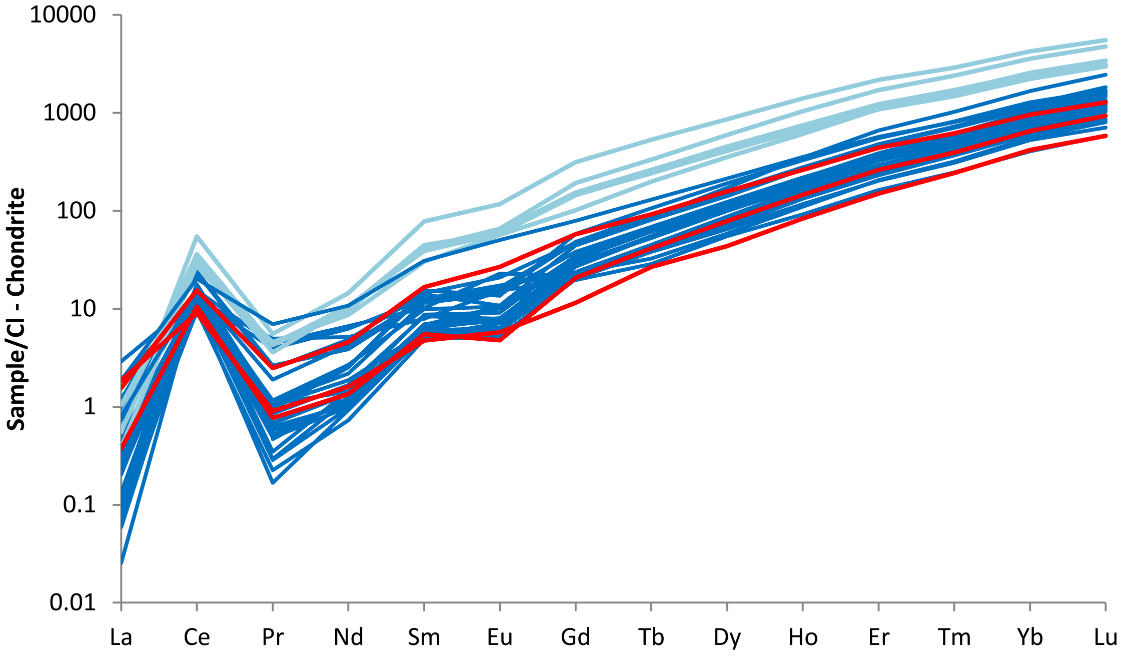

Figure 5.7: *CI-normalised REE-patterns of the zircons from gabbronorite ER1109. Red: inherited cores; dark blue: younger crystallisation phases; light blue: BSE and CL-bright zones. Normalisation factors after Sun and McDonnough (1995).*

5.4 Quartz-diorite from Kabalebo West

5.4.1 Zircon morphology

In total, 75 zircons were separated from drill core LA150 at three different depths (16, 28 and 55m). They have a colourless and transparent appearance, or are slightly pink and more clouded. Many zircons are fractured, which is possibly the result of mineral separation. The cracks are visible on the transmitted light and BSE images (Figure 5.8).

The zircon grains are sub- to euhedral shaped (Figure 5.8) and their length ranges from 50 to 250 µm. Their elongation varies from 1:1 to 5:1, but the majority has an elongation of 2:1 to 3:1. Only four grains with an equant habit (elongation 1:1) and eight long grains (elongation 3,5:1 to 5:1; Figure 5.8B) were present. Most grains with a columnar habit (elongation 2:1 – 3:1; Figure 5.8A, B-C) have well-developed pyramid tips (Figure 5.8A and C), but grains with a more rounded tip (Figure 5.8B, D-E) are also present.

BSE-images show differences in internal texture. Several zircon grains are completely homogeneous (Figure 5.8E) and have a grey appearance in the BSE-images.

Other zircons show oscillatory zoning (Figure 5.8A-D) where the zones vary from light to darker grey on the BSE-images. The morphology of these grains is often parallel to this zonation, but the zonation pattern can also be cut by the edge of the grains. All zircons show a thin, BSE bright rim (Figure 5.8A-E). A wider rim is locally present.

Inclusions are rare. If present, they can be spotted in the transmitted light images as elongated, colourless particles (Figure 5.8D). Smaller inclusions can be easily recognised as a light grey spot on the BSE images (Figure 5.8C).

The majority of the zircons shows oscillatory zoning, which is a predominant texture for magmatic zircons (*Hoskin & Schaltegger, 2003*). The zircons do not contain any inherited cores. Therefore it can be expected that the zircons crystallised from the quartz-diorite magma.

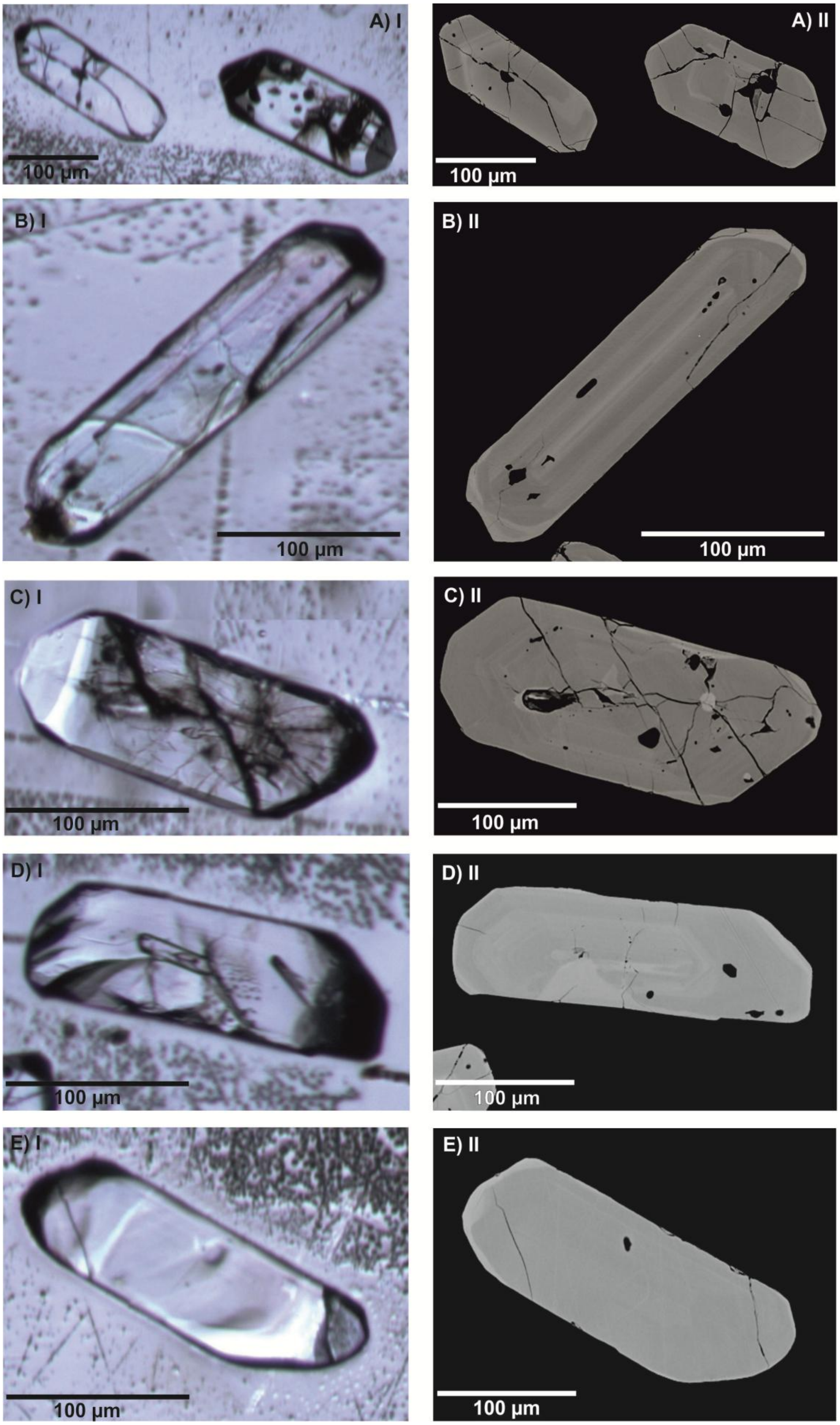
A) I
100 µm
A) II
100 µm
B) I
100 µm
B) II
100 µm
C) I
100 µm
C) II
100 µm
D) I
100 µm
D) II
100 µm
E) I
100 µm
E) II
100 µm

Figure 5.8: *Previous page. Transmitted light (I) and BSE-imaging (II) pictures of typical zircons from LA150.* ***A:*** *The zircons have a sub- to euhedral shape with well-evolved pyramid tips. Both zircons show oscillatory zoning with a thin, BSE-bright rim.* ***B:*** *The crystal is subhedral shaped and has a rare acicular habit with an elongation of 4,5:1. The interior shows oscillatory zoning and the BSE-bright rim is clearly visible. The rim varies in thickness, especially near the rounded tips.* ***C:*** *The zircon is euhedral shaped and has well-evolved pyramid tips. The crystal shows oscillatory zoning and a thin, BSE-bright rim. The BSE-bright spot in the interior is an inclusion which is not visible in the transmitted light image.* ***D:*** *The crystal has a subhedral shape. It shows oscillatory zoning and a thin, BSE-bright rim. An inclusion visible in the transmitted light image, but not in the BSE image, is present in the interior of the zircon.* ***E:*** *The crystal has a subhedral shape with rounded tips. This grain lacks oscillatory zoning, and has a homogeneous interior instead. A thin, BSE-bright rim is present.*

5.4.2 U-Pb dating

During LA-ICP-MS analysis at the Münster University, the zircon standards Plešovice and Z91500 were measured over the session to check for precision and accuracy. Both zircon standards showed rather good results (see Table 3.4). However during analysis of zircons from the quartz-diorite, the intensities often dropped rather quickly while, in view of the size of the zircons, they should be thick enough for normal signals. An explanation for this intensity drop could be that the zircons were polished down too much during sample preparation. Nevertheless, most runs were long enough to construct reliable ages. Additionally, the analyses based on short signals appear to be of good quality. Therefore, these results will be included in the age calculation.

The individual data points are scattered around the concordia. This scatter is also visible in the wide range of ^{207}Pb/^{206}Pb ages, from 2023 +/- 27 Ma to 1942 +/- 33 Ma. Its average weighted mean is 1983 +/- 6 (MSWD = 1,9; 95% confidence). The probability density plot (Figure 5.9) shows a normal distribution which is slightly asymmetrical. This shape is caused by the slightly older ages and the relatively higher amount of analyses from sample LA150-16 (Appendix IV). Despite this small deviation between the samples, no evidence of multiple zircon populations is found in the data.

The samples of LA150 show a concordia age of 1984 +/- 5 Ma (MSWD = 1,13; 95% confidence; Figure 5.9), which is in agreement with the ^{207}Pb/^{206}Pb average weighted mean. The MSWD is near unity, indicating that the age calculation is reliable.

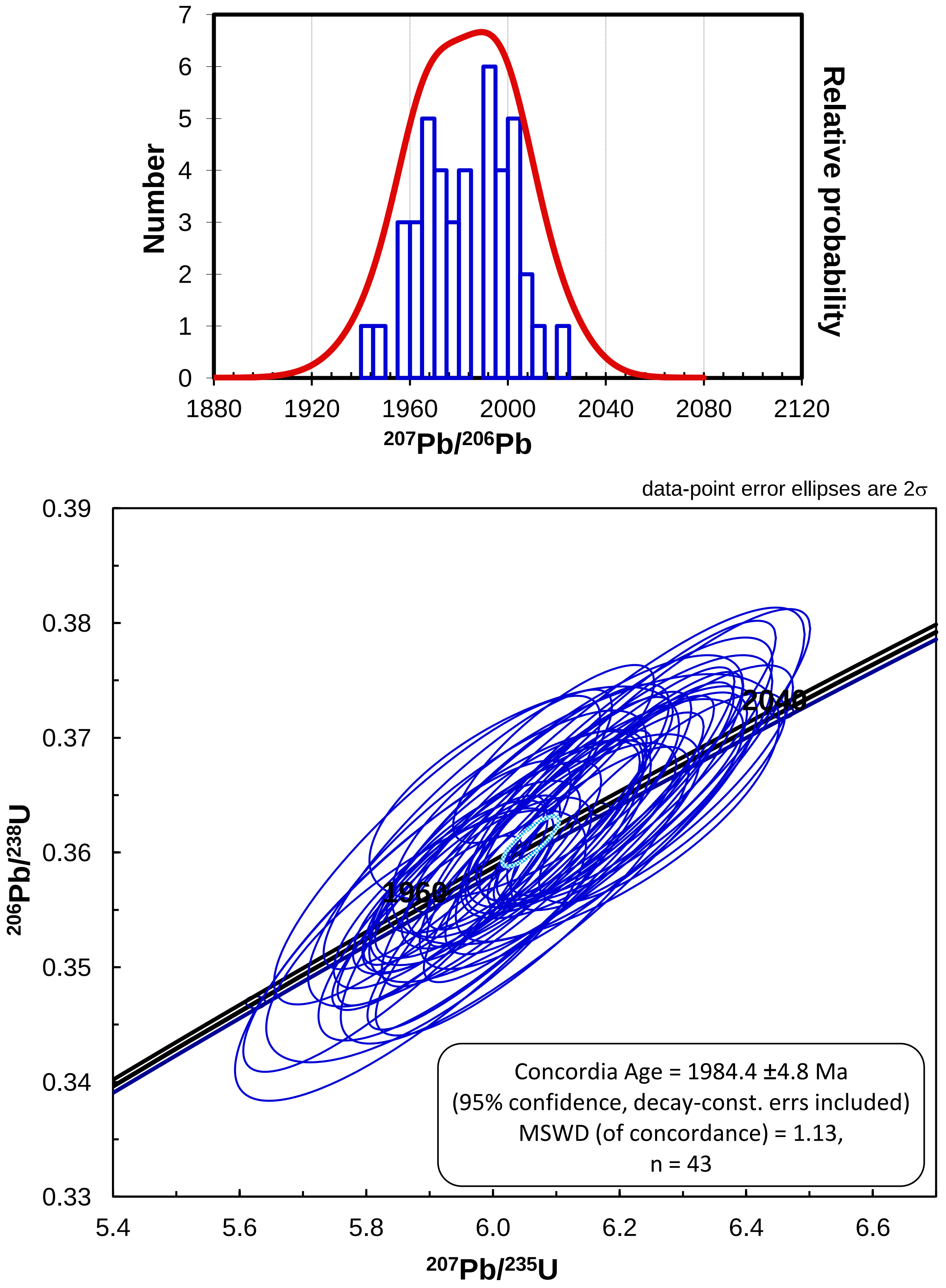

Figure 5.9: *U-Pb geochronological results for quartz-diorite LA150.* ***Upper graph:*** *Probability density plot of ^{207}Pb/^{206}Pb ages. The histogram shows the frequency and distribution of the ^{207}Pb/^{206}Pb ages.* ***Lower graph:*** *Conventional concordia diagram. See 5.6.2 for more explanation.*

6. GEOCHEMISTRY

6.1 Introduction

Sample selection for major and trace element analysis was based on the petrographic study of the mafic-ultramafic rocks (Chapter 4). The amount of cumulus minerals was used to choose samples representing the geochemical variation within the whole series. In total 42 samples were selected for major and trace element analyses by XRF, of which 15 Charlie Gabbro samples, 23 Moi-Moi Metagabbro samples and 4 Kilo Drie Metagabbro samples. The 18 most representative samples were chosen for ICP-MS trace element analysis. These included 7 Charlie Gabbro samples and 11 Moi-Moi Metagabbro samples. The results of the XRF and ICP-MS analysis can be found in Appendix II.

The major element chemistry and CIPW norm of an average gabbro (*Cox et al., 1989*) are used for reference during the chemical study of the rocks. This average is calculated from a range of gabbro compositions and is not related to the Charlie Gabbro or the Moi-Moi Metagabbro. In this thesis, it is only used to enable comparison between samples of one serie. The major element chemistry and CIPW norm of an average gabbro is given in Table 6.1, Appendix II and Appendix III.

6.2 The Charlie Gabbro

6.2.1 Geochemistry of the Charlie Gabbro

The Charlie Gabbro samples indicate a tholeiitic trend on the AFM-diagram (Figure 6.1), except for sample AT03A in the calc-alkaline field, which is considered as an outlier, probably as result of its high plagioclase content (Table 6.1). Figures 6.2 show the variation diagrams of the Charlie Gabbro. MgO is chosen for the x-axis because it shows a larger variation than the SiO_2 content. The average composition of olivine and plagioclase are plotted in the diagrams for reference. A bytownite to labradorite plagioclase composition was determined during the petrographic study (see 4.2.2). The olivine composition is based on the whole rock composition of olivine-rich sample Sur-207.

The variation diagrams (Figures 6.2) and the CIPW norm (Table 6.1) show a clear distinction between olivine-bearing and olivine-lacking samples. Olivine-lacking samples have a MgO < 8 Wt-% and contain no or less than 1 Wt-% olivine according to the CIPW norm. Only samples ER1115 and AT16B have 4 to 7 Wt-% olivine in the CIPW norm while their petrography lacks olivine. The olivine-bearing samples contain 8-15 Wt-% MgO, which is high compared to the average MgO content of a gabbro (7,59 Wt-%; *Cox et al., 1989*). They are enriched with olivine (CIPW norm: 7 to 25 Wt-%) compared to an average gabbro (CIPW norm: 0 Wt-%; *Cox et al., 1989*). In particular, MgO levels as high as 15 Wt-% can be explained only by accumulation of olivine.

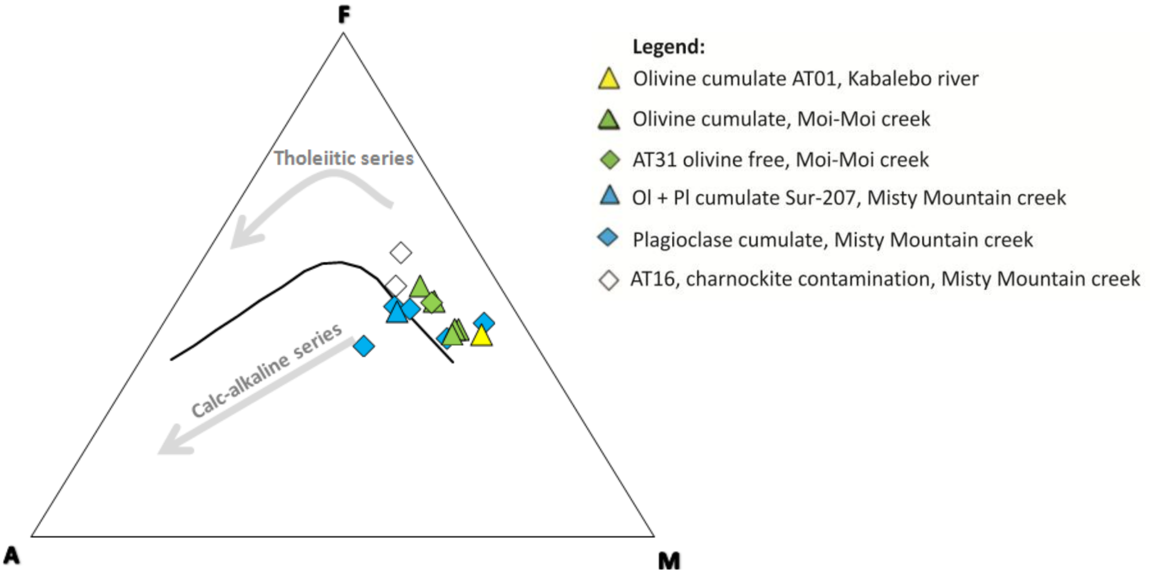

Figure 6.1: *AFM-diagram of the Charlie Gabbro. Abbreviations legend: Ol = olivine, Pl = plagioclase.*

Olivine-bearing and olivine-lacking samples are present in one body, therefore the sampling location does not influence the presence or absence of olivine. The majority of the Misty Mountain creek samples are olivine-lacking, but one olivine-bearing sample, Sur-207, is found. Additionally, the Moi-Moi creek samples are mainly olivine-bearing, but one olivine-lacking sample, AT31, is found.

A positive correlation, consistent with the fractionation of olivine, is present between FeO* and MgO (Figure 6.2). This trend shows a gap around 8 Wt-% MgO, which coincides with the transition of olivine-bearing to olivine-lacking samples. At lower MgO the trend line steepens. Olivine is the cumulus mineral in the Charlie Gabbro that includes substantial FeO, so the change in the slope of the trend line is probably caused by the presence or absence of olivine.

Other positive correlations with MgO are visible in the nickel and cobalt diagrams. Ni shows an inflection point at approximately 8 Wt-% MgO, after which the trend decreases in steepness (Figure 6.3). The inflection point divides the Charlie Gabbro in an olivine-bearing and an olivine-lacking trend. An average basalt contains between 75 and 150 ppm Ni (*Winter, 2001*). The concentration of 150 ppm is presented in the Ni variation diagram as a horizontal, red line. This line crosses the inflection point of the trend line. The olivine-lacking samples have Ni concentrations between 75 (AT03A) and 180 (AT02) ppm, which are in accordance with, or slightly higher than the average gabbroic magma. The olivine cumulates vary in Ni content from 190 ppm (AT18) to ≈700 ppm (AT01), which makes all these samples slightly to strongly enriched in Ni. Also Co shows a positive correlation with MgO, but the trend lacks an inflection point (Figure 6.3). The concentrations of Co vary from ≈20 ppm (AT03A) to ≈100 ppm (Sur-207). The transition between the olivine-bearing and the olivine-lacking samples is at ≈48 ppm. The concentration of Co in samples AT01 and Sur-207 is up to twice this value and indicates a clear enrichment of Co.

The enrichment in olivine (CIPW norm), Ni and Co can only be reached if the rocks were crystallised from an ultramafic magma or by accumulation of olivine in the olivine-bearing Charlie Gabbro samples. If olivine would be the only cumulus phase that influences the FeO trend, extrapolation of the olivine trend should end in the pure olivine composition. This happens for Na_2O, Al_2O_3 and CaO, but not for FeO*. The extrapolated trend in the FeO* diagram plots a few Wt-% below the value of pure olivine and suggests that another Fe-bearing cumulus mineral, probably Fe-Ti oxide, was crystallised earlier to lower the FeO* content.

Figures 6.2 shows the negative correlations between Na_2O resp. Al_2O_3 and MgO. Both diagrams show an inflection point at ≈8 Wt-% MgO which divides the samples in two trends that are based on the olivine content. AT31, AT16B and AT16C plot below the trend lines of Al_2O_3 which might be the result of contamination with

Sample	Olivine	Hypersthene	Diopside	Plagioclase	An:Ab (2:1)
AT01	23,22	16,67	9,05	47,40	2,26
AT02		31,60	0,92	63,83	2,31
AT03A	0,08	15,09	2,44	80,57	2,15
AT05B		26,04	3,83	66,70	1,95
AT06A		22,55	6,10	68,00	1,85
AT16B	4,53	23,20	11,02	51,01	1,74
AT16C		29,62	4,39	60,44	1,52
AT18	6,40	18,96	11,92	58,35	2,19
AT30	8,16	17,90	9,75	58,36	2,19
AT31		25,19	17,35	53,32	1,60
AT32	10,36	14,31	7,38	64,55	2,69
AT34A	10,49	16,62	6,79	60,56	2,55
AT34D	6,93	22,85	6,77	61,43	2,63
71-SUR-207	25,03	19,46	1,07	51,14	2,76
ER-1115	7,26	11,22	3,19	76,23	2,56
Avg. Gabbro*		22,13	13,70	48,86	1,41

Table 6.1: *CIPW-norm of the Charlie gabbro samples. Normative mineral assemblage of the average gabbro is taken from Cox et al. (1989).*

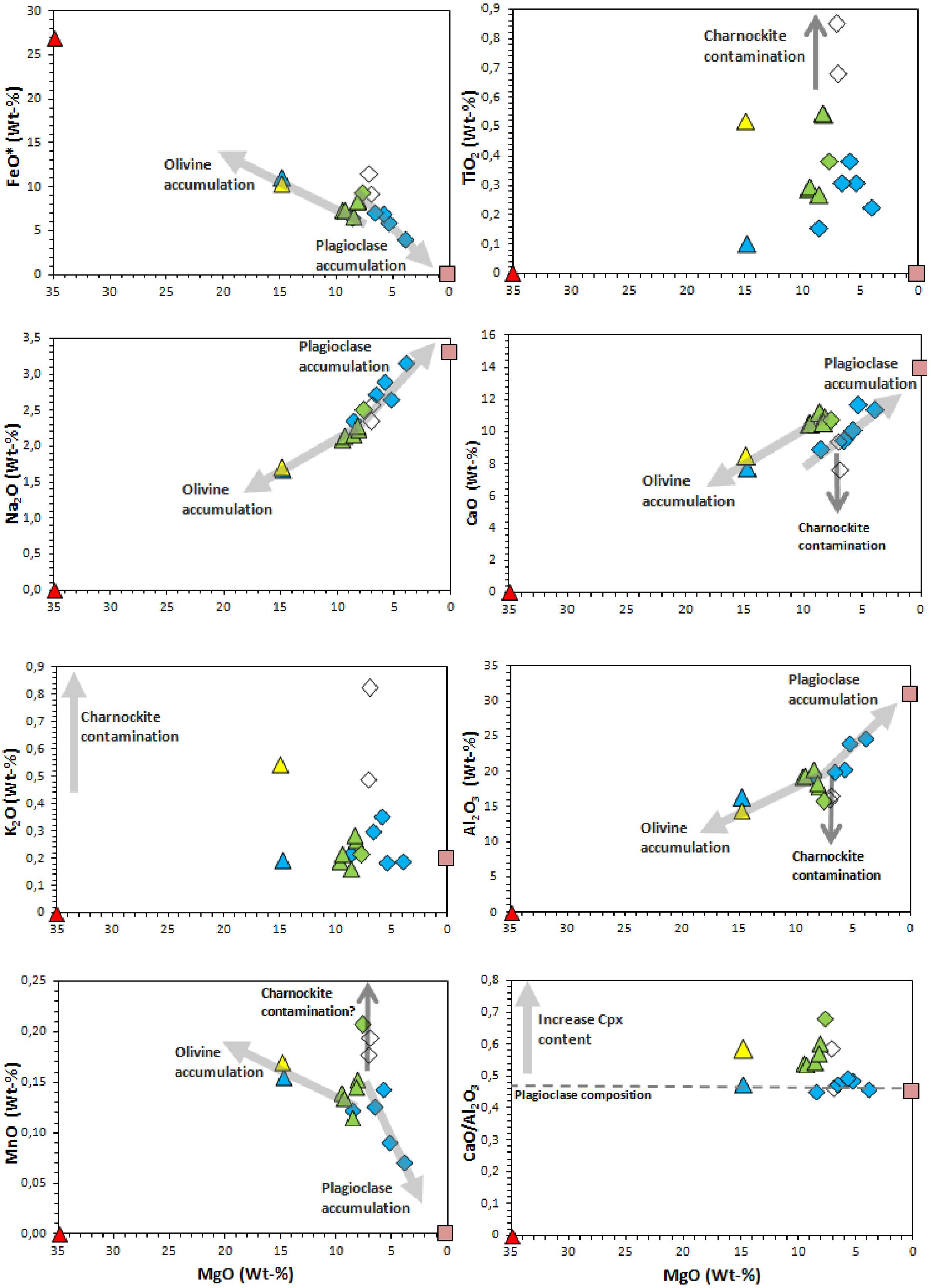
FeO* (Wt-%)
Olivine accumulation
Plagioclase accumulation
TiO$_2$ (Wt-%)
Charnockite contamination
Na$_2$O (Wt-%)
Plagioclase accumulation
Olivine accumulation
CaO (Wt-%)
Plagioclase accumulation
Olivine accumulation
Charnockite contamination
K$_2$O (Wt-%)
Charnockite contamination
Al$_2$O$_3$ (Wt-%)
Plagioclase accumulation
Olivine accumulation
Charnockite contamination
MnO (Wt-%)
Charnockite contamination?
Olivine accumulation
Plagioclase accumulation
CaO/Al$_2$O$_3$
Increase Cpx content
Plagioclase composition
MgO (Wt-%)
MgO (Wt-%)
35
30
25
20
15
10
5
0

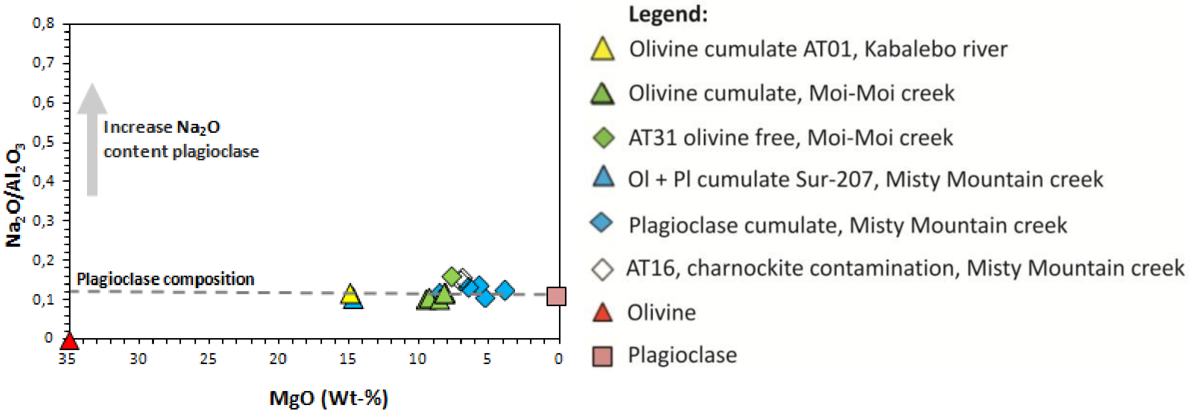

Figure 6.2: Including previous page. *Harker variation diagrams for major elements in the Charlie Gabbro samples. Major element data measured by XRF. Abbreviations: Ol = olivine, Pl = plagioclase, Cpx = clinopyroxene.*

surrounding charnockite. Most samples are enriched in Na_2O and Al_2O_3 compared to an average gabbro (Na_2O = 2,39 Wt-%; Al_2O_3 = 15,48 Wt-%, *Cox et al., 1989*). Especially the Misty Mountain creek samples are enriched. They contain Na_2O and Al_2O_3 contents up to respectively 3 and 25 Wt-%.

The Na_2O/Al_2O_3 ratio of the magma increases during crystallisation of plagioclase. For the Charlie Gabbro, the Na_2O/Al_2O_3 ratio (Figure 6.2) does not deviate significantly from the plotted plagioclase (labradorite to bytownite) ratio, indicating a constant plagioclase composition throughout the series. Therefore the trends in Na_2O, CaO and Al_2O_3 are concluded to represent an increase in plagioclase proportion in the samples. This increase is also visible in the CIPW norm where the plagioclase content increases from a minimum of 47 Wt% (AT01) to 80 (AT03A) Wt-% (Table 6.1) and is in agreement with the cumulate texture of the plagioclase minerals in the thin sections (see 4.2.2).

Europium is a REE which easily substitutes Ca^{2+} in plagioclase. The Eu-anomaly ($Eu/Eu^* = Eu_N / 0{,}5 \times (Sm_N + Gd_N)$) allows the identification of plagioclase accumulation. Samples with an Eu-anomaly near unity are interpreted as rocks with no or minimal plagioclase accumulation, while samples with a positive Eu-anomaly are interpreted as plagioclase cumulates. Olivine gabbronorites AT01 and AT30 have a Eu-anomaly near unity. All other samples show positive Eu-anomalies varying from 1,4 to 2,5 (Figure 6.3). However, the high Eu-anomaly in Sur-207, without significant plagioclase accumulation, and the lacking Eu-anomaly in AT30, with substantial plagioclase accumulation, cannot be explained.

Negative correlations are also present in the strontium and gallium diagrams (Figure 6.3). Gallium partially replaces aluminium in plagioclase while strontium substitutes for calcium. The concentration of Ga increases from ≈10 ppm in Sur-207 to ≈16 ppm in AT03A while the Sr content increases from ≈180 ppm in AT01 towards ≈450 ppm in AT03A. Sur-207 is enriched in Sr compared to the samples of the olivine accumulation trend.

The samples are relatively rich in CaO, which can reach values of 12 Wt-% (average gabbro CaO = 9,58 Wt-%, *Cox et al., 1989*). Two trends are present, based on the presence or absence of olivine. The CaO concentration is higher in the olivine cumulates (Figure 6.2). A similar difference is present in the CaO/Al_2O_3 diagram (Figure 6.2). **T**he CaO/Al_2O_3 ratio of plagioclase is plotted in this diagram for reference. In the plagioclase-rich samples the CaO/Al_2O_3 ratio is constant and the plagioclase composition does not change. A clearly higher ratio is present in the Moi-Moi samples, indicative of the presence of a calcium-bearing pyroxene. The difference in the CaO/Al_2O_3 ratio between the olivine and plagioclase cumulates is 0,2, which might be explained by a difference of intercumulus pyroxene between the series. Pigeonite, a calcium-poor clinopyroxene (*Deer et al., 1992*), is the major intercumulus phase in the olivine cumulates while orthopyroxene is present as the major intercumulus phase in the plagioclase cumulates (see 4.2.2; Table 6.1). The pigeonite could cause this small enrichment of CaO in the olivine cumulates.

The difference is also visible in the chromium diagram. Cr in the plagioclase cumulates varies between ≈50 ppm (ER1115) and ≈100 ppm (AT06A), along a subhorizontal trend. An exception is sample AT02, which has an elevated level of ≈360 ppm. The olivine cumulates show a small enrichment in Cr (≈140 ppm for AT30 to ≈300 ppm for AT34D), which is expected to be related to the intercumulus pigeonite. Sample AT01 has an elevated

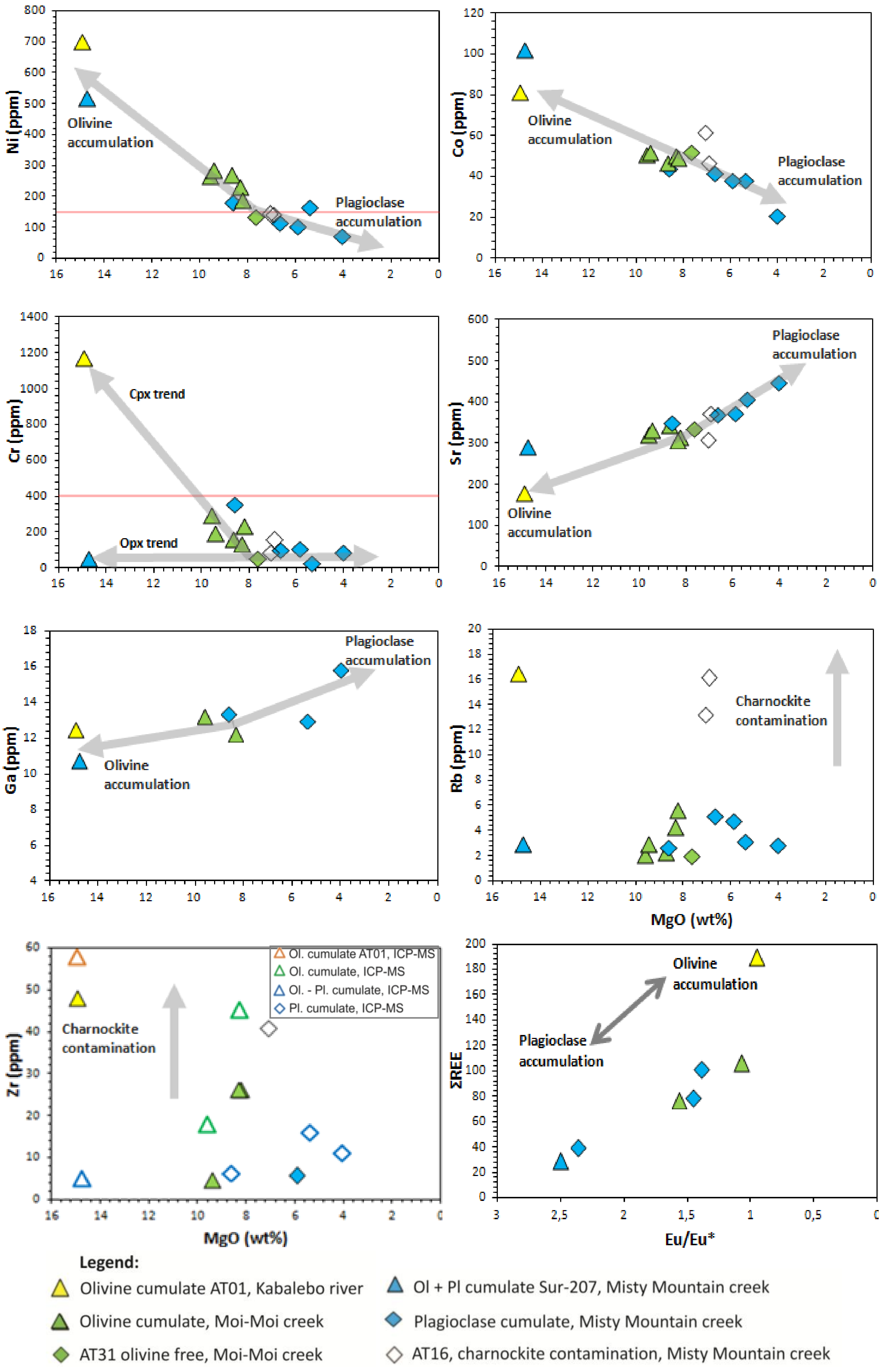

Ni (ppm)
Olivine accumulation
Plagioclase accumulation
Co (ppm)
Olivine accumulation
Plagioclase accumulation
Cr (ppm)
Cpx trend
Opx trend
Sr (ppm)
Plagioclase accumulation
Olivine accumulation
Ga (ppm)
Plagioclase accumulation
Olivine accumulation
Rb (ppm)
Charnockite contamination
MgO (wt%)
Zr (ppm)
Charnockite contamination
Ol. cumulate AT01, ICP-MS
Ol. cumulate, ICP-MS
Ol. - Pl. cumulate, ICP-MS
Pl. cumulate, ICP-MS
MgO (wt%)
ΣREE
Olivine accumulation
Plagioclase accumulation
Eu/Eu*
Legend:
Olivine cumulate AT01, Kabalebo river
Olivine cumulate, Moi-Moi creek
AT31 olivine free, Moi-Moi creek
Ol + Pl cumulate Sur-207, Misty Mountain creek
Plagioclase cumulate, Misty Mountain creek
AT16, charnockite contamination, Misty Mountain creek

Figure 6.3 (previous page): *Whole rock trace element data of the Charlie Gabbro. ICP-MS data is used for the Ga and ΣREE diagrams. Combined XRF and ICP-MS data is used in the Zr diagram. In this diagram, XRF data is given according to the legend. ICP-MS data is plotted as unfilled triangles and diamonds, marked by coloured lines. Blue triangle: Sur-207, Misty Mountain creek; blue diamonds: plagioclase cumulates, Misty Mountain creek; green triangles: olivine cumulates, Moi-Moi creek; yellow triangle: AT01, Kabalebo River. XRF data is used for remaining trace elements.*

concentration of 1174 ppm Cr, which exceeds the normal level of Cr in a basalt (Cr = 400 ppm; *Winter, 2001*). No evidence for clinopyroxene accumulation is found in the thin section of AT01. Sample AT01 shows several characteristics of charnockite contamination (see below), but charnockites are low in Cr *(Klaver, 2011)*. The actual cause for the high Cr level in sample AT01 remains unclear.

The remaining major elements show considerable scatter that reflects the low and variable proportions of the minerals, such as biotite and opaque minerals. For example, K_2O ranges from 0,25 to 0,35 Wt-% but no clear trend is visible. Samples AT16B and AT16C show elevated values of > 0,5 Wt-% K_2O, probably due to contamination at the contact with the surrounding charnockite. A similar value is present in sample AT01, in agreement with its higher amount of biotite (see 4.2.2). The TiO_2 diagram shows similar characteristics, with scatter between 0,1 and 0,5 Wt-%. AT16B and C have a higher TiO_2 levels. MnO shows a trend similar to FeO*, but the samples show more scatter. The elevated MnO concentrations in samples AT16B, AT16C and AT31 might indicate contamination by the surrounding charnockite.

Another characteristic of the Charlie Gabbro is the absence of significant incompatible trace element concentrations. Most trace elements have concentrations < 10 ppm (Appendix II) and show substantial scatter on the variation diagrams. Samples AT01, AT16A and AT16B show elevated concentrations in Rb, Ba, Hf, Zr and Pb (e.g. Figure 6.3) which is considered as evidence for contamination by the surrounding charnockite.

The ΣREE concentration varies considerably, from ≈30 ppm in Sur-207 to ≈190 ppm in AT01. There appears to be a relation between the low ΣREE and the amount of plagioclase accumulation. The samples with the highest Eu-anomaly have the lowest ΣREE (Figures 6.3 and 6.4). The REE are incompatible in the Charlie Gabbro and will stay in the melt, but the amount of interstitial liquid decreases with increasing plagioclase content, resulting in a lower ΣREE content in the plagioclase cumulates.

Figure 6.4 show Cl-normalised REE diagrams of Charlie Gabbro samples using Cl-Chondrite normalization values of *McDonough and Sun (1995)*. Normalised values can be recognized by the subscripted N after the element or element ratios. The patterns of the Charlie Gabbro are relatively flat ($(La/Lu)_N$ = 1,8 – 3,8), with only a minor light rare earth (LREE) or heavy rare earth (HREE) enrichment or depletion ($(La/Sm)_N$ = 1,8 – 2,7; $(Dy/Lu)_N$ = 0,6 – 1,2). A difference in $(Dy/Lu)_N$ is present between the olivine cumulates and the plagioclase cumulates. The plagioclase cumulates are slightly depleted in HREE compared to the olivine cumulates.

6.2.2 Pearce Element ratios

Pearce Element Ratios (PER) can test whether the members of a rock suite are comagmatic and can illustrate the causes of chemical diversity in comagmatic suites (*Russel and Nicholls, 1988*). Comagmatic rocks have constant ratios for elements conserved in the system during changes that led to chemical diversity (*Russel and Nicholls, 1988*). In basaltic systems, the incompatible elements Ti, K and P are often conserved (*Russel and Nicholls, 1988*). The plotted element ratios in the PER diagrams are chosen to test for the fractional crystallisation of a particular mineral or minerals (*Winter, 2001*). The denominator is the same for both axes and is not contained in the fractionating minerals while the numerators reflect the stoichiometry of the proposed fractionating mineral or minerals. The slope of the trend in a PER diagram is sensitive to the stoichiometry of the crystallising and segregating phases (*Russel and Nicholls, 1988*), unravelling the crystallization sequences of rock suites. PER diagrams do not prove that a particular mineral is fractionating, or even that fractional crystallisation is at work. They merely indicate whether or not the chemical composition of a suite of lavas is consistent with such process. See *Russel and Nicholls (1988)* for a more extended explanation of the PER diagrams.

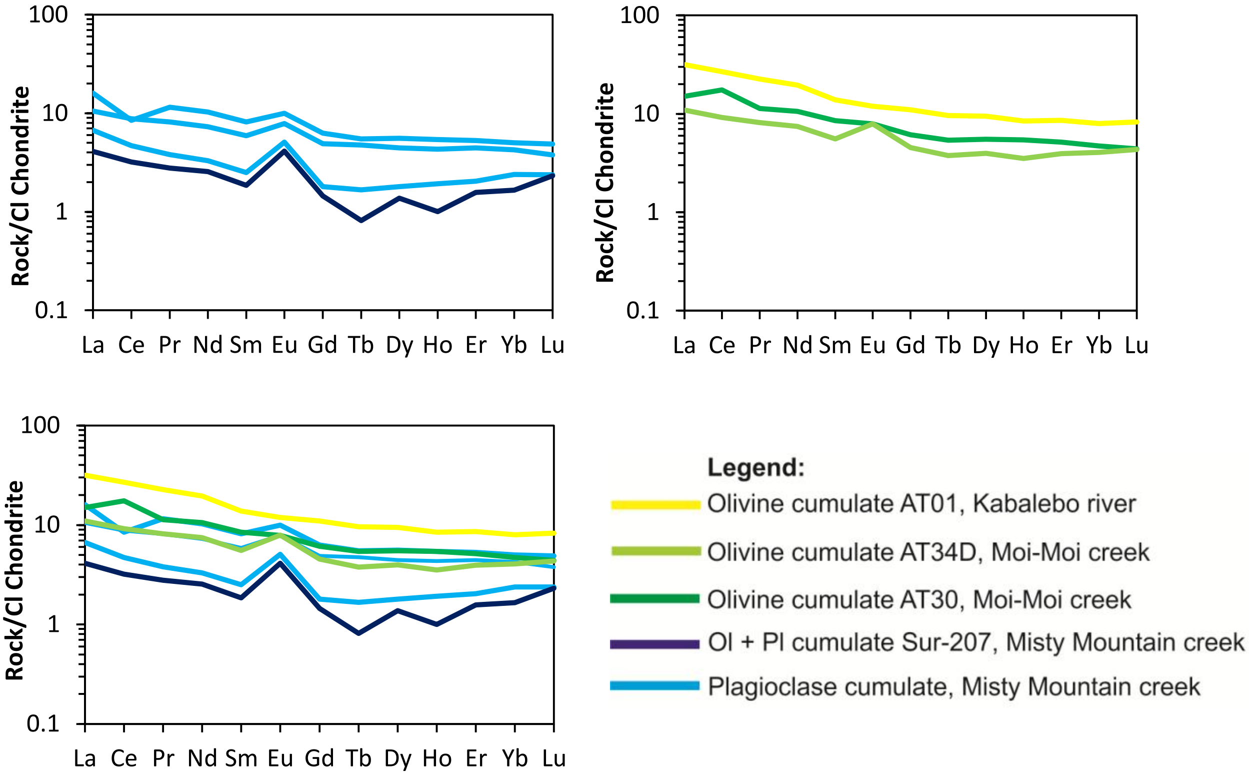

Figure 6.4: *CL-normalised REE diagrams of the Charlie Gabbro. The REE of the individual samples are measured by ICP-MS. The Cl-chondrite normalisation factors of McDonnough and Sun (1995) are used.*

The first step in the recognition of comagmatic lavas is plotting P/K versus Ti/K. Comagmatic basaltic rocks will plot as a tight cluster while dispersion of the data would imply that the data are not from comagmatic rocks or that at least one of the elements was not conserved. The P/K versus Ti/K plot (Figure 6.5) shows a considerable dispersion. The samples are derived from two nearby bodies, therefore it is considered to be unlikely that the rocks were not comagmatic. It is probable that one of the elements was not conserved during the earlier stages of crystallization. A separate primary K mineral is not present, but it is likely that Fe-Ti oxide crystallized and segregated early. Based on these observations, K will be used as denominator in the following PER diagrams.

The petrography and chemistry indicate that the rocks are formed by olivine and plagioclase accumulation. If olivine was the only early crystallising phase, the trend in the 0,5[Mg+Fe]/K versus Si/K PER diagram should define a slope of 1. However, if plagioclase was the only early crystallising phase, the trend in the 2Na+Al/K versus Si/K PER diagram should define a slope of 1. The addition of other phases containing these elements causes deviations from these slopes. The slope in the 0,5[Mg+Fe]/K diagram is 0,17 (Figure 6.5), indicating addition of at least one other phase containing Fe, Mg or Si. The slope in the 2Na+Al/K diagram is 0,73 (Figure 6.5), which also indicates the addition of at least one other phase containing Na, Al or Si. Accumulation of olivine and plagioclase takes place in the Charlie Gabbro, therefore it is possible that both minerals were an early crystallising phase. If so, the slope in the 0,5(Mg+Fe)+2Ca+3Na PER diagram should be 1,0. The slope is approx. 1 for the Charlie Gabbro (Figure 6.5), confirming olivine and plagioclase as early crystallising phases. In this diagram, clinopyroxene has a slope of >1,0, therefore, the slope of the Charlie Gabbro trend should be >1 if clinopyroxene was also an early crystallising phase. The slope of ≈1 excludes clinopyroxene as an early crystallising phase.

In summary, the PER suggest that chemical variation of the Charlie Gabbro samples is governed by early crystallization and segregation of olivine and plagioclase (by settling resp. floating), probably accompanied by Fe-Ti oxide.

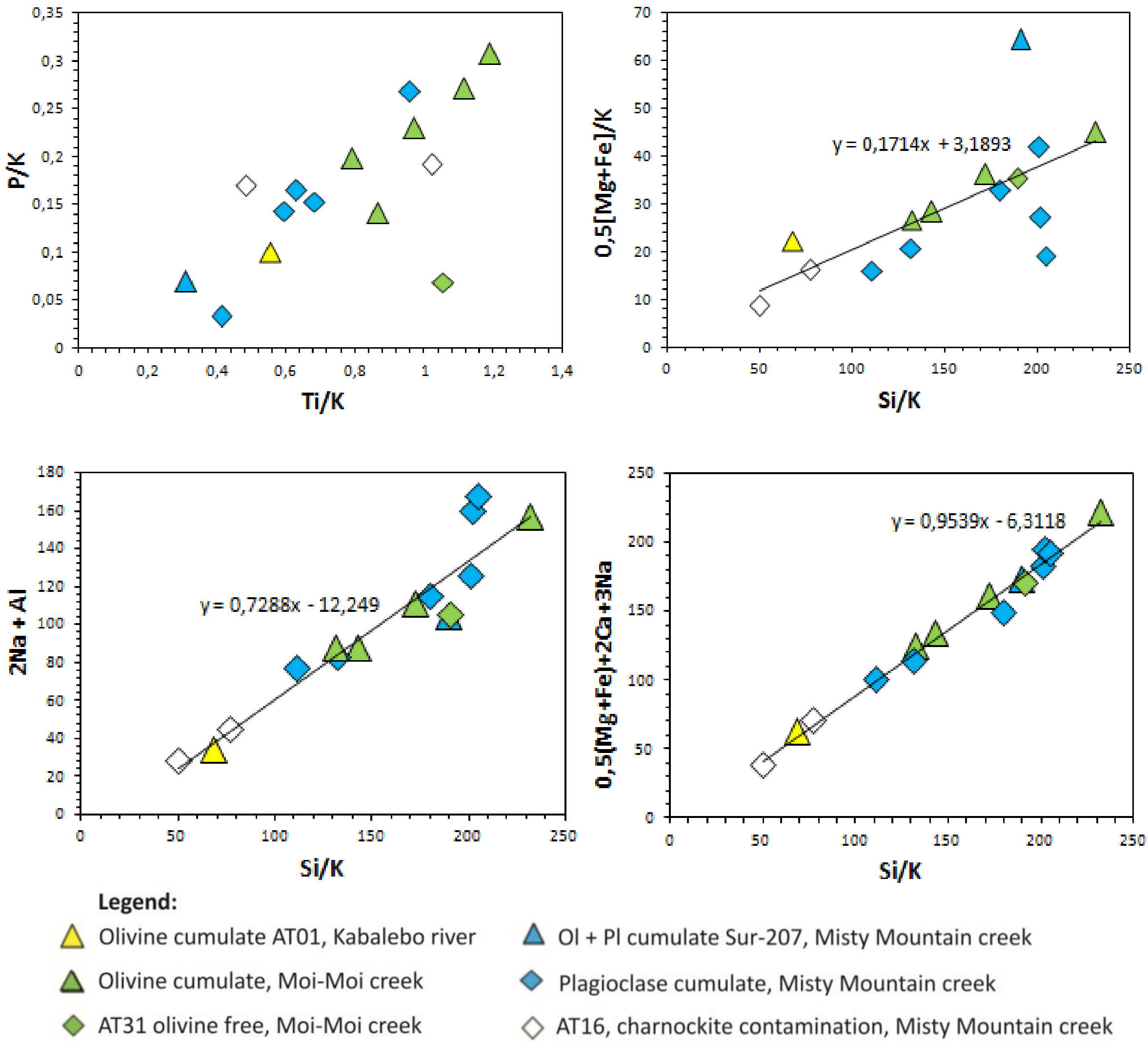

Figure 6.5: *Pearce Element Ratio diagrams of the Charlie Gabbro. Used data is measured by XRF.*

6.2.3 Multi-element variation diagrams

In multi-element variation diagrams normalised element concentrations of a rock are plotted in order to determine the relative variations of the (normalized) elements. In this study, the multi-element variation diagram introduced by *Pearce (1983)* and the N-MORB normalization factors of *Sun & McDonough (1989)* are used. In this plot the large ion lithophile elements (LILE) and the high field strength elements (HFSE) are grouped and the compatibility of the elements increases outwards. The most striking features in Figure 6.6 are the enrichment of LILE relative to N-MORB, the decoupling between LILE and HFSE and the Nb-Ta trough. These features are present in all samples and are characteristic for subduction zone related magmatism. The HFSE of the plagioclase cumulates appear to be depleted compared to N-MORB, which is probably the result of the low trace element concentration within these cumulates. Other features of the Charlie Gabbro are the depletion of several HFSE, such as Zr, Hf, and Ti, relative to the other HFSE. The negative zirconium anomaly is coupled with a negative hafnium anomaly in the plagioclase cumulates of the Misty Mountain creek. A small positive samarium anomaly appears to be present in the samples, but this could be the result of the depletion of its neighbouring elements. Finally, a positive barium anomaly is present compared to the already enriched LILE.

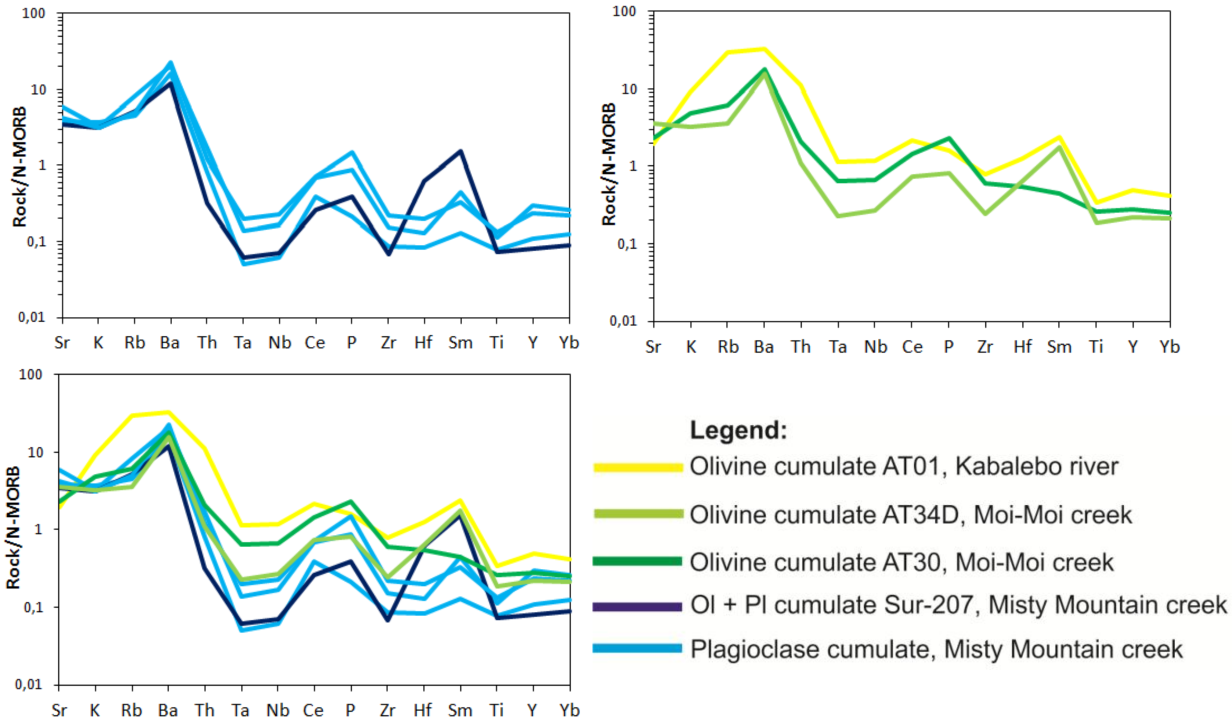

Figure 6.6: *Multi-element variation diagrams after Pearce (1983). The trace element concentrations of the individual samples are measured by ICP-MS and normalised with the N-MORB normalisation factors of Sun and McDonough (1989).*

6.2.4 Tectonic discrimination diagrams

Empirical results demonstrate that trace elements show distinctive trends and ratios for different tectonic settings and thus are good indicators for discrimination diagrams. Discrimination diagrams are especially useful for rocks that underwent metamorphism and in which the original texture is not present anymore, but immobile elements must be chosen then in order to gain reliable results. Unfortunately, the Charlie Gabbro consists of cumulate rocks and show rather low incompatible trace element values. As a result, the discrimination diagrams based on single trace element levels are not a trustworthy representation for the tectonic settings of the Charlie Gabbro. For other discrimination diagrams, such as the triangular discrimination diagrams of *Pearce and Cann (1973)*, it is assumed that cumulate crystals are only present in small amounts. This is clearly not the case for the Charlie Gabbro samples.

The most reliable discrimination diagram for the Charlie Gabbro is based on element ratios. Figure 6.7A displays a ratio-based discrimination diagrams introduced by *Pearce (2008, 2014)*. In this diagram the Th/Nb ratio is plotted against the Nb/Yb ratio. The axes are plotted with a logarithmic scale because of the log-normal element distribution of the incompatible elements *(Pearce, 2008)*. A short description of the diagram and the interpretation of the Charlie Gabbro samples is given in the following text. See *Pearce (2008; 2014)* for a more extended explanation of the discrimination diagram.

The Th/Yb ratio indicates the amount of crustal input, either by crustal contamination or by subduction and recycling of the subducting slab. The Th/Nb ratio is expected to be trustworthy because both thorium and niobium are immobile during weathering processes and are not influenced by metamorphism up to lower amphibolite facies (*Pearce, 2008*). The value of the Nb/Yb ratio reflects all source and melting variables other than crustal input and will give an indication of the magma composition that intruded. The N-MORB, E-MORB and OIB magma compositions are plotted in the diagrams as black squares. They are incorporated in the MORB-OIB array, which is the area in between the grey lines. This MORB-OIB array represent compositions that lack significant crustal input. However, if the sample compositions deviate from the array, as indicated by the black arrow in the diagram, magma-crust interaction occurs.

According to the diagram, almost all Charlie Gabbro samples deviate from the MORB-OIB array and fall in the volcanic arc array, indicating crustal input in the magma by crustal contamination or by subduction. Textural evidence (see 4.2.2) and major element compositions (see 6.2.2) indicate that crustal contamination is only expected in samples AT01, AT16B, AT16C and perhaps in AT31, while the other samples lack crustal contamination. With exception of AT01, only non-contaminated samples are plotted in the discrimination diagrams, so the crustal input in the Charlie Gabbro is expected to be caused by subduction and recycling of the subducting slab. Such recycling of the subducting slab would be in agreement with the characteristic subduction zone signature in the multi-element variation diagram (see 6.2.3).

The arc related field can be subdivided in Mid Ocean Ridge Basalt (MORB), island arc tholeiite (IAT) and boninite magma types (Figure 6.7B) using the V versus Ti discrimination diagram (*Shervais, 1982*). This diagram is influenced by 2 processes, Ti depletion and V enrichment. Of these, only V is subduction-specific (*Pearce, 2014*). Ti depletion is influenced by subduction derived water, which increases the degree of partial melting. Ti is then increasingly depleted in the melt as the degree of partial melting increases (*Pearce, 2014*). Another process that causes Ti reduction is the loss of small degrees of melt as the mantle flows towards the trench (*Pearce, 2014*). The Charlie Gabbro samples plot in the IAT field or at the transition of the IAT and MORB field, therefore, a slab-proximal tectonic setting is expected.

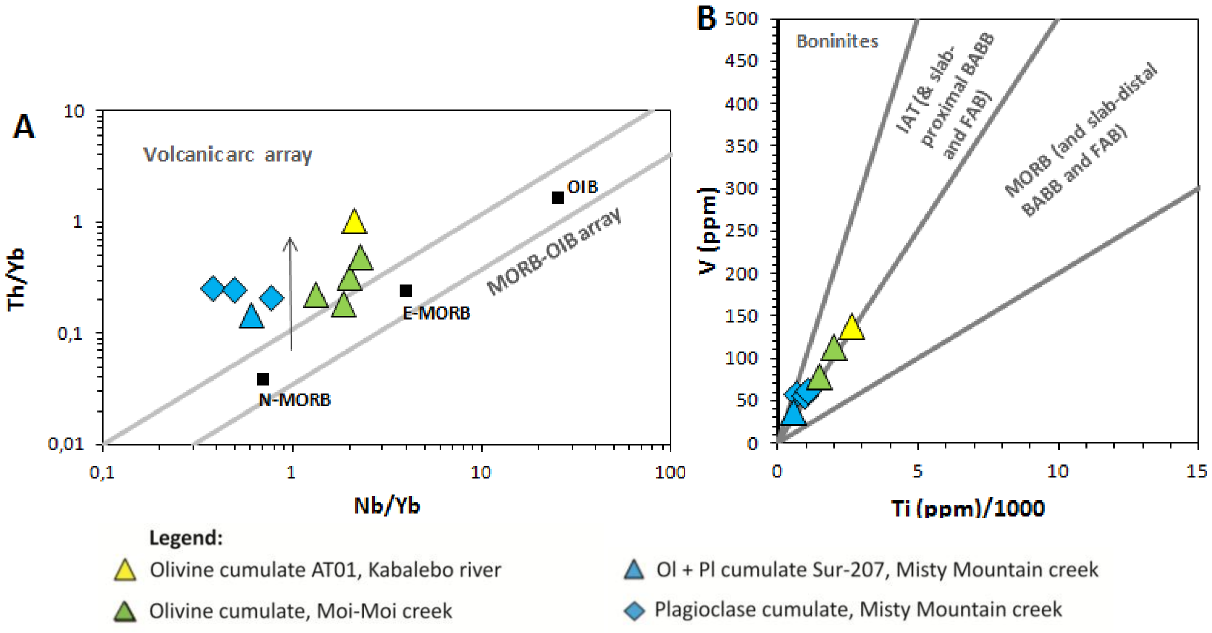

Figure 6.7; *Tectonic discrimination diagrams according to Pearce (2008, 2014).Trace element concentrations are measured by ICP-MS. B: Fields after Pearce (2014).*

6.3 The Moi-Moi Metagabbro

6.3.1 Geochemistry of the Moi-Moi Metagabbro

The Moi-Moi Metagabbro samples follow a tholeiitic trend on the AFM-diagram (Figure 6.8). Figure 6.7 shows the variation diagrams of the Moi-Moi Metagabbro. Additionally, the composition of single minerals from drill core LA148 (depth of 34 to 36 metre) is plotted in these diagrams. The mineral compositions were determined by wavelength dispersive X-ray spectroscopy (WDS) using a Microscan-9 microprobe at the VU University in Amsterdam. The analyses were performed at an acceleration voltage of 20 kV and the data were corrected using the ZAF correction method. They were performed by Piet Maaskant in 1981 and provided by E.W.F. de Roever. Several pyroxene, olivine, hornblende and phlogopite grains were analysed from which the average composition (Appendix II) is used for reference. The plagioclase composition was microscopically determined for pyroxene hornblende gabbronorites (see 4.3.2).

The lithologies of the Moi-Moi body, the Zandkreek body and the Kabalebo West body all show a cumulus texture (see 4.3.2) in which olivine, clinopyroxene, orthopyroxene and plagioclase may be cumulus phases. The whole rock chemistry reflects the differences in the type and amount of cumulus minerals present, resulting in a wide range of rock compositions.

The variation diagrams indicate three trends that originate from a common point at approximately 7 to 8 Wt-% MgO (see Figures 6.9 and 6.10). The first trend includes the Kabalebo West samples and can in many cases be extrapolated towards the olivine composition. These samples, which can be recognised by their high MgO content (20 – 28 Wt-%), indicate a clear trend in all diagrams except for K_2O, CaO/Al_2O_3, Rb and Zr. The second trend is represented by the Zandkreek samples and the Moi-Moi gabbronorites with a high MgO content (8 – 12 Wt-% MgO). This trend can be extrapolated to a point in between the orthopyroxene and clinopyroxene compositions. Noticeable is sample AT36A from the Zandkreek area, which has a chemistry similar to the high-Mg gabbronorites. The third trend contains all low-MgO samples from the Moi-Moi gabbronorites (4 – 6 Wt-% MgO). This is the only trend that evolves towards lower MgO contents. Quartz-diorite LA150 in many cases deviates from this trend and will be discussed separately.

The Kabalebo West trend shows a positive correlation of FeO* with MgO (Figure 6.9) , in agreement with the accumulation of olivine. The Kabalebo West samples have a high FeO* content (12,6 – 15,2 Wt-%) compared to an average gabbro (10,3 Wt-%, *Cox et al., 1989*). The trend can be extrapolated until approximately 2 Wt-% below the pure olivine composition, which probably indicates the presence of an additional Fe-bearing mineral, such as orthopyroxene or an intercumulus phase such as hornblende, or phlogophite. A similar trend is present in the MnO diagram where the trend can be extrapolated until approximately 0,1 Wt-% below the olivine composition. This indicates the presence of an additional Mn-bearing phase, probably the intercumulus hornblende.

Nickel and cobalt show a similar positive correlation with MgO (Figure 6.10). In the Kabalebo West samples Ni varies from 500 to 750 ppm and Co from 100 to 125 ppm. The Ni concentration far exceeds the normal level of an average gabbro (150 ppm, *Winter, 2001*) and, therefore, the Kabalebo West trend indicates olivine accumulation. The extrapolated trend crosses the 150 ppm Ni level at ≈ 8 Wt-% MgO.

The lower FeO* content of the Zandkreek samples results from the lack of olivine within the mela-gabbronorites, the majority of FeO* and MgO is incorporated in orthopyroxene and clinopyroxene. Only sample AT38 contains olivine and plots in between the Kabalebo West and Zandkreek trends (Figure 6.9). The lack of olivine is also visible in the Ni and Co diagrams (Figure 6.10). The Zandkreek samples and high-Mg gabbronorites show a large scatter and rather low Ni and Co values. Only sample AT38 fits on the olivine accumulation trend lines. It is unclear where the enrichment of FeO* and MnO in sample AT36A comes from.

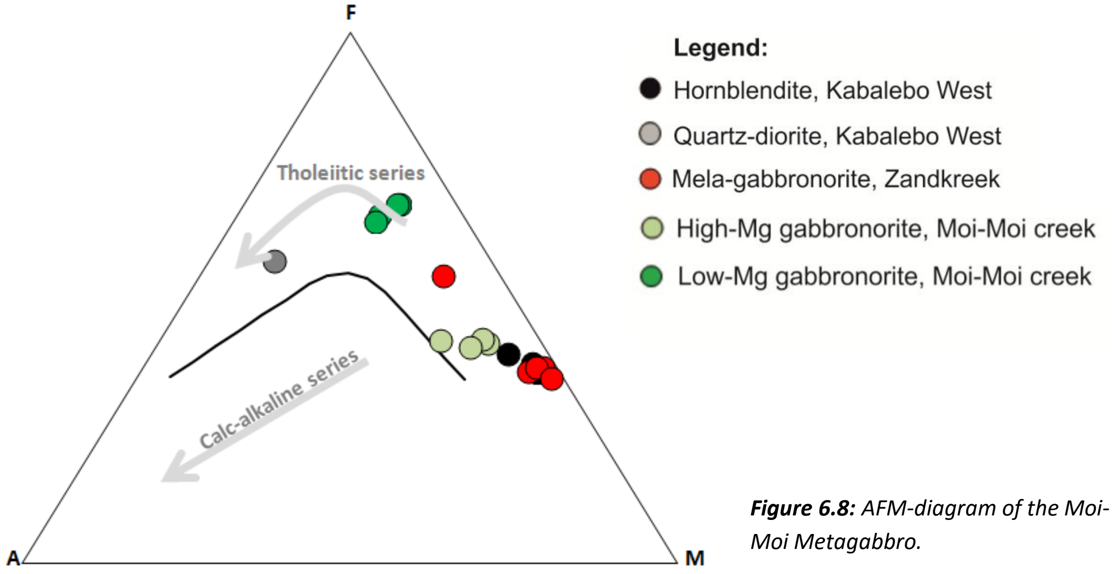

Figure 6.8: *AFM-diagram of the Moi-Moi Metagabbro.*

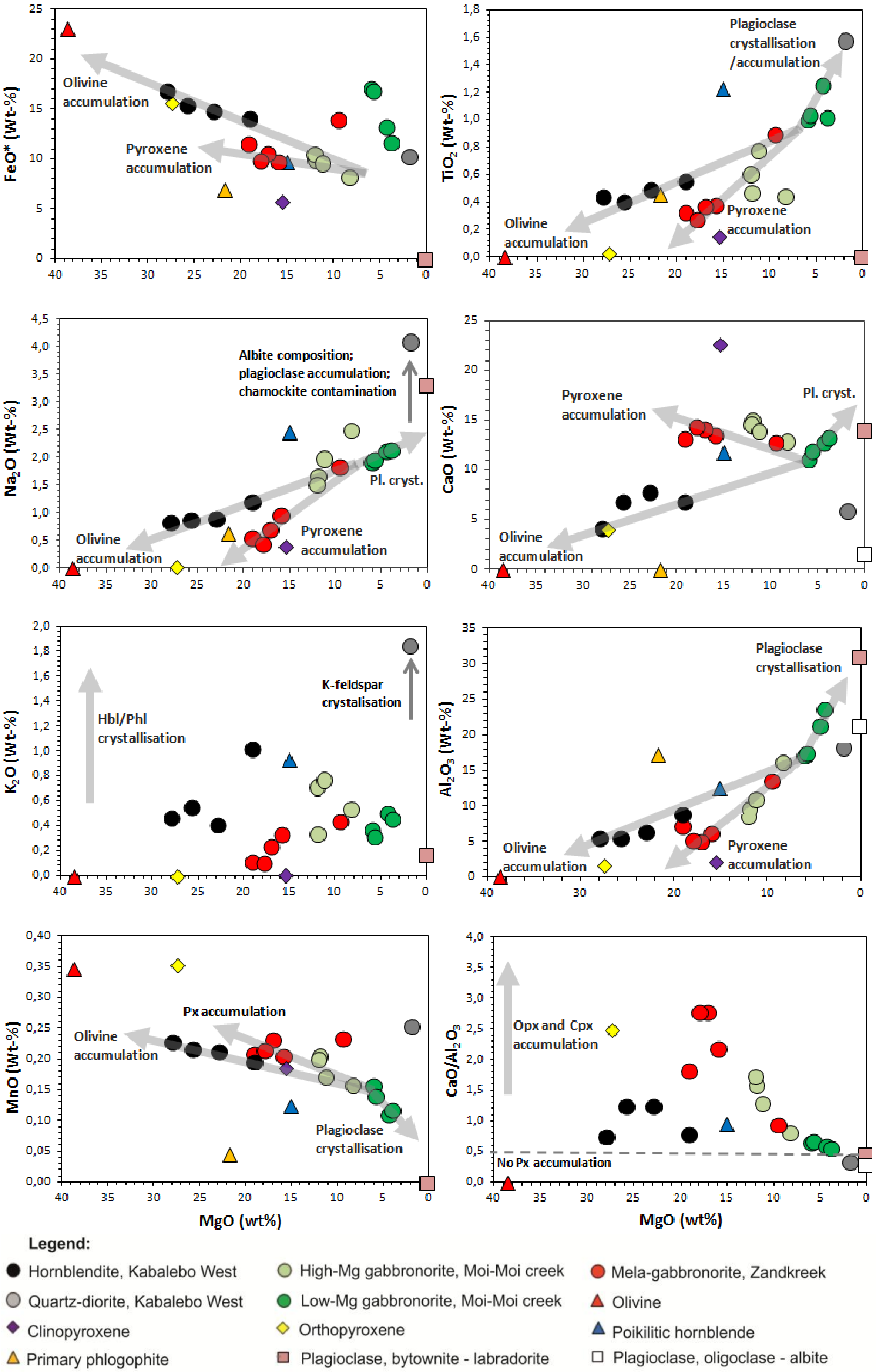
FeO* (Wt-%)
Olivine accumulation
Pyroxene accumulation
TiO$_2$ (Wt-%)
Plagioclase crystallisation /accumulation
Olivine accumulation
Pyroxene accumulation
Na$_2$O (Wt-%)
Albite composition; plagioclase accumulation; charnockite contamination
Pl. cryst.
Olivine accumulation
Pyroxene accumulation
CaO (Wt-%)
Pyroxene accumulation
Pl. cryst.
Olivine accumulation
K$_2$O (Wt-%)
Hbl/Phl crystallisation
K-feldspar crystalisation
Al$_2$O$_3$ (Wt-%)
Plagioclase crystallisation
Olivine accumulation
Pyroxene accumulation
MnO (Wt-%)
Px accumulation
Olivine accumulation
Plagioclase crystallisation
CaO/Al$_2$O$_3$
Opx and Cpx accumulation
No Px accumulation
MgO (wt%)
MgO (wt%)
Legend:
● Hornblendite, Kabalebo West
● Quartz-diorite, Kabalebo West
◆ Clinopyroxene
▲ Primary phlogophite
● High-Mg gabbronorite, Moi-Moi creek
● Low-Mg gabbronorite, Moi-Moi creek
◆ Orthopyroxene
■ Plagioclase, bytownite - labradorite
● Mela-gabbronorite, Zandkreek
▲ Olivine
▲ Poikilitic hornblende
□ Plagioclase, oligoclase - albite

Figure 6.9 (previous page): *Harker diagrams showing the different trends in the Moi-Moi Metagabbro. Whole rock samples are analysed by XRF. In-situ mineral analyses from sample LA148-34-36m, measured by EMP. Plagioclase compositions optically determined. See text for explanation.*

The low-MgO gabbronorites and quartz-diorite LA150 show elevated FeO* concentrations compared to an average gabbro and diorite (gabbronorites: 10,5 – 15,4 Wt-%; avg. gabbro 10,3 Wt-%, *Cox et al., 1989;* quartz-diorite: 9,1 Wt-%, avg. diorite 7,2 Wt-%, *Cox et al., 1989*), but it is not clear what caused these high concentrations. Ni concentrations are low (< 110 ppm) and cobalt show a large scatter (75 – 15 ppm) (Figure 6.10). However, a clear trend in MnO is present (Figure 6.9) in the gabbronorites and sample LA150 is enriched in MnO.

Three different trends are visible in the CaO diagram (Figure 6.9). The Kabalebo West samples are depleted in CaO (4,2 – 8,0 Wt-%) compared to an average gabbro, 9,58 Wt-%, *Cox et al., 1989*). The trend shows a negative correlation which can be extrapolated to slightly above the olivine composition, indicating the presence of an additional CaO-bearing cumulus phase. High chromium concentrations, 1600 to 2500 ppm, (avg. gabbro 400 ppm, *Winter, 2001*) most probably point to the presence of clinopyroxene as additional CaO-bearing cumulus phase.

The high-Mg Moi-Moi gabbronorites and the Zandkreek samples are enriched in CaO (12,7 – 14,8 Wt-%). CaO is incorporated in plagioclase and clinopyroxene, but plagioclase is not expected to be the source of enrichment due to the low strontium concentration and low intercumulus plagioclase content (see 4.3.2) in the Zandkreek samples. Cr varies from 200 to 410 ppm in the high-Mg gabbronorites and from 1050 to 1730 ppm in the Zandkreek samples. The high Cr concentration in the Zandkreek samples most probably indicates that clinopyroxene accumulation caused the CaO enrichment.

A negative correlation between CaO and MgO is present in the low-Mg gabbronorites (Figure 6.9). The trend can be extrapolated to ≈2 Wt-% above the plagioclase composition. The samples are slightly enriched in CaO (11 – 13 Wt-%) compared to an average gabbro but have a low Cr content (3 to 14 ppm). Their CaO/Al_2O_3 values are similar to the plagioclase composition (Figure 6.9), indicating that significant pyroxene accumulation did not occur in these samples. The samples lack an Eu-anomaly (Figure 6.10) that excludes plagioclase accumulation in these samples. The CaO concentration is expected to be related to the high proportion and composition of plagioclase and hornblende in the samples.

Finally, quartz-diorite LA150 has a CaO content of 5,8 Wt-%, similar to average diorite (6,58 Wt-%, *Cox et al., 1989*). This rather low calcium level compared to the gabbronorites is probably caused by the presence of a calcium-poor plagioclase (see 4.3.2). This composition, albite to oligoclase, is plotted in the diagrams as a white square. The small enrichment in CaO compared to this plagioclase composition is expected to be the result of the presence of apatite. LA150 has a low Cr concentration and a CaO/Al_2O_3 ratio similar to the albite to oligoclase plagioclase composition, indicating no or insignificant pyroxene accumulation.

The Moi-Moi Metagabbro samples show a positive correlation of Cr with MgO (Figure 6.10). An inflection point at ≈ 8 Wt-% MgO divides the trend into a clinopyroxene accumulation trend and a clinopyroxene crystallisation trend. The accumulation trend goes from the high-Mg gabbronorites towards the Zandkreek samples. The trend appears to represent increasing proportions of accumulated clinopyroxene, but this contradicts with the CaO/Al_2O_3 diagram (Figure 6.9). In this diagram, orthopyroxene and clinopyroxene have a CaO/Al_2O_3 value of respectively 2,5 and 10,8 (Appendix II), while plagioclase has a CaO/Al_2O_3 value of ≈0,5. A higher CaO/Al_2O_3 value of a sample than 0,5 would indicate the presence of clinopyroxene. All Zandkreek samples, together with some high-Mg gabbronorites, have a CaO/Al_2O_3 value of > 1,5, indicating a large proportion of clinopyroxene. The Kabalebo West samples vary in CaO/Al_2O_3 from 0,8 to 1,3, indicating less clinopyroxene than the Zandkreek samples. This difference in clinopyroxene is in agreement with the petrography but is not reflected in the Cr content of the samples. This might be caused by the presence of another Cr-bearing mineral in the Kabalebo West samples.

Negative correlations with MgO are present in the Na_2O and Al_2O_3 diagrams (Figure 6.9). The Kabalebo West samples are low in Na_2O (0,9 – 1,2 Wt-%) and Al_2O_3 (5,5 – 8,8 Wt-%) compared to an average gabbro (Na_2O: 2,39 Wt-%, Al_2O_3: 15,48 Wt-%, *Cox et al., 1989*) and show a low Sr concentration (150 – 255 ppm). Na_2O

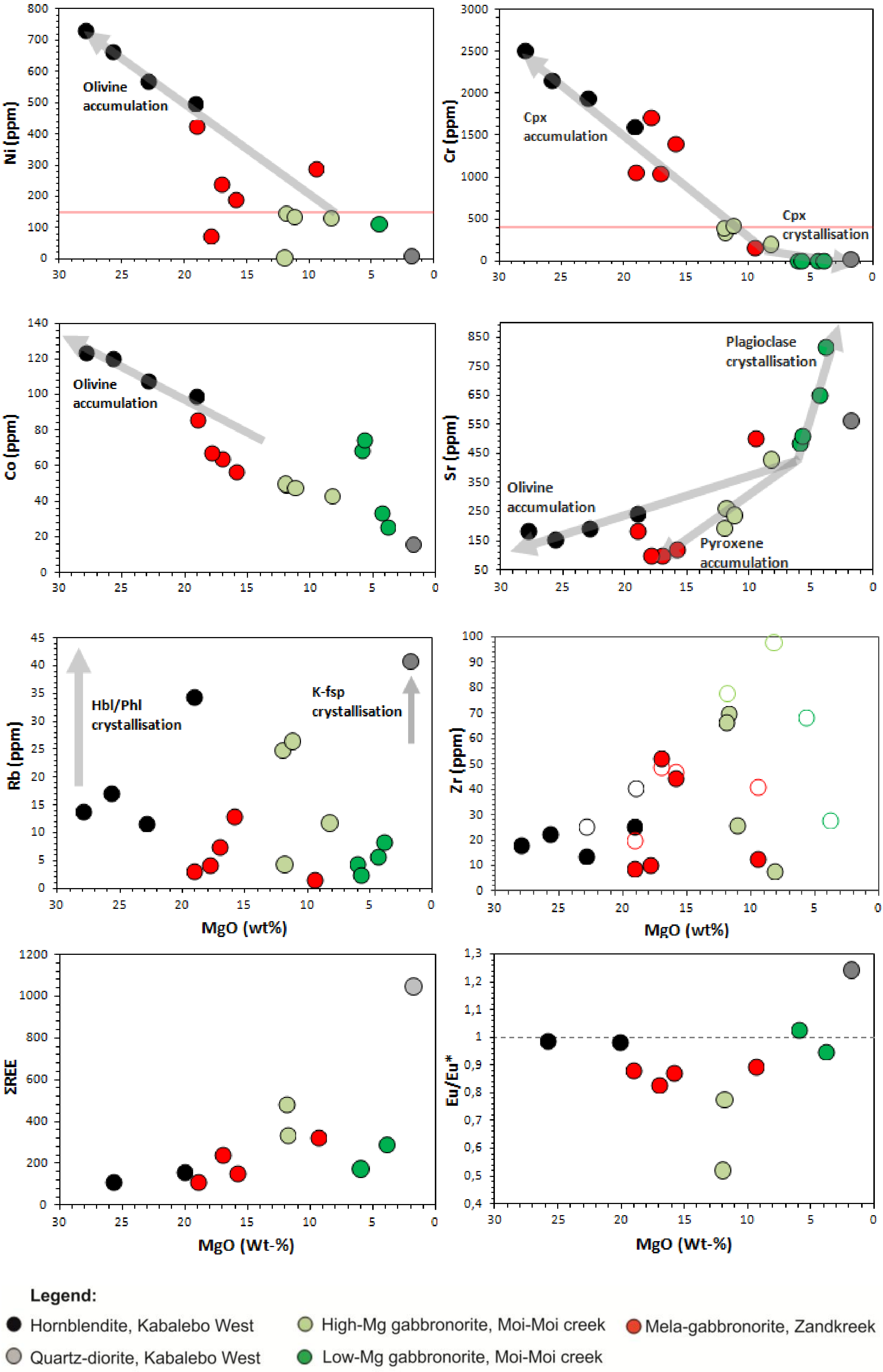
Ni (ppm)
Olivine accumulation
Cr (ppm)
Cpx accumulation
Cpx crystallisation
Co (ppm)
Olivine accumulation
Sr (ppm)
Plagioclase crystallisation
Olivine accumulation
Pyroxene accumulation
Rb (ppm)
Hbl/Phl crystallisation
K-fsp crystallisation
MgO (wt%)
Zr (ppm)
MgO (wt%)
ΣREE
MgO (Wt-%)
Eu/Eu*
MgO (Wt-%)
Legend:
● Hornblendite, Kabalebo West
● High-Mg gabbronorite, Moi-Moi creek
● Mela-gabbronorite, Zandkreek
● Quartz-diorite, Kabalebo West
● Low-Mg gabbronorite, Moi-Moi creek

Figure 6.10 (previous page): *Whole rock trace element data of the Moi-Moi Metagabbro. ICP-MS data is used for the ΣREE and Eu/Eu* diagrams. Combined XRF and ICP-MS data is used in the Zr diagram. In this diagram, XRF data is given according to the legend. ICP-MS data is plotted as unfilled circles, marked by coloured lines. Black: ultramafics Kabalebo West, red: Zandkreek, light green: High-Mg gabbronorites Moi-Moi creek, dark green: low-Mg gabbronorites Moi-Moi creek. XRF data is used for remaining trace elements.*

and Al_2O_3 is low in the cumulus olivine and pyroxenes, but high in the intercumulus phases, therefore, the low Na_2O and Al_2O_3 suggest that the intercumulus phases are only the minority content of the rocks.
The Zr versus MgO diagram shows large scatter (Figure 6.10). The highest concentrations are present in the gabbronorites of the Moi-Moi creek. These high values suggest Zr enrichment which could be related to the presence of zircon in at least one sample. The Zandkreek samples show enriched Zr concentrations compared to Kabalebo West. The processes responsible for Zr enrichment in gabbronorite ER1109 might have caused the enrichment in the Zandkreek sample.

The Moi-Moi Metagabbro samples show a weak negative correlation in the ΣREE content (Figure 6.9), with a large variation from ≈110 ppm in LA148-40 to ≈490 ppm in metagabbronorite AT09B. Quartz-diorite LA150 contains 1050 ppm ΣREE, much more than the other samples.

Figure 6.11 shows the Cl-normalised REE diagrams of the Moi-Moi Metagabbro samples. The REE patterns are relatively steep ($(La/Lu)_N$ = 2,0 – 5,9), but clear differences are present. The ultramafic Kabalebo West samples have a flat HREE ($(Dy/Lu)_N$ = 1,2 – 1,4) but are enriched in LREE ($(La/Sm)_N$ = 1,9 – 2,0). Differences between the ultramafic samples and quartz-diorite LA150 are the much higher ΣREE content of LA150 and its positive Eu-anomaly. The Zandkreek samples and the high-Mg gabbronorites vary in $(La/Sm)_N$ from 1,3 to 1,8. Most samples are depleted in lanthanum compared to the other LREE. An exception is AT38 which is depleted

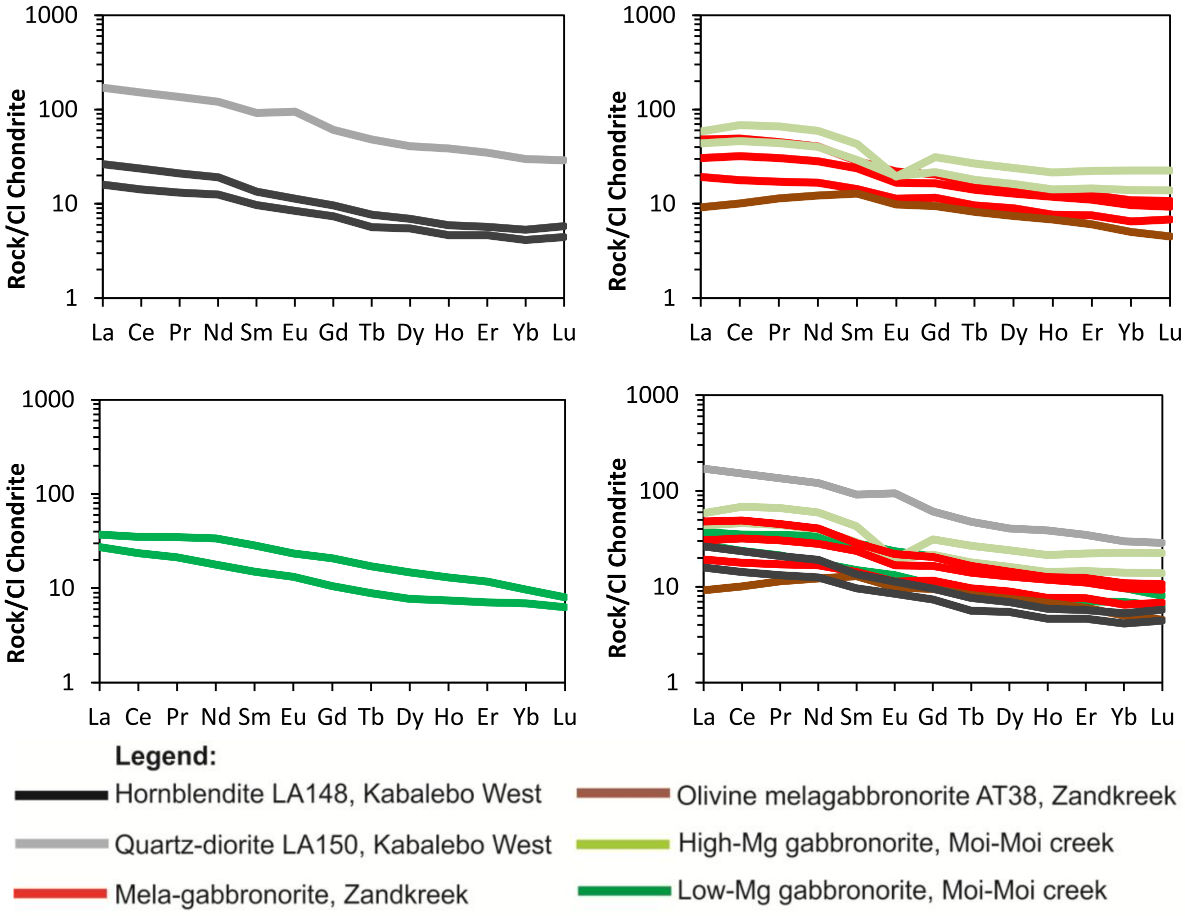

Figure 6.11: *CL-normalised REE diagrams of the Moi-Moi Metagabbro. The REE of the individual samples are measured by ICP-MS. The Cl-chondrite normalisation factors of McDonnough and Sun (1995) are used.*

in all LREE ($(La/Sm)_N$ = 0,7). These samples vary in $(Dy/Lu)_N$ from 1,1 to 1,8. All samples have a negative europium anomaly (Eu/Eu* = 0,5 – 0,9) where the highest anomalies are present in the gabbronorites. Finally, the low-magnesia Moi-Moi gabbronorites have a relatively flat LREE and HREE $(La/Sm)_N$ = 1,3 – 1,5; $(Dy/Lu)_N$ = 1,1 – 1,2).

6.3.2 Poikilitic hornblende

Petrographic evidence suggest a reaction of olivine, clinopyroxene and plagioclase grains with the surrounding hornblende (see 4.3.2) , therefore the poikilitic hornblende is expected to be formed by the reaction 'olivine + clinopyroxene + plagioclase → hornblende'. The CIPW norm of the poikilitic hornblendes (Table 6.2) resulted in a mineral assemblage from which > 75 Wt-% of the normative minerals are olivine, diopside and anorthite. Olivine, clinopyroxene and plagioclase are the cumulus phases in the Moi-Moi Metagabbro, but plagioclase can crystallise after the poikilitic hornblendes (see 4.3.2) and can be assumed as the intercumulus melt during the hornblende crystallisation in the ultramafic samples. This CIPW normative composition is in agreement with the reaction formula which is therefore expected to be realistic for the hornblende formation. Microprobe analysis of the poikilitic hornblende will be presented in the M.Sc. thesis of B. Uunk (*Uunk. 2015*).

	Ilmenite	**Orthoclase**	**Anorthite**	**Hematite**	**Diopside**	**Olivine**	**Nepheline**	**Leucite**	**Total**
Hbl	2,3	5,1	21,0	2,1	29,9	25,3	10,5	0,3	96,5

Table 6.2: *CIPW norm for the poikilitic hornblende. Norm calculated according to the methods in Winter (2001). The average hornblende composition from drill core LA148 (depth 34 – 36 m) is used for the CIPW norm calculation.*

6.3.3 Multi-element variation diagrams

Figure 6.12 show the multi-element variation diagram after *Pearce (1983).* The most outstanding features are the decoupling of the LILE from the HFSE and the presence of a small (LA150) to large (AT38) Nb-Ta trough, both characteristic for subduction zone magmas. Another prominent feature, in all samples, is the negative titanium anomaly. In addition, the samples are depleted in zirconium compared to N-MORB. In the majority of the samples the zirconium anomaly is coupled to a negative hafnium anomaly. However, quartz-diorite LA150 shows a positive Zr-Hf anomaly, which is the result of the presence of zircon in the sample. All samples are depleted in strontium compared to the other LILE. In some samples (AT36A, AT07B and ER1109) other LILE, such as potassium and rubidium, are also present in low concentrations.

6.3.4 Tectonic discrimination diagrams

All different lithologies from the Moi-Moi Metagabbro are cumulate rocks, so triangular tectonic discrimination diagrams would not be trustworthy (6.2.4). Instead, the ratio-based discrimination diagrams of *Pearce (2008, 2014)* are used for the identification of the tectonic settings of the Moi-Moi Metagabbro. In Figure 6.13A the Th/Yb ratio is plotted against the Nb/Yb ratio, which represents the presence of crustal input. Both thorium and niobium are immobile during weathering processes and are not influenced by metamorphism up to lower amphibolite facies (*Pearce, 2008*). The Moi-Moi Metagabbro underwent metamorphism under amphibolite to granulite facies (see 4.3.2), therefore the possibility of Nb or Th mobility exists and data interpretation should be done with caution.

The majority of the Moi-Moi Metagabbro samples plot in the volcanic arc array. No clear evidence of contamination by surrounding rocks was detected during field-work and the petrographical and chemical study of the samples, thus the crustal input is probably not related to crustal contamination, but rather to the recycling of a subducted slab. Figure 6.13B shows the V versus Ti discrimination diagram (*Shervais, 1982*). This diagram can only be applied on mafic samples, therefore quartz-diorite LA150 was not plotted. Sample AT07B plots in the MORB field, while all other samples plot as a trend in the IAT field. Amphibolite AT07B often deviates chemically from the metagabbroic trend, therefore a slab-proximal tectonic setting, as indicated by the IAT trend, is expected. The characteristic subduction zone signatures in the multi-element variation diagram (Figure 6.12) and the presence of large amounts of magmatic hornblende within the samples confirm the subductional setting of the Moi-Moi Metagabbro.

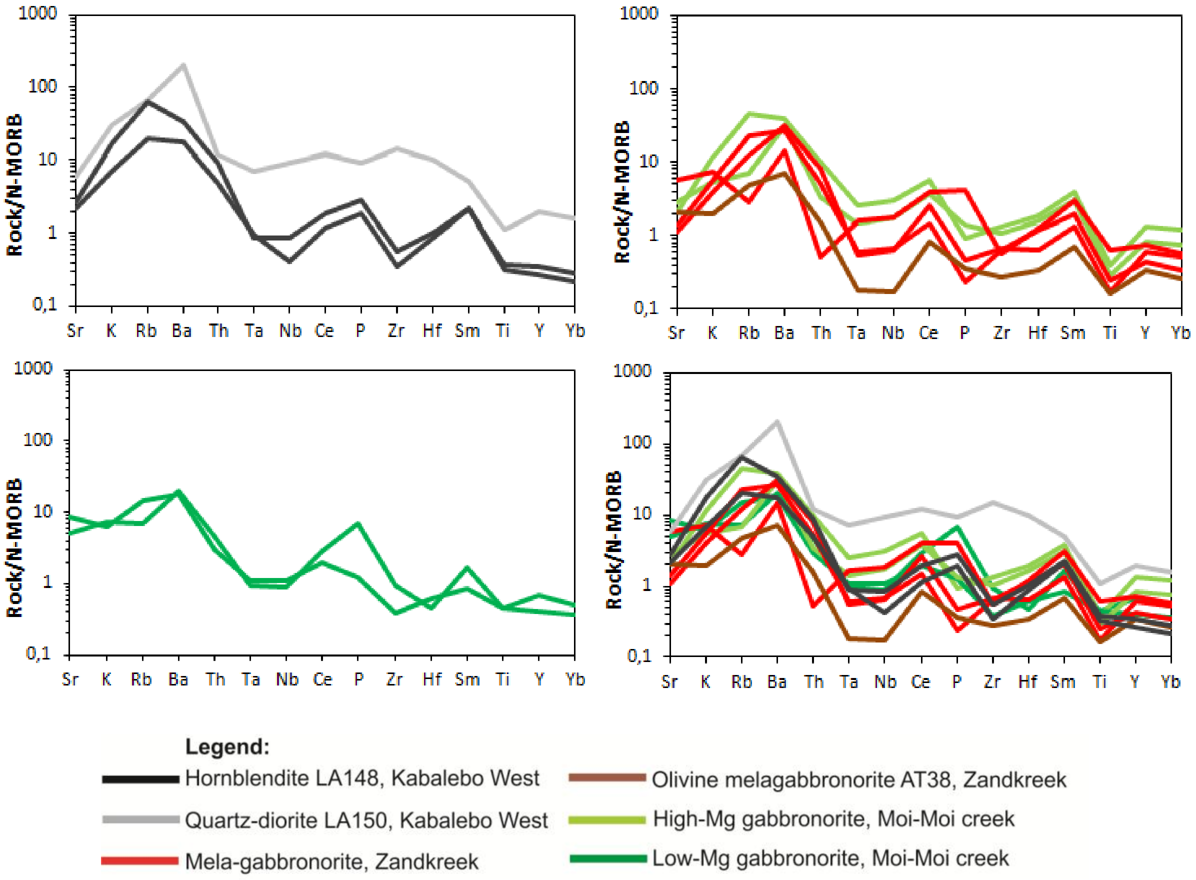

Figure 6.12; *Multi-element variation diagrams after Pearce (1983). The trace element concentrations of the individual samples are measured by ICP-MS and normalised with the N-MORB normalisation factors of Sun and McDonough (1989).*

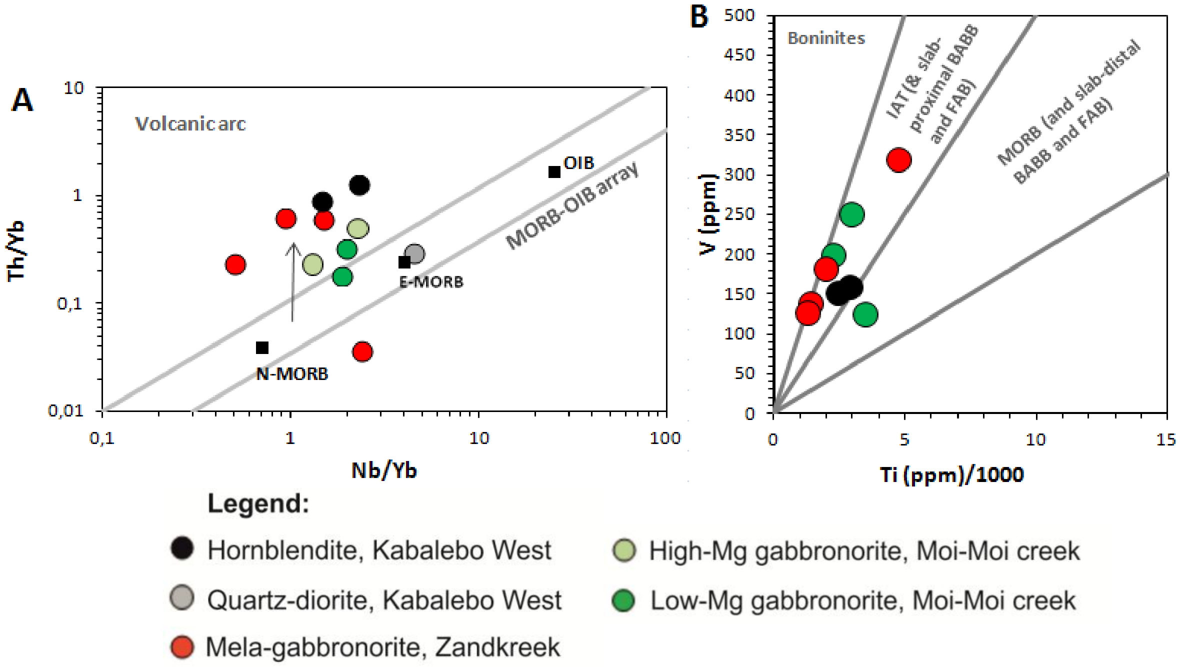

Figure 6.13; *Tectonic discrimination diagrams after Pearce (2008).Trace element concentrations are measured by ICP-MS. B: Fields after Pearce (2014).*

Petrography and geochemical data indicate a subduction related setting for the generation of the Moi-Moi Metagabbro. Arc related rocks have a rather typical compositions and can be classified with use of the AFM diagram. The Moi-Moi Metagabbro samples follow the tholeiitic arc-related trend in the AFM-diagram (Fig. 6.14) as defined by *Beard (1986)*. The majority of the olivine pyroxene hornblendites and the pyroxene hornblende mela-gabbronorites plot in the arc-related ultramafic cumulate field, while the high-Mg gabbronorites of the Moi-Moi creek, sample AT36A from the Zandkreek and LA148-58 from Kabalebo West plot in the arc related mafic cumulate field. On the other hand, the low-Mg gabbronorites of the Moi-Moi creek plot slightly above the arc-related non-cumulative gabbro and diorite field. According to their chemical composition, the samples did not accumulate plagioclase, pyroxene or olivine, making them the only non-cumulative samples from the Moi-Moi Metagabbro. Finally, quartz-diorite LA150 of Kabalebo West plots on the edge of the non-cumulative gabbro and diorite field. LA150 is largely non-cumulative, though it did accumulate minor amounts of plagioclase.

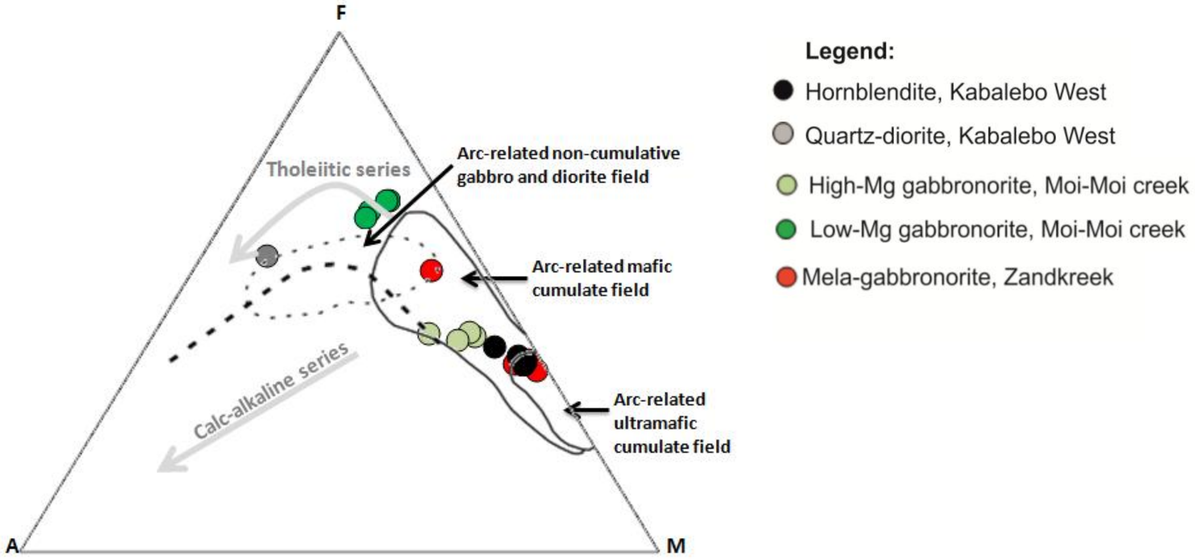

Figure 6.14; *AFM-diagram of the Moi-Moi Metagabbro, with arc-related cumulate fields after Beard (1986). The element concentrations are measured by XRF.*

6.4 Kilo Drie Metagabbro

A few samples, collected at the Kilo Drie creek, near the mouth of the Zandkreek and from an area south of the Misty Mountain, were analysed by XRF because they appear to differ in petrography from both the Charlie Gabbro and the Moi-Moi Metagabbro. A sound chemical characterisation could not be made due to the low amount of samples. However, their chemistry can be compared with that of the Charlie Gabbro and the Moi-Moi Metagabbro.

The Charlie Gabbro and the Moi-Moi Metagabbro compositions are plotted together in Figure 6.15 and 6.16. The contaminated samples (AT16B, C) have been omitted for the Charlie Gabbro. As visible from the diagrams, the Charlie Gabbro and the Moi-Moi Metagabbro compositions show considerable overlap. The most prominent difference is the wider range in element compositions in the Moi-Moi Metagabbro, which is the result of the presence of ultramafic and dioritic rocks.

The Charlie Gabbro has partially lower FeO*, TiO_2, CaO, K_2O, MnO and CaO/Al_2O_3 and partially higher Al2O3 than the Moi-Moi Metagabbro (Figure 6.15). The trace elements show even more overlap. The Kilo Drie Metagabbro samples plot in the CaO and, CaO/Al_2O_3 diagrams inside the Charlie Gabbro field but outside or nearly outside the Moi-Moi Metagabbro field (Figure 6.15 and 6.16), and exactly the opposite for K2O (and Rb). Other elements plot mostly in the Charlie Gabbro field, but sample AT29D plots outside, and in the Moi-Moi Metagabbro field. Only Sr in AT29D plots outside both compositions. It is unclear what caused this enrichment. If the Kilo Drie Metagabbro samples correspond in chemistry to the Charlie Gabbro samples, the high K and Rb concentrations might be explained in the same way as high K and Rb concentrations seen in a

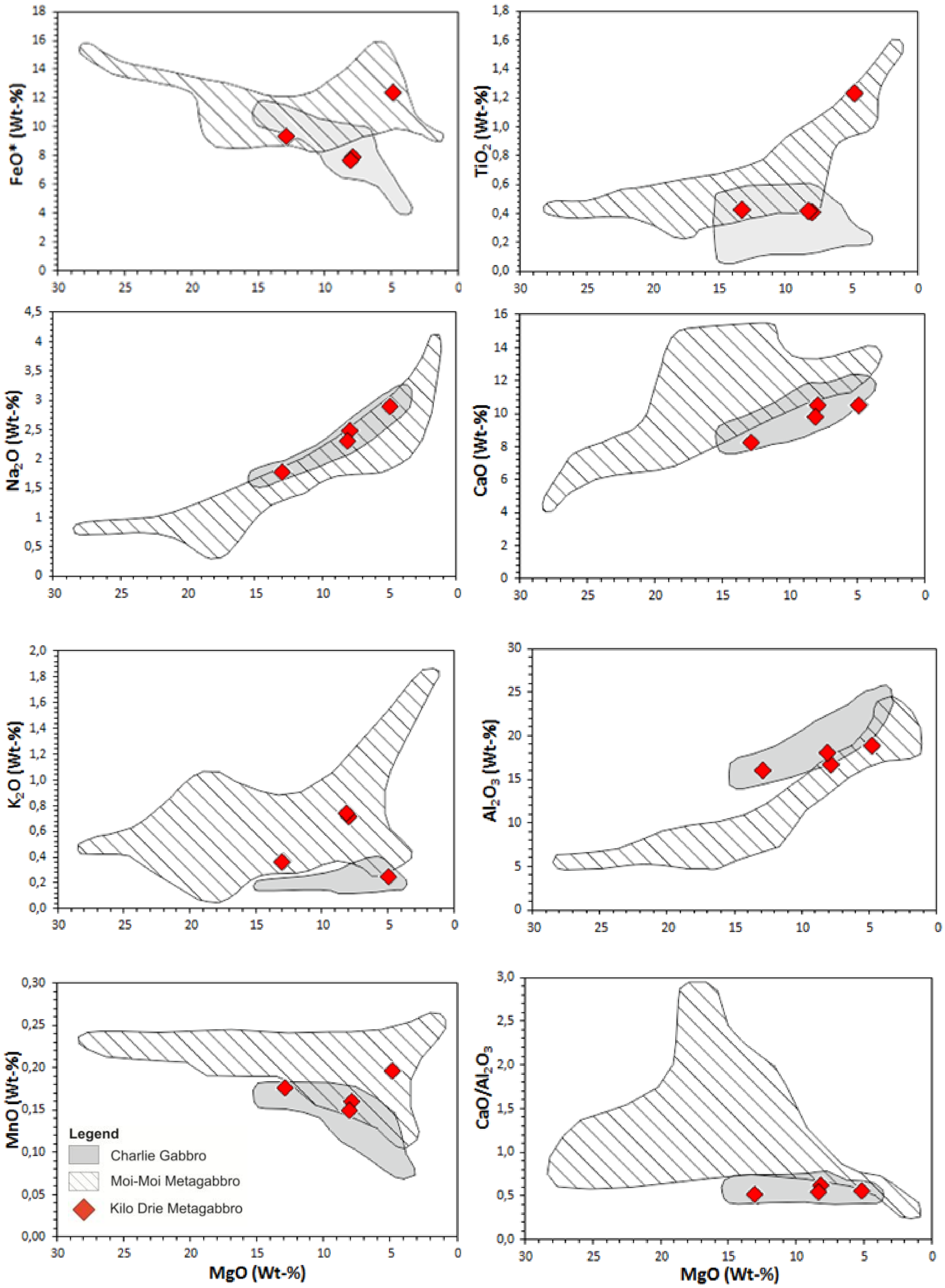

Figure 6.15: *Whole rock major element data of the Charlie Gabbro, the Moi-Moi Metagabbro and the Kilo Drie Metagabbro. All elements are measured by XRF.*

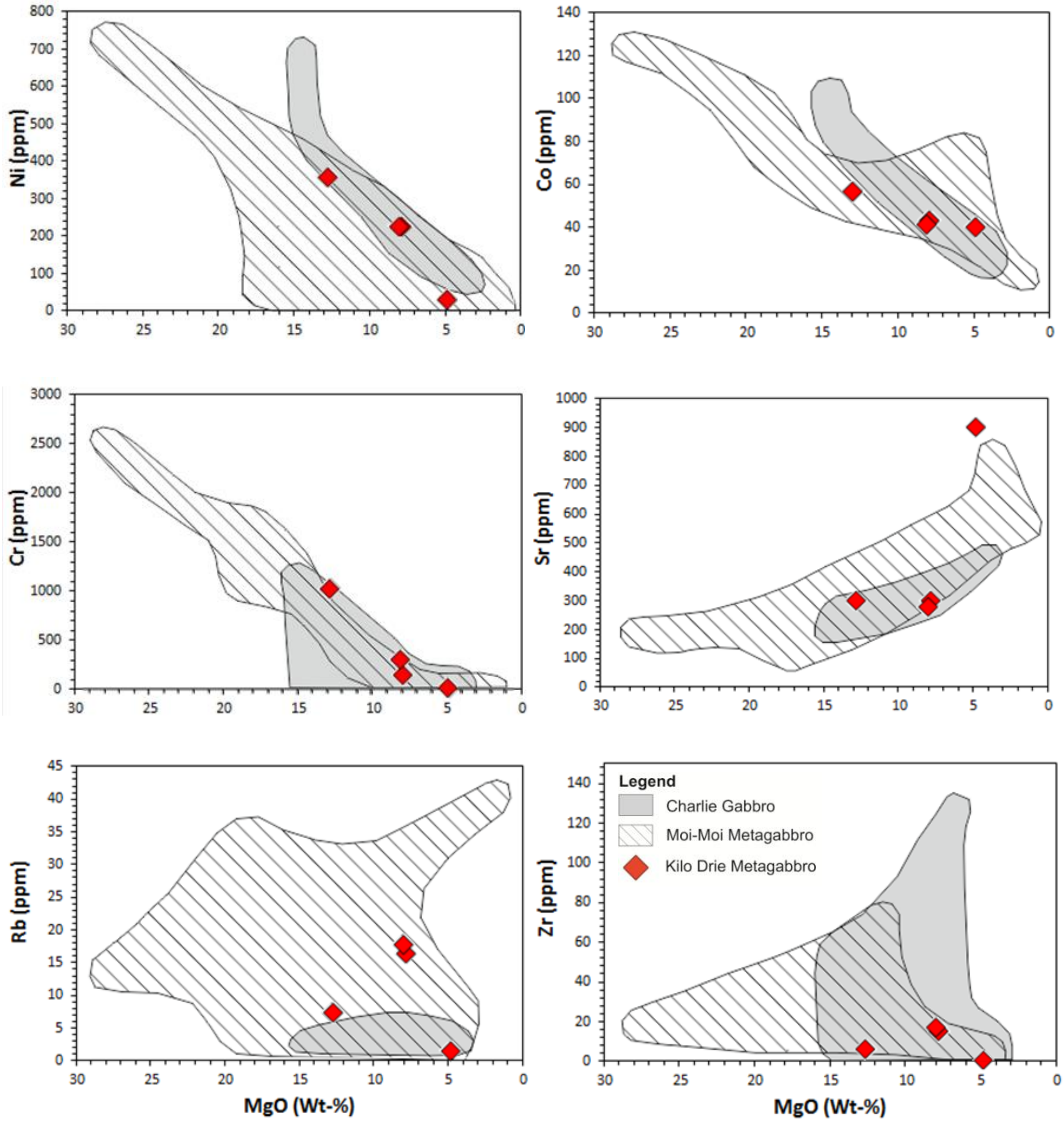

Figure 6.16: *Whole rock trace element data of the Charlie Gabbro, the Moi-Moi Metagabbro and the Kilo Drie Metagabbro. All elements are measured by XRF. Only the Zr diagram contains combined XRF and ICP-MS data for the Charlie Gabbro and the Moi-Moi Metagabbro. Quartz-diorite LA150 is excluded in this diagram due to its deviating Zr-content.*

few Charlie Gabbro samples, i.e. by contamination with adjacent charnockite. Plots of the Charlie Gabbro together with the Kilo Drie samples are given in the Appendix (see Appendix V). Summarizing, the Kilo Drie Metagabbro samples are suggested to have a similar composition as the Charlie Gabbro but were contaminated by nearby charnockite.

7. DISCUSSION

7.1 Timing of the mafic magmatism in the BGB

Fieldwork, petrographical study, chemical analysis and U-Pb dating indicate two distinctive generations of mafic intrusions in the BGB. The Moi-Moi Metagabbro bodies show a metamorphic overprint, which is absent in the Charlie Gabbro, and are, therefore, expected to be older. The dated baddeleyite grains of the Charlie Gabbro body crystallised from the gabbroic melt and represent the intrusion age of Charlie Gabbro at 1970 +/- 17 Ma.

The interpretation of the zircon data from Moi-Moi metagabbronorite ER1109 is less straightforward. The old inherited cores have an age of 2091 +/- 32 Ma, identical to the age of the UHT metamorphism in the BGB (*De Roever et al., 2003*). The main growth zones (2 – 4) are separated by resorption boundaries, suggesting that the zircons might be xenocrysts in the gabbroic melt. If xenocrystic, zones 2 and 3 represent zircon crystallisation in the host rock, zone 4 is the main overgrowth zone and would represent crystallisation in the gabbroic melt. In this case the age of 1984 +/- 4 Ma, the average age of zones 2 – 4, should be interpreted as maximum age of the Moi-Moi Metagabbro. The Moi-Moi Metagabbro is older than the Charlie Gabbro, which restrict the emplacement of the metagabbro to a time interval of 1984 – 1970 (+/- 17) Ma. An alternative hypothesis is that zones 2 – 4 all crystallised in the Moi-Moi gabbroic melt, indicating the age of intrusion. Complex internal resorption patterns do not always indicate a polyphase evolution (*Hoskin and Schaltegger, 2003*).

The younger outer rim is interpreted as subsolidus zircon growth. The rim was dated at 1950 +/- 13 Ma, younger than the Charlie Gabbro. The Charlie Gabbro lacks a metamorphic overprint, therefore the event that caused the subsolidus zircon growth, and probably caused the metamorphism in the Moi-Moi Metagabbro and the Kilo Drie Metagabbro, cannot be younger than 1970 +/- 17 Ma.

The petrography, geochemistry and field relations of the quartz-diorite (LA150) show that it is part of the Moi-Moi Metagabbro. The morphology and internal structure of the zircons indicate that they crystallised from the quartz-diorite magma and thus their age represents the age of intrusion of the Moi-Moi Metagabbro. The zircons are dated at 1984 +/- 5 Ma, identical to the age of the zircon main growth zones from ER1109, confirming an intrusion age of 1984 +/- 5 Ma for the Moi-Moi Metagabbro.

7.2 Source rock of the xenocrystic zircons

The presence of old inherited cores in the zircons of ER1109 indicates that they represent xenocrysts in the metagabbronorite. The main growth phases of the zircons comprise sector and oscillatory zoning, indicative for magmatic zircons (*Hoskin and Schaltegger, 2003*). Therefore the zircons should have been taken up from country rock with an igneous origin. The age of the main growth phases corresponds to the range of zircon ages from the surrounding charnockites (1984,4 – 1992,5 Ma, *Klaver et al., 2015a*). Old inherited cores were not found in the charnockite zircons (*Klaver, 2011*), but this could be caused by the zircon sampling criteria for the charnockites. *Klaver (2011)* only sampled euhedral zircons < 180 µm while old inherited cores were found in anhedral zircons with a size > 400 µm.

The trace element compositions of charnockite and metagabbronorite zircons were compared in order to determine if the latter correspond with the charnockite zircon compositions. The main group of the gabbronorite zircons have U, Th and Nb concentrations that overlap with those of the charnockite zircons (Figure 5.6), but they contain lower ΣREE values. The BSE and Cl-bright group is enriched in U, Th and Nb compared to the charnockite zircons, but have a similar ΣREE content. Additionally, the analysed metagabbronorite zircons have a Ce-anomaly similar to the charnockite zircons, while their Eu-anomaly is smaller. Other differences are present in the REE patterns. The metagabbronorite zircons show a shallower LREE slope than the charnockite zircons, but their HREE slope is steeper (see Figure 5.6). This indicates that the zircons from the metagabbronorite crystallised from a more ΣREE poor melt that had a shallower LREE and a steeper HREE slope.

Klaver et al. (2015b) compared the Hf isotopic composition of both zircon types and concluded that the initial ε_{Hf} at 1984 Ma of the main zircon growth domains (2-4) was identical to the $\varepsilon_{Hf(i)}$ of the Kabalebo charnockites, but different from the $\varepsilon_{Hf(i)}$ of metagabbronorite ER1109. This indicates that the zircons are not in equilibrium with the metagabbroic melt and must have been taken up from country rock, most likely the charnockites. *Klaver et al. (2015b)* argues that the difference in REE content between the charnockite and metagabbronorite zircons is caused by the entrainment of the charnockite zircons into the Zr undersaturated metagabbroic melt, which led to changes in the distribution of elements that are less compatible within the zircon structure compared to the elements that are more compatible.

The inheritance of the metagabbronorite zircons from the charnockites indicates assimilation of charnockite by the (meta-)gabbroic magma. This would mean that the metagabbroic magma post-dated the charnockite magmatism, which is in agreement with the age range of the charnockite magmatism, but not with the field observations. At the contact of charnockite and metagabbronorite at the Moi-Moi waterfall, the metagabbronorites are coarse grained and chilled margins were not found (Klaver, 2011). Additionally, cm-wide charnockite veins intrude the metagabbronorite, suggesting that the charnockite magmatism is younger than the metagabbroic magmatism.

The lower age limit of the charnockite magmatism is identical to the age of metagabbronorite emplacement. In addition, the lack of significant age differences between zones 2 – 4 of the zircons indicate crystallisation at a similar age. Metadolerite enclaves are common within the charnockites (*Klaver et al., 2015a*). They are petrographically and chemically identical to the metagabbronorite and are expected to be the result of mingling between the immiscible metagabbroic and charnockitic melts (*Klaver et al., 2015a*). This process is expected to be responsible for the zircon crystal transfer from the charnockites towards the metagabbronorite.

7.3 The Charlie Gabbro

7.3.1 Parental magma composition

The parental magma composition of intrusive rocks is often determined by analysis of chilled margins. Chilled margins are fine grained or glassy zones at the edge of an intrusive body, which cooled rapidly due to the temperature difference between the hot intruding magma and the cold surrounding rocks. The fast cooling solidifies the magma before fractionation processes take place, maintaining the original composition of the intruding magma. At one location a finer-grained chilled margin (AT16B) was found in the Charlie Gabbro at the contact with charnockite. However, the composition of this sample appears to be contaminated by reaction with the adjacent charnockite, so the parental magma composition must be reconstructed based on the composition of the available samples.

The Charlie Gabbro samples accumulated a certain amount of olivine or plagioclase, samples that reflect the parental magma composition were not found. The parental magma composition of cumulates can be reconstructed by using partition coefficients to calculate the liquid which was in equilibrium with the cumulus minerals. This requires chemical analysis of the cumulus minerals. Mineral analysis was not planned for this investigation, so the parental magma composition should be calculated from the whole rock chemistry of the cumulates. Mass balance calculations will not work since the trends in the Charlie Gabbro do not represent the liquid lines of descent of the original magma. However, some estimations of the composition of the parental magma could be made based on the whole rock composition of the Charlie Gabbro samples.

Firstly, plagioclase accumulation occurred throughout the Charlie Gabbro and is best represented by the Eu-anomaly. The Eu-anomaly is absent in samples AT01 and AT30, which indicates that these samples have not accumulated plagioclase. It can be expected that, based only on the absence of plagioclase accumulation, their composition is rather close to the parental magma composition. Secondly, in olivine cumulates the amount of accumulated olivine increases with increasing MgO. This means that the composition of olivine cumulates with the lowest MgO-content, such as AT18 and AT30, are rather close to the original magma composition. Combined with the lack of an Eu-anomaly, sample AT30 is identified as the sample with a composition similar to the parental magma composition. According to the CIPW norm, it accumulated ≈ 10 Wt-% olivine, so the parental magma composition is expected to be slightly depleted in MgO compared to this sample.

Both the olivine and plagioclase cumulate trends appear to evolve from a point with a MgO-content of ≈ 8 Wt-% towards higher resp. lower MgO. This point is expected to represent the parental magma composition. The concentrations of the other elements can be found from the variation diagrams if clear trends are present. The resulting parental magma composition (Table 7.1) is in agreement with the composition of sample AT30 and, therefore, is expected to be realistic.

The estimated parental magma composition of the Charlie Gabbro is compared with the average magma composition of Mid-Ocean Ridge Basalt (MORB), Island Arc Basalt (IAB), High Alumina Basalt (HAB) and Ocean Island Basalt (OIB) (Table 7.1). The Charlie Gabbro parental magma composition is slightly depleted in SiO_2, FeO* and CaO, but strongly enriched in Al_2O_3 compared to the average MORB. Compared to the average IAB, the parental magma is slightly depleted in SiO_2 and FeO*, slightly enriched in MgO and strongly enriched in Al_2O_3. A strong enrichment in Al_2O_3 and a depletion of FeO* and MgO characterizes the compositional differences with the average OIB. These deviations suggest a parental magma composition which is different from MORB, IAB and OIB. The high Al_2O_3 content is typical for High Alumina Basalt (HAB) magmas. Additionally, the parental magma composition fits well with the range of typical HAB magmas, therefore it is concluded that the parental magma composition of the Charlie Gabbro was similar to a tholeiitic HAB magma.

	Charlie Gabbro	AT30	Avg. MORB	Avg. IAB	HAB	Avg. OIB	Moi-Moi Metagabbro	AT13B
SiO_2 (Wt-%)	49.0	48.9	50.47	51.56	48.0 - 53.0	49.2	-	43.6
Al_2O_3	20.0	18.6	14.7	17.51	17.0 - 22.0	12.8	16	17.1
FeO*	8.0	8.6	10.43	9.25	7.0 - 11.0	11.45	8	15.4
MgO	8.0	8.4	7.58	6.19	4.0 - 9.0	10.0	6.0 - 7.0	6
CaO	9.2 - 11.2	10.6	11.39	10.35	8.5 - 12.0	10.8	11	11.2
Na_2O	2.3	2.3	2.79	2.65	1.5 - 3.5	2.12	1.9	1.9
TiO_2	-	0.5	1.68	0.89	0.5 - 1.5	2.57	0.9	1
MnO	≈ 0.1	0.1	0.18	0.17	-	0.17	≈ 0.1	0.2

Table 7.1: *Whole rock compositions of the Charlie Gabbro, the Moi-Moi Metagabbro, Mid Ocean Ridge Basalt, Island Arc Basalt, Ocean Island Basalt and High Alumina Basalt. The composition of MORB after Gale et al. (2013). The average IAB composition is taken from Perfit et al. (1980).The average OIB composition is taken from Murata and Richter (1966). The HAB composition is taken from data and graphs in Draper and Johnston (1992).*

7.3.2 The Charlie Gabbro: part of a Large Igneous Province?

HAB magmas are largely restricted to subduction zones, but their origin is controversial *(Winter, 2001)*. There are two main mechanisms for the generation of HAB magmas. The first, generally accepted, mechanism suggests that HAB magmas are derivative magmas, created by the extensive fractionation and/or accumulation of olivine, clinopyroxene, chrome-spinel and plagioclase from a mantle derived primary magma *(Brophy, 1986; Crawford et al., 1987; Draper & Johnston, 1992; Johnston, 1986)*. The second mechanism suggests that HAB magmas are primary magmas, generated by partial melting of subducted oceanic crust (*Brophy and Marsh, 1986; Draper & Johnston, 1992).*

The multi-element variation diagrams and the tectonic discrimination diagrams of the Charlie Gabbro are consistent with a subduction related source. The main subduction event in the Guiana Shield was during the Trans-Amazonian orogeny. In the first part of this period a NS oriented convergence, with southward subduction, of the Amazonian and the West African Cratons took place, which culminated in UHT metamorphism in the BGB (2,07 – 2,05 Ga; *Delor et al., 2003a*). *Fraga et al., (2009b)* and *Klaver et al. (2015a)* suggest that collisional processes continued in a later stage of the Trans-Amazonian orogeny, but now with northward subduction, which is represented by a large belt of felsic volcanism (UTS in Figure 2.3). The 1,99 –

1,98 Ga charnockitic magmatism in the BGB, which is generated during a second UHT-like event, is spatially and temporally associated with this felsic volcanism (*Klaver et al., 2015a*).

The Charlie Gabbro is approximately 15 Ma younger than the Moi-Moi Metagabbro. The generation of the Charlie Gabbro might be explained if subduction continued until approx. 1970 Ma. However, no clear evidence of subduction younger than approx. 1,98 Ga has yet been found. The question is whether the characteristic subduction signature of the Charlie gabbro samples is directly related to contemporaneous subduction.

Melting of the subducting oceanic slab often generates a hydrous melt, often resulting in the presence of hydrous mineral phases, such as hornblende and mica. The Charlie Gabbro lack significant amounts of hydrous minerals. Biotite is present in most samples in small amount and it is often questionable if the biotite is a primary or a secondary mineral (see 4.2.2). The subduction signature of the Charlie Gabbro may be inherited from a mantle source modified by earlier subduction during the Trans-Amazonian orogeny. After the end of subduction, the underlying mantle needs a long time to re-equilibrate to its new tectonical setting and will still have the characteristic subduction trace element patterns. The Avanavero dolerite forms large dikes and sills in W Suriname (including the BGB), Guyana and NW Brazil. They have been dated at 1,79 - 1,78 Ga *(Reis et al., 2013*), indicating that they intruded in the Guiana shield long after the extinction of the subduction zone. However, they still show the characteristic subductional signature (*Elliot, 1993; Reis et al., 2013*), suggesting that even after 190 Ma the trace element concentrations in the mantle were not re-equilibrated to its new tectonical setting. Therefore, the subduction signature of the Charlie Gabbro, even if emplaced only 10 to 15 Ma after the subduction related Moi-Moi Metagabbro (see 7.4.3), does not need to be explained by active subduction. Instead, the lithospheric mantle below the BGB could already be modified by the earlier subduction event.

So far, the Charlie Gabbro has only been recognized at a few locations in the BGB, but not in the surrounding terrains in W Suriname. Recently, three dyke swarms in central Venezuela have been dated by the LIP commission (pers. comm; confidential, unpublished LIP commission report.). The Guaniamo, Rio Aro and Monteco-Supamo dyke swarms were dated at 1975 +/- 4 Ma, 1981 +/- 2 Ma and 1988 +/- 2 Ma, ages which are mostly within the age error of the Charlie Gabbro and indicate a widespread distribution of mafic dyke formation at 1.97 – 1,99 Ga. The authors consider the dyke swarms as a Large Igneous Province (LIP) because the swarms lie more than 200 km apart (Fig. 7.1). LIPs are short-lived voluminous magmatic events which originate via processes other than ‘normal’ seafloor spreading or ‘normal’ subductional processes *(Bryan et al., 2002; Coffin and Eldholm, 1994)*. They also mention a potential extension of the LIP to the Charlie Gabbro bodies in W Suriname. The Venezolan dykes are tholeiitic, but chemical data have not yet been provided. Several models are proposed for LIP magmatism *(e.g. Ernst et al., 2005 and references therein; Saunders, 2005; Saunders et al., 2007)*, such as slab detachment (*Dilek and Altunkaynal, 2009; Şengör et al., 2003; Van de Zedde and Wortel, 2001; Von Blanckenburg and Davies, 1995)*, lithospheric thinning by continental lithosphere delamination (*Dilek and Altunkaynal, 2009; Elkins-Tanton, 2005; Elkins-Tanton and Hager, 2000; Lustrino, 2005;)* and the mantle plume hypothesis (*Campbell and Griffiths, 1990; Richards et al., 1989; White and McKenzie, 1989*).

A northward subduction underneath the North Guiana TTG-greenstone belt has been postulated during the emplacement of the Moi-Moi Metagabbro (see 7.4.3), but subduction might have ended before the intrusion of the Charlie Gabbro. A logical explanation might be detachment of the subducted slab, which resulted in asthenospheric mantle upwelling and partial melting at shallow depth in the overriding plate, producing the tholeiitic magma of the Charlie Gabbro. Chemical data suggest that the Charlie Gabbro source is a subduction metasomatised lithospheric mantle. The absence of an OIB signature (see 6.2.3) and the major element composition of the Charlie Gabbro parental magma (see 7.3.1) does not suggest an asthenospheric input, therefore, slab detachment is not expected to have generated the Charlie Gabbro magmatism.

Delamination of the continental lithosphere can produce shallow, anhydrous melting under cratonic lithospheres (*Elkins-Tanton, 2005*). After slab detachment, the orogenic lithosphere becomes gravitationally unstable which can result in delamination and detachment of the lithospheric mantle (*Elkins-Tanton, 2005; Lustrino, 2005*). As a result, an upward migration of hot, buoyant asthenosphere takes place, resulting in dry adiabatic melting of the asthenosphere and basaltic magmatism at the surface (*Elkins-Tanton, 2005; Lustrino,* *2005*). However, the source rock for the Charlie Gabbro magmatism is the metasomatised lithospheric mantle, therefore magmatism as a result of delamination is not expected for the Charlie Gabbro.

In the mantle plume hypothesis lateral buoyancy variations in the deep mantle, which are expected to result from an unstable (thermal) boundary in the deep Earth, cause asthenospheric upwelling towards the base of the plates. Decompression and extensive melting occur during upwelling, resulting in the formation of large volumes of magma. There are two end-member models within the mantle plume hypothesis. The first model is the plume head model (*Campbell and Griffiths, 1990; Richards et al., 1989*) which suggests LIP formation due to a starting mantle plume. This starting plume rises to the base of the lithosphere where melting of the plume head occurs due to adiabatic decompression (*Campbell and Griffiths, 1990)*, resulting in igneous activity along the area of the plume head. The second model was proposed by *White and McKenzie (1989).* In this model, the mantle plume forms an anomaly of hot mantle beneath the continental lithosphere. The continental lithosphere rifts along the thermal anomaly, resulting in passively upwelling and partial melting of the asthenosphere. The generated melts get accreted to the crust and partly penetrate the surface, resulting in voluminous basaltic flows. This magmatism is mostly followed by continental rifting with continental break-up as a result.

The orientation of the Guaniamo, Rio Aro and the Monteco-Supamo dyke swarms in Central Venezuela suggests a fanning pattern (confidential report LIP commission). Such radiating dyke swarm patterns are a geometrical indicator of the location of the mantle plume head that impinged the lithosphere (*Ernst and Buchan, 1997*). Extrapolation of the dominant trends would define a common intersection in the northern part of the Roraima state of Brazil (Figure 7.1). This Yanomami plume-head is in close temporal and spatial association with the BGB (confidential report LIP commission) and might be responsible for the intrusion of the Charlie Gabbro. However, mantle plume magmatism has an OIB signature. The Charlie Gabbro lacks this signature (see 6.2.3) and its parental magma composition deviates from the average OIB (see 7.3.1). Therefore, it is not expected that the Charlie Gabbro was generated by a mantle plume.

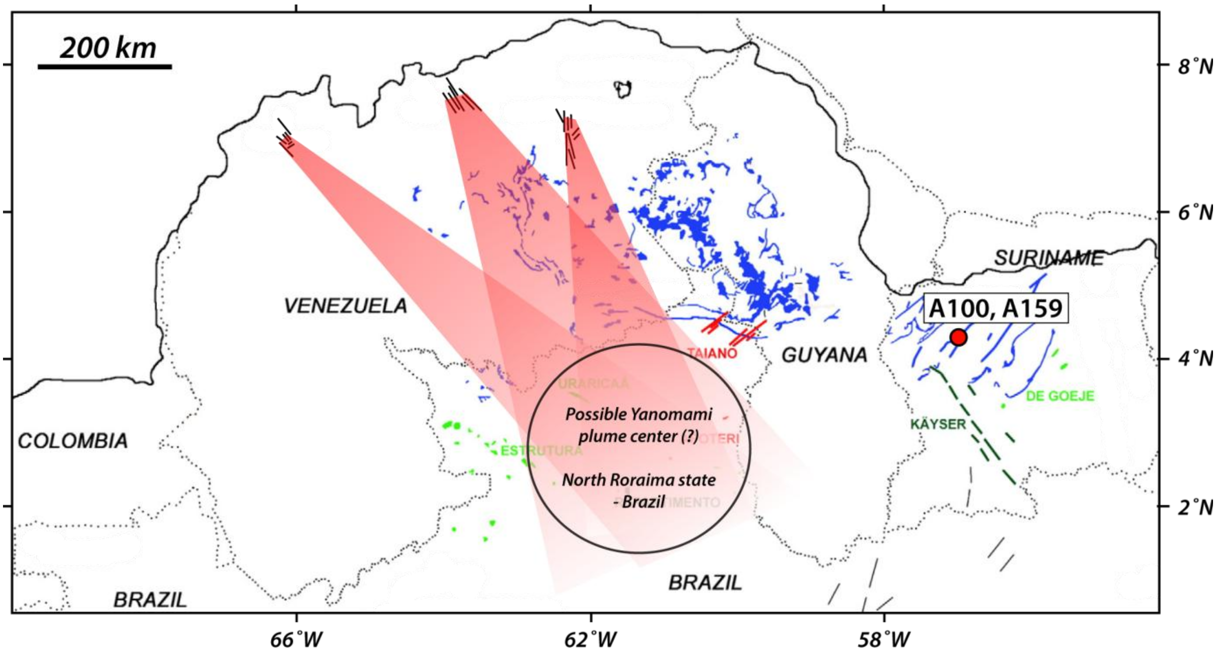

Figure 7.1: *The location and orientation of the Guaniamo, Rio Aro and the Monteco-Supamo dyke swarms in Central Venezuela and the expected location of the mantle plume. The mantle plume is named after the Yanomami reservation in the Brazilian Amazon jungle, which is located west of the plume. The red dot (A100, A159) represent the locations of sample ER1115 (Charlie Gabbro) and ER1109 (Moi-Moi Metagabbro). Figure provided by the LIPs commission.*

These models show that the Charlie Gabbro was not generated by post-subductional processes which leaves the possibility of magma generation due to subduction. Hydrous minerals, characteristic for subduction related rocks, are formed from magmas that contain a high amount of water. The Charlie Gabbro is a HAB magma. These magmas can form from arc magmas that contain a low amount of water *(Crawford, 1987; Johnston, 1986)* resulting in a hydrous magma that lack hydrous minerals after crystalisation. This suggests that the Charlie Gabbro could be related to the subduction zone described by *Fraga et al., (2009b)* and *Klaver et al. (2015a)* even though no other supportive evidence for simultaneous subduction is found. The Charlie Gabbro is expected to mark the end of the Trans-Amazonian orogeny (see 7.7) and is therefore expected to be related to the waning stage of subduction. This would imply that the northward subduction continued until and extinguished around 1970 +/- 17 Ma.

7.4 The Moi-Moi Metagabbro

7.4.1 Parental magma composition

Chilled margins that represent the parental magma composition were not detected during the field trip, so the parental magma composition of the Moi-Moi Metagabbro must be reconstructed based on the composition of the samples. The parental magma composition of cumulate rocks can be calculated if the mineral trace element geochemistry is known. Only the whole rock geochemistry and some major element mineral analyses are present for the Moi-Moi Metagabbro samples. The lack of single mineral trace element analyses prevents reconstruction of the magma composition in equilibrium with the cumulus minerals. The whole rock composition cannot be used for the parental magma calculation because the majority of the trends do not represent the liquid lines of descent of the original magma. However, it is possible to make some estimations about the parental magma from the available data.

Most Moi-Moi Metagabbro samples are cumulate rocks. Only the low-Mg gabbronorites from the Moi-Moi creek lack any visible sign of crystal accumulation. This group shows a trend which is expected to represent the magma evolution. The two samples with the lowest MgO content are expected to be the most evolved. The parental magma composition is expected to lie close to the high-Mg end of this group, which suggests that samples AT10B and AT13B are rather close to the parental magma composition.

The Moi-Moi Metagabbro contains three different trends in the variation diagrams (see 6.3.1) which cross each other at a point between 5 and 8 Wt-% MgO. This point coincides with the transition between the cumulate and non-cumulate rocks in the major and trace element variation diagrams and is expected to represent the parental magma composition from which the three trends evolved. The MgO content of the parental magma composition differs for each diagram, but is mainly at a MgO content of 6 – 7 Wt-%. This concentration is used as average for the parental magma composition. The concentrations of other elements can be determined from the variation diagrams if a clear trend is present. The resulting magma composition (Table 7.1) resembles that of sample AT13B and is, therefore, expected to be realistic. Only the FeO* content deviates with ≈ 7 Wt-% from AT13B, which is expected to be the result of FeO* enrichment in the low-Mg metagabbronorites.

The parental magma composition is slightly enriched in Al_2O_3 and slightly depleted in FeO* compared to MORB but only slightly depleted in Al_2O_3 compared to IAB, therefore, an IAB-like parental magma composition is expected. This composition is confirmed by the V versus Ti discrimination diagram, which indicated an IAT magma composition. Therefore it is likely that the Moi-Moi Metagabbro was similar to a tholeiitic, hydrous magma generated in a volcanic arc.

7.4.2 Poikilitic hornblende

The petrography of the samples and the chemistry of the analysed hornblendes suggest a reaction between olivine, clinopyroxene and plagioclase for the formation of the primary hornblendes. This reaction formula is confirmed in the experiments of *Cawthorne (1976)*, who showed that in the system CaO-MgO-Al_2O_3-SiO_2-Na_2O-H_2O at 5 kbar and 960 ^{o}C there is an invariant point at which Mg-olivine, orthopyroxene, clinopyroxene, amphibole, plagioclase, liquid and vapour can coexist. Below that temperature, amphibole can be formed by reaction of the liquid with olivine, clinopyroxene and plagioclase.

7.4.3 The Moi-Moi Metagabbro: an Alaskan-type complex

The Moi-Moi Metagabbro intrusions form small, round or oval shaped bodies which are concentrated in the southwest of the BGB. Most bodies show gradual vertical or concentric zoning that varies from an ultramafic centre towards a gabbroic edge. Cumulate rocks are common and the presence of large poikilitic hornblende is a characteristic feature. The geochemistry and mineralogy of these bodies are analogous to Alaskan-type complexes (*Beard, 1986; Farahat and Helmy, 2006; Himmelberg and Loney, 1995; Nixon et al., 1989*). Alaskan-type complexes are now commonly considered as the roots of volcanic arc complexes (*Batanova et al., 2005*; *Brügmann et al., 1997; Jagoutz and Schmidt, 2013*). This tectonic setting is in agreement with the Late Trans-Amazonian setting proposed by *Fraga et al. (2009b)* and *Klaver et al. (2015a)*.

However, some features do not match the characteristics of Alaskan-type complexes. Firstly, the ultramafic cumulates of Kabalebo West contain orthopyroxene as a major cumulus phase. In classical Alaskan-type complexes the presence of orthopyroxene in ultramafic cumulates is extremely rare, but not impossible *(Himmelberg and Loney, 1995),* and if present, orthopyroxene is mainly an interstitial mineral (e.g. Kane Peak Complex, Alaska. *Himmelberg and Loney, 1995*). However, older Proterozoic Alaskan-type complexes, in eastern/southeastern Egypt *(El-Rahman et al., 2012; Helmy and Mahallawi, 2003; Helmy et al., 2014)* and northeastern Turkey *(Eyuboglu et al., 2010)* do contain orthopyroxene as cumulus phase in their ultramafic cumulates. The early appearance of orthopyroxene could be attributed to crustal contamination (*Campbell, 1985*), which increases the SiO_2 content of the magma and facilitates orthopyroxene crystallisation. The presence of charnockitic zircons in metagabbronorite ER1109 and of metadolerite enclaves in the charnockite suggest magma mingling of Moi-Moi Metagabbro and Kabalebo charnockites. This magma mingling is confirmed by Isotope Dilution studies of the Moi-Moi Metagabbro (*Uunk, 2015*).

Secondly, LREE enrichment is expected for subduction related magmatism (*Pearce, 1982*) and most Alaskan-type complexes show these LREE enriched patterns. The Moi-Moi Metagabbro samples have a flat to slightly depleted LREE slope, which is especially visible in the pyroxene cumulates of the Zandkreek. Similar LREE depletions are seen in the clinopyroxenites of Alaskan-type complex of Blashka Island in Alaska (*Himmelberg and Loney, 1995*) and the Abu Hamamid intrusion, Egypt (*Helmy et al., 2015*). The flat to depleted LREE slopes might be related to the high pyroxene content in the samples.

Several authors (e.g. *Mues-Schumacher et al., 1996; Tistl et al., 1994*) argue that the generation of tholeiitic magma in Alaskan-type complexes requires melting at anomalously high mantle temperatures. *Tistl et al. (1994)* argue that these high temperatures are likely to occur if the arc-related convergent system changes to a system with local tectonic extension. This environment can be created by slab roll-back which causes passive mantle upwelling, resulting in an anomalously high mantle temperature and partial melting of the upper mantle under influence of the subducted slab. A second possibility could be delamination and detachment of the subducted slab. However, subduction probably continues until the intrusion of the Charlie Gabbro at 1970 +/- 17 Ma (see 7.3.2), therefore, delamination and detachment of the subducted slab is not expected.

Based on the petrological and geochemical characteristics, the Moi-Moi Metagabbro can be interpreted as subduction related magmatism. If it intruded during normal subduction, magmatism might occur over several millions of years. Until now, two age determinations from Moi-Moi Metagabbro bodies in the BGB gave only a restricted intrusion age of 1984 +/- 5 Ma. Zircon Pb-Pb evaporation dating of a similar metagabbro body in the Coeroeni Gneiss in SW Suriname gave an age of 1985 +/- 2 Ma (*Kroonenberg et al., in press*), so the possibility exists that the Moi-Moi Metagabbro is intruded within a short period. Dating of other Moi-Moi Metagabbroic bodies is required to confirm this.

7.4.4 Heat source of Kabalebo charnockite magmatism

An external heat source was suggested by *Klaver et al. (2015a)* for both the UHT metamorphism at 2,07-2,05 Ga (*De Roever et al., 2003*) and the Kabalebo charnockite magmatism at 1,98 Ga (*Klaver, 2011; Klaver et al., 2015a)*. UHT metamorphism is considerably older than the Moi-Moi Metagabbro magmatism, therefore, the intrusion of the Moi-Moi Metagabbro can be excluded as the heat source for UHT metamorphism. The Moi-Moi Metagabbro is contemporaneous with the charnockite magmatism (see 7.1) and is expected to be the external heat source. Charnockite crystallisation exceeded 950 ^{o}C, therefore UHT-like temperatures are needed to melt the UHT granulites to generate the charnockite magmatism (*Klaver et al., 2015a*). UHT conditions cannot be reached during normal subduction or syncollisional processes (*Santosh et al., 2008*). If the Moi-Moi Metagabbro was generated during normal subduction, the extreme heat is expected to have been generated by underplating of the gabbroic magma. The underplated magma was hotter than the lower crust, resulting in partial melting of the UHT granulites. The lower crust might still retain some heat from the earlier 2,07 – 2,05 Ga UHT event, making it easier to reach UHT conditions.

7.5 Kilo Drie Metagabbro

Kilo Drie Metagabbro has a metamorphic overprint, which is absent in the Charlie Gabbro, but lacks the large poikilitic hornblende characteristic for the Moi-Moi Metagabbro. This suggests the presence of a third generation of gabbroic intrusions. The Kilo Drie Metagabbro shows metamorphism in the high amphibolite facies to possibly granulite facies, indicating that it intruded before the Charlie Gabbro but lacks the foliation of the UHT mafic granulites formed at 2,07 – 2,05 Ga (*De Roever et al., 2003*), restricting the emplacement of the metagabbro to an age interval of approx. 2,05 – 1,97 Ga.

The absence of poikilitic hornblende indicates magma similar to the Charlie Gabbro which also lacks hydrous primary minerals. Additionally, the chemistry of the Kilo Drie Metagabbro appears to be similar to the Charlie Gabbro and the high Al_2O_3 content (17 – 19 Wt-%) of the samples points towards a HAB magma. Therefore, the Kilo Drie Metagabbro might represent an earlier pulse of Charlie Gabbro-like magmatism. However, the Kilo Drie Metagabbro might perhaps also have formed before the Moi-Moi Metagabbro. Clearly more research is required regarding the age and geochemistry of this metagabbro type.

7.6 Metamorphism in the BGB

The Moi-Moi Metagabbro and the Kilo Drie Metagabbro show evidence of metamorphism in the high amphibolite facies to possibly granulite facies (see 4.3.2 and 4.4.2). Metamorphism must have taken place after emplacement of the bodies at 1984 +/- 5 Ma. Another mafic intrusion in the BGB is the Mozeskreek Anorthosite body, described by *De Roever et al. (2003)*. This body shows granoblastic recrystallisation of the plagioclase and intensive replacement of clinopyroxene by hornblende (*Uunk, 2015*), also suggesting metamorphism in the amphibolite facies. Zircon Pb-Pb evaporation dating of this body resulted in an age of 1980 +/- 5 Ma (*De Roever et al., 2003*), therefore, the metamorphic event is expected to have taken place after 1980 +/- 5 Ma. These ages point to intermediate to high grade metamorphism shortly after the charnockite magmatism (*Klaver, 2011; Klaver et al., 2015a*) and can be considered as a late stage of the UHT-like event. However, the UHT-like event at 1.99 – 1.98 Ga was probably accompanied by high-grade metamorphism, as well, at least in the charnockite-dominated SW part of the BGB.

The absence of a metamorphic overprint in the Charlie Gabbro indicates that intermediate to high grade metamorphism related to the UHT-like event, and subsequent high-grade metamorphism in the Moi-Moi Metagabbro and Mozeskreek Anorthosite had completely ended at 1970 +/- 17 Ma. This results in a time interval of 1985 to 1953 Ma in which intermediate to high grade metamorphism related to the UHT-like event occurred in the BGB. This metamorphic event represents the final stage of the Trans-Amazonian orogeny.

A large metagabbroic body in the Coeroeni Gneiss (dated at 1985 +/- 2 Ma; *Kroonenberg et al., in press*) of a similar type as the Moi-Moi Metagabbro, shows a granoblastic texture and other evidence indicative of metamorphism at the high amphibolite facies to possibly granulite facies (*Kroonenberg, 1976; Kroonenberg et al., in press*), suggesting that this metamorphism occurred regionally and is not a local phenomenon restricted to the SW part of the BGB.

The banded and foliated UHT granulites and metapelitic gneisses of the BGB have a steep dip to a subvertical position. The anorthosite body shows igneous layering, which is steeply dipping , as well, parallel to the foliation of the surrounding granulites (*De Roever et al., 2003*), indicating that the deformation event leading to this steep dip has taken place after the anorthosite intrusion at 1980 +/- 5 Ma. This would imply that all mafic and felsic intrusive bodies older than 1980 +/- 5 Ma, were tilted to a steeply dipping position. The deformation event responsible occurred after 1980 +/- 5 Ma, similar in timing to the last stage of (Trans-Amazonian) high-grade metamorphism mentioned above. The non-metamorphic Charlie Gabbro formed after the high-grade metamorphism and probably after the deformation event , suggesting that the Charlie Gabbro might retain its original intrusion position. However, no evidence has been found for the position of the Charlie Gabbro bodies.

7.7 Implications for the evolution of the BGB and the Guiana Shield

A Late Trans-Amazonian event caused UHT metamorphism in the BGB (*De Roever et al., 2003*) at 2,07-2,05 Ga. Ongoing collisional processes resulted in a new subduction zone south of the TTG-greenstone belt (*Fraga et al., 2009b; Klaver et al., 2015a*). The Moi-Moi Metagabbro and the Charlie Gabbro were emplaced in the BGB as the result of normal subduction processes. The metagabbro bodies are most voluminous in the SW part of the BGB, but also intruded – though scattered and few in number - in the Coeroeni Gneiss Belt and in the metavolcanic rocks of the CSID belt, suggesting widespread metagabbroic magmatism. In the BGB, the intrusion of the Moi-Moi Metagabbro caused UHT-like temperatures, partial melting of UHT granulites and the Kabalebo charnockite magmatism, at 1,98 - 1,99 Ga (*Klaver et al., 2015a*). The volcanics of the CSID-belt (UTS in Figure 2.3), a 1400 km long belt of felsic metavolcanic rocks and subvolcanic granites which extends from Venezuela to Suriname (*Delor et al., 2003*), show ages of 1,99 – 1,98 Ga (*Kroonenberg & De Roever, 2010; Santos et al., 2004*). The metavolcanics and associated granites surround at least the southern and central parts of the BGB. The Moi-Moi Metagabbro association with the Kabalebo charnockite and the scattered distribution of metagabbroic bodies in the CSID belt suggest that possibly Moi-Moi magmatism caused the Late Trans-Amazonian magmatism in the CSID belt. The volcanics in the CSID belt show large open folding and low-grade metamorphism. Deformation of the metavolcanics in the belt must have taken place after 1.98 Ga, which is similar to the Late Trans-Amazonian metamorphic event in the BGB that caused amphibolite to granulite facies metamorphism in the mafic intrusions and resulted in deformation/tilting of banding and foliation in the BGB to a subvertical position. This metamorphic event is the latest deformation phase of the Trans-Amazonian orogeny in the BGB, just as folding of the volcanics in the CSID-belt is the final stage of the Trans-Amazonian orogeny in the Guiana Shield.

At 1970 +/- 17 Ma, the intrusion of the HAB-like Charlie Gabbro took place. Since intermediate to high grade metamorphism takes place after 1980 +/- 5 Ma, but before the intrusion of the Charlie Gabbro, the end of the Trans-Amazonian orogeny in the central part of the Guiana Shield is expected to be around 1970 Ma or slightly later in view of the large error. This is in contrast with the western end of the Guiana Shield. The tholeiitic dyke swarms in Venezuela indicate that the Trans-Amazonian metamorphism and deformation ended here before 1988 +/- 2 Ma, the age of the oldest dyke swarm dated. This suggests that the Trans-Amazonian orogeny ended at 1,99 Ga in the western part of the Guiana Shield but continued in the central part until approx. 1,97 Ga.

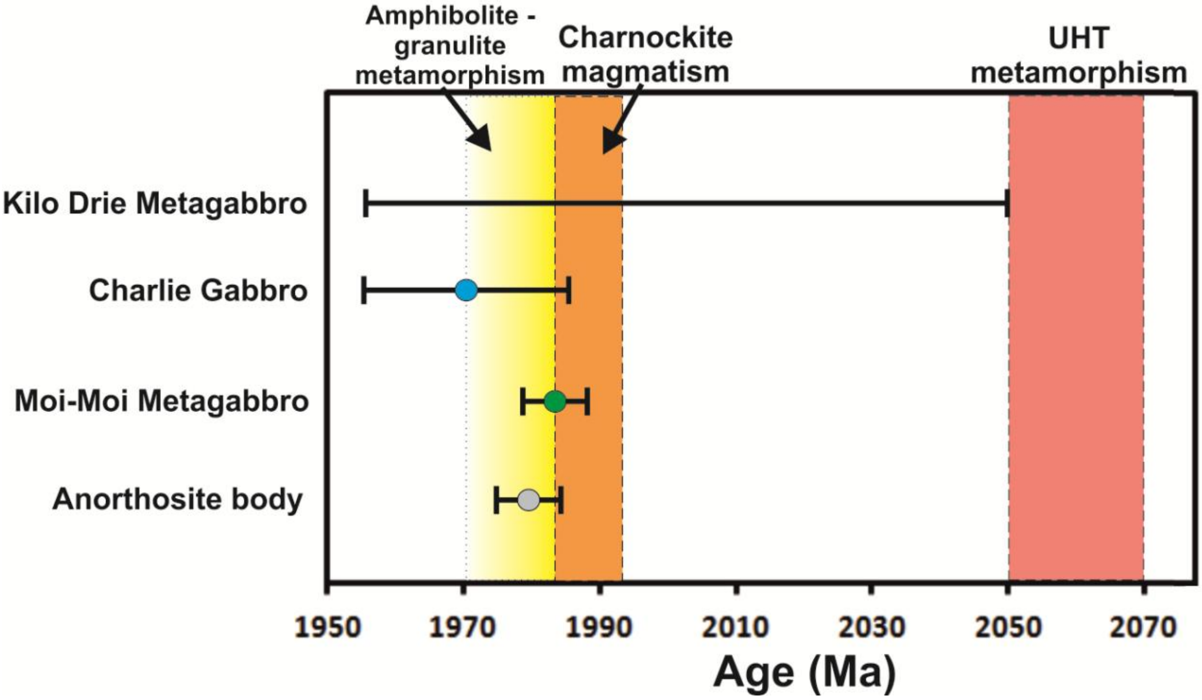

Figure 7.2: *Geochronological data for the BGB. The red coloured bar represents UHT metamorphism (2,07 – 2,,05 Ga) determined for high-grade metamorphism in the east and central part of the BGB (De Roever et al., 2003). The orange coloured bar represents the charnockite magmatism (1984,4 – 1992,5 Ma, Klaver et al., 2015a), created during a younger, UHT-like event. Rather precise zircon ages of 1980 +/- 5 Ma (De Roever et al., 2003) and 1984 +/- 5 Ma were determined for the anorthosite body and Moi-Moi Metagabbro. Baddeleyite dating of Charlie Gabbro resulted in an age of 1970 +/- 17 Ma. The actual age of the Charlie Gabbro is expected to be towards the younger side of this range. The Kilo Drie Metagabbro magmatism and amphibolite-granulite metamorphism ranges are based on the present chronological data (see text).*

8. CONCLUSIONS

The petrography, geochemistry and U-Pb dating of mafic intrusions in BGB indicate the presence of at least 2, and possibly 3 generations of mafic magmatism during the later part of the Trans-Amazonian orogeny. 2 of the generations contain a metamorphic overprint, suggesting metamorphism at higher amphibolite to granulite facies. One of these generations is the Kilo Drie Metagabbro. Its chemistry indicates a HAB parental magma, comparable to the Charlie Gabbro. Therefore, the Kilo Drie Metagabbro might represent an earlier pulse of the tholeiitic magmatism that created the Charlie gabbro.

The second generation with a metamorphic overprint is the primary hornblende-bearing Moi-Moi Metagabbro. The metagabbro occur throughout the northwest and central part of the Guiana shield as small bodies commonly with gradual vertical or concentric zoning from an ultramafic centre towards a gabbroic or quartz-diorite edge. The intrusions appear to be similar to Alaskan-type complexes, which are generally considered to represent the root zones of volcanic arc complexes. This tectonic setting is in agreement with their formation above a northward oriented subduction zone during the later part of the Trans-Amazonian orogeny. The metagabbros in the BGB show metamorphic overprinting in the amphibolite to granulite facies, which resulted in a granoblastic texture and the formation of secondary hornblende.

The chemistry of the metagabbro indicates magma evolution from a hydrous, tholeiitic IAB-like magma due to fractionation and accumulation of olivine, clinopyroxene, orthopyroxene and, in part, plagioclase. Trace elements confirm magma generation in subduction-zone environment. No clear signs of crustal contamination have been found, but field relations and the presence of charnockite zircon in the metagabbro suggest magma mingling between the metagabbro and the surrounding charnockites.

In one of the metagabbro bodies complex xenocrystic zircons were found, with different growth zones. CL-bright inherited cores were dated at 2091 +/- 32 Ma, similar to the age of UHT metamorphism in the BGB. The main growth zones were dated at 1984 +/- 4 Ma, which is identical to zircon growth in the surrounding charnockites. With exception of REE, the trace elements of these complex metagabbronorite zircons are comparable to the charnockite zircons. In particular, the initial hafnium ($\varepsilon_{Hf(i)}$) is identical to that of zircon in the surrounding charnockites, but different from that of the metagabbroic melt, indicating that the Kabalebo charnockites are the source rocks for the zircons. The difference in REE is interpreted as re-equilibration of the zircons in the metagabbroic magma. Finally, the metamorphic zircon rim was dated at 1950 +/- 13 Ma, which is expected to represent the age of the metamorphic overprint in the Moi-Moi Metagabbro. U-Pb dating on zircons from the quart-diorite edge of an ultramafic-mafic Moi-Moi body resulted in an age of 1984 +/- 4,8 Ma. This age represents the intrusion age of the Moi-Moi Metagabbro and is identical to the age of the main growth zones of the xenocrystic zircons in the metagabbro, confirming that at least the last growth zone may have formed in the gabbroic magma.

The age of the Moi-Moi Metagabbro significantly post-dates the UHT metamorphism in the BGB, but is identical to the charnockite magmatism, therefore the intrusion of the metagabbro is expected to have been the heat source for the charnockite magmatism. Underplating of the metagabbroic magma is suggested to create the UHT-like conditions that caused melting of the UHT granulites resulting in the charnockite magmatism.

The youngest mafic generation is the Charlie Gabbro. In Suriname, these mafic intrusions have only been discovered in the BGB. The Charlie Gabbro shows a clear cumulate texture and lacks the metamorphic overprint present in the Moi-Moi Metagabbro and Kilo Drie Metagabbro. Contamination with the surrounding charnockites did occur at the edge of the bodies and resulted in a deviating chemistry and petrography. U-Pb dating on baddeleyite resulted in an age of 1970 +/- 17 Ma. The age post-dates the UHT metamorphism and charnockite magmatism in the BGB. The absence of a metamorphic overprint suggest that all Trans-Amazonian metamorphic and deformation processes ended during the intrusion of the Charlie Gabbro. Therefore, the Charlie Gabbro is expected to mark the end of the Trans-Amazonian orogeny in the BGB.

The chemistry of the Charlie gabbro indicates magma evolution from a tholeiitic HAB magma due to fractionation and accumulation of olivine and plagioclase. The trace elements and the HAB composition suggest a subduction related environment but significant amounts of hydrous mineral phases are absent, contrary to the Moi-Moi Metagabbro. Therefore the Charlie Gabbro magmatism is expected to be related to the waning stage of northward subduction during the final phase of the Trans-Amazonian orogeny.

RECOMMENDATIONS FOR FUTURE RESEARCH

1. The cumulate character of the samples made it difficult, or even impossible, to calculate the parental magma composition. Major and Trace element analysis of the cumulus minerals and the intercumulus hornblende might provide a better estimate of the parental magma composition and better information about the tectonic setting These data might help confirm the hypotheses that were proposed in this thesis.

2. Fieldwork, petrographical study and chemical data collected for this thesis point to the presence of a third generation of mafic magmatism, the Kilo Drie Metagabbro. A trustworthy geochemical interpretation of this generation could not be made due to the low amount of samples found and analysed. Moreover, no time was available for investigation of the third type.

   The Kilo Drie metagabbro should be investigated thoroughly in order to get a complete picture of the mafic magmatism in the BGB. At this moment, some sample material is available for further chemical characterisation. Samples from other bodies are needed, as well, but their location is not yet known

3. The age constraints of the mafic-ultramafic intrusions are important for the tectonic reconstruction of the Guiana Shield. However, it is still unknown at which time the Late Trans-Amazonian subduction stopped. It is not even certain that subduction continued during the later part of the Trans-Amazonian orogeny. The felsic volcanism and Moi-Moi Metagabbro emplacement would indicate subduction at 1.99-1.98 Ga. The absence of metamorphism in the Charlie Gabbro, emplaced at 1.97 Ga, would indicate the end of the Trans-Amazonian orogeny. A more precise dating of the Charlie Gabbro and possibly of the Kilo Drie Metagabbro might give a better understanding of the timing of the processes that occurred during the Late Trans-Amazonian.

ACKNOWLEDGEMENTS

First of all, I want to thank Emond de Roever, who has given me the opportunity to work with him on this interesting project and to learn so much about the interesting geology of the Guiana Shield. Emond is an enthusiastic supervisor who always makes time to answer questions or to give advice. His knowledge of the Bakhuis Mountains and his experience as geologist for the GMD were of important value for this thesis. Emond's enthusiasm can be seen in the provision of extra samples for this thesis and to stay in touch with the LIPs Commision for the dating of zircon and baddeleyite of the mafic samples. This thesis would not have been the same without these arrangements.

Secondly, I want to thank Gareth Davies for being the first supervisor of this thesis and giving advice about the zircon analysis. Furthermore I want to thank Fraukje Brouwer for her help during this thesis and being the second supervisor.

One person who might not be forgotten in this list is Martijn Klaver. Martijn was the person who did the preparational work for the baddeleyite and zircon dating of samples ER1109 and ER1115 and established contact with the LIPs commission. His work on these samples saved me a lot of work, while it gave me fantastic data. His experience with zircons resulted in good advice for the interpretations of my zircons. Additionally, Martijn went to Münster and Frankfurt to measure the trace elements and hafnium isotopes in my zircons when it was impossible to measure this at the VU University due to broken machinery. Finally, Martijn gave assistance during the ICP-MS analysis and with the CL-microscope. In short, Martijn's work is much appreciated!

This thesis could not have been made without the financial support of the Stichting Dr. Schürmann Fonds, the Stichting Molengraaff Fonds and the Faculty of Earth and Life Sciences (FALW). The Stichting Dr. Schürmann Fonds provided the funds for the fieldwork by me and my supervisor while the Stichting Molengraaff Fonds covered my travel and lodging costs. The Stichting Dr. Schürmann Fonds also paid for the LA-ICP-MS zircon analysis in Münster. This support is very much appreciated!

I want to thank the GMD, and especially M. Autar, who is head of the GMD, for their help with this research. Besides giving permission to export the samples, they also provided drill cores of the mafic-ultramafic intrusions in the BGB. Naturalis, the museum of natural history in Leiden, provided a sample, as well.

There are too many people to thank for their help during the field trip in Suriname. For this reason I will only mention the ones with who I had the most contact. Firstly, Karel and Joyce Dawson, the owners of the Kabalebo Nature Resort, made our special fieldwork program possible and provided a discount for our stay at the resort. Secondly, I want to thank Armida for providing the information and logistics for our field trips. These field trips could not have been this successful without our experienced guide, Mr. Jozef Jogi. He never left our side and always made extra fun of the day by pointing out animals which we, as inexperienced tourists, would have missed. In addition to this list, I want to thank Norman Mac-Intosh for preparing and guiding our field trip into the jungle by four-wheel drive. He took good care of us and made us survive a week of camping with hammocks in the rain forest.

Many people at the VU University helped during the development of this thesis and deserve my gratitude for their help. Firstly, I want to thank Bouk Lacet and Wynanda Koot for preparing an enormous amount of thin sections. In addition, Bouk spended several hours in the basement of the VU in order to help me with sawing my samples. Wynanda is also thanked for mounting the zircons. Secondly, I want to thank Roel van Elsas for help with crushing and grinding my samples. Roel also helped me with the zircon separation and with finding a way to take transmitted light pictures of the zircons when the microscope which is normally used was broken.

Many thanks go to Sergei Matveev, Richard Smeets, Suzette Timmermans and Bas van der Wagt, who all helped me during the labwork. Sergei helped me with the XRF analyses and did not complain about several remeasurements. Additionally, he assisted during the BSE imaging with the EMP. Richard made the clean laboratory available and guided me through the processes of the laboratory. He also gave useful advise which will help me in the future if I must ever work in such a laboratory again! Suzette was my main guidance through the processes of dissolving my samples for ICP-MS measurements. I learned a lot from her and am grateful that she put so much effort in helping me out in the clean laboratory. Finally, I want to thank Bas for measuring my first series of ICP-MS samples.

The members of the LIPs Commision, who dated the zircons and baddeleyite minerals of samples ER1109 and ER1115, and Jasper Berndt, who dated my zircons from drill core LA150, cannot be forgotten in this list. The U-Pb dating of the zircons and baddeleyite grains could not be this successful if it was done by me.

Finally, I want to thank Bertram Uunk, a fellow student who is studying the isotopic ratios and mafic dykes of the Bakhuis Mountains, for sharing this fantastic field trip and parts of the lab work with me. His support during the last weeks is much appreciated! However, the most important of all are my family and friends who helped me through the hard parts of this thesis and gave me the support to continue and finish this thesis!

References

Anczkiewicz, R., Oberli, F., Burg, J.P., Villa, I.M., Günther, D. and Meier, M., 2001, Timing of normal faulting along the Indus Suture in Pakistan Himalaya and a case of major 231Pa/235U initial disequilibrium in zircon. *Earth and Planetary Science Letters* **191***, 101-114*.

Arima, M., Gower, C.F., 1991, Osumilite-bearing granulites in the Eastern Grenville Province, Eastern Labrador, Canada: mineral paragneises and metamorphic conditions. *Journal of Petrology 32, p. 29 - 61*

Avelar, V.G. de, Lafon, J.-M., Delor, C., Guerrot, C., Lahondère, D., 2003, Archean crust remnants in the easternmost part of the Guiana Shield: Pb-Pb and Sm-Nd geochronological evidence for Meso-archean versus Neo-archean signatures. *Geology of France and surrounding areas, no. 2-3-4, p. 83 – 99*

Barbosa, J., Nicollet, C., Leite, C., Kienast, J.R., Fuck, R.A., Macedo, E.P., 2006, Hercynitequartz-bearing granulites from Brejões Dome area, Jequié block, Bahia, Brazil: influence of charnockite intrusion on granulite-facies metamorphism. *Lithos 92, p. 537 – 556*

Batanova, V.G., Pertsev, A.N., Kamenetsky, V.S., Ariskin, A.A., Mochalov, A.G., Sobolev, A.V., 2005, Crustal Evolution of Island-Arc Ultramafic Magma: Galmoenan Pyroxenite-Dunite Plutonic Complex, Koryak Highland (Far East Russia). *Journal of Petrology, Vol. 46, p. 1345 – 1366.*

Beard, J.S., 1986, Characteristic mineralogy of arc-related cumulate gabbros: Implacations for the tectonic setting ofgabbroic plutons and for andesite genesis. *Geology, vol. 14, p. 848 – 851*

Berrangé, J.P., 1977, The Geology of Southern Guyana, South America, London: institute of Geological Sciences, Overseas Division, Memoir 4, 112

Bohlen S.R., Mezger, K., 1989, Origin of Granulite Terranes and the Formation of the Lowermost Continental Crust. *Science, vol. 244, p. 326 – 329*

Bosma, W., Kroonenberg, S.B., Mass, K., De Roever, E.W.F., 1983, Igneous and metamorphic complexes of the Guyana shield in Suriname. *Geol. Mijnb. Dienst Suriname, vol. 62, p. 241-254*

Bosma, W., Kroonenberg, S.B., Van Lissa, R.V., Maas, K., De Roever, E.W.F., 1984, An explanation to the geology of Suriname. *Geol. Mijnb. Dienst Suriname, vol. 27, p. 31-82*

Brophy, J.G., 1986, The Cold Bay Volcanic Center, Aleutian Volcanic Arc. I. Implications for the origin of Hi-Alumina Arc Basalt. *Contributions to Mineralogy and Petrology 93, p. 368 – 380.*

Brophy, J.G., Marsh, B.D., 1986, On the origin of high-alumina arc basalt and the mechanics of melt extraction. *Journal of Petrology, vol. 27, p. 763 – 789.*

Brown, M., 2006, Duality of thermal regimes is the distinctive characteristic of plate tectonics since the Neoarchean. *Geology, vol. 34, no. 11, p. 961-964*

Brown, M., 2007, Metamorphic Conditions in Orogenic Belts: A Record of Secular Change. *International Geology Review, Vol. 49, p. 193-234*

Brown, M., Korhonen, F.J., 2009, Some Remarkt on Melting and Extreme Metamorphism of Crustal Rocks, in *Gupta et al. (eds), Physics and Chemistry of the Earth's Interior*

Brügmann, G.E., Reischmann, T., Naldrett, A.J., Sutcliffe, R.H., 1997, Roots of an Archean volcanic arc complex: the Lac des Iles area in Ontario, Canada. *Precambrian Research 81, p. 223 – 239.*

Bryan, S.E., Riley, T.R., Jerram, D.A., Leat, P.T., Stephens, C.J., 2002, Silicic volcanism: an under-valued component of large igneous provinces and volcanic rifted margins, in Magmatic Rifted Margins. In*: Menzies, M.A., Klemperer, S.L., Ebinger, C.J., Baker, J. (Eds.), Magmatic Rifted Margins, Geological Society of America Special Paper, 362, p. 99 – 120*

Campbell, I.H., 1985, The difference between oceanic and continental tholeiites: a fluid dynamic explanation. *Contribution to Mineralogy and Petrology 91, p. 37 – 43.*

Campbell, I.H., Griffiths, R.W., 1990, Implications of mantle plume structure for the evolution of flood basalts. *Earth and Planetary Science Letters 99, p. 79 – 93.*

Cawthorne, R.G., 1976, Melting Relations in Part of the System CaO-MgO-Al_2O_3-SiO_2-Na_2O-H_2O uder 5 kb Pressure. *Journal of Petrology, Vol. 17, Part I, p. 44 – 72.*

Cherniak, D.J., Hanchar, J.M., Watson, E.B., 1997, Diffusion of tetravalent cations in zircon. *Contribution to mineral petrology, vol 127, p. 383-390*

Cherniak, D.J., Watson, E.B., 2003, Diffusion in Zircon. *Reviews in Mineralogy and geochemistry, vol. 53, p 113 – 143*

Coffin, M.F., Eldholm, O., 1994, Large igneous provinces: crustal structure, dimensions, and external consequences. *Reviews of Geophysics 32, p. 1 – 32*

Cordani, U.G., Teixeira, W., 2007, Proterozoic accretionary belts in the Amazonian Craton. *The geological society of America, Memoir 200, p. 297 – 320*

Cordani, U.G., Teixeira, W., D'Agrella-Filho, M.S., Trindade, R.I., 2009, The position of the Amazonian Craton in supercontinents. *Gondwana research 15, p. 396 – 407*

Cox, K.G., Bell, J.D., Prankhurst, R.J., 1989, The interpretation of Igneous Rocks. *London: George Allen & Unwin.*

Crawford, A.J., Falloon, T.J., Eggins, S., 1987, The origin of island arc high-alumina basalts. *Contributions to Mineralogy and Petrology 97, p. 417 – 430.*

Da Rosa-Costa, L.T., Lafon, J.M., Delor, C., 2006, Zircon geochronology and Sm-Nd study: Further constraints for the Archean and Paleoproterozoic geodynamical evolution of the south-eastern Guiana shield,North Amazonian craton, Brazil. *Gondwana research vol. 10, p. 277 – 300*

Da Rosa-Costa L.T., Monié, P., Lafon, J-.M., Arnaud, N.O., 2009, ^{40}Ar-^{39}Ar geochronology across Archean and Paleoproterozoic terranes from southeastern Guiana Shield (north of Amazonian Craton, Brazil): Evidence for contrasting cooling histories. *Journal of South American Earth Sciences 27, p. 113 – 128*

Dahlberg, E.H., 1973, Lithostratigraphical correlation of granulite-facies rocks of the Guiana Shield. *Secondo Congrese Latino-Americano, Caracas, Venezuela. Also: Geol. Mijnb. Dienst Sur., Med., vol. 23, p. 26-33*

Dawson, J.B., Harley, S.L., Rudnick, R.L., Ireland, T.R., 1997, Equilibration and reaction in Archean quartz-sapphire granulite xenoliths from the Lace kimberlite pipe, South Africa. *Journal of metamorphic Geology 15, p. 253-266*

Day, W.C., Tosdal, R.M., Acosta, E.L., Aruspon, J.C., Carvajal, A.L., Cedeño, E., Lowry, G., Martinez, L.F., Noriega, J.A., Nuñez, F.J., Rojas, J., Prieto, F., 1995, Geology of the Lo Increíble Mining District and U-Pb Age of the Early Proterozoic Yuruari Formation of the Pastora Supergroup, Guayana Shield, Venezuela. *U.S. Geol. Surv. Open File Rep., 2124, pp. E1-E13.*

De Groot, K., 2008, Geothermo(baro)metry of ultrahigh-temperature metamorphism in the Bakhuis Mountain, Surinam. *MSc-thesis, Vrije Universiteit Amsterdam.*

De Roever, E.W.F., 1975, Geology of the Central part of the Bakhuis Mountians (W. Suriname). *Geol. Mijnb. Dienst Sur., vol. 23, p. 65-101*

De Roever, E.W.F., Lafon, J-.M., Delor, C., Cocherie, A., Rossi, P., Guerrot, C., Potrel, A., 2003, The Bakhuis ultrahigh-temperature belt (Suriname): I. petrological and geochronological evidence for a counterclockwise P-T path at 2.07-2.05 Ga. *Geology of France and surrounding areas, N^{o} 2-3-4, p. 175 – 205*

Deer, W.A., Howie, R.A., Zussman, J., 1992, An Introduction to the Rock Forming Minerals. *Longman, London.*

Delor, C., Lahondère, D., Egal, E., Lafon, J.-M., Cocherie, A., Guerrot, C., Rossi, P., Truffert, C., Théveniaut, H., Phillips, D., Avelar, V.G. de, 2003a, Trans-Amazonian crustal growth and reworking as revealed by the 1:500,000-scale geological map of French Guiana (2nd edition). *Geology of France and surrounding areas, no. 2-3-4, p. 5 – 57*

Delor,C., De Roever, E.W.F., Lafon, J.-M., Lahondère, D., Rossi, P., Cocherie, A., Guerrot, C., Potrel, A., 2003b, The Bakhuis Ultrahigh-temperature belt (Suriname): II. Implications for Late Trans-Amazonian crustal stretching in a revised Guiana shield framework. *Geology of France and surrounding areas, no. 2-3-4, p. 207 – 230*

Dilek, Y., Altunkaynak, Ş., 2009; Geochemical and temporal evolution of Cenozoic magmatism in western Turkey: mantle response to collision, slab break-off, and lithospheric tearing in an orogenic belt. From: *Van Hinsbergen, D.J.J., Edwards, M.A., Grovers, R. (eds.), Collision and collapse at the Africa-Arabia-Eurasia Subduction Zone. The Geological Society, London, Special Publications 311, P. 213-233*

Draper, D.S., Johnston, A.D., 1992, Anhydrous PT relations of an Aleutian high-MgO basalt: an investigation of the role of olivine-liquid reaction in the generation of arc high-alumina basalts. *Contributions to Mineralogy and Petrology 112, p. 501 – 519.*

Elliot, R.G., 1992; The Geology and Geochemistry of the Omai Goldfield, Guyana. *PhD thesis of the Oxford Brooks University*

El-Rahman, Y.A., Helmy, H.M., Shibata, T., Yoshikawa, M., Arai, S., Tamura, A., 2012, Mineral chemistry of the Neoproterozoic Alaskan-type Akarem Intrusion with special emphasis on amphibole: Implications for the pluton origin and evolution of subduction-related magma. *Lithos 155, p. 410 – 425.*

Elkins-Tanton, L.T., 2005; Continental magmatism caused by lithospheric delamination. *Geological Society of America Special Paper 388, p. 449 – 461*

Elkins Tanton, L.T., Hager, B.H., 2000; Melt intrusion as a trigger for lithospheric foundering and the eruption of the Siberian flood basalts. *Geophysical Research Letters, Vol. 27, Issue 23. P. 3937 – 3940*

Ernst, R.E., Buchan, K.L., 1997, Giant radiating dyke swarms: their use in identifying pre-Mesozoic large igneous provinces and mantle plumes. In: *Mahoney, J.J., Coffin, M.F. (eds.), Large Ignaous Provinces: Continental, Oceanic, and Planetary Flood Volcanism. American Gophysical Union Geophysical Monograph 100, p. 297 – 333.*

Ernst, R.E., Buchan, K.L., Campbell, I.H., 2005; Frontiers in Large Igneous Province research. *Lithos 79, p. 271 - 297*

Eyuboglu, Y., Dilek, Y., Bozkurt, E., Bektas, O., Rojay, B., Sen, C., 2010, Structure and geochemistry of an Alaskan-type ultramafic-mafic complex in the Eastern Pontides, NE-Turkey. *Gondwana Research 18, p. 230 – 252.*

Farahat, E.S., Helmy, H.M., 2006, Abu Hamamid Neoproterozoic Alaskan-type complex, south Eastern Desert, Egypt. *Journal of African Sciences 45, p. 187 – 197.*

Fraga, L.M., Macambire, M.J.B., Dall'Agnoll, R., Costa, J.B.S., 2009a, 1.94 – 1.93 Ga charnokitic magmatism from the central part of the Guyana Shield, Roraima, Brazil: Single-zircon evaporation data and tectonic implications. *Journal of South American Earth Sciences 27, p. 247 – 257*

Fraga, L.M., Reis, N.J., Dall'Agnoll, R., 2009b, Cauarne-Coeroeni Belt – the main tectonic feature of the Central Guyana Shield, Northern Amazonian Craton. *SBG-Nucleo Norte, Simpósio de Geologia da Amazônia, 11 (Manaus, AM, Expanded Abstracts)*

Gale, A., Daltin, C.A., Langmuir, C.H., Su, Y., Schilling, J.-G., 2013, The mean composition of ocean ridge basalt. *Geochemistry, Geophysics, Geosystems, vol. 14, nr. 3, p. 489 – 518.*

Gibbs, A.K., Barron, C.N., 1993, Geology of the Guiana Shield, Oxford: Oxford University Press, 246 pp.

Götze, J., 2012, Application of Cathodoluminescence Microscopy and Spectroscopy in Geosciences. *Microscopy and microanalysis 18, p1270-1284*

Griffin, W., Powell, W., Pearson, N. and O'Reilly, S., 2008, GLITTER: data reduction software for laser ablation ICP-MS. Laser Ablation-ICP-MS in the Earth Sciences. *Mineralogical Association of Canada Short Course Series 40, 204-207*

Guo, J.-H., Peng, P., Chen, Y., Jiao, S.-J., Windley, B.F., 2012, UHT sapphirine granulite metamorphism at 1,93-1,92 Ga caused by gabbronorite intrusions: Implications for tectonic evolution of the norther margin of the North China Craton. *Precambrian Research, vol. 222-223, p. 124-142*

Harley, S.L., 1998, On the occurrence and characterization of ultrahigh-temperature crustal metamorphism, in: Treloar, P.J., O'Brien, P.J., (eds), What Drives Metamorphism and Metamorphic Reactions? *Geological Society, London, Special Publications 138, p. 81 – 107*

Harley, S.L., 2004, Extending our understanding of Ultrahigh temperature crustal metamorphism. *Journal of Mineralogical and Petrological Sciences, Vol. 99, p. 140-158*

Harley, S.L., 2008, Refining the P-T records of UHT crustal metamorphism. *Journal of metamorphic Geology, vol. 28, p. 125 – 154*

Harley, S.L., Hensen, B.J., Sheraton, J.W., 1990, Two-stage decompression in orthopyroxene-sillimanite granulites from Forefinger Point, Enderby Land, Antarctica: implications for the evolution of the Archean Napier Complex. *Journal of Metamorphic Geology 8, p. 591-613*

Heaman, L.M., LeCheminant, A.N., 1993, Paragenesis and U-Pb systematic of baddeleyite (ZrO_2). *Chemical Geology, vol. 110, p. 95 – 126.*

Helmy, H.M., El-Rahman, Y.M.A., Yoshikawa, M., Shibata, T., Arai, S., Tamura, A., Kagami, H., 2014, Petrology and Sm-Nd dating of the Genina Gharbia Alaskan-type complex (Egypt): Insights into deep levels of Neoproterozoic island arcs. *Lithos 198-199,p. 263 – 280.*

Helmy, H.M., Mahallawi, M.M., 2003, Gabbro Akarem mafic-ultramafic complex, Eastern Desert, Egypt: a Late Precambrian analogue of Alaskan-type complexes. *Mineralogy and Petrology 77, p. 85 – 108.*

Helmy, H.M., Yoshikawa, M., Shibata, T., Arai, S., Kagami, H., 2015, Sm-Nd and Rb-Sr isotope geochemistry and petrology of Abu Hamamid intrusion, Eastern Desert, Egypt: An Alaskan-type complex in a backarc setting. *Precambrian Research 258, p. 234 – 246.*

Himmelberg, G.R., Loney, R.A., 1995, Characteristics and Petrogenesis of Alaskan-Type Ultramafic-Mafic Intrusions, Southeastern Alaska. *U.S. Geological Survey, Professional Papers 1564, p. 1 – 47.*

Hinton, R.W., Upton, B.G.J., 1991, The chemistry of zircon: variations within and between large crystals from syenite and alkali basalt xenoliths. *Geochimica et Cosmochimica Acta 55 p. 3287- 3302*

Hoskin, P.W.O., Schaltegger, U., 2003, The composition of Zircon and igneous and metamorphic petrogenesis. *Reviews in Mineralogy and Geochemistry, vol. 53, p. 27 – 62*

Hyndman, R.D., 1995, Subduction zone backarcs, mobile belts, and orogenic heat. *Geological Society of America Today, vol. 15, p. 4 – 10*

Jackson, M.D., Cheadle, M.J., Atherton, M.P., 2003; Quantitative modelling of granitic melt generation and segregation in the continental crust. *Journal of Geophysical Research, Vol. 108, No. B7*

Jagoutz, O., Schmidt, M.W., 2013, The composition of the foundered complement to the continental crust ans a re-evaluation of fluxes in arcs. *Earth andPlanetary Science Letters 371 – 372, p. 177 – 190.*

Jarvis, K.E., 1988, Inductively Coupled Plasma Mass Spectrometry: A new technique for the rapid or ultra-trace level determination for the rare-earth elements in geological materials. *Chemical Geology 68, p 31-39*

Johnston, A.D., 1986, Anhydrous P-T phase relations of near-primary high-alumina basalt from the South Sandwich Islands. Implications for the origin of island arcs and tonalite-trondhjemite series rocks. *Contributions to Mineralogy and Petrology 92, p. 368 – 382.*

Kelsey, D.E., 2008, On ultrahigh-temperature crustal metamorphism. *Gondwana Research 13, p. 1-29*

Kelsey, D.E., Hand, M., 2015, On ultrahigh temperature crustal metamorphism: Phase equilibria, trace element thermometry, bulk composition, heat sources, time scales and tectonic settings. *Geoscience Frontiers 6, p. 311 – 356.*

Klaver, M., 2011, The relationship between dry granitoid magmatism and UHT-metamorphism, Bakhuis granulite belt, Western Suriname. *MSc-thesis Vrije Universiteit Amsterdam.*

Klaver, M., De Roever, E.W.F., Nanne, J.A.M., Mason, P.R.D., Davies, G.R., 2015a, Charnockites and UHT metamorphism in the Bakhuis Granulite Belt, western

Suriname: Evidence for two separate UHT events. *Precambrian Research 262, p. 1 – 19*

Klaver, M., De Roever, E.W.F., Thijssen, A.C.D., Bleeker, W., Ernst, R., Söderlund, U., Chamberlain, K., Berndt, J., Zeh, A., 2015b, Mafic magmatism in the Bakhuis Granulite Belt (western Suriname): relationship with charnockite magmatism and UHT metamorphism. *Journal of the Geological Society of Sweden*

Kooijman, E., Berndt, J., Mezger, K., 2011, U-Pb dating of zircon by laser ablation ICP-MS:recent improvements and new insights. *European Journal of Mineralogy, vol. 24, p. 5 – 21*

Kroonenberg, S.B., 1976, Amphibolite facies and granulite-facies metamorphism in the Coeroeni-Lucie area, southwestern Surinam. *Mededeling Geologisch Mijnbouwkundige Dienst van Suriname, nr. 25, p. 109 – 289.*

Kroonenberg, S.B., De Roever, E.W.F., 2010, Geological evolution of the Amazonian Craton, in *Amazonia, Landscape and Species Evolution: A look into the Past*

Kroonenberg, S.B., De Roever, E.W.F., Fraga, L.M., Reis, R., Faraco, T., Lafon, J-.M., Cordani, U., Wong, T.E., in press, Paleoproterozoic evolution of the Guiana Shield in Suriname: a revised model. *Netherlands Journal of Geosciences.*

Le Maitre, R.W., Bateman, P., Dudek, A., Keller, J., Lameyre, J., Le Bas, M.J., Sabine, P.A., Schmid, R., Sørensen, H., Streckeisen, A., Wooley, A.R., Zanettin, B., 1989, A Classification of Igneous Rocks and Glossary of Terms. Recommendations of the IUGS Subcommission on the Systematic of Igneous Rocks.

Lowery Claiborne, L.L., Walker, B.A., Wooden, J.L., Mazdab, F.K., Bea, F., 2006, Tracking magmatic processes through Zr/Hf ratios in rocks and Hf and Ti zoning in zircons: An example from the Spirit Mountain batholiths, Nevada. *Mineralogical Magazine vol. 70(5), p. 515 – 543*

Ludwig, K.R., 2012, Isoplot 3.75: A geochronological toolkit for Microsoft Excel. Berkeley Geochronological Center, Special Publication, Vol. 5.

Lustrino, M., 2005; How the delamination and detachment of lower crust can influende basaltic magmatism. *Earth-Science Reviews 72, p. 21 – 38.*

Murata, K.J., Richter, D.H., 1966, Chemistry of the lavas of the 1959-60 eruption of Kilauea volcano, Hawaii, *USGS Prof. Paper, 537-A.*

Marshall, D.J., 1988, Cathodoluminescence of geological materials, Unwin Hyman Ltd, London, ISBN 0-04-552026-7

McDonough, W.F., Sun, S.-S., 1995, The composition of the Earth. *Chemical Geology, Vol.120, p. 223 -253*

McFarlane, C.R.M., Carlson, W.D., Connely, J.N., 2003, Prograde peak, and retrograde P-T paths from aluminium in orthopyroxene: high-temperature contact metamorphism in the aureole of the Makhavinekh Lake pluton, Nain Plutonic Suite, Labrador. *Journal of Metamorphic Geology 21, p. 405-423*

Mezger, K., Krogstad, E.J., 1997, Interpretation of discordant U-Pb zircon ages: An evaluation. *Journal of metamorphic geology, Vol. 15, p. 127 – 140*

Montgomery, C.W., Hurley, P.M., 1978, Total-rock U-Pb and Rb-Sr systematic in the Imataca series, Guayana shield, Venezuela. *Earth and Planetary Science letters 39, p281-290*

Mues-Schumacher, J.K., Kononova, V.A., Suddaby, P.J., 1996, Mineral chemistry and geochronology of the potassic alkaline ultramafic Inagli complex, Aldan Shield, eastern Siberia. *Mineralogical Magazine 60, p. 711 – 730.*

Nanne, J.A.M., 2013, The Regional Extent of Ultrahigh-temperature Metamorphism in the Bakhuis Granulite Belt, W Surinam. *MSc-thesis Vrije Universiteit Amsterdam*

Nixon, G.T., Ash, C.H., Connelly, J.N., Case, G., 1989, Alaskan-type mafic-ultramafic rocks in British Columbia: the Gnat Lakes, Hickman, and Menard Creek complexes. *BC Ministry of Energy, Mines and Petroleum Resources, Geological Fieldwork 1988, Paper 1989-1, p. 429 – 442*.

Norcross, N., Davis, D.W., Spooner, E.T.C., Rust, A., 2000, U-Pb and Pb-Pb age constraints on Paleoproterozoic magmatism, deformation and gold mineralization in the Omai area, Guyana Shield. *Precambrian Research 102, p. 69 - 86*

Pearce, J.A., 1982, Trace element characteristics of lavas from destructive plate boundaries. In: Thorphe, R.S., (eds.), *Andesites. John Wiley & Sons.*

Pearce, J.A., 1983, Role of the sub-continental lithosphere in magma genesis at active continental margins. *In Hawkesworth, C.J., and Norry, M.J. eds., Continental basalts and mantle xenoliths, Nantwich, Cheshire: Shiva Publications, p. 230 -249*.

Pearce, J.A., 2008, Geochemical fingerprinting of oceanic basalts with applications to ophiolite classification and the search for Archean oceanic crust. *Lithos 100, p. 14 – 48.*

Pearce, J.A., 2014, Immobile Element Fingerprinting of Ophiolites. *Elements, Vol. 10, p. 101 – 108.*

Pearce, J.A., Cann, C.R., 1973, Tectonic setting of basic volcanic rocks determined using trace element analyses. *Earth and Planetary Science letters 19, p. 290 – 300.*

Perfit, M.R., Gust, D.A., Bence, A.E., Arculus, R.J., Taylor, S.R., 1980, Chemical characteristics of island-arc basalts: implications for mantle sources. *Chemical geology, Vol. 30, p. 227 – 256.*

Priem, H.N.A., Boelrijk, N.A.I.M., Hebeda, E.H., Verdurmen, E.A.TH., Verschure, R.H., 1971, Isotopic Ages of the Trans-Amazonian Acidic Magmatism and the Nickerie Metamorphic Episode in the Precambrian

Basement of Suriname, South America. *Geological Society of America Bulletin vol. 82, p. 1667 – 1680*

Reis, N.J., Teixeira, W., Hamilton, M.A., Bispo-Santos, F., Almeida, M.E., D'Agrella-Filho, M.S., 2013, Avanavero mafic magmatism, a late Paleoproterozoic LIP in the Guiana Shield, Amazonian Craton: U-Pb ID-TIMS baddeleyite, geochemical and paleomagnetic evidence. *Lithos 174, p. 175-195*

Richards, M.A., Duncan, R.A., Courtillot, V.E., 1989, Flood basalts and hot spot tracks: Plume heads and tails. *Science, Vol. 246, p. 103 – 107.*

Rollinson, H.R., 1993, Using Geochemical Data: Evaluation, Presentation, Interpretation, Longman Group UK Ltd, ISBN 0 582 06701 4

Russel, J.K., Nicholls, J., 1988, Analysis of petrologic hypotheses with Pearce element ratios. *Contribution to mineralogy and petrology, vol. 99, p. 25 – 35.*

Santos, J.O.S., Hartmann, L.A., Haudette, H.E., Groves, D.I., Mcnaughton, N.J., Fletcher, I.R., 2000, A New Understanding of the Provinces of the Amazonian Craton Based on Intergration of Field Mapping and U-Pb Sm-Nd Geochronology. *Gondwana research v3, no. 04, p. 453 – 488*

Santos, J.O.S., Potter, P.E., Reis, N.J., Hartmann, L.A., Fletcher, I.R., McNaughton, N.J., 2003, Age, Source and Regional stratigraphy of the Roraima Supergroup and Roraima-like outliers in northern South America based on U-Pb geochronology. *The Geological Society of America Bulletin, vol. 115, nr. 3, p. 331 – 348*

Santos, J.O.S., Van Breemen, O.B., Groves, D.I., Hartmann, L.A., Almeida, M.E., McNaughton, N.J., Fletcher, I.R., 2004, Timing and evolution of multiple Paleoproterozoic magmatic arcs in the Tapajós Domain, Amazon Craton: constraints from SHRIMP and TIMS zircon, baddeleyite and titanite U-Pb geochronology. *Precambrian research 131, p. 73 – 109*

Santosh, M., Omori, S., 2008, CO_2 windows from mantle to atmosphere: Models on ultrahigh-temperature metamorphism and speculations on the link with melting of snowball Earth. *Gondwana Research 14, p. 82-96*

Saunders, A.D., 2005; Large Igneous Provinces: Origin and Environmental Consequences. *Elements Vol. 1, p. 259 – 263.*

Saunders, A.D., Jones, S.M., Morgan, L.A., Pierce, K.L., Widdowson, M., Xu, Y.G., 2007, Regional uplift associated with continental large igneous provinces: The oles of mantle plumes and the lithosphere. *Chemical Geology 241, p. 282 – 318*.

Schmitt, A.K., Chamberlain, K.R., Swapp, S.M., Harrison, T.M., 2010, In situ U-Pb dating of micro-baddeleyite by secondary ion mass spectrometry. *Chemical Geology, Vol. 269, p., 386 – 395*

Şengör, A.M.C., Özeren, S., Genç, T., Zor, E., 2003, East Anatolian high plateau as a mantle-supported, north-south shortened domal structure. *Geophysical Research Letters, Vol. 30, No. 24, TUR 8.*

Shannon, R.D. (1976); Revised effective ionic radii and systematic studies of interatomic distances in halides and chalcogenides. *Acta Crystallographica A32 p. 751-767*

Shervais, J.W., 1982, Ti-V plots and the petrogenesis of modern and ophiolitic lavas. *Earth and Planetary Science Letters 59, p. 101 – 118.*

Sláma, J., Košler, J., Condon, D.J., Crowley, J.L., Gerder, A., Hanchar, J.M., Horstwood, M.S.A., Morris, G.A., Nasdala, L., Norberg, N., Schaltegger, U., Schoene, B., Tubrett, M.N., Whitehouse, M.J., 2008, Plešovice zircon: A new natural reference material for U-Pb and Hf isotopic microanalysis. *Chemical Geology 249, p. 1 – 35*.

Söderlund, U., Johansson, L., 2002, A simple way to extract baddeleyite (ZrO_2). *Geochemistry, Geophysics, Geosystems, Vol. 3, number 2, p. 1 –*

Sun, S.-S., McDonough, W.F., 1989, Chemical and isotopic systematics of oceanic basalts: implications for mantle composition and processes, in: Saunders, A.D., Norry, M.J. Eds. , Magmatism in Ocean Basins. *Geol. Soc. Spec. Publ., London, pp. 313–345.*

Tassinari, C.C.G., Munhá, J.M.U., Teixeira, W., Palácios, T., Nutman, A.P., Cesar Sosa S., Santon, A.P., Calado, B.O., 2004, The Imataca Complex, NW Amazonian Craton, Venezuela: Crustal evolution and integration of geochronological and petrological cooling histories. *Episodes, vol. 27, p. 3-12*

Théveniaut, H., Delor, C., Lafon, J.M., Monié, P., Rossi, P., Lahondère, D., 2006, Paleoproterozoic (2155-1970 Ma) evolution of the Guiana Shield (Transamazonian event) in the light of new paleomagnetic data from French Guiana. *Precambrian Research 150, p. 221-256*

Tistl, M., Burgath, K.P., Höhndorf, A., Kreazer, H., Muñoz, R., Salinas, R., 1994, Origin and emplacement of Tertiary ultramafic complexes in northwest Colombia: Evidence from geochemistry and K-Ar, Sm-Nd and Rb-Sr isotopes. *Earth and Planetary Science Letters 126, p. 41 – 59.*

Totland, M., Jarvis, I., Jarvis, K.E., 1992, an assessment of dissolution techniques for the analysis of geological samples by plasma spectrometry. *Chemical Geology 95, p 35 – 62*

Uunk, B.A., 2015, Radiogenic isotopes and geochemistry of mafic dykes and plutons in the Bakhuis belt, Western Suriname and their relationship to UHT metamorphism. *M.Sc. thesis VU University.*

Van de Zedde, D.M.A., Wortel, M.J.R., 2001; Shallow slab detachment as a transient source of heat at midlithospheric depths. *Tectonics, Vol. 20, No. 6, p. 868 – 882.*

Vanderhaeghe, O., Ledru, P., Thiéblemont, D., Egal, E., Cocherie, A., Tegyey, M., Milési, J.-P., 1996, Contrasting mechanisms of crustal growth Geodynamic evolution of the Paleoproterozoic granite-greenstone belts of French Guiana. *Precambrian Research 92, p. 165 – 193*

Verma, H.R., 2007, Atomic and nuclear analytical methods, Springer-Verlag Berlin Heidelberg, ISBN 10 3-540-30277-8

Von Blanckenburg, F., Davies, J.H., 1995, Slab breakoff: A model for syncollisional magmatism and tectonics in the Alps. *Tectonics, Vol. 14, No. 1, p. 120-131.*

Wetherill, G.W., 1956, Discordant uranium lead ages. *Trans. Amer. Geophys. Union, vol. 37, p. 320-326*

White, R., McKenzie, D., 1989, Magmatism at Rift Zones: The Generation of Volcanic Continental Margins nd Flood Basalts. *Journal of Geophysical Research, Vol. 94, No. B6, p. 7685 – 7729.*

Whitney, D.L., Evans, B.W., 2010, Abbreviation for names of rock-forming minerals. *American mineralogist 95, p. 185 – 187*

Wiedenbeck, M., Allé, P., Corfu, F., Griffin, W.L., Meier, M., Oberli, F., Von Quadt, A., Roddick, J.C., Spiegel, W., 1995, Three natural zircon standards for U-Th-Pb, Lu-Hfm trace element and REE analyses. *Geostandards Newsletter 19, p. 1 – 23*

Winter, J.D., 2001, An Introduction to Igneous and Metamorphic Petrology, Prentice-Hall Inc., ISBN 0-13-240342-0

Appendix I: Sample locations (1)

Sample	Rock serie	Rock type	Location	Coordinates (UTM 21N/WGS84)	Thinsection	XRF	ICP-MS	Zircons
AT01	Charlie gabbro	Olivine gabbronorite	Kabalebo river near resort	474900E 486630N	MKS61	x	x	
AT02	Charlie gabbro	Gabbronorite	Misty Mountain creek	476140E 485087N	x	x	x	
AT03A	Charlie gabbro	Gabbronorite	Misty Mountain creek	476127E 484987N	x	x	x	
AT03B		Dolerite dyke	Misty Mountain creek	476127E 484987N				
AT04A		Charnokite dyke	Misty Mountain creek	476122E 484933N				
AT04B		Dolerite dyke	Misty Mountain creek	476122E 484933N	x			
AT04C	Charlie gabbro	Gabbronorite	Misty Mountain creek	476122E 484933N	x			
AT04D	Charlie gabbro	Weathered olivine with px-corona	Misty Mountain creek	476122E 484933N				
AT05A		Dolerite dyke	Misty Mountain creek	476120E 484920N				
AT05B	Charlie gabbro	Gabbronorite	Misty Mountain creek	476120E 484920N	x	x		
AT05C		Dolerite dyke	Misty Mountain creek	476120E 484920N				
AT06A	Charlie gabbro	Gabbronorite	Misty Mountain creek	476345E 484925N	x	x		
AT06B		Dolerite dyke	Misty Mountain creek	476345E 484925N	x			
AT07A	Moi-Moi Metagabbro	Pyroxene hornblende gabbronorite	Lower part Moi-Moi creek	478740E 488828N	x	x		
AT07B	Moi-Moi Metagabbro	Amphibolite	Lower part Moi-Moi creek	478740E 488828N	x	x	x	
AT07C	Moi-Moi Metagabbro	Amphibolite	Lower part Moi-Moi creek	478740E 488828N	x	x		
AT07D	Moi-Moi Metagabbro	Pyroxene hornblende gabbronorite	Lower part Moi-Moi creek	478740E 488828N	x	x		
AT07E		Pegmatitic vein	Lower part Moi-Moi creek	478740E 488828N				
AT08A	Moi-Moi Metagabbro	Pyroxene hornblende gabbronorite	Lower part Moi-Moi creek	478740E 488828N	x			
AT09A		Dolerite vein	Lower part Moi-Moi creek	478740E 488828N	x			
AT09B	Moi-Moi Metagabbro	Pyroxene hornblende gabbronorite	Lower part Moi-Moi creek	478740E 488828N	x	x	x	
AT10A	Moi-Moi Metagabbro	Pyroxene hornblende gabbronorite	Lower part Moi-Moi creek	478800E 488740N	x			
AT10B	Moi-Moi Metagabbro	Pyroxene hornblende gabbronorite	Lower part Moi-Moi creek	478800E 488740N	x	x		
AT11		Dolerite, block with dol. + char. Chaotic structures	Lower part Moi-Moi creek	478800E 488740N	x			
AT12A	Moi-Moi Metagabbro	Pyroxene hornblende gabbronorite	Lower part Moi-Moi creek	478835E 488686N	x			
AT13A	Moi-Moi Metagabbro	Pyroxene hornblende gabbronorite (weathered surface)	Lower part Moi-Moi creek	478373E 488644N				
AT13B	Moi-Moi Metagabbro	Pyroxene hornblende gabbronorite	Lower part Moi-Moi creek	478373E 488644N	x	x	x	
AT14		Dolerite, adjacent to charnockites	Misty Mountain creek	476470E 484660N				
AT15A		Dolerite, adjacent to charnockite, chaotic structures	Misty Mountain creek	476613E 484964N	x			
AT15B		Dolerite, adjacent to charnockite, chaotic structures	Misty Mountain creek	476613E 484964N	x			
AT16A		Metadolerite	Misty Mountain creek	476515E 484910N	x			
AT16B	Charlie gabbro	Gabbronorite	Misty Mountain creek	476515E 484910N	x	x		
AT16C	Charlie gabbro	Gabbronorite	Misty Mountain creek	476515E 484910N	x	x		
AT17A	Charlie gabbro	Olivine gabbronorite	Upper part Moi-Moi creek	478765E 487810N	x			
AT18	Charlie gabbro	Olivine gabbronorite	Upper part Moi-Moi creek	479250E 487870N	x	x		
AT20	Moi-Moi Metagabbro	Pyroxene hornblende gabbronorite	Zandkreek	472675E 484432N	x	x		
AT22	Kilo Drie metagabbro	Metagabbronorite	Misty Mountain	475867E 482590N	x			
AT23A	Kilo Drie metagabbro	Metagabbronorite	Kilo Drie creek	482418E 491232N	x			
AT23B	Kilo Drie metagabbro	Metagabbronorite	Kilo Drie creek	482418E 491232N	x			
AT24	Kilo Drie metagabbro	Metagabbronorite	Kilo Drie creek	483515E 490755N	x	x		
AT25	Kilo Drie metagabbro	Metagabbronorite	Kilo Drie creek	483610E 490670N	x	x		

Appendix I: Sample locations (2)

Sample	Rock serie	Rock type	Location	Coordinates (UTM 21N/WGS84)	Thinsection	XRF	ICP-MS	Zircons
AT26	Kilo Drie metagabbro	Metagabbronorite	Kilo Drie creek	483714E 490670N	x			
AT27	Kilo Drie metagabbro	Metagabbronorite	Kilo Drie creek	483088E 490786N	x			
AT28	Kilo Drie metagabbro	Metagabbronorite	Misty Mountain	476460E 482050N	x	x		
AT29D	Kilo Drie metagabbro	Metagabbronorite	Misty Mountain	476600E 481860N	x	x		
AT29E	Kilo Drie metagabbro	Metagabbronorite	Misty Mountain	476600E 481860N	x			
AT30	Charlie gabbro	Olivine gabbronorite	Upper part Moi-Moi creek	478725E 487826N	x	x	x	
AT31	Charlie gabbro	Gabbronorite	Upper part Moi-Moi creek	479284E 487723N	x	x		
AT32	Charlie gabbro	Olivine gabbronorite	Upper part Moi-Moi creek	479276E 487690N	x	x		
AT33	Charlie gabbro	Olivine gabbronorite	Upper part Moi-Moi creek	479460E 487640N	x			
AT34A	Charlie gabbro	Olivine gabbronorite	Upper part Moi-Moi creek	479460E 487640N	x	x		
AT34B	Charlie gabbro	Olivine gabbronorite	Upper part Moi-Moi creek	479460E 487640N	x			
AT34C	Charlie gabbro	Olivine gabbronorite	Upper part Moi-Moi creek	479460E 487640N	x			
AT34D	Charlie gabbro	Olivine gabbronorite	Upper part Moi-Moi creek	479460E 487640N	x	x	x	
AT35	Charlie gabbro	Olivine gabbronorite	Upper part Moi-Moi creek	479368E 487585N	x			
AT36A	Moi-Moi Metagabbro	Amphibolite	Zandkreek	471800E 483100N	x	x	x	
AT36B	Moi-Moi Metagabbro	Pyroxene hornblende mela-gabbronorite	Zandkreek	471800E 483100N	x	x		
AT37A	Moi-Moi Metagabbro	Pyroxene hornblende mela-gabbronorite	Zandkreek	471770E 483112N	x	x	x	
AT37B	Moi-Moi Metagabbro	Pyroxene hornblende mela-gabbronorite	Zandkreek	471770E 483112N	x	x	x	
AT37C	Moi-Moi Metagabbro	Gabbronorite with pyroxene hornblendite bump	Zandkreek	471770E 483112N	x			
AT37D	Moi-Moi Metagabbro	Pyroxenite bump	Zandkreek	471770E 483112N				
AT38	Moi-Moi Metagabbro	Olivine hornblende pyroxenite	Zandkreek	471740E 483148N	x	x	x	
AT40	Avanavero dolerite		Kabalebo Nature Resort	-	x			
AT40A	Avanavero dolerite		Kabalebo Nature Resort	-	x			
71-SUR-207	Charlie gabbro	Olivine gabbronorite	Misty Mountain creek	478710E 488980N	x	x	x	
ER-1115	Charlie gabbro	Gabbronorite	Misty Mountain creek	476360E 484910N	x	x	x	(Bdy)
ER1109	Moi-Moi Metagabbro	Pyroxene hornblende gabbronorite	Lower part Moi-Moi creek	478710E 488980N		x	x	x
MKS61	Charlie gabbro	Olivine gabbronorite, outcrop AT01	Kabalebo river near resort	475000E 486500N	x			
LA148-40,0m	Moi-Moi Metagabbro	Olivine pyroxene hornblendite	Kabalebo West (40,00-40,20m)	479060E 495780N	x	x	x	
LA148-58,5m	Moi-Moi Metagabbro	Hornblende pyroxenite	Kabalebo West (58,50-58,90m)	479060E 495780N	x	x	x	
LA148-69,7m	Moi-Moi Metagabbro	Ultramafic	Kabalebo West (69,70-70,10m)	479060E 495780N				
LA149-21,5m	Moi-Moi Metagabbro	Ultramafic	Kabalebo West (21,50-21,80m)	478760E 495740N				
LA149-40,0m	Moi-Moi Metagabbro	Olivine pyroxene hornblendite	Kabalebo West (40,00-40,40m)	478760E 495740N	x	x		
LA149-64,5m	Moi-Moi Metagabbro	Olivine pyroxene hornblendite	Kabalebo West (64,50-64,80m)	478760E 495740N	x			
LA149-71,5m	Moi-Moi Metagabbro	Olivine pyroxene hornblendite	Kabalebo West (71,50-71,80m)	478760E 495740N	x	x		
LA150-16,0m	Moi-Moi Metagabbro	Quartz-diorite	Kabalebo West (16,00-16,30m)	478880E 495740N	x			x
LA150-27,9m	Moi-Moi Metagabbro	Quartz-diorite	Kabalebo West (27,90-28,10m)	478880E 495740N	x	x	x	x
LA150-55,5m	Moi-Moi Metagabbro	Quartz-diorite	Kabalebo West (55,50-55,80m)	478880E 495740N	x			x

Appendix II: Whole rock major element geochemistry (Wt-%) - XRF

Sample	Fe_2O_3	MnO	TiO_2	CaO	K_2O	P_2O_5	SiO_2	Al_2O_3	MgO	Na_2O	BaO	LOI (X 10^-2)	Sum
AT01	11.51	0.17	0.52	8.52	0.55	0.08	47.67	14.45	14.93	1.71	0.03	0.42	**100.12**
AT02	7.36	0.12	0.16	8.95	0.22	0.01	50.84	19.74	8.63	2.36	0.01	0.31	**98.41**
AT03A	4.56	0.07	0.23	11.44	0.20	0.05	51.01	24.98	4.05	3.17	0.02	0.43	**99.77**
AT05B	8.05	0.13	0.31	9.52	0.31	0.07	51.36	20.05	6.68	2.73	0.04	0.52	**99.23**
AT06A	7.81	0.14	0.39	10.17	0.36	0.09	51.21	20.47	5.91	2.90	0.02	0.97	**99.48**
AT07A	9.49	0.17	0.77	13.83	0.76	0.04	50.69	10.83	11.17	1.96	0.02	0.35	**99.73**
AT07B	11.69	0.12	1.02	13.42	0.45	0.35	44.19	23.49	3.89	2.14	0.02	0.39	**100.79**
AT07C	13.25	0.11	1.26	12.86	0.50	0.74	42.76	21.25	4.38	2.10	0.01	0.63	**99.22**
AT07D	8.13	0.16	0.44	12.78	0.53	0.06	50.92	16.06	8.20	2.47	0.03	1.01	**99.77**
AT09B	10.38	0.20	0.60	14.51	0.71	0.05	52.52	8.48	11.95	1.49	0.03	0.72	**100.92**
AT10B	16.80	0.14	1.04	12.01	0.31	0.03	44.16	17.39	5.74	1.97	0.01	1.07	**99.60**
AT13B	17.16	0.16	1.01	11.19	0.37	0.06	43.62	17.05	5.99	1.90	0.02	0.41	**98.52**
AT16B	12.76	0.18	0.85	9.37	0.49	0.14	48.28	16.02	7.05	2.34	0.03	0.82	**97.51**
AT16C	10.20	0.19	0.68	7.63	0.82	0.21	52.52	16.52	6.91	2.57	0.11	0.24	**98.37**
AT18	9.49	0.15	0.54	10.95	0.27	0.13	49.10	18.03	8.25	2.24	0.02	0.45	**99.16**
AT20	10.41	0.18	0.49	8.33	0.38	0.12	52.84	16.26	12.94	1.80	0.03	0.03	**103.75**
AT24	8.56	0.15	0.48	9.91	0.76	0.14	53.79	18.26	8.13	2.35	0.04	0.31	**102.57**
AT25	8.78	0.16	0.47	10.61	0.73	0.15	52.77	16.91	7.95	2.53	0.05	0.15	**101.10**
AT28	10.87	0.16	0.76	7.91	0.57	0.16	43.57	15.17	5.87	2.22	0.03	-0.75	**87.28**
AT29D	13.85	0.20	1.24	10.62	0.27	0.84	47.10	19.15	4.94	2.94	0.04	0.28	**101.17**
AT30	9.54	0.15	0.55	10.63	0.29	0.12	48.92	18.56	8.35	2.30	0.02	0.55	**99.42**
AT31	10.39	0.21	0.38	10.67	0.21	0.02	51.30	15.72	7.64	2.50	0.02	0.48	**99.06**
AT32	7.49	0.12	0.27	11.24	0.16	0.06	48.28	20.51	8.70	2.17	0.01	0.53	**99.01**
AT34A	8.36	0.14	0.30	10.52	0.22	0.07	48.61	19.50	9.44	2.15	0.02	0.46	**99.32**
AT34D	8.35	0.14	0.29	10.53	0.19	0.04	49.87	19.45	9.60	2.09	0.01	0.45	**100.56**
AT36A	14.03	0.23	0.90	12.78	0.43	0.21	45.12	13.49	9.47	1.85	0.01	0.43	**98.53**
AT36B	9.90	0.22	0.28	14.44	0.10	0.01	51.40	5.19	17.90	0.44	0.01	1.24	**99.90**
AT37A	10.61	0.23	0.37	14.10	0.24	0.02	51.61	5.06	17.06	0.71	0.03	0.43	**100.03**
AT37B	9.76	0.20	0.38	13.56	0.33	0.01	51.72	6.20	15.90	0.97	0.02	0.39	**99.06**
AT38	11.60	0.21	0.33	13.13	0.12	0.02	48.02	7.18	19.08	0.55	0.01	0.52	**100.25**
71-SUR-207	12.32	0.16	0.10	7.69	0.19	0.02	46.57	16.25	14.74	1.67	0.01	1.26	**99.73**
ER1109	9.78	0.20	0.46	14.86	0.33	0.07	52.39	9.47	11.83	1.65	0.03	0.68	**101.06**
ER-1115	6.70	0.09	0.31	11.76	0.19	0.08	48.99	24.10	5.40	2.65	0.02	1.18	**100.30**
LA150-28	10.16	0.25	1.57	5.78	1.84	0.47	57.76	18.12	1.76	4.07	0.17	0.46	**101.94**
LA149-40	15.36	0.22	0.41	6.91	0.56	0.12	46.23	5.46	25.77	0.88	0.02	1.06	**101.93**
LA149-71	16.92	0.23	0.44	4.19	0.47	0.11	43.62	5.48	27.95	0.82	0.02	1.47	**100.26**
LA148-40	14.79	0.21	0.49	7.96	0.42	0.10	45.46	6.34	22.93	0.89	0.02	1.46	**99.62**
LA148-58	14.05	0.20	0.56	6.88	1.02	0.14	45.58	8.76	19.13	1.20	0.03	1.95	**97.57**
	Fe_2O_3	**MnO**	**TiO_2**	**CaO**	**K_2O**	**P_2O_5**	**SiO_2**	**Al_2O_3**	**MgO**	**Na_2O**	**FeO**		**Sum**
Avg. gabbro*	3.10	0.10	1.10	9.50	0.90	0.20	50.10	15.50	7.60	2.40	7.60		**98.10**
Avg. Diorite*	2.50	0.10	1.00	6.60	1.80	0.30	57.50	16.70	3.70	3.50	4.90		**98.60**

* Average values taken from Cox et al. (1989)

Appendix II: Whole rock trace element geochemistry (ppm) - XRF (1)

Sample	Mo	Nb	Y	Zr	Sr	U	Rb	Th	Pb	La	Ce	Pr	Nd	Sm	Ga
AT01	1.23	2.58	13.98	48.26	179.18	0.68	16.51	1.42	2.03	7.59	9.26	0.63	7.92	3.06	13.97
AT02	1.62	0.14	2.47		349.89		2.69		0.07	1.38				0.59	14.98
AT03A	1.39	0.34	3.79		450.12		2.87		0.04	3.53				0.33	16.32
AT05B	1.23	0.68	9.03		371.83	0.05	5.23	0.03	0.26	6.82	2.09	0.84	1.19	1.06	16.28
AT06A	1.11	1.14	9.21	5.59	374.65		4.75			5.17	5.44	1.10	3.45	1.58	16.72
AT07A	0.98	9.05	49.06	26.37	237.24	0.47	26.38	1.58	3.40	19.66	59.78	7.36	35.89	7.24	15.50
AT07B	0.63	2.38	21.01		819.57		8.45	0.60	3.55	9.68	28.69	4.53	18.59	4.46	25.43
AT07C	0.64	3.90	28.17		650.75		5.64	1.90	3.21	16.52	40.89	6.19	27.13	5.88	24.77
AT07D	1.05	2.48	23.48	8.31	428.36	0.33	11.71	2.50	3.22	10.68	24.29	3.42	16.32	3.70	16.65
AT09B	0.67	6.64	37.73	66.80	192.30	0.52	24.75	1.30	2.13	16.10	47.94	6.24	29.06	6.44	12.93
AT10B	0.47	4.41	22.29		510.92		2.32	0.53	3.30	6.98	11.00	2.45	9.68	3.79	23.21
AT13B	1.09	2.30	12.31		488.35		4.40	0.92	2.51	9.20	8.76	2.30	6.38	3.44	21.90
AT16B	0.83	1.91	20.33	40.82	307.68	0.28	13.17	0.65	1.77	5.97	12.11	2.28	7.99	3.11	17.40
AT16C	0.29	4.54	29.77	125.04	370.75		16.10	0.94	3.20	17.98	31.81	4.94	16.27	4.22	16.98
AT18	1.22	1.71	13.52	26.70	307.13		4.40	0.48	0.82	8.33	7.89	1.45	4.50	2.01	15.37
AT20	1.24	1.85	13.18	18.33	296.24		7.55	0.48	1.35	10.51	8.89	0.80	7.89	2.73	13.86
AT24	1.07	2.63	18.44	50.23	276.16		18.16	0.75	2.16	15.28	19.41	2.92	8.55	2.87	15.89
AT25	1.04	2.76	20.06	31.23	296.83		16.68	0.45	3.32	15.32	26.51	3.43	11.88	3.15	16.38
AT28	0.69	3.51	27.73	76.39	318.44	0.07	13.34	0.67	2.74	14.05	27.71	3.87	15.58	3.84	18.78
AT29D	0.46	1.60	21.14		905.65		1.65	0.41	2.19	18.11	50.80	6.15	30.75	5.95	22.84
AT30	1.17	1.58	13.27	26.62	316.38	0.06	5.78	0.52	0.54	7.18	8.46	1.75	3.76	2.14	15.60
AT31	1.04	0.06	8.01		335.47	0.04	1.98			2.86		0.30		1.01	16.56
AT32	1.36	0.64	6.18		345.88	0.03	2.32	0.51		3.83	0.21	0.48	0.67	1.24	14.51
AT34A	1.16	1.06	7.08	4.89	333.24	0.01	3.04	0.37	0.19	4.95	5.90	1.25	4.69	1.97	14.90
AT34D	1.32	0.70	5.70		320.55		2.13	0.13		3.25		0.23		1.26	14.51
AT36A	0.48	4.07	20.12	12.75	507.57		1.63	0.01	0.34	12.02	28.33	4.03	18.84	4.71	17.08
AT36B	1.27	0.45	16.42	10.56	104.16	0.52	4.15	0.22		10.72	13.38	1.25	17.07	4.30	6.87
AT37A	0.82	1.58	19.23	52.24	101.94	0.74	7.39	0.84	0.59	10.22	16.75	1.76	12.88	3.78	8.05
AT37B	1.00	1.82	12.23	44.54	125.82	0.57	13.07	0.91	0.73	7.36	2.65		6.51	2.60	8.65
AT38	0.93	0.42	10.29	9.06	189.47		3.03	0.01		3.67	0.22		4.61	2.22	8.01
71-SUR-207	1.29	0.15	1.55		291.58		3.00			1.70		0.63		1.17	10.98
ER1109	0.26	4.16	24.08	70.09	259.48		4.30	0.55	1.42	12.10	28.27	3.76	17.43	4.18	12.76
ER-1115	1.37	0.55	7.56		409.10		3.14			2.92	0.67	0.18		0.83	15.31
LA150-28		21.33	61.36	1086.29	562.68	0.40	40.81	1.74	11.17	43.88	122.37	15.23	62.56	11.49	23.63
LA149-40	1.18	1.56	7.84	22.78	155.67	0.59	17.24	0.75	1.62	7.37				2.85	7.60
LA149-71	1.29	1.33	6.45	18.52	187.07	0.06	13.91	1.22	0.80	6.74				2.79	7.33
LA148-40	1.37	1.03	7.38	14.09	197.30	0.26	11.87	0.91	0.73	4.03			1.33	2.79	8.70
LA148-58	1.06	2.01	9.40	25.43	248.64	0.59	34.67	1.26	1.93	6.81	2.08		3.37	2.93	10.82

Appendix II: Whole rock trace element geochemistry (ppm) - XRF (2)

Sample	Zn	W	Ta	Cu	Hf	Er	Ni	Yb	Dy	V	Cr	Co	Ba	Sc
AT01	83.31	9.32	7.83	63.88	3.99	6.92	701.20		8.41	146.54	1176.44	81.20	234.92	21.79
AT02	54.89	1.86	1.16	54.05	1.17	1.45	181.84		0.67	75.21	360.70	43.75	117.12	22.69
AT03A	37.11	1.30		15.49	0.84	0.67	75.06			66.38	91.57	20.88	127.80	17.79
AT05B	61.38	1.28		46.68	0.89	1.55	116.48	0.11		103.28	99.76	41.67	345.78	23.36
AT06A	56.01	0.66	0.82	43.38	1.76	2.32	105.45	1.43	1.50	116.01	105.89	38.11	184.05	24.62
AT07A	71.52	2.31	0.63	149.18	2.07	5.20	132.88	4.31	6.92	297.96	411.10	47.42	188.69	61.73
AT07B	87.81			119.55	1.76	1.73	2.37	2.33	6.24	145.00	3.37	25.70	136.34	31.81
AT07C	81.75	0.29		21.71	1.98	2.43		2.67	6.81	193.58	3.04	34.04	116.95	38.11
AT07D	65.74	0.62	0.22	133.95	2.08	2.05	111.59	1.40	2.90	177.51	196.41	42.97	211.78	43.35
AT09B	80.31	1.28	1.30	54.18	3.21	4.67	130.91	3.28	6.60	270.23	388.98	49.71	309.41	55.69
AT10B	87.76			157.19	1.00	2.06		3.53	11.49	622.70	13.59	75.18	118.56	37.72
AT13B	102.42			140.86	0.86	1.02		2.87	8.70	598.21	13.89	69.16	157.29	38.15
AT16B	101.99	0.98	1.15	82.04	2.75	2.98	141.85	1.57	7.55	251.45	84.21	61.37	243.86	32.49
AT16C	121.17	1.08	0.36	45.26	4.00	3.22	139.88	2.23	7.00	123.89	153.92	46.50	1015.09	27.21
AT18	71.45	2.64	1.26	63.89	2.25	3.13	191.11		2.03	141.93	236.78	49.78	152.12	27.23
AT20	80.18	4.84	3.66	73.83	3.00	3.38	364.09		4.81	140.05	1053.80	57.36	228.26	28.83
AT24	73.19	3.11	2.12	71.90	2.80	2.56	228.22		2.06	140.48	321.26	41.97	365.41	27.74
AT25	75.39	3.55	2.10	147.26	2.44	3.89	229.17		1.83	145.11	165.17	43.29	425.22	29.30
AT28	104.69	2.36	0.59	90.48	3.48	3.65	127.44	1.29	6.37	206.05	80.13	53.68	333.09	30.02
AT29D	143.94	0.22	0.06	85.90	2.51	2.85	32.52	2.26	5.87	233.27	33.75	40.41	352.14	29.20
AT30	73.39	3.03	0.65	62.74	1.89	1.80	235.93		2.61	137.51	137.35	50.99	154.73	24.99
AT31	77.90	0.87	0.21	120.58	1.26	1.28	136.60		2.29	140.68	51.10	52.09	147.30	34.17
AT32	54.74	3.52	1.21	40.72	1.63	1.30	273.44			81.19	159.42	47.23	97.63	20.57
AT34A	64.23	3.42	2.40	37.14	1.97	2.78	287.47		0.77	82.27	196.73	52.27	192.08	20.66
AT34D	62.46	3.82	2.53	42.07	2.02	2.21	270.12			90.32	299.33	51.55	107.12	21.83
AT36A	114.73			108.06	2.04	2.31	77.22	1.13	7.97	329.45	168.37	66.20	99.96	48.96
AT36B	70.73	3.04	2.88	21.48	1.80	4.03	293.78		4.78	149.56	1729.70	67.88	97.57	55.50
AT37A	91.55	2.88	1.74	15.38	2.83	4.54	241.97		6.61	166.08	1046.35	64.16	260.45	56.11
AT37B	66.59	1.65	2.24	28.93	2.71	2.66	193.76	0.79	5.00	200.73	1403.69	56.78	199.30	53.67
AT38	78.62	5.20	3.43	35.31	2.45	3.07	426.85		6.05	146.46	1066.57	86.47	55.86	47.02
71-SUR-207	111.02	6.80	5.97	49.67	2.26	2.64	520.69		3.71	43.51	54.92	102.53	73.97	14.52
ER1109	77.64	1.21	1.04	234.48	2.97	2.85	145.18	1.49	4.92	217.80	336.88	48.70	233.32	56.39
ER-1115	49.76	1.75	1.11	34.91	1.65	1.09	168.07			82.40	28.10	38.51	179.45	17.22
LA150-28	215.30			18.71	23.15	6.91	7.37	6.26	11.95	46.44	16.34	15.76	1452.29	26.41
LA149-40	106.65	8.54	5.93	28.82	3.40	4.94	668.08		9.40	132.98	2172.50	120.38	156.59	25.02
LA149-71	133.37	9.39	8.22	27.91	4.61	6.03	736.81		12.93	133.34	2533.06	123.89	134.67	17.07
LA148-40	104.30	7.73	5.19	40.89	3.27	5.68	571.67		9.29	166.24	1953.33	107.57	122.36	29.53
LA148-58	109.67	5.81	5.49	56.69	3.67	4.11	501.72		8.27	168.15	1614.13	98.98	228.43	24.09

Appendix II: Whole rock trace element geochemistry (ppm) - ICP-MS

Sample	Ni	Co	Cr	Ga	V	Cu	Sr	Ba	Rb	Pb	Ta	Zr	Hf	Th	U	Nb
AT01	659.26	80.85	1087.06	12.50	137.37	63.92	176.41	205.73	16.73	1.97	0.15	57.80	2.57	1.35	0.32	2.71
AT02	163.29	41.48	311.15	13.42	60.27	52.39	348.38	101.33	2.51	0.88	0.01	6.42	0.17	0.10	0.02	0.14
AT03A	71.77	22.18	91.76	15.95	57.95	14.20	539.08	131.29	4.69	1.35	0.02	11.34	0.26	0.20	0.02	0.40
AT06B	155.02	56.83	85.52	15.87	200.05	53.21	282.22	269.05	17.23	2.11	0.22	99.29	3.54	1.64	0.29	4.10
Sur-207	524.88	108.51	56.08	10.71	36.90	51.26	313.93	75.34	2.93	0.50	0.01	5.09	1.30	0.04	0.01	0.16
ER115	144.85	34.53	26.23	13.05	63.44	28.46	383.49	143.17	2.79	0.92	0.03	16.23	0.41	0.15	0.02	0.52
AT07B	4.11	20.79	6.33	22.38	125.57	107.49	209.69	112.12	3.46	1.74	0.08	45.45	1.10	0.25	0.08	1.56
AT09B	122.34	50.89	340.33	11.24	250.77	53.06	321.14	98.17	1.98	0.84	0.03	17.98	1.34	0.13	0.02	0.62
AT13B	1.74	64.15	5.09	19.99	735.57	124.72	455.67	126.43	3.97	4.82	0.13	68.67	0.94	0.55	0.27	2.04
ER1109	137.51	48.80	295.84	11.44	199.21	257.62	186.29	243.87	25.52	3.93	0.33	97.74	3.94	1.18	0.52	7.17
AT30	212.57	46.05	106.81	12.28	114.90	56.81	769.87	116.05	8.15	3.49	0.15	28.50	1.26	0.36	0.19	2.54
AT34D	262.54	50.44	273.54	13.30	81.48	43.52	256.44	201.01	3.90	6.10	0.19	77.77	3.30	0.41	0.14	4.15
AT36A	131.69	68.86	150.04	16.40	319.92	146.80	513.07	92.28	1.57	4.37	0.21	41.37	2.50	0.06	0.02	4.18
AT37A	209.24	58.36	865.27	6.94	138.69	10.15	99.29	198.69	6.89	1.40	0.07	49.00	1.32	0.96	0.20	1.46
AT37B	181.40	55.72	1255.86	7.99	183.52	27.01	126.97	168.99	13.03	2.27	0.08	47.36	2.38	0.63	0.18	1.56
AT38	393.14	83.65	930.80	7.11	126.63	30.24	187.86	44.61	2.65	0.59	0.02	20.25	0.69	0.19	0.06	0.40
LA150	6.08	10.79	17.21	21.32	50.36	12.77	533.55	1289.15	38.34	11.97	0.93	1080.19	20.50	1.43	0.73	21.68
LA148-58	466.79	96.17	1484.86	10.09	159.77	56.82	250.13	215.61	35.75	2.85	0.12	40.62	2.07	1.07	0.37	1.97
LA148-40	520.67	103.05	1751.89	7.58	151.52	37.86	195.13	112.50	11.52	1.31	0.13	25.61	1.79	0.59	0.20	0.97

Sample	Ti	Sc	Y	La	Ce	Pr	Nd	Sm	Eu	Gd	Tb	Dy	Ho	Er	Yb	Lu
AT01	2578.43	20.59	13.85	7.50	16.46	2.10	8.91	2.05	0.67	2.19	0.35	2.33	0.46	1.38	1.29	0.20
AT02	596.02	19.55	3.05	1.59	2.88	0.35	1.51	0.37	0.29	0.36	0.06	0.44	0.10	0.33	0.38	0.06
AT03A	861.14	17.79	8.35	3.80	5.18	1.07	4.70	1.20	0.56	1.25	0.20	1.37	0.30	0.85	0.80	0.12
AT06B	4330.20	28.67	25.95	12.53	27.50	3.53	15.30	3.47	1.00	3.83	0.62	4.02	0.85	2.46	2.34	0.38
Sur-207	553.27	12.68	2.28	0.97	1.97	0.26	1.17	0.27	0.23	0.29	0.03	0.34	0.05	0.25	0.27	0.06
ER115	1012.43	10.05	6.67	2.49	5.38	0.75	3.32	0.87	0.44	0.97	0.17	1.09	0.24	0.71	0.68	0.09
AT07B	1950.10	22.65	18.81	3.56	10.74	1.05	4.85	1.26	0.44	1.22	0.20	1.36	0.30	0.82	0.76	0.11
AT09B	1425.51	61.08	36.71	2.59	5.62	0.76	3.40	0.82	0.45	0.91	0.14	0.98	0.19	0.63	0.66	0.11
AT13B	3426.37	34.57	11.09	8.81	21.48	3.22	15.48	4.22	1.32	4.15	0.62	3.62	0.71	1.89	1.56	0.20
ER1109	2950.15	58.57	23.48	13.87	41.89	6.16	27.17	6.36	1.09	6.24	0.97	5.90	1.17	3.57	3.63	0.55
AT30	3446.88	15.30	7.79	6.51	14.52	1.98	8.12	2.22	0.74	2.10	0.32	1.89	0.40	1.13	1.12	0.16
AT34D	2238.68	19.05	6.08	10.38	28.40	4.09	18.30	4.31	1.11	4.30	0.65	3.98	0.78	2.33	2.25	0.34
AT36A	4694.49	49.05	20.45	11.41	30.18	4.19	18.51	4.20	1.24	4.07	0.60	3.53	0.69	1.97	1.75	0.26
AT37A	1328.51	59.26	17.19	7.26	19.69	2.84	12.87	3.51	0.94	3.28	0.51	3.16	0.65	1.78	1.56	0.23
AT37B	1899.92	55.82	12.03	4.58	10.95	1.59	7.65	2.11	0.64	2.31	0.35	2.20	0.42	1.21	1.05	0.17
AT38	1221.57	48.50	9.66	2.18	6.20	1.06	5.61	1.91	0.56	1.88	0.30	1.83	0.37	0.97	0.81	0.11
LA150	8293.10	26.50	55.30	40.39	93.14	12.57	55.35	13.56	5.34	12.13	1.73	10.00	2.11	5.57	4.82	0.71
LA148-58	2845.28	23.25	9.77	6.24	14.44	1.95	8.71	1.99	0.64	1.91	0.28	1.71	0.32	0.91	0.86	0.14
LA148-40	2407.62	30.03	7.53	3.78	8.73	1.22	5.72	1.43	0.48	1.47	0.20	1.34	0.25	0.74	0.67	0.11

Appendix III: CIPW-norm (1) (Calculated according to Winter, 2001)

Sample	Apatite	Ilmenite	Orthoclase	Albite	Anorthite	Hematite	Diopside	Olivine	Hypersthene	Quartz	Nepheline	Total
AT01	0.19	0.98	3.23	13.56	30.61	2.50	9.05	23.22	16.67			**100.01**
AT02	0.03	0.30	1.31	18.74	43.27	1.60	0.92		31.60	0.50		**98.26**
AT03A	0.10	0.43	1.15	25.20	54.22	0.99	2.44	0.08	15.09			**99.71**
AT05B	0.15	0.59	1.80	21.68	42.30	1.75	3.83		26.04	0.92		**99.06**
AT06A	0.21	0.74	2.13	23.04	42.55	1.75	6.08		22.55	0.27		**99.33**
AT07A	0.10	1.46	4.50	15.58	19.03	2.06	39.89	11.08	5.90			**99.61**
AT07B	0.81	1.94	2.67	12.00	53.74	2.54	8.96	15.28			2.72	**100.66**
AT07C	1.71	2.40	2.95	12.18	47.63	2.88	9.57	17.31			2.46	**99.09**
AT07D	0.13	0.83	3.12	19.62	31.85	1.77	25.40	6.53	10.36			**99.61**
AT09B	0.11	1.13	4.17	11.87	14.76	2.26	46.16	3.58	16.78			**100.83**
AT10B	0.07	1.97	1.85	14.31	38.22	3.65	17.82	20.86			0.71	**99.48**
AT13B	0.15	1.91	2.17	15.13	37.42	3.73	14.94	22.49	0.47		0.51	**98.91**
AT16B	0.33	1.62	2.88	18.63	32.38	2.77	11.02	4.53	23.20			**97.36**
AT16C	0.48	1.29	4.89	20.79	31.63	2.23	4.39		29.62	3.13		**98.45**
AT18	0.29	1.03	1.59	17.81	38.95	2.06	11.92	6.40	18.96			**99.03**
AT20	0.26	0.90	2.19	14.30	30.11	2.22	7.74	1.83	40.53			**100.08**
AT24	0.31	0.89	4.40	18.62	32.61	1.84	12.06		26.20	2.18		**99.10**
AT25	0.34	0.90	4.31	20.07	33.34	1.91	15.11		24.57	0.39		**100.94**
AT28	0.36	1.44	3.35	17.66	30.34	2.36	6.66	2.84	22.13			**87.15**
AT29D	1.94	2.35	1.57	23.38	39.05	3.01	7.01	12.51	10.17			**100.99**
AT30	0.28	1.04	1.71	18.27	40.09	2.07	9.75	8.16	17.90			**99.28**
AT31	0.05	0.72	1.25	19.84	31.73	2.26	17.35		25.19	0.49		**98.90**
AT32	0.13	0.51	0.96	17.25	46.34	1.63	7.38	10.36	14.31			**98.88**
AT34A	0.16	0.56	1.31	17.06	43.50	1.82	6.77	10.49	17.53			**99.19**
AT34D	0.10	0.54	1.15	16.61	43.68	1.82	6.77	6.93	22.85			**100.43**
AT36A	0.48	1.71	2.56	12.16	27.74	3.05	28.23	21.12			1.37	**98.42**
AT36B	0.03	0.53	0.60	3.51	12.00	2.15	47.70	6.60	26.75			**99.86**
AT37A	0.48	1.29	4.89	20.79	31.63	2.23	4.39		29.62	3.13		**98.45**
AT37B	0.03	0.72	1.96	7.74	11.82	2.12	44.50	4.96	25.16			**99.00**
AT38	0.04	0.63	0.70	4.39	16.92	2.52	38.63	23.32	13.06			**100.21**
71-SUR-207	0.05	0.19	1.13	13.29	36.72	2.68	1.07	25.03	19.46			**99.62**
ER1109	0.18	0.59	1.12	21.08	54.03	1.46	3.19	7.26	11.22			**100.13**

Appendix III: CIPW-norm (2) (Calculated according to Winter, 2001)

Sample	**Apatite**	**Ilmenite**	**Orthoclase**	**Albite**	**Anorthite**	**Hematite**	**Diopside**	**Olivine**	**Hypersthene**	**Quartz**	**Nepheline**	**Total**
ER-1115	0.18	0.59	1.12	21.08	54.03	1.46	3.19	7.26	11.22			**100.13**
LA150-28	1.03	2.94	10.67	32.30	22.26	2.19	3.20		15.08	8.86		**98.52**
LA149-40	0.26	0.76	3.23	6.94	9.33	3.29	18.84	48.42	9.28			**100.35**
LA149-71	0.25	0.84	2.80	6.50	10.12	3.68	8.03	55.77	12.21			**100.20**
LA148-40	0.23	0.94	2.47	7.08	12.30	3.22	21.37	40.46	11.48			**99.55**
LA148-58	0.33	1.09	6.15	9.77	15.93	3.12	14.34	37.37	11.36			**99.45**

Sample	**Apatite**	**Ilmenite**	**Orthoclase**	**Albite**	**Anorthite**	**Magnetite**	**Diopside**	**Olivine**	**Hypersthene**	**Quartz**	**Nepheline**	**Total**
Avg. gabbro*	0.56	2.13	5.49	20.26	28.60	4.36	13.70		22.13	0.71		**97.94**
Avg. diorite*	0.68	1.80	10.42	29.96	24.40	3.63	4.67		12.56	10.28		**98.40**

* Average values taken from Cox et al. (1989)

Appendix IV: Trace element content zircons ER1109 (ppm) (1)

	IT42, 6-1	IT42,6-2	IT42,7-1	IT42,7-2	IT42,8-1	IT42,8-2	IT42,9-1	IT42,0-1	IT42,1-1
Li7	50.20	<11.38	24.38	19.01	46.09	11.68	<11.22	<12.60	<12.28
B11	0.65	0.71	<0.62	<0.64	<0.56	<0.65	<0.77	<0.91	<0.94
Si29	151684.03	151684.03	151684.02	151684.03	151684.03	151684.03	151684.02	151684.02	151684.02
Ca43	<88.82	940.63	119.50	863.74	<87.50	<87.59	<105.84	<127.64	<123.58
Sc45	810.46	798.49	801.63	829.30	838.61	819.97	794.24	720.57	727.36
Ti47	4015.92	4018.02	3977.55	4030.66	4003.25	4014.50	3873.63	3506.62	3489.75
Ti49	8.00	9.14	7.02	7.80	10.63	8.33	7.42	7.58	8.48
V51	0.47	0.62	0.55	0.32	0.23	1.14	0.29	<0.146	0.29
Cr53	<1.23	<1.32	<1.06	<1.15	<1.11	1.77	<1.39	<1.60	<1.38
Co59	<0.087	<0.097	<0.093	0.20	<0.093	<0.089	<0.122	<0.130	<0.113
Cu63	<0.221	<0.213	0.32	<0.215	<0.204	2.73	<0.263	0.26	<0.29
Zn66	<0.44	0.38	0.66	0.64	<0.41	0.70	<0.50	1.36	<0.58
Ga69	<0.079	0.08	<0.075	<0.076	0.05	<0.076	<0.077	<0.097	<0.090
Ge72	0.68	<0.70	<0.67	<0.69	<0.64	<0.67	<0.79	<0.99	<0.88
Rb85	<0.067	<0.055	0.07	<0.063	0.10	0.10	<0.062	0.08	0.11
Sr88	0.29	0.81	0.33	1.00	0.34	0.29	0.27	0.23	0.31
Y89	345.99	210.97	338.00	366.52	376.92	571.41	300.91	292.43	372.05
Zr90	465017.63	462793.34	463496.22	476077.38	477092.84	479349.13	452562.25	413774.28	417932.44
Nb93	2.34	1.67	2.09	2.43	2.36	2.24	2.07	1.87	2.12
Cs133	0.05	0.04	0.05	<0.025	0.04	0.04	<0.034	<0.032	0.03
Ba137	<0.176	0.22	0.37	0.30	<0.171	0.27	0.19	0.33	0.35
La139	0.02	0.69	0.11	0.07	0.02	0.03	0.02	0.02	0.06
Ce140	9.30	7.76	8.14	9.10	8.69	10.92	6.64	7.46	8.30
Pr141	0.03	0.37	0.06	0.08	0.05	0.09	0.02	0.03	0.11
Nd146	0.55	2.86	0.62	0.76	0.52	1.15	0.42	0.44	1.22
Sm147	0.89	1.86	0.85	1.24	0.96	2.29	0.80	0.88	1.47
Eu153	0.36	0.98	0.36	0.45	0.42	0.77	0.33	0.34	0.59
Gd157	5.35	4.65	5.75	6.32	5.43	11.56	4.74	4.54	6.82
Tb159	1.95	1.17	1.91	2.25	1.99	3.83	1.62	1.51	2.25
Dy163	24.76	14.45	24.66	26.82	26.61	46.87	21.49	20.64	27.64
Ho165	10.17	6.00	9.94	11.17	11.31	17.95	9.20	8.76	11.32
Er166	54.27	32.84	52.17	58.14	60.54	88.60	46.96	46.68	57.80
Tm169	13.06	7.88	12.26	13.90	14.96	20.17	11.14	11.38	13.53
Yb172	141.47	89.44	129.82	147.60	168.78	206.59	120.23	121.75	144.94
Lu175	30.27	19.72	27.60	32.08	36.43	41.77	26.49	27.93	33.18
Hf178	9337.52	9119.66	9186.95	9316.20	9945.45	9683.00	8801.71	8623.95	8530.51
Ta181	0.78	0.43	0.57	0.79	0.77	0.64	0.63	0.66	0.70
Pb208	17.47	9.12	16.31	18.09	17.88	28.50	14.67	19.54	21.68
Th232	97.64	49.72	87.60	98.44	95.68	153.28	77.53	90.05	101.12
U238	193.97	117.49	174.44	193.71	231.01	242.32	154.04	182.87	192.53
(Lu/La)$_N$	48351.86	274.94	2314.21	4176.53	15529.73	12734.76	15281.95	14014.67	5026.12
(Sm/La)$_N$	235.77	4.31	11.85	26.88	67.95	116.05	76.52	73.48	37.01
(Lu/Dy)$_N$	12.23	13.65	11.19	11.96	13.69	8.91	12.33	13.53	12.00
ΣREE	292.45	190.67	274.25	309.98	336.71	452.59	250.09	252.35	309.23
Ce/Ce*	3.72	95.25	3.69	22.91	25.52	46.20	32.94	90.81	66.40
Eu/Eu*	0.39	0.96	0.36	0.39	0.45	0.37	0.40	0.42	0.47

Appendix IV: Trace element content zircons ER1109 (ppm) (3)

	IT32,1	IT31,1*	IT31,1	IT31,1	IT31,1	IT31,1	IT31,1-1	IT31,2-1	Z513-1
Li7	32.20	11.10	<6.88	14.83	10.55	7.95	9.35	6.95	33.05
B11	<0.58	<0.82	<0.74	1.02	<0.70	<0.82	0.64	<0.59	4.97
Si29	151684.05	151684.05	151684.05	151684.03	151684.05	151684.05	151684.03	151684.03	151684.05
Ca43	<87.33	137.83	<105.40	<109.00	<95.83	<112.10	<94.12	<81.12	481.74
Sc45	830.83	850.42	793.59	768.11	889.29	770.78	845.48	812.99	833.21
Ti47	3825.04	3641.23	3665.69	3534.27	3735.02	3505.98	3758.81	3687.47	3692.88
Ti49	7.14	8.84	7.27	12.76	4.71	9.13	5.77	3.60	8.67
V51	0.28	1.51	0.28	0.46	0.36	0.43	0.30	0.16	1.55
Cr53	<1.15	<1.49	<1.45	<1.48	<1.09	<1.38	<1.14	<1.14	<2.11
Co59	0.10	<0.115	<0.137	<0.136	0.32	<0.123	<0.101	<0.094	<0.181
Cu63	<0.232	<0.25	<0.246	<0.25	40.37	<0.26	<0.224	<0.201	1.72
Zn66	0.38	<0.54	0.50	<0.38	1.51	0.58	0.45	<0.35	4.17
Ga69	<0.061	<0.100	<0.089	0.10	0.08	<0.106	<0.065	<0.058	<0.151
Ge72	<0.61	<0.74	<0.80	<0.85	<0.71	<0.80	<0.69	<0.60	<1.46
Rb85	0.10	0.24	0.13	0.11	0.17	<0.078	<0.059	0.08	0.57
Sr88	0.34	0.33	0.30	0.33	0.36	0.21	0.28	0.32	0.76
Y89	342.29	1126.74	273.39	245.36	617.17	249.10	394.10	204.59	1060.50
Zr90	498674.06	479301.22	474676.44	458974.88	497149.25	462340.25	501990.84	494044.88	479345.78
Nb93	2.54	2.23	1.79	1.79	2.20	1.81	2.46	1.50	2.28
Cs133	0.04	0.03	0.04	0.04	0.03	0.05	0.04	0.04	0.07
Ba137	<0.162	0.40	<0.219	0.26	0.73	<0.167	0.26	0.23	2.11
La139	0.01	0.17	0.06	0.03	0.28	0.02	0.01	0.03	0.25
Ce140	****	16.83	7.00	7.84	14.18	5.86	9.13	5.76	16.15
Pr141	0.04	0.40	0.10	0.05	0.23	0.02	0.03	0.05	0.42
Nd146	0.57	4.90	0.85	0.46	2.22	0.33	0.66	0.50	3.96
Sm147	1.03	5.77	0.87	0.82	2.13	0.72	1.29	0.78	4.47
Eu153	0.45	3.30	0.59	0.35	1.18	0.30	0.51	0.40	3.21
Gd157	5.71	28.83	4.38	4.14	9.34	3.99	6.98	4.03	20.13
Tb159	1.99	8.85	1.51	1.43	3.10	1.48	2.30	1.38	7.16
Dy163	24.67	100.80	19.85	17.47	42.24	17.09	29.15	15.98	86.82
Ho165	10.09	37.36	8.13	7.45	19.02	7.26	11.80	6.38	33.14
Er166	53.71	174.77	43.32	39.60	105.47	39.23	61.99	32.58	174.90
Tm169	12.98	37.62	10.47	9.51	25.26	9.39	15.17	7.65	37.35
Yb172	143.79	370.75	113.72	101.77	269.06	102.32	163.13	84.87	375.19
Lu175	31.38	76.40	25.37	22.73	60.37	23.05	36.10	17.40	76.40
Hf178	10112.78	6931.68	9355.98	9023.89	8421.60	9345.41	9824.39	8718.84	7959.33
Ta181	0.89	0.44	0.54	0.42	0.53	0.46	0.86	0.24	0.47
Pb208	25.35	42.27	12.46	12.23	23.99	12.25	21.67	6.28	51.97
Th232	138.00	224.80	66.21	63.53	127.12	61.24	117.64	35.56	294.7
U238	279.29	210.23	139.65	127.62	204.94	127.29	228.87	81.75	279.6
(La/Lu)$_N$	22067.12	4230.17	4333.66	8326.39	2055.17	10003.02	24842.33	6231.75	2967.94
(La/Sm)$_N$	120.74	53.10	24.59	49.75	12.05	52.08	147.55	46.25	28.86
(Dy/Lu)$_N$	12.72	7.58	12.78	13.01	14.29	13.49	12.38	10.89	8.80
ΣREE	286.42	866.75	236.22	213.63	554.08	211.06	338.26	177.79	839.55
Ce/Ce*	11.52		10.89	17.80	42.93	12.67	59.96	73.17	9.40
Eu/Eu*	0.45	0.64	0.76	0.47	0.68	0.42	0.42	0.56	0.87

Appendix IV: Trace element content zircons ER1109 (ppm) (2)

	IT42,2-1	**IT42,2-2**	**IT41,3-1***	**IT41,3-2**	**IT41,3-3**	**IT41,4-1**	**IT41,4-2**	**IT31,1***	**IT31,2**
Li7	<12.00	18.17	<10.51	<18.68	29.62	<8.70	<15.47	9.42	<12.86
B11	<0.83	<0.80	1.34	<1.51	<1.31	<0.84	<1.53	<0.75	<1.42
Si29	151684.03	151684.03	151684.02	151684.02	151684.05	151684.03	151684.05	151684.05	151684.05
Ca43	<130.53	<120.84	<116.85	<233.21	<203.03	<117.48	<213.51	<99.68	<180.87
Sc45	738.15	754.47	849.17	719.06	753.92	791.85	762.85	872.12	807.56
Ti47	3585.32	3560.61	3588.54	3496.66	3585.06	3623.42	3472.28	3749.38	3727.43
Ti49	9.71	9.52	7.47	<2.91	8.66	2.33	<2.85	6.68	9.62
V51	0.34	0.27	0.96	<0.251	0.45	<0.121	0.30	1.17	0.49
Cr53	<1.33	<1.54	<1.44	<2.50	<2.73	<1.80	<3.21	<1.31	4.33
Co59	<0.147	0.12	<0.138	3.17	<0.233	<0.132	<0.220	<0.119	<0.264
Cu63	<0.36	<0.31	0.44	165.38	29.48	<0.26	0.84	<0.240	<0.44
Zn66	<0.53	<0.41	<0.53	2.94	1.90	<0.45	<0.97	<0.46	<0.79
Ga69	0.08	<0.098	<0.10	<0.169	<0.134	<0.093	<0.144	<0.078	<0.118
Ge72	<0.96	<0.96	<0.83	<1.63	<1.55	<0.92	<1.48	0.76	<1.42
Rb85	<0.065	0.09	0.48	0.50	0.19	<0.077	0.18	0.26	0.15
Sr88	0.23	0.25	0.41	0.77	0.37	0.27	0.30	0.30	0.25
Y89	265.65	485.87	2294.53	161.04	236.74	320.17	297.94	1220.87	478.91
Zr90	433292.69	434794.56	437047.81	419342.53	437532.28	458158.06	438699.47	484364.38	471200.31
Nb93	1.76	2.39	3.54	1.26	2.03	1.49	1.45	2.11	1.91
Cs133	<0.033	0.06	0.05	0.08	<0.055	0.05	<0.056	0.05	<0.049
Ba137	0.28	<0.202	<0.189	3.85	0.75	<0.190	0.41	0.30	0.40
La139	0.09	0.05	0.13	0.45	0.22	0.02	0.10	0.14	0.18
Ce140	6.45	10.65	33.62	7.62	9.41	6.62	6.65	20.22	9.31
Pr141	0.07	0.09	0.52	0.46	0.41	0.06	0.10	0.40	0.18
Nd146	0.62	1.17	6.58	2.35	3.04	0.62	0.65	4.71	1.95
Sm147	0.81	2.08	11.54	1.17	1.51	1.02	0.92	6.11	1.84
Eu153	0.27	0.61	6.61	0.87	1.29	0.59	0.44	3.53	0.85
Gd157	4.11	8.84	62.44	3.91	4.34	5.88	4.53	30.62	9.56
Tb159	1.50	2.93	19.21	1.04	1.44	1.93	1.59	9.44	3.28
Dy163	19.30	34.90	212.32	13.54	16.82	24.51	20.71	108.63	38.58
Ho165	7.95	14.57	76.70	5.03	7.26	9.68	9.33	40.11	15.24
Er166	41.90	76.77	348.08	26.07	36.78	51.99	52.72	192.92	75.95
Tm169	9.75	17.80	71.37	6.10	9.10	12.02	13.20	41.28	17.33
Yb172	104.84	195.95	684.24	65.15	96.53	132.33	151.82	412.98	178.35
Lu175	23.03	44.98	135.50	14.44	21.09	29.27	36.83	84.28	37.46
Hf178	8994.16	8698.53	6635.47	7812.70	8935.29	8053.99	8531.20	7408.48	8942.01
Ta181	0.47	0.96	0.70	0.20	0.56	0.25	0.43	0.53	0.56
Pb208	12.93	30.74	151.79	5.93	14.19	10.42	19.23	60.26	29.68
Th232	63.37	148.60	728.29	26.55	73.83	51.05	95.85	308.09	128.14
U238	125.79	291.55	468.76	59.43	166.13	76.84	200.78	280.13	183.54
(La/Lu)$_N$	2492.97	8990.54	10034.03	307.78	927.78	14029.43	3544.71	5965.95	2027.50
(La/Sm)$_N$	14.65	69.10	142.04	4.15	11.04	81.10	14.72	71.89	16.55
(Dy/Lu)$_N$	11.93	12.89	6.38	10.66	12.54	11.94	17.78	7.76	9.71
ΣREE	220.68	411.39	1668.86	148.19	209.24	276.54	299.59	955.36	390.05
Ce/Ce*	18.91	18.45	28.44	17.92	3.63	5.74	28.01	14.57	13.60
Eu/Eu*	0.36	0.37	0.60	1.12	1.43	0.58	0.54	0.64	0.50

Appendix IV: Trace element content zircons ER1109 (ppm) (4)

	Z513-2	**Z513-3**	**Z543-1**	**Z543-2**	**Z543-3**	**Z543-4**	**Z585-1**	**Z585-2**	**Z585-3**
Li7	23.21	<11.36	<13.96	<13.92	<13.70	<13.67	<17.86	<10.00	13.68
B11	<1.60	1.67	3.05	<1.41	<1.60	<1.28	<2.17	<1.18	<1.30
Si29	151684.05	151684.05	151684.06	151684.06	151684.08	151684.08	151684.06	151684.05	151684.06
Ca43	508.81	285.26	<191.31	<185.05	<182.04	<172.95	3303.29	<151.23	<163.74
Sc45	860.69	830.89	821.56	916.66	919.45	875.44	742.43	835.23	859.12
Ti47	3848.81	3875.16	3622.46	3766.75	3809.21	3784.89	3493.85	3959.29	3852.05
Ti49	7.18	7.52	29.12	7.86	7.83	6.12	<4.04	4.61	6.52
V51	14.22	2.80	0.70	0.83	0.54	1.01	1.03	0.58	1.64
Cr53	<2.57	<2.53	<2.40	<2.83	<2.35	<2.38	<4.24	2.33	<2.26
Co59	0.18	<0.189	1.53	<0.190	0.19	1.34	<0.34	<0.183	0.65
Cu63	1.01	2.80	<0.50	<0.49	<0.43	<0.46	4.55	0.43	3.49
Zn66	1.09	1.71	2.49	<0.92	<0.86	2.50	3.16	<0.71	2.26
Ga69	<0.166	0.23	0.28	<0.132	<0.172	<0.148	3.62	<0.153	<0.159
Ge72	<1.90	<1.74	<1.70	<1.69	<1.73	<1.75	<2.81	<1.38	<1.50
Rb85	0.66	0.37	7.36	0.30	0.16	0.22	0.31	<0.084	0.18
Sr88	0.81	0.53	1.15	0.42	0.36	0.55	37.21	0.29	0.49
Y89	1707.14	458.61	440.24	1260.67	1122.41	595.82	141.76	322.99	371.02
Zr90	491059.09	484833.09	478880.41	499367.38	505450.53	512669.59	433671.38	503289.97	508419.28
Nb93	3.16	1.63	1.87	2.63	2.27	1.66	1.40	1.70	1.87
Cs133	<0.044	<0.048	1.50	<0.039	0.08	0.07	<0.072	0.05	<0.042
Ba137	3.05	2.71	2.26	0.28	<0.31	<0.29	90.55	<0.31	1.81
La139	0.19	0.17	0.37	0.09	0.13	0.44	0.44	0.05	0.19
Ce140	22.15	14.50	9.44	17.56	17.12	12.41	5.57	7.68	9.24
Pr141	0.40	0.25	0.23	0.33	0.41	0.65	0.08	0.06	0.11
Nd146	4.39	1.77	2.09	4.79	4.62	4.92	0.73	0.48	1.00
Sm147	6.22	1.78	2.46	6.36	6.61	4.58	0.70	0.93	1.70
Eu153	3.70	0.93	1.51	3.43	3.36	2.83	0.32	0.57	0.80
Gd157	38.26	9.59	11.47	30.62	29.38	15.81	2.29	6.38	7.61
Tb159	12.01	3.04	3.33	9.37	8.74	4.69	0.97	2.21	2.47
Dy163	146.30	37.78	38.90	111.92	102.02	52.77	10.74	26.00	30.37
Ho165	56.86	15.05	14.31	40.68	36.47	19.38	4.55	10.20	11.93
Er166	272.29	76.50	70.58	196.25	173.64	91.03	24.02	51.90	59.58
Tm169	59.38	17.91	15.27	42.30	36.57	19.82	6.01	12.35	13.62
Yb172	576.36	185.08	154.23	404.95	357.18	197.20	67.42	132.42	141.03
Lu175	117.19	40.08	31.59	84.11	73.39	39.96	14.31	26.84	29.40
Hf178	7730.23	8640.15	7370.26	7461.25	7528.27	7729.23	8271.40	9183.80	8604.75
Ta181	0.63	0.35	0.29	0.45	0.52	0.31	0.21	0.22	0.27
Pb208	91.02	20.12	12.77	46.00	36.71	15.00	7.62	9.68	14.22
Th232	528.8	106.6	73.2	269.7	211.0	89.0	40.4	57.9	78.9
U238	424.1	139.2	93.0	251.6	199.5	105.5	82.2	83.6	112.9
$(La/Lu)_N$	6005.46	2244.98	827.02	8875.44	5316.17	871.00	313.33	5130.57	1475.23
$(La/Sm)_N$	52.98	16.57	10.70	111.55	79.59	16.59	2.55	29.55	14.18
$(Dy/Lu)_N$	8.01	10.61	8.12	7.52	7.19	7.57	13.32	10.32	9.68
ΣREE	1315.70	404.42	355.78	952.76	849.64	466.49	138.16	278.07	309.04
Ce/Ce*	14.22	14.06	7.62	14.42	11.19	4.58	6.58	29.91	15.53
Eu/Eu*	0.56	0.55	0.72	0.62	0.62	0.91	0.71	0.53	0.57

Appendix V: Kilo Drie Metagabbro composition compared to the Charlie Gabbro composition

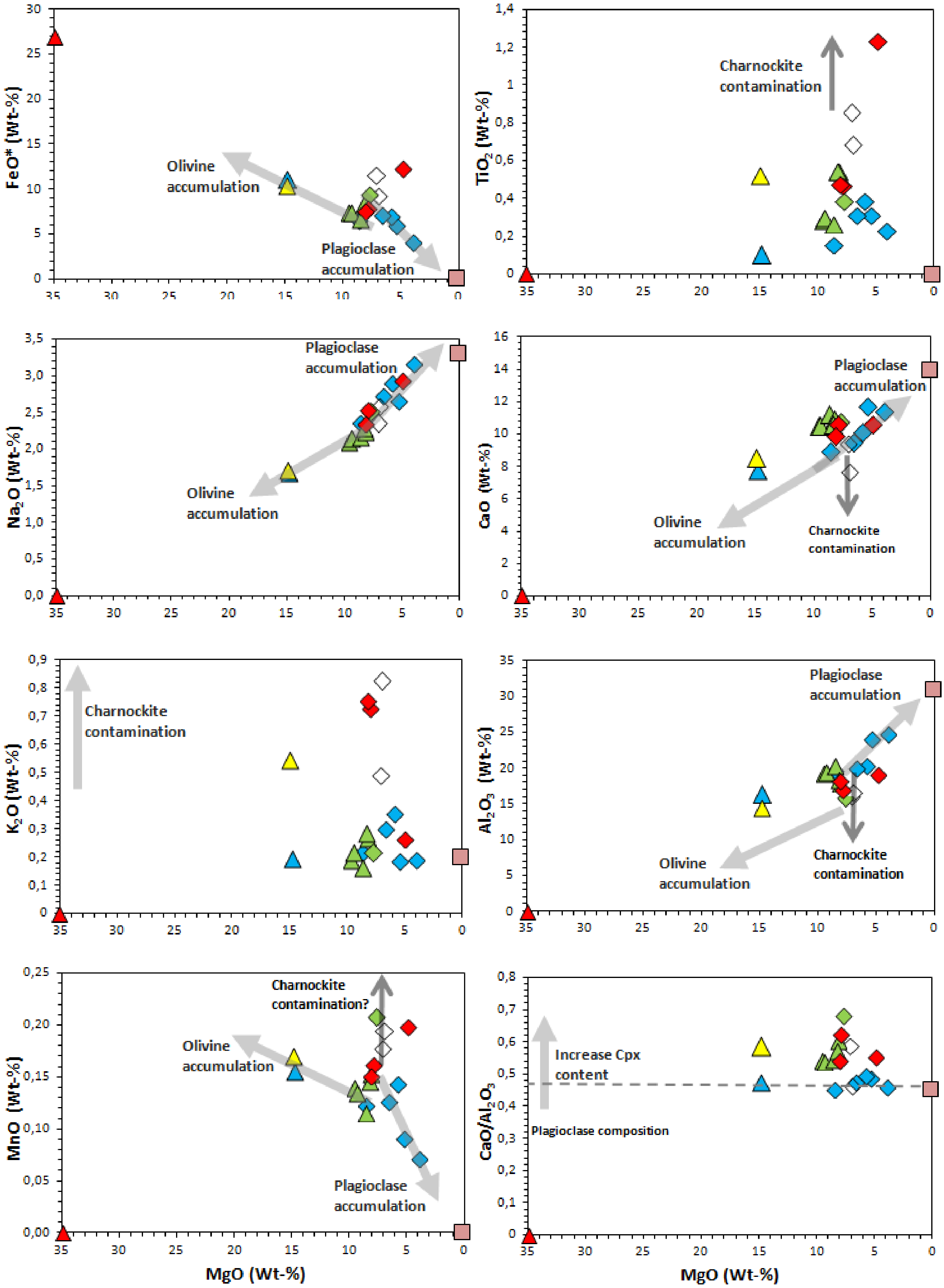

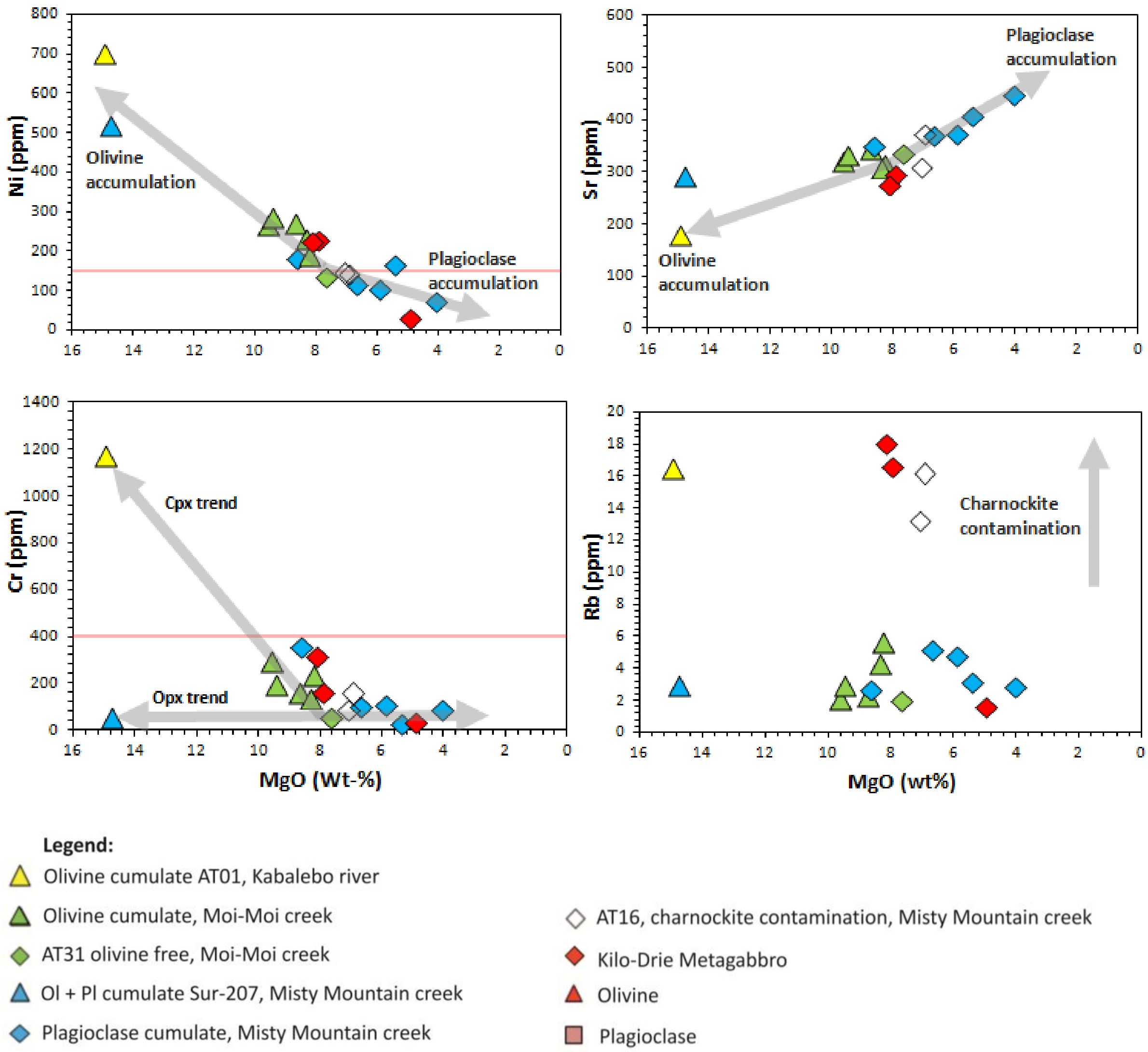
Ni (ppm)
Olivine accumulation
Plagioclase accumulation
Sr (ppm)
Plagioclase accumulation
Olivine accumulation
Cr (ppm)
Cpx trend
Opx trend
MgO (Wt-%)
Rb (ppm)
Charnockite contamination
MgO (wt%)
Legend:
Olivine cumulate AT01, Kabalebo river
Olivine cumulate, Moi-Moi creek
AT31 olivine free, Moi-Moi creek
Ol + Pl cumulate Sur-207, Misty Mountain creek
Plagioclase cumulate, Misty Mountain creek
AT16, charnockite contamination, Misty Mountain creek
Kilo-Drie Metagabbro
Olivine
Plagioclase